ABSTRACT

Title of Document: MICROTURBOPUMP UTILIZING MICROBALL BEARINGS

Christopher M. Waits, Doctor of Philosophy, 2008

Directed By: Professor Reza Ghodssi
Department of Electrical and Computer Engineering
Institute for Systems Research

This dissertation presents the development of a microfabricated turbopump capable of delivering fuel with the flow rates and pressures required for portable power generation. The device is composed of a spiral-groove viscous pump that is driven by a radial in-flow air turbine and supported using a novel encapsulated microball bearing.

First, the encapsulated microball bearing and methods to investigate the wear and friction behaviors were developed. Two primary raceway designs, point-contact and planar-contact designs, were developed with the key design factor being wearing of the raceway. A modification to the planar-contact design was made for the final turbopump that reduced both wear and debris generation.

Second, two air turbine platforms were developed using the encapsulated microball bearings to characterize both the bearing and the turbine drive mechanism. A tangential air turbine platform was first developed and characterized using the point-contact bearing mechanism. Rotational speeds >37,000 rpm were demonstrated

and long-term operation (>24 hours) using this platform, but with large driving pressures (tens of psi) and large raceway wear (tens of microns). Furthermore, the circumferential asymmetry of the turbine design led to difficulty in measuring pressure distribution and sealing for pump applications.

Results from the tangential air turbine platform led to an axisymmetric radial in-flow air turbine platform using a planar-contact bearing design. Rotational speeds greater than 85,000 rpm with turbine pressure differentials in the range of 1 psi were demonstrated using this platform. The wear of the raceway was observed to be on the order of single microns (a 10x improvement). The radial in-flow air turbine platform allowed an empirical model to be developed relating the friction torque to the rotational speed and load for the planar-contact bearing. This enabled calculation of the power balance for pumping and a method to characterize future bearing designs and materials.

Lastly, a microfabricated turbopump was demonstrated based on a spiral-groove viscous pump and the radial in-flow turbine platform using the planar-contact bearing. Pumping operation was demonstrated with a differential pressure up to +0.3 psi and flow rates ranging from 35 mL/hour to 70 mL/hour, within the range relevant to portable power generation.

MICROTURBOPUMP UTILIZING MICROBALL BEARINGS

By

Christopher M. Waits

Dissertation submitted to the Faculty of the Graduate School of the
University of Maryland, College Park, in partial fulfillment
of the requirements for the degree of
Doctor of Philosophy
2008

Advisory Committee:
Professor Reza Ghodssi, Chair
Professor P.S. Krishnaprasad
Professor Isaak D. Mayergoyz
Professor Martin Peckerar
Professor Christopher Cadou

Acknowledgements

The work presented in this dissertation could not have been possible without the support of many people.

First and foremost, I would like to thank my advisor, Dr. Reza Ghodssi, for his guidance and support throughout my graduate career. I would also like to thank my dissertation committee members Prof. Krishnaprasad, Prof. Christopher Cadou, Prof. Mayergoyz, and Prof. Peckerar.

All members of the MEMS Sensors and Actuators Laboratory (MSAL) are thanked, but special thanks go to Dr. Matthew McCarthy for his large technical contribution to this work, many hours of discussion, help in the design of the successful turbopump, and the thorough editing performed on this dissertation. I would also like to thank past members of MSAL, now Drs. Nima Ghalichechian and Alireza Modafe for their initial help in the design of the microball bearing mechanism. Additionally, I have significantly benefited from conversations with Dr. Brian Morgan and also thank him for the superb editing job he did for this dissertation.

All of the work contained within this dissertation was performed in the magnificent cleanroom facilities at the Army Research Laboratory. It would not have been possible without the perpetual upkeep required by the cleanroom manager Dr. Brett Piekarski and the wonderful cleanroom staff. Special thanks go to Mr. Nelson Mark for his endless aide during cleanroom troubles and to Dr. Madhumita Roy for the thermal oxidation growths. I would also like to thank Mr. Bruce Geil for his guidance at the Army Research Laboratory and discussions on this work.

I am so grateful to all of my friends and family who have supported me up to this point in my life. I am most grateful to my parents, Michael and Carol. Without their continuing support and push, I would have never begun or endured graduate school.

Most of all, I am deeply grateful to my wife, Caroline Duffy, for her unending support and love. I could not have finished this work without her.

Table of Contents

Acknowledgements ii
Table of Contents iv
List of Tables vi
List of Figures vii
List of Figures vii
1 Introduction 1
1.1 PowerMEMS Fuel Delivery 1
1.2 Summary of Contributions 3
1.3 Literature Review 6
1.3.1 MEMS Mechanical Liquid Pumping Technologies 7
1.3.2 Microfabricated Turbopumps 9
1.3.3 Bearing Mechanisms Review 12
1.4 Thesis Objective and Structure 18
2 Microball Bearings for Silicon Turbomachinery 22
2.1 Encapsulated Microball Bearings 23
2.1.1 Microball bearing material and geometry 26
2.1.2 Fabrication sequence 28
2.1.3 Alignment and Bonding 30
2.2 Bearing Contact Mechanics 38
2.3 Tangential Flow Microturbine using the Point-contact Bearing 44
2.3.1 Point-contact Bearing Design 45
2.3.2 Tangential Flow Microturbine Design 46
2.3.3 Rotor sag 48
2.3.4 Bearing Contact Analysis 50
2.3.5 Fabrication 52
2.3.6 Testing 57
2.3.7 Results and discussion 62
2.4 Radial In-flow Microturbine using the Planar-Contact Bearing 68
2.4.1 Planar-Contact Bearing Design 69
2.4.2 Radial In-flow Microturbine Design 71
2.4.3 Rotor sag 73
2.4.4 Bearing Contact Analysis 75
2.4.5 Fabrication 78
2.4.6 Characterization 80
2.4.7 Spin-down Friction Testing 89
2.5 Summary 93
3 Microfabricated Turbopump Designs 95
3.1 Micro Turbopump Requirements 97
3.2 Centrifugal Turbopump 98

3.2.1 Impeller design 100
3.2.2 Volute design 104
3.2.3 Fabrication 106
3.2.4 Testing 109
3.2.5 Summary 114
3.3 Spiral-Groove Viscous Turbopump 115
3.3.1 Design Overview 116
3.3.2 Spiral-groove design 118
3.3.3 Power Balance 123
3.3.4 Design Summary 129
3.3.5 Layout and fabrication 130
3.4 Turbopump Summary 150
4 Micro Turbopump Characterization 152
4.1 Experimental Apparatus and Test Setup 153
4.1.1 Device Testing Jig 154
4.1.2 Measurement Suite 157
4.2 Assembled Device 160
4.3 Turbine Characterization 161
4.4 Pump Characterization 166
4.4.1 Start-up Behavior 168
4.4.2 Device 1 Characterization 171
4.4.3 Device 2 Characterization 176
4.5 Summary 178
5 Conclusions and Future Work 180
5.1 Summary 180
5.2 Summary of Accomplishments 184
5.3 Future Work 187
5.3.1 Microball Bearings 187
5.3.2 Standalone Bearing Module 190
5.3.3 Turbopump Considerations 192
5.3.4 Integrated MEMS micromotor and micropump 193
Bibliography 196
Record of Publication for Related Work 202

List of Tables

Table 1.1. Timeline of technology development 20

Table 2.1. Material properties of microballs and silicon [50]..... 27

Table 2.2. Curve-fit values [54]. 44

Table 2.3. Dimensions of the point-contact ball bearing mechanism. 46

Table 2.4. Parameters for the planar-contact bearing. 70

Table 3.1. Centrifugal turbopump parameters 99

Table 3.2. Symbols used for the design of the viscous groove turbopump. 119

Table 3.3. Table showing designed values for the spiral-groove turbopump. ... 121

Table 3.4. Spiral-groove turbopump critical parameter summary. 130

Table 4.1. Characteristics of devices tested. 161

Table 5.1. Timeline of technology development 181

List of Figures

Figure 1.1. Plot showing energy densities of liquid portable power sources including diesel engines, Direct Methanol Fuel Cells (DMFC), Proton Exchange Membrane Fuel Cells (PEMFC), and primary batteries.....2

Figure 1.2. Illustrations demonstrating the operation of a reciprocating displacement pump. (a) Shows the top view and cross-section while (b) shows the discharge and suction strokes (Santiago et al., 2004).....8

Figure 1.3. Schematic of a centrifugal turbopump supported by air bearings and driven by a single radial in-flow air turbine. The centrifugal geometry is at the center of the air turbine and pumps radially outward (Diez, 2003).....10

Figure 1.4. Schematic of a spiral-groove viscous turbopump supported by air bearings and driven using a multi-stage radial in-flow air turbine (Lee, 2006).....11

Figure 1.5. Optical photograph (top) and schematic (bottom) of a microturbine-driven hydrostatic bearing rig (Fréchette et al., 2005).....13

Figure 1.6. Schematic diagrams demonstrating the operation of the hydrostatic gas bearing (Fréchette et al., 2005).....14

Figure 1.7. (a) Schematic showing the linear variable capacitance micromotor and (b) an optical picture showing the stator and electrical poles (Modafe et al., 2006).....16

Figure 1.8. (a) Schematic depicting the assembly of the slider, microballs, and stator; (b) schematic depicting the operation of the linear tribology experiments; and (c) optical photograph of the linear tribology testing platform (Hanrahan, 2007).....17

Figure 1.9. Schematic illustrating the micro-turbopump design concept.....19

Figure 2.1. Schematic showing the cross-section and top down views of the centrally located encapsulated bearing configuration.....24

Figure 2.2. Schematic showing the cross-section and top down view of the periphery encapsulated microball bearing configuration.....25

Figure 2.3. Illustrations of possible microfabricated raceway geometries: (a) a rounded race, (b) an angular contact race and (c) a square-groove race.....28

Figure 2.4. Fabrication flow for the periphery microball bearing.....29

Figure 2.5. Schematic of (a) top view and (b) cross section A-A' view of the alignment pits and microball for wafer level and die level alignment.....31

Figure 2.6. Plot of maximum misalignment as a result of etch depth inaccuracies up to 25 μm.....33

Figure 2.7. Schematic (a) showing the anodic bond demonstration piece and (b) anodic bonding demonstration with stainless steel microball.....34

Figure 2.8. Infrared images showing stainless steel balls encapsulated within a silicon trench using silicon fusion bonding.....36

Figure 2.9. Phase diagram for Au-Sn alloys (Chuang et al., 2004).....37

Figure 2.10. Geometrical reference for ball bearings. (a) depicts the top down view and (b) depicts the cross section A-A'.....40

Figure 2.11. Schematic showing the point-contact microball bearing design. The rotational axis of the rotor is shown by the A-A' dashed line.....45

Figure 2.12. Schematic drawing of a tangential air turbine design for microball bearing characterization: (a) tangential air turbine design on one side, (b) measurement geometry on the other side, and (c) cross-sectional view.....47
Figure 2.13. Schematic cross-section of the tangential air turbine.....48
Figure 2.14. Schematic of the point-contact bearing showing the dimensions including fabrication tolerances.....49
Figure 2.15. Schematic of the point-contact bearing describing the geometry for contact area calculation.....50
Figure 2.16. Initial contact area and corresponding maximum compressive stress on the raceway plotted for increasing raceway curvature due to wear and ball load of 500mN.....51
Figure 2.17. The raceway deformation plotted for increasing raceway curvature due to wear with a ball load of 500mN.....52
Figure 2.18. Fabrication sequence for the point-contact microball bearing support for the tangential air turbine.....53
Figure 2.19. Optical photograph of a finished rotor layer before bonding.....55
Figure 2.20. Optical photograph showing a release tangential air turbine with the inlet and outlet.....56
Figure 2.21. SEM image of a released rotor showing the divots caused by an over etch during the release.....56
Figure 2.22. Schematic demonstrating the metal over flow trench.....57
Figure 2.23. Flow used for testing the tangential air turbine.....58

Figure 2.24. Screenshot of the LabView program front panel used to control the N2 line pressure, collect ODS data, and compute the revolutions per minute.....59

Figure 2.25. Example of captured data from the optical displacement sensor showing rotation.....60

Figure 2.26. (a) Schematic and (b) optical picture of the tangential air turbine test fixture.....61

Figure 2.27. Plot showing rotational rate versus N2 line pressure.....62

Figure 2.28. Graph of a turbine run at a constant 10 psi N2 line pressure for over 24 hours.....63

Figure 2.29. Edge view of the silicon race on the rotor after more than 25 hours of operation at an average speed of 20,000rpm.....64

Figure 2.30. SEM showing the outer race after more than 25 hours of operation at an average speed of 20,000 rpm. The microballs exhibited minimal damage and were lightly adhered to the race surface..... 65

Figure 2.31. Schematic drawing showing how the rotor is shifted up due to the N2 pressure.....65

Figure 2.32. Contact area and maximum compressive stress plotted for a range of estimated raceway curvatures and an estimated ball load of 4.3N.....67

Figure 2.33. Schematic of the planar-contact design employing an off-center journal.....70

Figure 2.34. Illustrations showing: (a) cross-sectional view of the radial in-flow turbine supported by the encapsulated microball bearing; (b) radial in-flow air turbine design; and (c) planar-contact bearing orientation.....72

Figure 2.35. Illustration of the packaging scheme for the microturbine tribology device.....72

Figure 2.36. Schematic of the planar-contact bearing for a normal load in the (a) designed direction, (b) non-designed direction, and (c) a schematic showing the geometry required to calculate the sag of the rotor.....75

Figure 2.37. Schematics showing the planar bearing design radius of curvature in (a) the top down view of the raceway and (b) profile view.....76

Figure 2.38. Plot showing the contact area and maximum compressive stress (σMax) trends for a 500mN load and increasing raceway curvature of a planar-contact bearing.....77

Figure 2.39. Fabrication sequence for the microturbine tribology device.....79

Figure 2.40. Photos of a completed microturbine device showing (a) the turbine side and (b) the thrust bearing side of the device with the cross-section A-A' in (c).....80

Figure 2.41. Schematic of the experimental apparatus used for testing the microturbine tribology device.....81

Figure 2.42. Optical photograph of a packaged microturbine showing various pneumatic connections and the optical displacement sensor.....82

Figure 2.43. Turbine performance curves showing the rotational speed, rotor normal force (without applied thrust pressure) and turbine flowrate plotted for turbine operation pressures.....83

Figure 2.44. Speed plotted against time for the microturbine after successive cleaning procedures showing the microturbine having longer stable operation with increased revolutions.....84

Figure 2.45. SEM images of (a) the microturbine rotor and (b) an image of the unworn race and (c) an image of the worn race.....85

Figure 2.46. Cartoon drawing describing the rotor shift and eventual rubbing on the stator. (a) shows ideal case, (b) shows areas of misalignment and wear, (c) shows contact points when rotor rubs due to whirl.....87

Figure 2.47. SEM image showing evidence of the rotor rubbing.....87

Figure 2.48. SEM showing the misalignment between the topside journal definition and backside journal definition.....88

Figure 2.49. SEM image showing the wear exhibited at the bond interface between the two raceways; the radial bearing surface. (a) shows the profile view of the rotor raceway and (b) shows the top-down view of the bond interface wear.....88

Figure 2.50. Spin-down data showing the angular position and the thrust force over time. Region 1 exhibits the constant operation of the turbine. At the beginning of region two, the turbine driving flow was turned off (can see the spike from flipping the valve) and region 3 is when the thrust load equilibrates to the load prescribed by the thrust bearing.....91

Figure 2.51. Spin-down data for thrust loads of 6, 14, 25, and 50 mN.....92

Figure 2.52. Plot of τ/ω versus the normal load on the rotor.....92

Figure 3.1. Schematic illustrating the micro turbopump concept.....96

Figure 3.2. Schematic of the centrifugal turbopump.....98

Figure 3.3. Schematic drawing of the pump rotor level showing the rotating component inside the dotted line.....100

Figure 3.4. Velocity vectors for the pump impeller where subscript 1 denotes inlet flow, subscript 2 denotes outlet flow, U is the mean velocity vector (rotational vector), and W is the relative velocity vector.....102

Figure 3.5. Graphs showing the relationship between impeller rotational speed and: (a) volumetric flow rate, (b) the pressure rise across the impeller, and (c) the required torque for the desired flow rate and pressure rise. In these graphs, the inner radius is set to 100μm, the height of the leading edge flow passage is 100μm, the flow angle is 67°, and JP-8 diesel fuel is assumed.....103

Figure 3.6. Schematic for the design of the centrifugal pump volute.....105

Figure 3.7. Fabrication sequence for the centrifugal turbopump.....107

Figure 3.8 Optical image showing a completed centrifugal impeller and volute.....108

Figure 3.9. SEM images of a partially released rotor demonstrating the non-uniform etching during the release process. The race (a) extending across the volute exit is released before (b) other areas due to the effect of the DRIE fillet radius.....109

Figure 3.10. Optical image of the aluminum testing fixture with the Nitrogen line hooked up and the ODS in place within the fixture.....110

Figure 3.11. Plot demonstrating centrifugal and turbine operation.....111

Figure 3.12. Illustration of the centrifugal volute and the critical sealing gap.....112

Figure 3.13. Illustration of the force balance between two fluids.....113

Figure 3.14. Plot showing the relationship between the critical gap and the allowed pressure difference between two fluids for sealing.....113

Figure 3.15. Schematic cross-section of the spiral-groove turbopump.....116

Figure 3.16. Diagram illustrating the groove geometry and gap within the spiral-groove viscous pump. The rotational axis is denoted by the A-A' dashed line.....119

Figure 3.17. Pump curve for a gap of 10um.....122

Figure 3.18. Plot showing the relationship between the Flow Ratio, δ, and g1 for a spiral angle α=16.6∨ and groove to blade width ratio γ=1.....122

Figure 3.19. Pump curves for gaps ranging from 10 μm to 22 μm.....123

Figure 3.20. Illustration of the spiral-groove region, the gap, *h2,* within the viscous pump, and the sealing region. The rotational axis is denoted by the A-A' dashed line.....126

Figure 3.21. Power curves showing the ideal and deviated turbine power considering bearing friction and the power dissipated due to viscous forces on the pump side for a minimally wetted surface area.....128

Figure 3.22. Schematic showing the bottom of the pump plumbing layer.....131

Figure 3.23. Schematic of the logarithmic spiral.....132

Figure 3.24. Schematic showing the top of the pump plumbing layer.....134

Figure 3.25. Fabrication sequence for the pump plumbing layer including the spirals.....135

Figure 3.26. Optical image showing the topside of the pump plumbing layer and the residue left behind from the Cool Grease DRIE carrier attachment.....136

Figure 3.27. Optical image showing (a) the bottom of the pump plumbing layer and (b) a close up view of the spirals.....136

Figure 3.28. Schematic drawing of the planar-contact bearing V.2 implemented in the spiral-groove turbopump.....137

Figure 3.29. SEM images showing the planar bearing race fabricated with (a) the nested masking technique and (b) the spray coating technique.....138

Figure 3.30. (a) Original planar bearing fabrication process using nested photoresist and silicon dioxide masks and (b) new planar bearing fabrication process eliminating the nested masking technique for a smooth bearing surface.....140

Figure 3.31. Optical photograph of a silicon trench cross-section demonstrating the buildup of photoresist at the corners of a trench. Note the different photoresist thickness between the wafer surface and the trench bottom.....141

Figure 3.32. Optical image showing (a) the turbine side of the rotor layer #2 and (b) a close up of a released turbine rotor.....143

Figure 3.33. Schematic showing the top of the rotor layer.....144

Figure 3.34. Schematic showing the top of the rotor layer.....145

Figure 3.35. Fabrication flow of the turbine plumbing layer (Layer #1)……146

Figure 3.36. Optical images showing (a) the top of the turbine plumbing layer with the silicon dioxide layer still present and (b) the bottom of the turbine plumbing layer.....147

Figure 3.37. Schematic of the assembly and ports for the turbopump device.....148

Figure 3.38. Optical image showing tubulations attached to the bottom of the turbine plumbing layer.....148

Figure 3.39. Optical photograph of a completed spiral-groove turbopump.....150

Figure 4.1. Liquid and gas designations for the spiral groove turbopump.....153

Figure 4.2. Schematic of the assembly and ports for the turbopump device.....154

Figure 4.3. Illustration of the mechanical jig with the turbopump inside.....155

Figure 4.4. Photograph of the turbopump jig.....155

Figure 4.5. Photograph showing a completely packaged turbopump device.....156

Figure 4.6. Illustration of the packaged turbopump without the pump plumbing layer to characterize the turbine operation.....157

Figure 4.7. Liquid and gas experimental setup diagram for the spiral-groove turbopump.....158

Figure 4.8. Screen shot of the LabView program written for the testing the spiral-groove turbopump.....160

Figure 4.9. Turbine performance curve without liquid using planar-contact bearing V.2 and packaged without the pump plumbing layer.....163

Figure 4.10. Turbine performance curve without liquid using planar-contact bearing V.2 and packaged with pump plumbing layer.....164

Figure 4.11. Demonstration of high-speed operation with the planar-contact V.2 bearing and the radial in-flow air turbine.....166

Figure 4.12. Illustration demonstrating the pump priming procedure. The thrust balance channel pressure (tan) is elevated above the liquid (blue) pressure at the pump outlet to seal.....168

Figure 4.13. Turbopump results when liquid is introduced while rotor is spinning.....169

Figure 4.14. Start up behavior for the turbopump with a turbine flow rate set to 8 slm and liquid flow rate in the range of 45 mL/hour and 60 mL/hour.....171

Figure 4.15. Turbopump demonstration with a turbine flow rate of 8slm and liquid flow rate ranging from 45 mL/hour to 60 mL/hour.....172

Figure 4.16. Re-print of the plot shown in Figure 4.15, but with the normal force calculation added in.....174

Figure 4.17. Power curves for the turbine power with ±10% flow deviation with bearing friction taken into account and the power loss due to viscous forces on the pump side for a maximum and minimum wetted surface area.....175

Figure 4.16. Re-print of the plot shown in Figure 4.15, but with the normal force calculation added in.....177

Figure 4.19. Turbopump characterization and comparison to analytical with an estimated gap of 12 μm.....178

Figure 5.1. Rotational speed plotted for increasing line pressure before and after JP-8 droplets were introduced into the microball bearing race.....189

Figure 5.2. Generic fabrication flow for alternative application.....191

Figure 5.3. Illustration of the electrically driven micropump evolution.....194

1 Introduction

1.1 PowerMEMS Fuel Delivery

Since the mid 1990s, Power Micro Electro Mechanical Systems (PowerMEMS) components and systems have received increased attention for portable power applications. Complete PowerMEMS systems and components are continually being developed for mobile (100s W to 1s kW) and portable (<100 W) power generation applications. Systems currently being investigated for portable power include: gas turbine generators (Brayton thermodynamic cycle) [1, 2], steam engine generators (Rankine thermodynamic cycle) [3], mini/micro rotary engine generators (Otto thermodynamic cycle) [4],[5] and fuel cells [6, 7] to name a few. These systems are envisioned to take advantage of the high density energy stored in hydrocarbons (40-50 MJ/kg) by converting the stored chemical energy first to mechanical and then to electrical energy by turbogenerators or directly to electrical energy from chemical energy by thermal electrics or fuel cells.

Even with relatively low generator efficiencies, a liquid hydrocarbon fueled system, such as a diesel fueled generator, has the potential to achieve greater than 10 times the energy density of current primary batteries, which makes these devices very attractive [8]. As demonstrated in Figure 1.1, which compares the various power sources available for portable power, liquid hydrocarbons offer the most promise [8]. A diesel turbogenerator with efficiency between 5-10% has the potential to provide significantly more energy density than current primary batteries. It can also compete with fuel cell technology without requiring efficiencies greater than 30%.

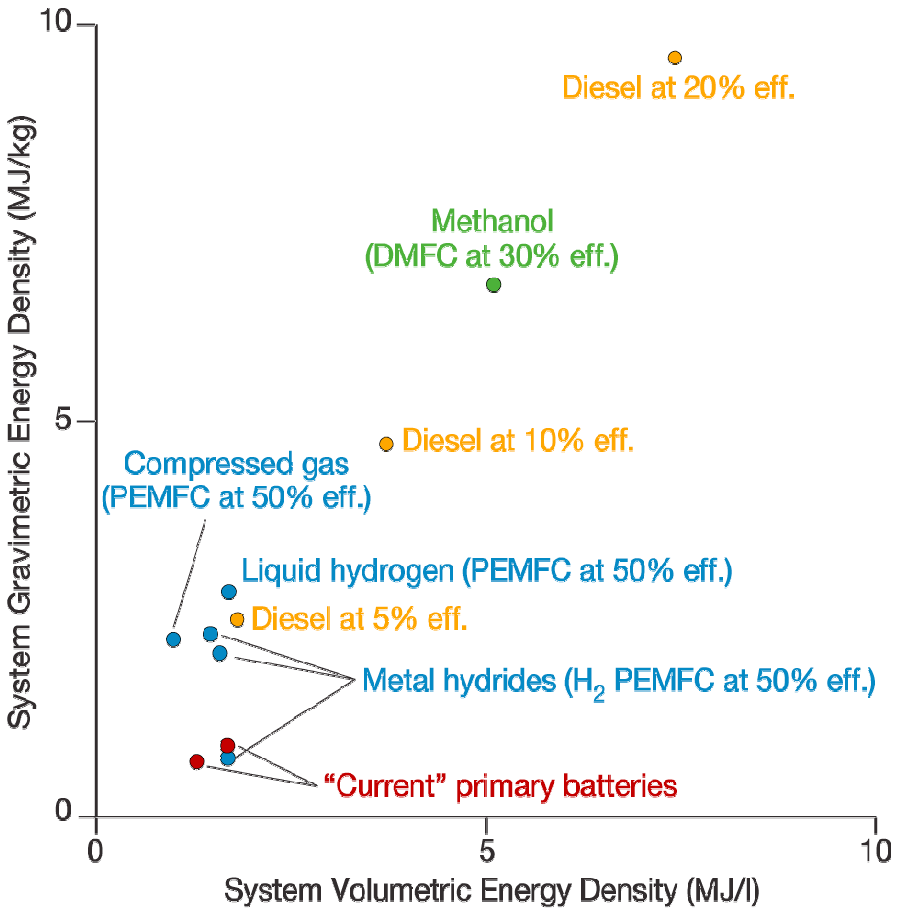

Figure 1.1. Plot showing energy densities of liquid portable power sources including diesel engines, Direct Methanol Fuel Cells (DMFC), Proton Exchange Membrane Fuel Cells (PEMFC), and primary batteries (Epstein, 2005).

In addition to complete systems, PowerMEMS liquid fuel components have been investigated for their use in meso-scale applications requiring <1kW. Some key PowerMEMS components for power generation applications are microfabricated electrospray devices for fuel injection [9, 10], magnetic and electrostatic generators for electrical conversion [11, 12], combustors for fuel reformation [13, 14] and thermal electrics for thermal energy recuperation [15].

Important to any liquid fueled power source is the manner in which the liquid is delivered to the system. Control mechanisms for conventional liquid fuel burning systems adjust the flow rate to deliver the requested power and to maintain peak performance. Fuel delivery components capable of such control for compact liquid fuel systems have not received much attention. The majority of research has been on the engine or generators rather than the ancillary components that enable increased performance. Therefore, compact liquid fuel pumps that can be directly integrated with microfabricated generators or assembled into meso-scale packages are critical for portable power applications.

Silicon microfabrication and MEMS technology lend themselves to developing compact components with high precision while maintaining or even increasing performances. All devices mentioned in this introduction were developed on a silicon platform due to its good mechanical and electrical properties and well established fabrication methods. Building a fuel pump in the same manner will not only allow compact designs, but will also allow direct integration with those power generation systems.

1.2 Summary of Contributions

The first silicon turbopump with a microball bearing support mechanism has been developed for fuel delivery PowerMEMS applications. Before demonstration of the pump, robust rotary microball bearing and drive mechanisms had to be developed and demonstrated. The following are key contributions to this dissertation:

1. **Design, fabrication and demonstration of a spiral groove turbopump supported by a microball bearing**. Integration of encapsulated ball bearings, an air turbine, and spiral-groove geometry was demonstrated in an application for fluidic pumping. Flow rates in the range of 10 mL/hour to 80 mL/hour with differential pump pressures of 0 to 1.2 psi respectively were achieved. The flow rates and pressure capabilities of the developed turbopump demonstrate its potential use for fuel delivery in portable power applications.

2. **Encapsulated microball bearing**. The most influential contribution made is the development of the encapsulated microball bearing for the support of rotary actuation mechanisms. An encapsulation process during the fabrication enables real world applications of the microball bearing technology, which are currently being utilized within the MEMS Sensors and Actuators Laboratory (MSAL) at the University of Maryland. Three microball bearing configurations were investigated along with two different turbine drive mechanisms.
   a) The first encapsulated microball bearings were demonstrated by rotating a square die about a released disc [16, 17]. This device allowed initial investigation of a point-contact bearing design.
   b) A tangential air-turbine drive mechanism was developed to further investigate high speeds and wear within the point-contact bearing design. This device enabled high speed demonstration (speeds reached beyond 35,000 rpm) and characterization of the point-contact raceway wear [18]. The tangential air-turbine and point-contact bearing designs were assessed and found not to be

optimal designs for a micro turbopump application where tight gap tolerances are required.

c) A radial in-flow air turbine actuator was developed to further investigate the tribology characteristics of the encapsulated microball bearing [19]. This device permitted the extraction of an empirical formula for frictional torque versus normal force on a silicon race with and without solid lubrication. In addition to tribology information, this device was used to characterize a planar-contact bearing design. The highest microball bearing speed (>85,000 rpm) was demonstrated using the combination of the radial in-flow air turbine and planar-contact bearing design. Reliability of this configuration was confirmed with more than 2,000,000 revolutions without turbine performance degradation. These experiments concluded that the radial in-flow and planar-contact bearings are well suited for the turbopump application as well as other high-speed, high reliability rotary applications.

3. **Novel device alignment technique**. To facilitate die level bonding, a novel alignment technique using the microballs and alignment pits was developed. This method can be utilized in many applications and is not limited to the fabrication of the microball bearing design or the silicon turbopump. Alignments less than 2 μm can be routinely achieved without the need for specialized equipment.

1.3 Literature Review

Microfabricated pumping devices using MEMS technology have been developed over the past two decades for use in a broad range of applications. Of interest are pumping technologies capable of producing pressures on the order of 1 psi and flow rates on the order of 10's mL/hour for less than 100 W powers with less than 10% efficiency [8, 9]. In addition to these interests, it is preferable that a micropump designed for power generation is capable of pumping a variety of fuels without any dependence on electrical, magnetic, or chemical properties of the fuel. These requirements eliminate most non-mechanical pumps such as magnetic, electro hydrodynamic, or electro osmotic pumping. In contrast, some research on mechanical pumps demonstrates the possibility to operate in the regions of interest while meeting those requirements. A review of MEMS mechanical pumps focusing on potential pumping technologies for liquid fueled power devices follows in section 1.3.1 and 1.3.2.

Since a turbopump is envisioned, it is critical to explore the bearing mechanisms developed for rotary MEMS applications in addition to the pumping technologies. Some constraints, which will be made apparent in the discussion of the design of the turbopump, have been determined for the bearing mechanism. First, the required operational speed of the bearing was determined to be in the 1-50 krpm range for the required flowrate, pressure rise and size being investigated. Second, the complexity of the bearing mechanism should also be considered due to reliability and robustness. Bearing mechanisms previously implemented on a MEMS platform will be reviewed in section 1.3.3, which focuses on the current status of MEMS microball bearings.

1.3.1 MEMS Mechanical Liquid Pumping Technologies

Liquid pumping technologies developed on a MEMS platform offer a wide range of operation and mechanisms. Flow rates from below a μL/min to greater than 10mL/min, with pressure increases well into the psi range, have been achieved [20, 21]. The pump geometry and configurations are thereby dictated by the driving mechanisms and the material selections that meet the criteria for each application.

MEMS mechanical pumps can be classified into two categories, positive displacement and dynamic (or continuous). Displacement pumps exert pressure forces on the fluid through moving structures, thereby adding momentum to the fluid which can be converted into pressure by flow resistances.

Of the assorted displacement pumps reported in literature, reciprocating diaphragm pumps are the most common due to the ability to utilize surface micromachining [21]. Figure 1.2 is a demonstration of a diaphragm pump operating scheme [21]. The pump consists of a reservoir with a deformable membrane as well as an inlet and an outlet both controlled by valves. At the start of a pump cycle, the membrane is un-deformed, both the inlet and outlet valves are closed and the reservoir is filled with liquid. To pump the liquid, the outlet valve is opened and the membrane deformed. Then, to draw in more liquid, the outlet valve is closed, the inlet valve opened, and the membrane returned to the un-deformed state. These steps are repeated with a prescribed frequency and force enabling fluid pumping.

Together, the frequency and force limit the pressure capabilities for pumping with low power consumption and without requiring rectification. However, and more importantly, the inlet and outlet sealing valves are an added complexity and reliability

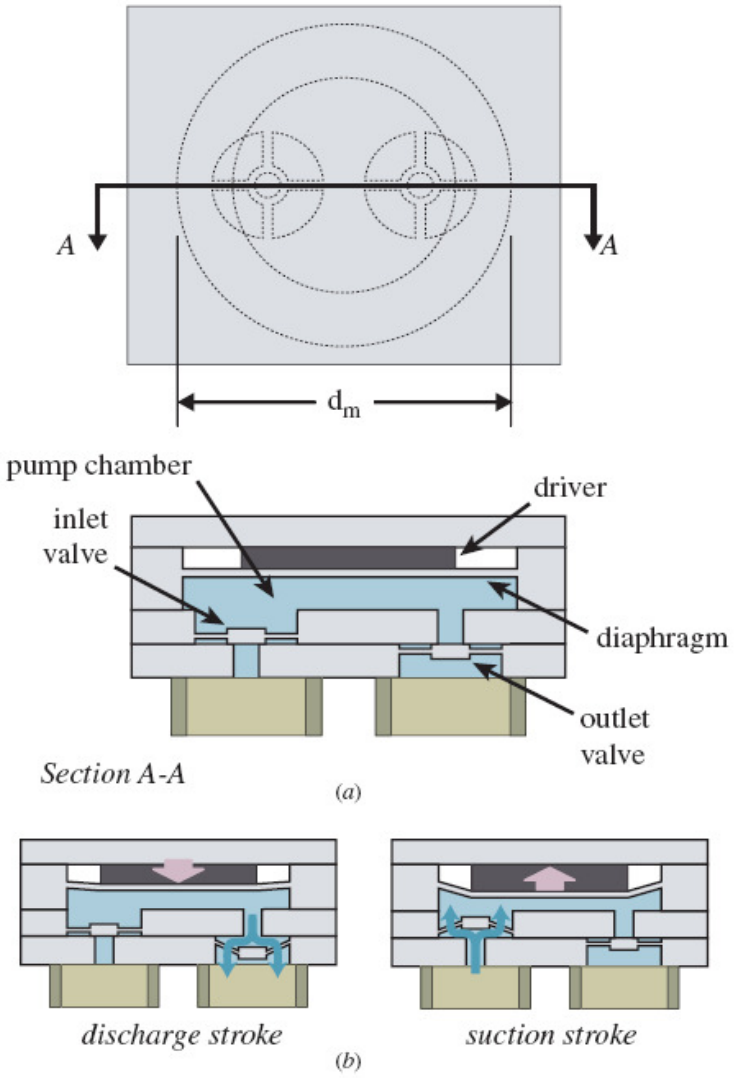

Figure 1.2. Illustrations demonstrating the operation of a reciprocating displacement pump. (a) Shows the top view and cross-section while (b) shows the discharge and suction strokes (Santiago et al., 2004).

concern. Moreover, timing circuitry is necessary and required to be integrated with the pump monolithically for compact designs.

For the required flow rate and pressure, even this type of pump would require a large volume. The diaphragm pumps rely on the compressibility of the fluid and the compression ratio (stroke volume/dead space) [21] . At very small scales, due to the difficulty in the conformity of the deformed diaphragms, the compression ratio decreases,

making it difficult to achieve high pressures. The dead volume causes these pumps to be susceptible to bubble formation, which increases the compressibility, thereby decreasing the maximum pressure available.

Dynamic pumps, the most common pumping mechanism at the macro-scale, have been developed over centuries and do not require valves or rectification. These pumps are characterized by a continuous addition of energy to the working fluid. Dynamic pumps are usually broken up into two types: 1) turbopumps and 2) electromagnetic field driven pumps. A major drawback to electromagnetic driven pumps is dependency on fluid type. For instance, the operation of an electro hydrodynamic pump requires a dielectric fluid and the performance of electro osmotic pumps rely heavily on the pH of the fluid [21]. The pumping action of a turbopump, however, does not depend on the type of fluid being pumped. Only the viscosity or density of the fluid and geometry play roles in determining performance. Unlike other microfabricated pumps, the driving mechanism is purely mechanical for a turbopump, a distinct advantage for integration into heat engines. Additionally, it is possible to exploit the energetic exhaust from heat engines to drive a turbopump, allowing the utilization of wasted energy instead of an external power supply.

1.3.2 Microfabricated Turbopumps

MEMS turbopumps have been studied previously by two groups both emanating from the gas lubricated bearing and micro gas turbine engine work performed at Massachusetts Institute of Technology (MIT). Two different pumping mechanisms were investigated; one group focused on centrifugal-type pumps [22-24] and the other focused

on viscous-type pumps [25]. Both technologies were based on a hydrostatic air bearing support mechanism, which has a complex fabrication process, requires external components, and has not yet been reliably demonstrated. A review of bearing mechanisms will be discussed in section 1.3.3.

A MEMS centrifugal type pump (Figure 1.3) was previously studied for micro propulsion [22-24] at MIT. The requirements for propulsion are such that high pressures (greater than 2 psi) and flow rates (2.5 g/s, approximately 200 ml/hour for JP-8 diesel fuel) are needed for large thrusts. The MIT turbopump required high-speed operation (greater than 300,000 rpm) to obtain the high pressure and flow rates. This created the need for a high-speed bearing mechanism. Currently, gas lubricated bearings, or air bearings, are being investigated for high rotational speeds [26]. In that work, *Deux* was able to achieve approximately 10 psi at 110,000 rpm with a liquid flowrate of 723 mL/hour using water.

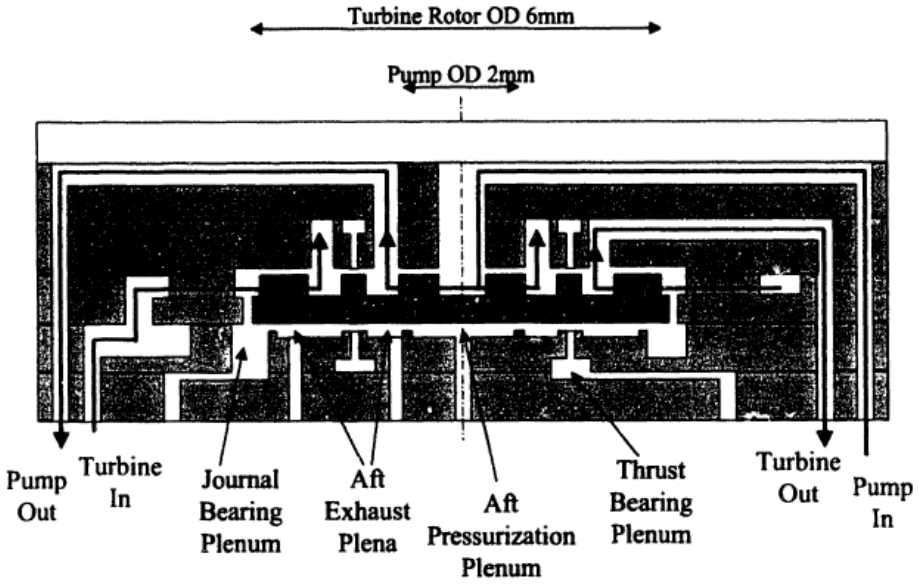

Figure 1.3. Schematic of a centrifugal turbopump supported by air bearings and driven by a single radial in-flow air turbine. The centrifugal geometry is at the center of the air turbine and pumps radially outward (Diez, 2003).

The viscous pump developed by *Lee* [25] was designed to deliver fuel to an external combustor for steam engine application (Figure 1.4). *Lee* argues that at these scales viscous forces are comparable to pumping forces; therefore, it is more beneficial to utilize the viscous forces for pumping rather than pumping against them. A pump efficiency of 7.2% was demonstrated using a spiral-groove viscous turbopump, which they claimed is greater than any other MEMS pump demonstrated. Additionally, viscous pumps typically demonstrate a linear relationship between pressure rise and flowrate [27]. *Lee* demonstrated a nearly linear pump curve with back pressures ranging up to 30 psi at 120,000 rpm for a water flowrate of 36 mL/hour, more than sufficient for portable power applications. Like the centrifugal pump, this viscous pump was demonstrated using an air bearing support mechanism.

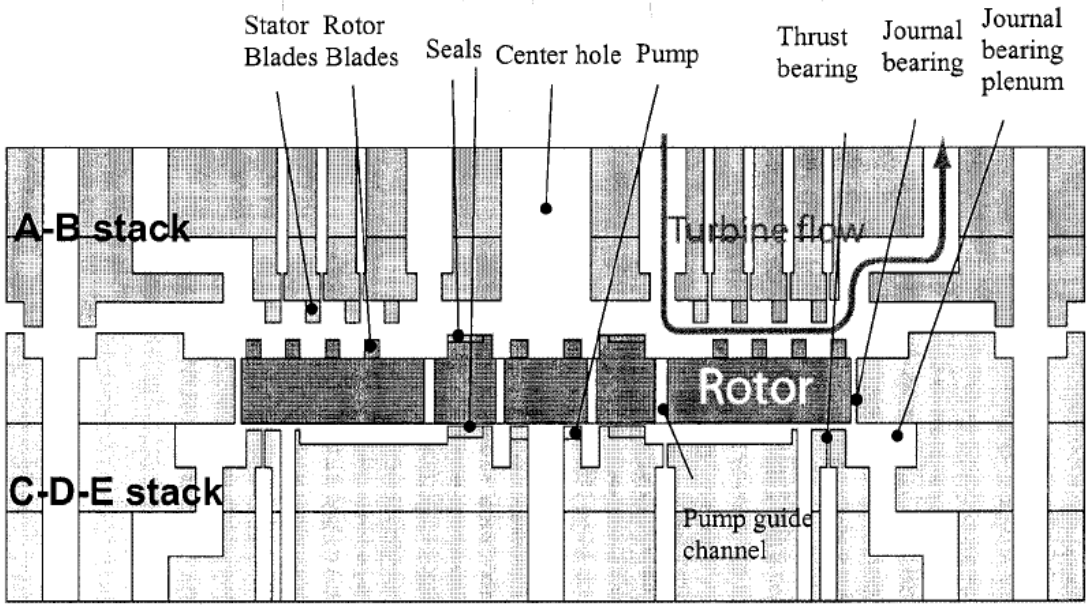

Figure 1.4. Schematic of a spiral-groove viscous turbopump supported by air bearings and driven using a multi-stage radial in-flow air turbine (Lee, 2006).

Although the two pump technologies just described have demonstrated the capability to pump water within the desired pressure and flowrate ranges, there are some drawbacks and concerns in real world applications. The primary concern lies in the air bearing support mechanism, which has yet to demonstrate operation without external pressure sources and requires complex multi-wafer fabrication. The bearing mechanism is a significant limiting factor for any application and will be discussed in the following section.

1.3.3 Bearing Mechanisms Review

MEMS bearing mechanisms were developed as early as 1988 for applications in surface micromachined motors and gears [28]. Application of microfabricated bearings for silicon turbomachinery has been in the development stage since the mid 1990s. In the case of silicon turbomachinery, the bearing mechanism is complex in both fabrication and operation, directly affecting the device reliability, component performance, and overall manufacturability [14]. In all cases, the bearing design and characteristics limit the capabilities of the component or system, namely the maximum speed of rotation and minimum driving power.

Both contact and non-contact bearings have been incorporated within MEMS devices. Non-contact bearings, such as electrostatic bearings or air/gas bearings, allow for the lowest frictional losses. However, they have complex manufacturing steps, exhibit poor stability, and require many ancillary control components [[26]].

A prime example of a non-contact MEMS bearing is the gas lubricated, hydrostatic air bearing mentioned in the previous section [26]. A bearing rig was

designed to test the performance of the air bearing using a radial in-flow air turbine (Figure 1.5) [29]. A schematic is also provided to elucidate more on the bearing operation (Figure 1.6) [29]. The turbine rotor is encased within a silicon housing that provides pressurized gas. Above and below the center portion of the rotor is a hydrostatic bearing that maintains its stiffness using externally controlled pressurized gas (60-85 psi) allowing for large thrust loads. At the periphery of the rotor a journal bearing is provided. An externally controlled pressure plenum below the rotor allows a pressurized flow between the bottom of the rotor and the top where the pressure must be that of the turbine driving flow coming out of the diffuser vanes. The stability of the rotor relies on the stiffness of the journal bearing since the pressurization at this point is coupled to the turbine driving flow and desired to be kept at a minimum.

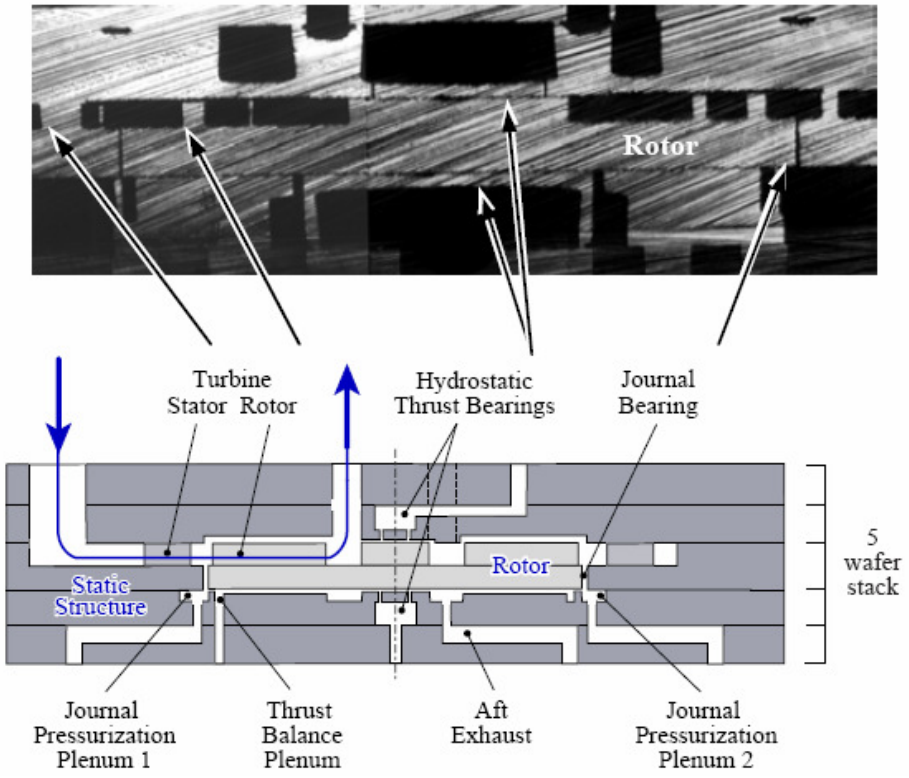

Figure 1.5. Optical photograph (top) and schematic (bottom) of a microturbine-driven hydrostatic bearing rig (Fréchette et al., 2005).

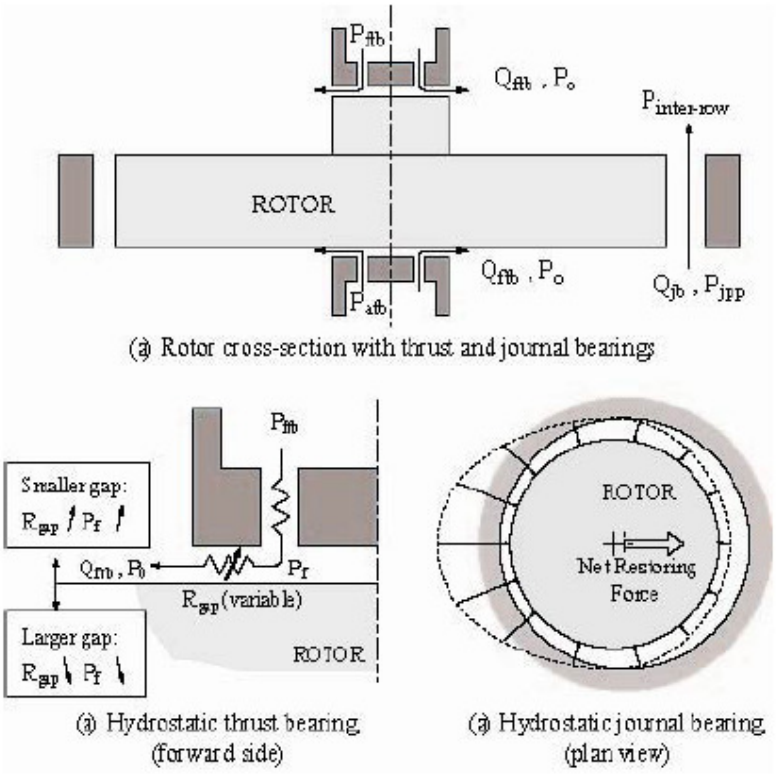

Figure 1.6. Schematic diagrams demonstrating the operation of the hydrostatic gas bearing (Fréchette et al., 2005).

Rotational speeds up to 1.4 Mrpm have been demonstrated; however, there are many issues still being investigated [29]. One issue is the requirement of many external air pressure controls for the journal and thrust bearings. Currently, to allow for the required bearing stiffness, pressures up to 85 psi are being used and are only obtainable by external sources. Additionally, the hydrostatic air bearing requires complex multi-wafer fabrication with extreme tolerances that limit the number of devices per wafer to obtain sufficient device yields.

Other non-contact, minimal friction bearings have been developed using electrostatics, magnetic and electromagnetic mechanisms [30-34]. These bearings were developed for surface micromachined motors and actuators and were demonstrated with

speeds typically less than 1500 rpm and levitations as high as 300 μm. Their utilization in larger volume applications that require a bulk micromachined implementation has not been investigated.

Contact bearings, such as center-pin bearings with sliding bushings, operate passively and are more stable, yet have significantly more friction due to sliding of the surfaces in contact [28, 35-37]. Although speeds up to 15,000 rpm have been demonstrated, the rubbing surfaces cause wear, fracture, stiction, and contamination-based failure modes making this type of bearing non-ideal for high-speed or long-term operation.

Alternatively, rotary ball bearings are attractive due to three characteristics [38]: 1) manufacturing the bearing is simplified compared to other methods [39]; 2) rolling contact yields less friction than sliding contact (yet greater friction than air/gas lubricated); and 3) the balls provide passive rigid stability.

Microball bearings were first used in micromotors within our group, the MEMS Sensors and Actuators Laboratory (MSAL); however the balls within the bearings were not fully enclosed in the silicon structure [4]. Application of a variable capacitive micromotor (Figure 1.7) has a completely free slider held in place by a linear microball bearing channel (race) and the electrostatic force between the stator and slider [40, 41]. In this dissertation there will be no electrostatic force to account for the thrust loads; instead, enclosing the balls inside a silicon race is necessary to account for all loads (radial and both thrust loads). This adds a previously ignored complexity to the fabrication of devices supported by microball bearings. Therefore, an encapsulated design for microball bearings will be pursued.

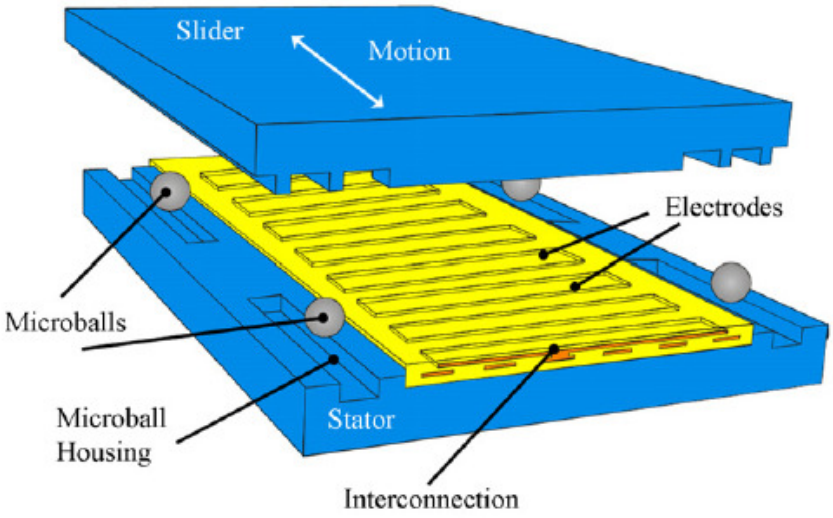

(a)

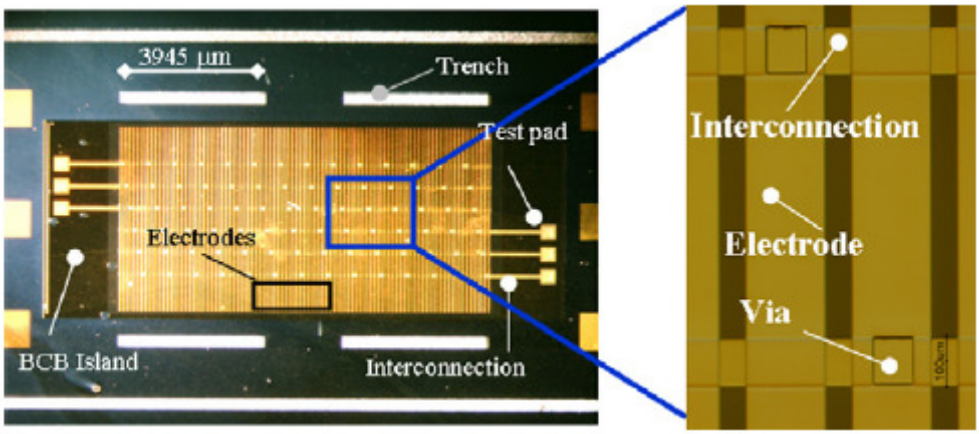

(b)

Figure 1.7. (a) Schematic showing the linear variable capacitance micromotor and (b) an optical picture showing the stator and electrical poles (Modafe et al., 2006).

Investigations to determine the frictional behavior of microball bearings began in 1993 when initial measurements of friction were extracted by simple tilt experiments [42]. Over the past several years, a more complex and comprehensive testing platform was developed using the relative motion between a slider and a stator (Figure 1.8) [43-45]. In this setup, the raceway geometry is etched into a silicon slider and stator.

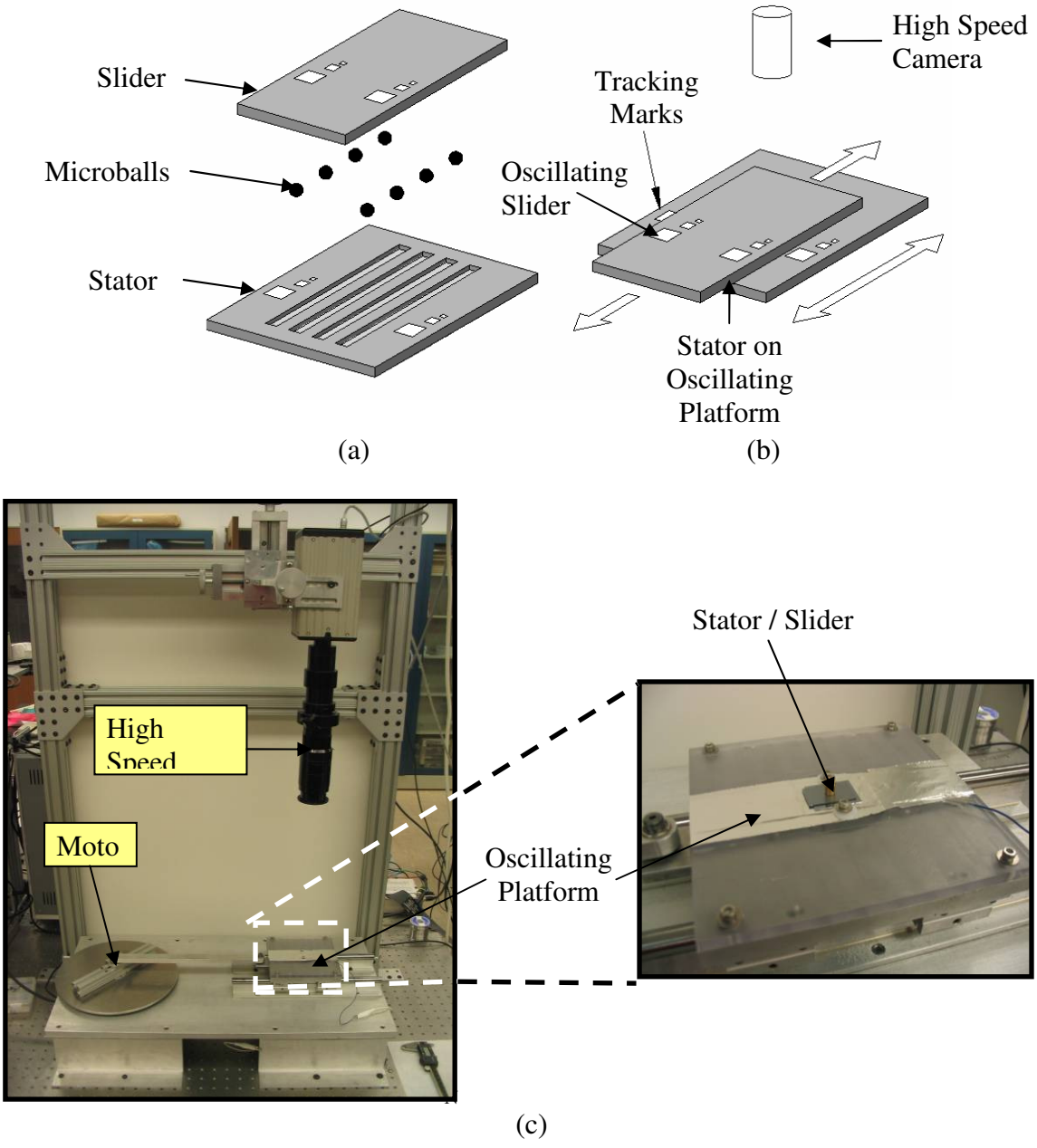

Figure 1.8. (a) Schematic depicting the assembly of the slider, microballs, and stator; (b) schematic depicting the operation of the linear tribology experiments; and (c) optical photograph of the linear tribology testing platform (Hanrahan, 2007).

The stator is adhered to a linearly actuated stage. Microballs are placed into the stator race and the slider is placed on top. A high-speed camera tracks the relative motions, between the actuated stator and the slider, that are caused by the frictional forces between the microballs and the silicon races. Values of less than 0.01 have been measured for the coefficient of friction between a stainless steel microball and a v-groove silicon race. These values were measured for low speeds ranging up to 0.1 m/s, much less than the envisioned speeds required in a micro turbopump for fuel delivery.

1.4 Thesis Objective and Structure

The objective of this dissertation is two-fold: to demonstrate the first liquid fuel delivery micro turbopump with a high speed, high reliability bearing mechanism and to establish encapsulated microball bearings as an attractive support mechanism for high-speed rotary applications. These objectives will enable the delivery of liquid fuel to systems with prescribed pressures and flow rates for portable and mobile power generation applications.

A micro turbopump was pursued for three reasons: (1) the pumping action is purely mechanical; (2) the design can be batch microfabricated allowing for a compact design; and (3) the turbopump is scalable to meet most flow rate and pressure requirements. Figure 1.9 is a conceptual drawing of the developed micro turbopump pointing out the key elements; the pumping structure, the turbine drive mechanism, and the microball bearing support mechanism.

To meet the objectives outlined above this dissertation focuses on the pump structure and the microball bearing supporting both the turbine driving mechanism and the pump

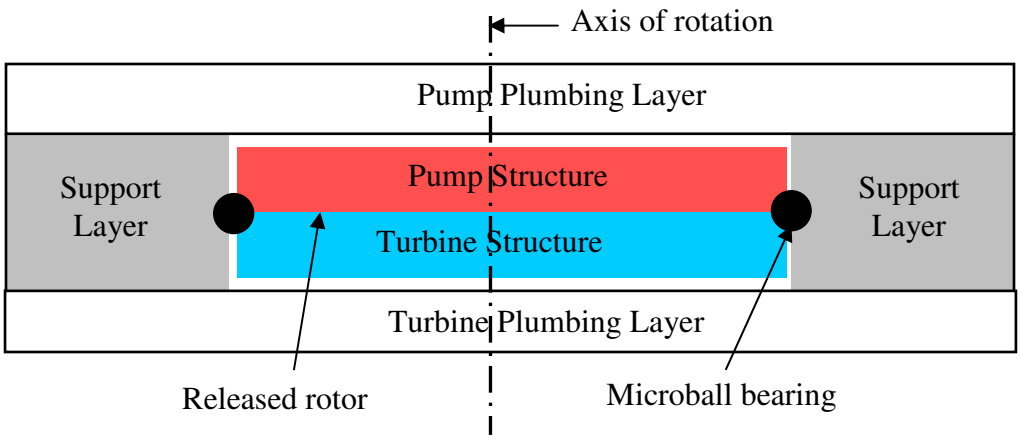

Figure 1.9. Schematic illustrating the micro-turbopump design concept.

structures. Both centrifugal-type and viscous-type pumping mechanisms were designed and fabricated with the end goal of evaluating which type will be best suited for the flow rates and pressure ranges required for portable power generation. Encapsulated microball bearing mechanisms were developed to support the pump and turbine structures and have proven to be an attractive support mechanism for high-speed rotary applications. A summary and timeline of the technologies developed is provided in Table 1.1. References are given for those that have been published to date.

Chapter 1 reviewed the motivation for liquid fueled power sources and the need for liquid fuel control by use of silicon microfabrication. Key research in MEMS micropumps and bearings was presented along with the contributions and objectives of the research performed for this dissertation.

Chapter 2 will focus on the design, fabrication, and testing of two encapsulated microball bearing designs. Key elements characterizing ball bearings will be presented leading to the design methodology for the two encapsulated microball bearings. The fabrication and incorporation of the encapsulated microball bearing in three different

devices will also be presented. This will lead to a more comprehensive tribology testing platform for microball bearings. Included in the fabrication process presented is the novel alignment technique and metal adhesion bonding used throughout this dissertation.

Technology Developed	Critical Knowledge	Fabrication	Reference
1. Point-Contact Bearing	• 1st encapsulated microball bearing demonstrated • 18,000 rpm demonstrated	• 2 wafer levels • 4 optical masks • 25 Process Steps • 1 bonding layer	[16, 17]
2. Tangential Air Turbine w/Point-Contact Bearing	• 1st integrated motor • > 37,000 rpm demonstrated • >24hr operation demonstrated • Exhibited high wear	• 2 wafer levels • 5 optical masks • 1 bonding layer • 25 Process Steps	[18]
3. Centrifugal pump implementation w/ technology 1 & 2	• 1st turbopump fabricated • Determined axisymmetric design requirement	• 3 wafer levels • 9 optical masks • 2 bonding layer • 45 Process Steps	
4. Planar-Contact Bearing with Radial In-Flow Turbine	• Low-wear demonstrated • Spin-down testing • > 85,000 rpm demonstrated	• 3 wafer levels • 10 optical masks • 2 bonding layer • 45 Process Steps	[19, 46]
5. Viscous pump implemented with technology 4	• 1st turbopump demo w/microball bearing • 10-80 mL/hour and 0-1.2 psi	• 5 wafer levels • 15 optical masks • 3 bonding layer • 80 Process Steps	[47]

Table 1.1. Timeline of technology development

Chapter 3 presents the design and fabrication of the microfabricated turbopump. This chapter will begin with the design and implementation of a centrifugal-based pump using a tangential air turbine. The results of this implementation led to the development of the viscous-type pump using a radial in-flow air turbine. The fundamental design equations for a spiral groove viscous pump will be investigated and pumping curves developed for operation within the scope of portable power applications. Critical parameters with respect to microfabrication will be specified and their effects on the pump performance will be examined. Finally, the issue of sealing within the turbopump itself will be addressed along with the fabrication process.

Chapter 4 presents the turbopump experimental testing set-up developed in this dissertation. The results from the micro turbopump demonstration and a discussion on its operation and performance will follow.

Chapter 5 will conclude this dissertation with a summary of contributions and key results. A discussion about the future of both the encapsulated microball bearing and the microfabricated turbopump will be included.

2 Microball Bearings for Silicon Turbomachinery

A high-speed bearing mechanism and turbine structure must first be developed and demonstrated in order to realize the micro turbopump. Micro gas turbines enable compact designs and are integrated on the rotor containing the pump structure in a shaft-less implementation all supported by the microball bearings. Therefore, it is critical in the design and fabrication of the turbopump to establish an encapsulated microball bearing as an attractive support mechanism for high-speed rotary applications.

In this chapter, the encapsulated microball bearing design along with the key fabrication processes developed to realize such a bearing is introduced. Two silicon microball bearing race designs were investigated. The first, a point-contact design, was integrated into a tangential air turbine platform to characterize the performance and wear of the bearings as well as demonstrate high-speed rotation. The results of this device led to the improved design, a planar-contact design, allowing for reduced wear; required for the application of the turbopump.

A radial in-flow air turbine, using lower driving pressures than the tangential air turbine and with added measurement capabilities, was developed to characterize the planar-contact bearing design. Furthermore, a microturbine tribology device was created with the planar-contact bearing and radial in-flow microturbine to characterize friction and wear phenomenon. The results detailed in this chapter serve as the foundation for development of the turbopump introduced in Chapter 3.

The design, fabrication, and testing of the first radial in-flow air turbine was performed by Dr. Matthew McCarthy (2.4.2 and 2.4.5), a post-doctoral associate at that

time within the MEMS Sensors and Actuators Laboratory (MSAL). Dr. McCarthy led the experiments by characterizing the device with the first planar-contact bearing raceway (planar-contact V.1) and developing the empirical relationship between friction torque and speed with the normal force exerted on the rotor (Sections 2.4.6 and 2.4.7). This work has been included in this dissertation, because it is critical in determining the final radial in-flow air turbine design and the system power balance of the turbopump developed in Chapter 3.

2.1 Encapsulated Microball Bearings

Studies performed by *Lin et al.* [43] and *Tan et al.* [45] demonstrated that silicon races and precision balls can provide low-friction bearings (friction coefficients below 0.01 for velocities in the mm/sec range) between stainless steel microballs and a silicon v-groove race design. In their studies, microballs were placed in a v-groove trench etched into a silicon stator. A silicon slider, with an identical trench, was placed on top of the balls. *Modafe et al.* and *Ghalichechian et al.* demonstrated similar configurations in the application of micromotors (described in Chapter 1) [40, 41, 48]. In both cases the slider is forced to contact the microballs only by gravity when the motor is off. When the motor is turned on the electrostatic force pulls the slider and maintains contact between the slider and the microballs.

A key difference between the previous applications and the turbopump is the necessity for the microball bearing to support loads in all directions. Without an electrostatic force or other external force, the turbopump must contain a bearing mechanism that accommodates all radial and thrust loads. Hence, a rotary ball bearing

mechanism wherein the microballs are encased within the silicon framework will be presented.

The microballs must be encased within the rotor and surrounding device to achieve full support of a rotor. Two possible configurations are envisioned; a microball housing above and below the rotor creating a central shaft (Figure 2.1) or microball housing at the periphery of the rotor without a shaft (Figure 2.2).

The first configuration with the central shaft encases the microball bearings at the center of the supported rotor. This design allows a lower friction moment arm and

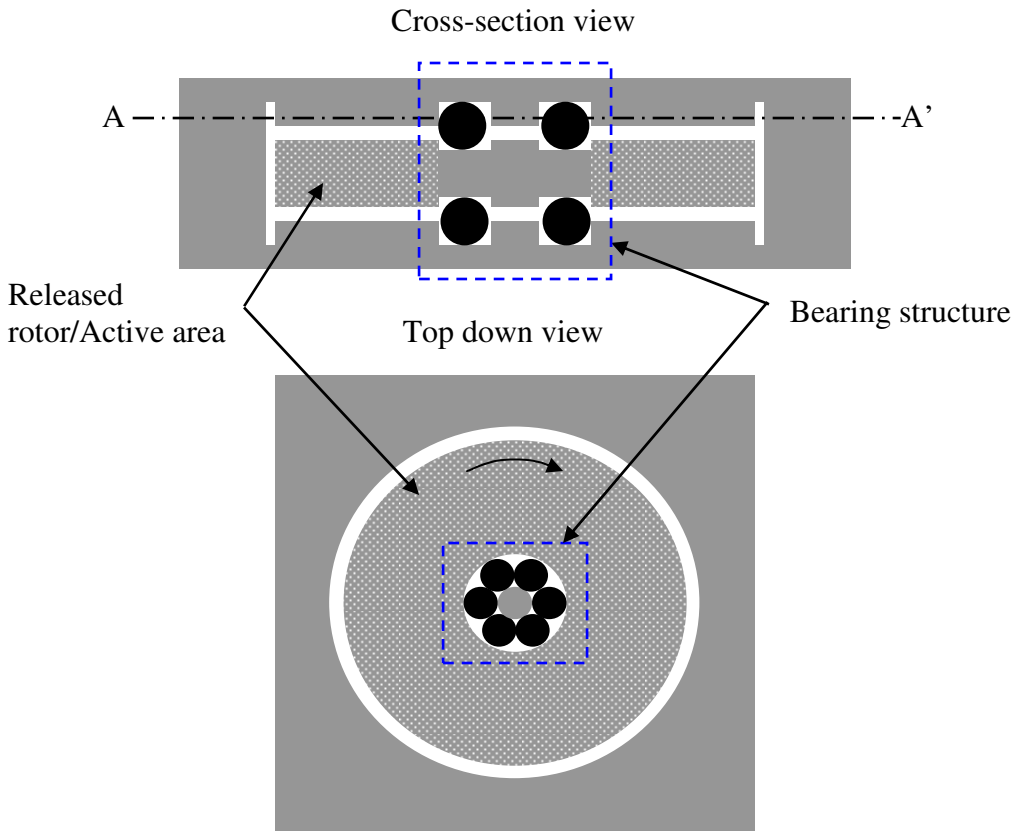

Figure 2.1. Schematic showing the cross-section and top down views of the centrally located encapsulated bearing configuration.

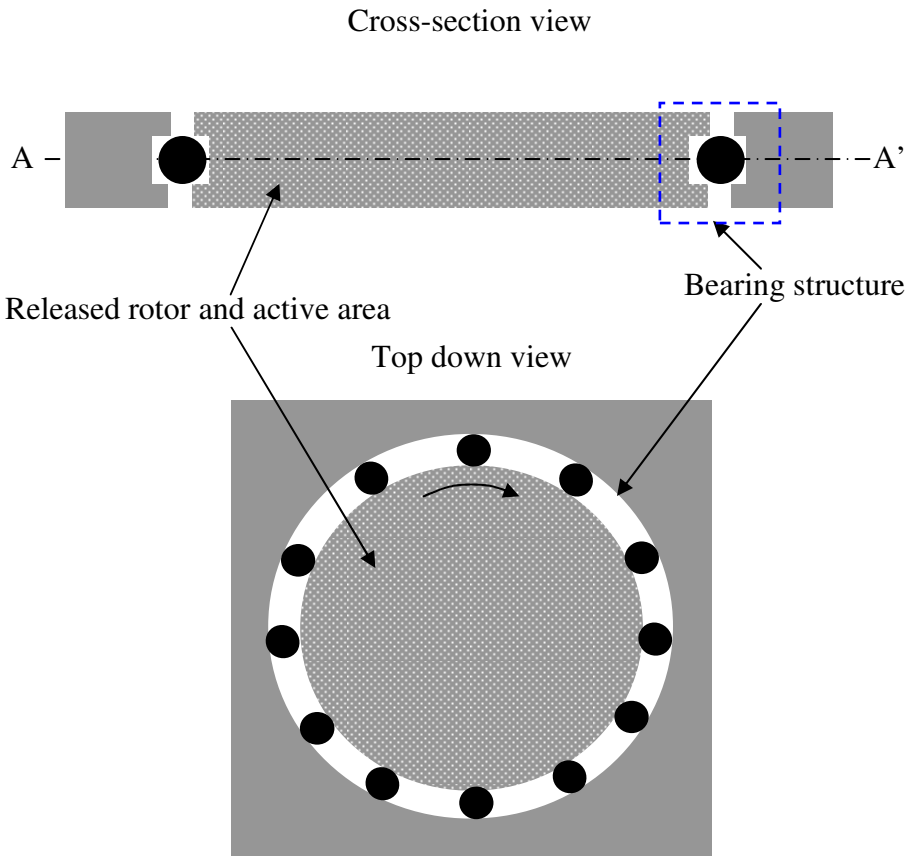

Figure 2.2. Schematic showing the cross-section and top down view of the periphery encapsulated microball bearing configuration.

lower ball velocities than the configuration that encases the microballs at the periphery. The central design is also conducive to axial-type turbomachinery where access to the periphery of the rotor is more crucial. However, the central design requires a more complex fabrication scheme incorporating two housing units, one above and one below the rotor. This design is more susceptible to wobble since the instabilities at the tip of the rotor have larger moment arms than the bearing mechanism.

The second configuration places the bearing mechanism at the periphery of the rotor, which is the best for stability. Furthermore, only one housing unit is required making this configuration more conducive to radial or mixed flow turbomachinery

applications where access to the entire rotor surface is more beneficial. Although the microballs rotate at higher velocities and larger moment arm, which make the frictional properties of this design worse than the central design, the normal load can be distributed over a much greater number of balls. The distribution of the normal load means a smaller contact area and deformation for each microball that leads to smaller compressive stress between the ball and raceway and, therefore, lowers potential wear. Following sections will describe how these factors relate to the wear and friction properties.

There are tradeoffs in choosing the periphery design configuration over the central design. First, the larger radius of the periphery design allows for increased stability but also increases the ball velocity. Second, even though the greater number of balls allows for lower compressive stress between the ball and the raceway, there will also be more ball-to-ball collisions and rubbing. The periphery configuration was chosen for this work due to a larger active area and higher stability necessary for a radial turbopump design.

2.1.1 Microball bearing material and geometry

Two critical elements make up the microball bearing structure; the precision microball and the bearing raceway. Silicon microfabrication techniques and stainless steel precision balls, which provide a compact design, are utilized to integrate the microball bearing structure within the turbopump. This work utilizes 440C stainless steel microballs, commercially available from Thomson Precision Ball Company, LLC. Table 2.1 provides the material properties pertinent to the bearings and the geometrical properties of the microballs.

It should be noted that the ball and raceway materials are not limited to 440C stainless steel and silicon respectively. Work to investigate different lubricating films deposited on the silicon race, such as silicon carbide and ultrananocrystalline diamond, and to investigate different ball materials using the platforms developed in this chapter is ongoing [49].

The geometry of the silicon raceway strongly affects the friction and wear behavior; therefore, it is critical to investigate the race design. The bearing analysis methods provided in section 2.2 offer insights into the relationship between geometry and the friction and wear behavior. First, a review of the raceway geometries possible using microfabrication techniques is necessary.

Figure 2.3 provides a summary of the type of geometry available using silicon bulk micromachining. The rounded race (Figure 2.3a) and angular contact race (Figure

Material Property		
Property	**Value**	
Material	440C stainless steel	Silicon
Modulus of elasticity (GPa)	199	110
Tensile strength (GPa)	1.89	7.00
Knoop hardness (kg/mm^2)	660	1100
Diameter (μm)	284.5	-
Tolerance (μm)	0.25	-
Surface roughness, Ra (nm)	25.4	-
Ball Grade	10	-

Table 2.1. Material properties of microballs and silicon [50]

2.3b) are better optimized for load and performance capabilities but are not readily microfabricated. A rounded race could be fabricated using wet isotropic etching or dry isotropic reactive ion etching (RIE); however, slow etch rates are required to maintain good dimensional control and, as experienced within our lab, the shape of the etch profile exhibits poor repeatability. An angular contact race can be obtained by either a modified deep reactive ion etch (DRIE) process or the utilization of gray-scale technology [51]. The square-groove race (Figure 2.3c) was chosen for this dissertation, because it can be readily fabricated using well controlled DRIE steps.

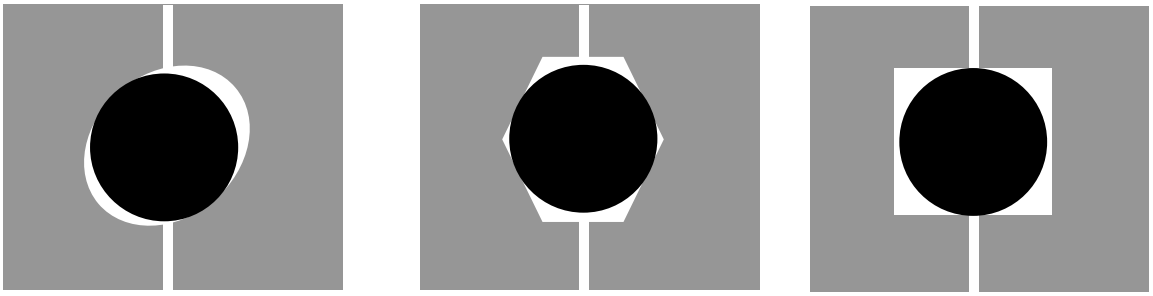

(a) (b) (c)

Figure 2.3. Illustrations of possible microfabricated raceway geometries: (a) a rounded race, (b) an angular contact race and (c) a square-groove race.

2.1.2 Fabrication sequence

The periphery configuration of the encapsulated microball bearing is fabricated in two silicon layers with the end result of a single released rotor. It is possible in the fabrication process to define patterns on both sides of the rotor. The two layer rotor construction is summarized in Figure 2.4 without any detail of the raceway or fabrication processes, which are covered in later sections. The bearing is fabricated by patterning half of the annular square-groove raceway into two separate substrate layers. Microballs

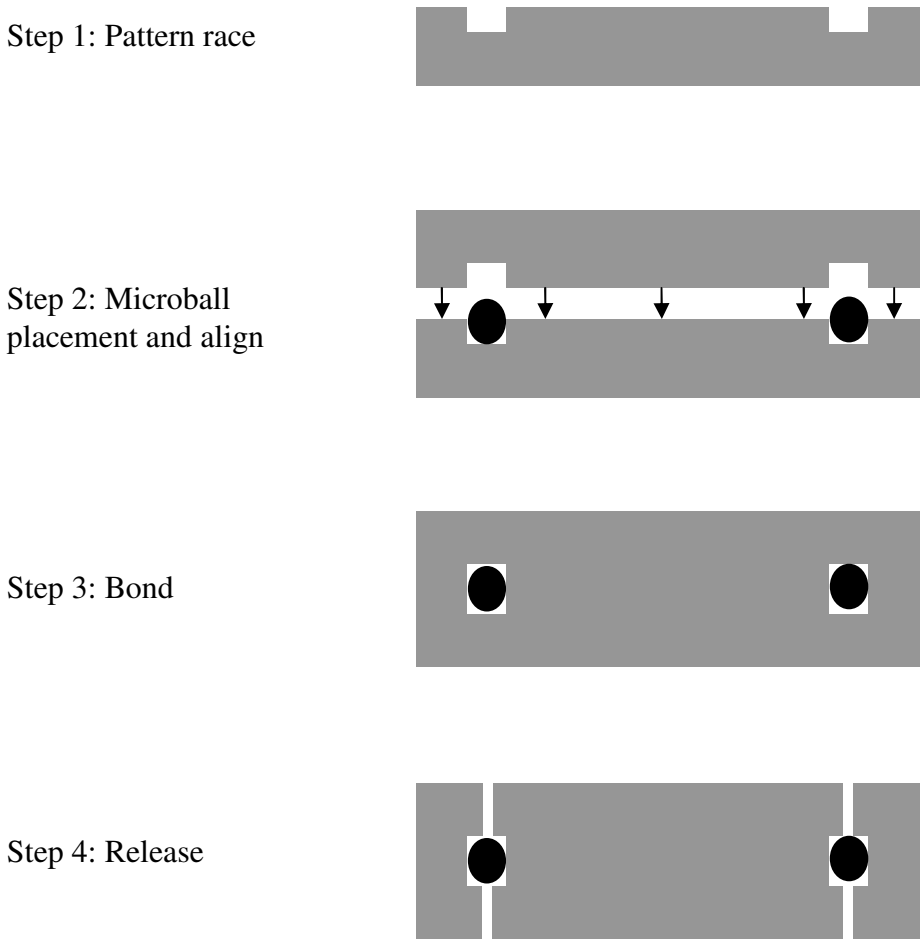

Figure 2.4. Fabrication flow for the periphery microball bearing.

are then placed into one of the race substrates. The second layer is aligned to the first layer and the stack bonded together.

As seen in the silicon race process flow, there are four key steps to the fabrication process: 1) the raceway definition and patterning; 2) alignment of the two layers; 3) bonding the two layers together; and 4) releasing the rotor. Two silicon race configurations will be covered in detail in sections 2.3.1 and 2.4.1. A novel alignment technique, developed to align the wafers or die together, will be described in the

following section along with the bonding methods investigated. The release of the rotor will occur during other fabrication steps covered in sections 2.4 and 2.6.

Two square-groove designs are used at the periphery of the rotor and are described in later sections of this chapter. Both raceway designs use the 285 μm diameter 440C stainless steel microballs and are based on the microfabricated silicon square-groove. The first is a square-groove point-contact design (denoted as 'point-contact bearing' from here on) that allows controlled contact angles between the load on the microball and the raceway, at the cost of high compressive stresses. The second design, a square-groove planar-contact bearing (denoted as 'planar-contact bearing' from here on), exhibits a reduced compressive stress on the raceway allowing for reduced wear of the race and microball.

2.1.3 Alignment and Bonding

The encapsulated microball bearing requires the balls to be bonded within the microfabricated annular square-grooves. Many permanent bonding techniques are available to bond the two layers together forming the rotor. However, in developing the turbopump and focusing on the bearing development it is useful to apply an impermanent bonding method. That is, a bond with enough strength to hold the rotor together during operation that can be readily taken apart afterward for inspection of the race and microballs. It is critical, nevertheless, to demonstrate permanent bonding methods such as anodic bonding and silicon fusion bonding when fabricating the turbopump for applications requiring high reliability and mechanical robustness.

Accurate alignment between the two raceway layers with the microballs in between is critical to the performance of the bearing structure. Large misalignments result in uneven wear and wobbling of the rotor that could affect the operation of the pump or turbine being supported. Conventional bond-aligning tools specifically made to do such alignment can conceivably be used for wafer-level alignment; however they have not been successful. Agitation of the microballs during the aligning procedure caused the balls to be displaced from the raceway and prevented bonding.

A new alignment technique requiring no special tools was developed and can be utilized for both wafer and die level alignment. Square alignment pits are patterned on the bonding surface of each layer using photolithography and DRIE with an etch depth, *h*, and width, *w*, just greater than the microball diameter. This way, a microball can be placed in a minimum of two patterned pits on one wafer or die and the other wafer/die fitted on top (Figure 2.5).

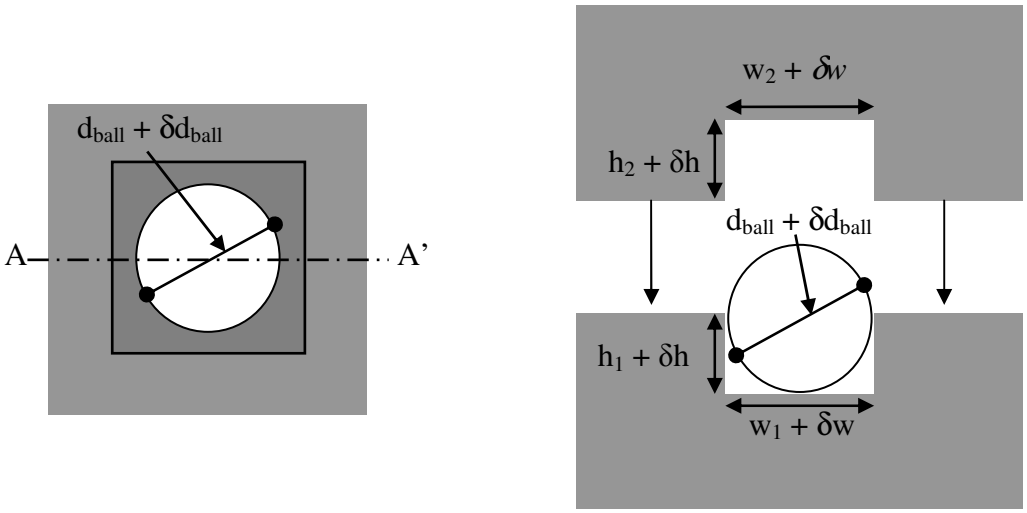

Figure 2.5. Schematic of (a) top view and (b) cross section A-A' view of the alignment pits and microball for wafer level and die level alignment.

In order for perfect alignment, the widths w_1 and w_2 must equal the diameter, d_{ball}, of the microball and the etch depths h_1 and h_2 must equal the microball radius. Photolithography tolerances for alignment and resolution as well as control of the etch depth and profile require the widths and etch depths to be larger, denoted by an increase of δw and δh respectively. Additionally, the diameters of the microballs are not all the same and have a tolerance, δd_{ball}. The misalignment, m, which occurs due to these fabrication tolerances can be found by geometry to be:

$$m = \partial w + \frac{1}{2}\left(d_{ball} - \sqrt{d_{ball}^2 - (2\partial h)^2} \right) + \partial d_{ball} \qquad \text{Equation 2.1.}$$

The misalignment is fairly insensitive to the etch depth control where etch variations on the order of 1 μm are typically seen in DRIE (Figure 2.6). From Table 2.1, the tolerance in the diameter of the microball, δd_{ball}, is 0.25 μm. Therefore, looking at Equation 2.1, it is more critical to match the width of the pit as close as possible to the microball diameter. Typical contact photolithography alignment and resolution make this tolerance on the order of 1 μm (projection lithography would be better than 0.5 μm). Additional change of the width may arise by slight undercutting of the masking layer during DRIE, but this would typically be less than 1 μm.

State-of-the-art bond aligners can obtain bond alignments better than 1 μm, but are not readily obtained in most laboratories. Conventional bond aligners, such as the Karl Suss BA-6, in combination with the bonding chucks available for the Karl Suss SB6 bonder are limited to alignments in the range of 5 μm. The total misalignment between

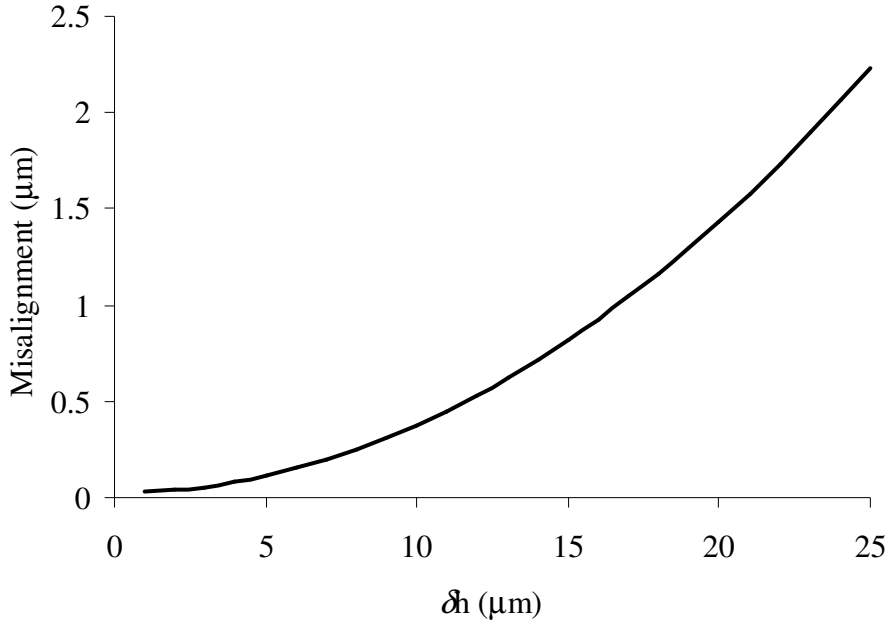

Figure 2.6. Plot of maximum misalignment as a result of etch depth inaccuracies up to 25 μm.

two layers using the microball technique just described can be estimated to be close to 2 μm using conventional contact lithography and close to 1 μm using projection lithography. Furthermore, this alignment technique uses conventional microfabrication tools available in most silicon fabrication facilities.

Three bonding mechanisms have been demonstrated using the stainless steel microballs. The prime concern during the bonding process is the change of the microball surface and the possibility of adhering to other surfaces due to the high temperatures. Anodic bonding was first investigated between a blank Pyrex wafer and a silicon wafer patterned with an annular trench etched with a width and height of 290 μm (Figure 2.7a). A successful bond, in which the ball is free to move within the raceway, is shown in Figure 2.7b.

A 4-inch silicon wafer was first patterned using a 6 µm photoresist layer and the pattern was etched into the silicon wafer by DRIE to a depth of 290 µm. The silicon wafer and the 4-inch Pyrex wafer were cleaned in a 2:1 Sulfuric to Hydrogen Peroxide solution (Piranha) to ensure cleanliness of organic materials. Then, 285 µm diameter stainless steel microballs were placed into the annular trench. The Pyrex and silicon were manually aligned on a bonding chuck that allows the two wafers to remain

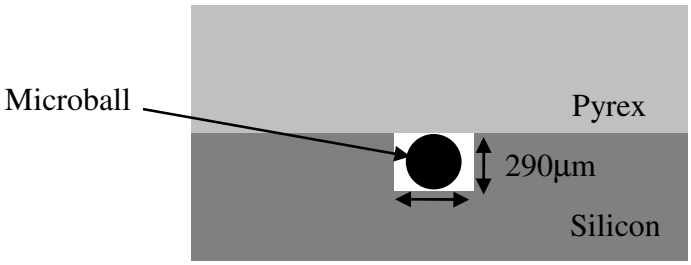

(a)

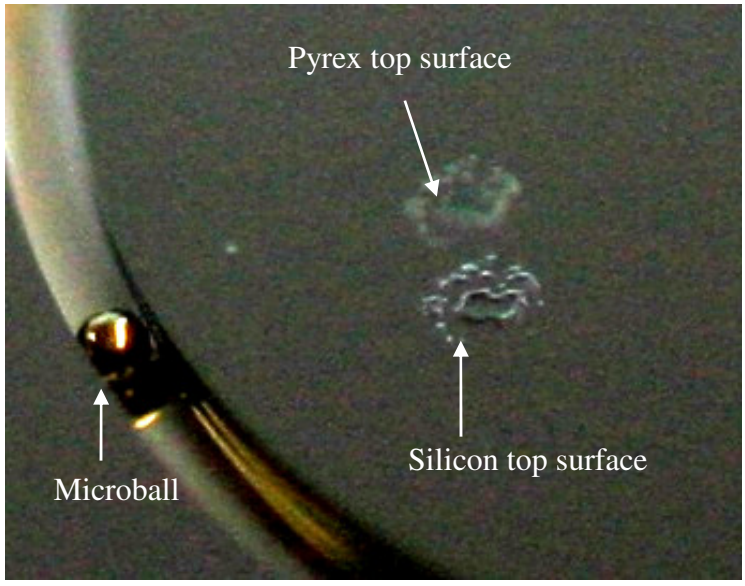

(b)

Figure 2.7. Schematic (a) showing the anodic bond demonstration piece and (b) anodic bonding demonstration with stainless steel microball.

separated with a spacer while clamps ensure stability of the alignment. The stack was placed into a Karl Suss SB6 bonder and anodically bonded.

Another widely used bonding method is fusion bonding between silicon substrates. This method again results in a permanent bond between the layers, but can be directly applied to the bonding of the silicon layers making up the rotor. As with the anodic bond demonstration, a trench was fabricated into the silicon, but this time on two silicon substrates. A point-contact bearing, which will be detailed in Section 2.3.1, was implemented. Both wafers were first soaked in an RCA 1 (0.75:1:5, NH_4OH : H_2O_2: H_2O) bath for 10 minutes at 80˚C to remove organic material and concentrated HF for 2 minutes at room temperature to strip the silicon dioxide layer required for the point-contact bearing fabrication. It should be noted that a 1:1:5 ratio is the conventional RCA 1 clean; however, for silicon fusion bonding a 0.75:1:5 is used to reduce the possibility of pitting on the silicon surface.

Once cleaned, the wafers were again aligned on the bonding chuck using the spacers to maintain separation. Contact was made in a $1x10^{-4}$ mTorr nitrogen atmosphere inside the Karl Suss SB6 bonder to minimize the trapping of any gas. Once contacted, a low strength bond was achieved at low temperatures, in our case 450C for 1 hour under vacuum. Annealing at 600C was performed for 3 hours under nitrogen flow to drive out the hydrogen and create a covalent bond at the interface. Figure 2.8 shows a demonstration of encapsulated microballs within a silicon race using the silicon fusion bonding method.

While the above techniques are suitable for applications requiring a permanent bond between the two rotor layers, an impermanent bonding scheme is desired to

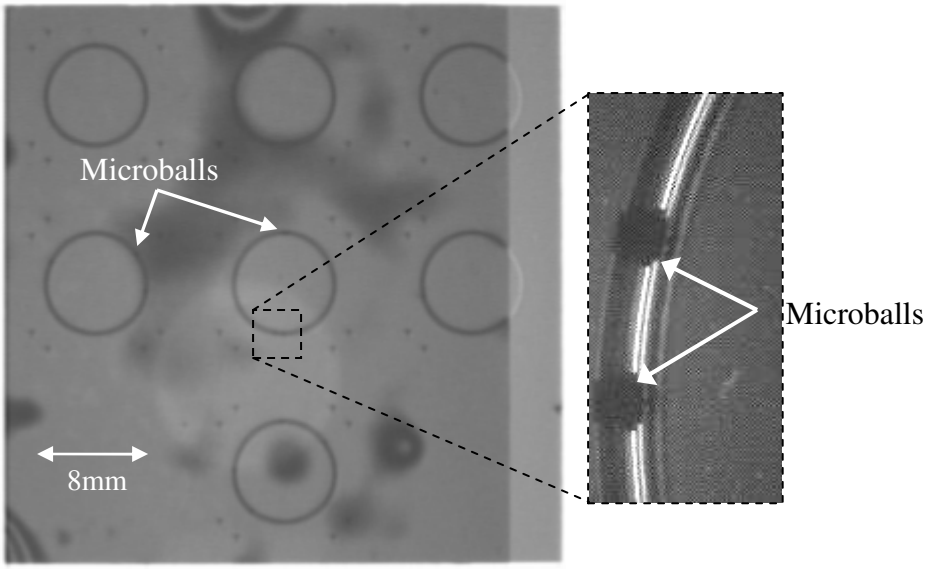

Figure 2.8. Infrared images showing stainless steel balls encapsulated within a silicon trench using silicon fusion bonding.

facilitate raceway investigation after the microball bearings are operated. A $Au_{80}Sn_{20}$ eutectic bonding method was adopted from microelectronic packaging for this purpose. The bond strength is sufficient for the purpose of the turbopump demonstration and bearing investigation, having a reported tensile strength of 275 MPa and a yield strength of 220 MPa [52].

The eutectic temperature of $Au_{80}Sn_{20}$ is 280˚C and is the most common AuSn alloy used for bonding [52]. As seen in the phase diagram (Figure 2.9), moving away from the ideal composition causes the eutectic temperature to rise sharply. Electron beam evaporation is used to deposit the AuSn layer using $Au_{80}Sn_{20}$ pellets. This ensures correct composition at the start of the deposition; however, the Au and Sn may evaporate at different rates causing the composition to change over time. This must be accounted for during the bonding procedure by adjustments to the temperature. In addition, it was

found that a composition very close to $Au_{80}Sn_{20}$ can be obtained using fresh pellets for each deposition run.

Metal layers consisting of 50-nm Cr, 50-nm Au, 1-μm $Au_{80}Sn_{20}$, and a fourth layer of 50-nm Au were deposited on each substrate through a shadow masking process. The gold layers protect the AuSn from oxidizing and adhere to the Chromium adhesion layer which in turn adheres readily to silicon and acts as a silicon diffusion barrier. Also, to counteract oxidized layers, the stack was bonded in a 5% H_2 and 95% N_2 atmosphere at 1 kTorr.

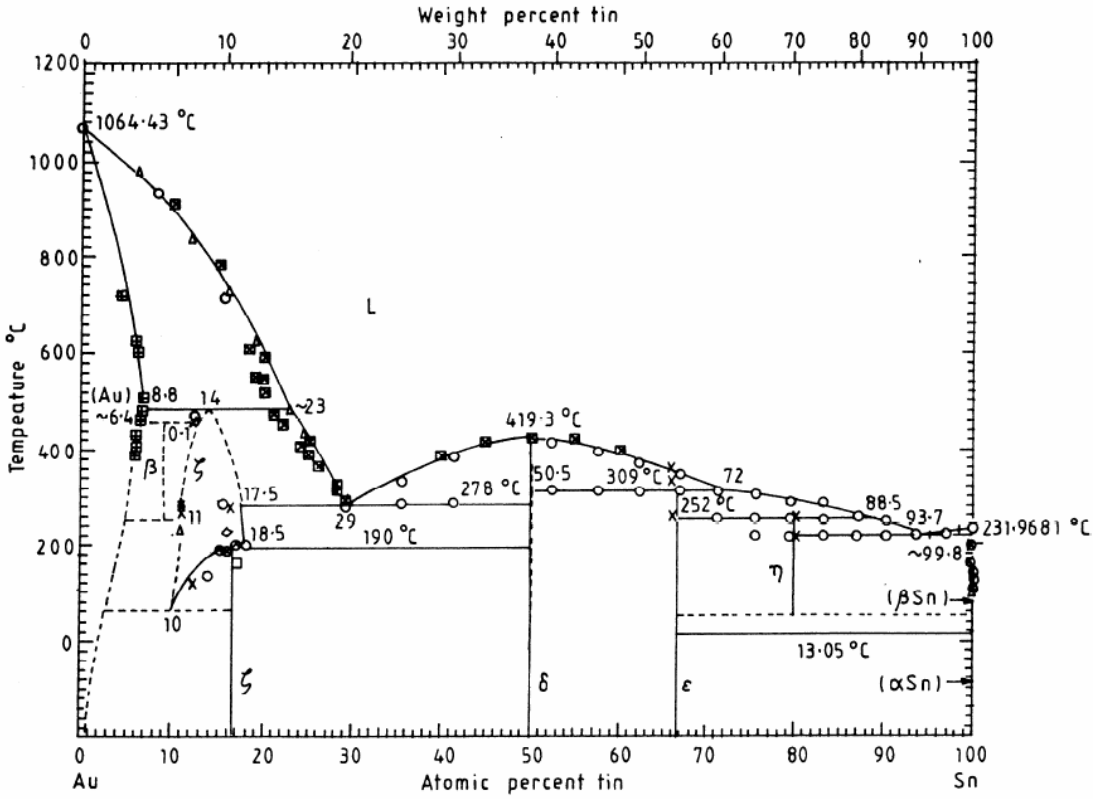

Figure 2.9. Phase diagram for Au-Sn alloys (Chuang et al., 2004).

The bonding procedure began by cleaning the surfaces successively in acetone, methanol, and isopropanol baths. In some cases, to ensure cleanliness an O_2 plasma was used, although sufficient bonding was completed without this surface treatment. The bonding surfaces were contacted in air using the microball alignment technique described in the previous section. The Karl Suss SB6 bonder was used to apply a force of 250 N at a temperature of 285˚C and a pressure of 1 kTorr H_2/N_2. Later bonding recipes used temperatures up to 330˚C due to the uncertainty of the AuSn composition deposited by the E-beam evaporator and poor temperature uniformity on the surface of the bonding chuck.

2.2 Bearing Contact Mechanics

The compressive stress exerted by the microball on the raceway and the resulting deformations are important factors to understand both the friction and wear behavior of the system. The following bearing contact analysis was performed for both bearing race designs presented in Sections 2.3.1 and 2.4.1. This allowed comparison of two designs and provided insight into their behaviors during operation.

The analysis is based on Hertzian contact mechanics, which typically overestimates the contact area (and therefore underestimates the compressive stress) between the ball and the raceway due to a load [53]. This allows the calculation of the compressive stress and deformation caused by a load on the ball bearing and, furthermore, provides an understanding of the wear and friction behavior during operation.

The maximum stress, σ_{max}, occurs at the central point of the contact area and can be estimated as [53]:

$$\sigma_{\max} = \frac{3Q}{2\pi ab} \qquad \text{Equation 2.2.}$$

The stress, σ, at other points within an elliptical contact area is:

$$\sigma = \frac{3Q}{2\pi ab}\left[1 - \left(\frac{x}{a}\right)^2 - \left(\frac{y}{b}\right)^2\right]^{1/2} \qquad \text{Equation 2.3}$$

where Q denotes the load exerted normal to the race by the ball ($Q = Q_{radial} + Q_{thrust}$), and a and b are the semi-major and semi-minor radii of the elliptical contact area.

As seen from Equation 2.2 and Equation 2.3 knowing the contact area is critical to determine the compressive stress exerted on the raceway by the normal load. There is an entire field of study dedicated to the prediction of contact mechanics that accounts for surface roughness of various length scales, adhesion forces, and atomic interactions, to name just a few. Although Hertzian contact mechanics grossly overestimates the contact area of two spherical surfaces in compression with one another it does not require numerical computation [53]. Figure 2.10 shows the geometries of microball and raceway relevant to the contact area described. In this case, the semi-major and semi-minor axis radii are:

$$a = a^* \left[\frac{3Q}{2\Sigma\rho} \left(\frac{\left(1-\nu_I^2\right)}{E_I} + \frac{\left(1-\nu_{II}^2\right)}{E_{II}} \right) \right]^{1/3} \qquad \text{Equation 2.4}$$

$$b = b^* \left[\frac{3Q}{2\Sigma\rho} \left(\frac{\left(1-\nu_I^2\right)}{E_I} + \frac{\left(1-\nu_{II}^2\right)}{E_{II}} \right) \right]^{1/3} \qquad \text{Equation 2.5}$$

$$a^* = \left(\frac{2\kappa^2 \varepsilon}{\pi} \right)^{1/3} \qquad \text{Equation 2.6}$$

$$b^* = \left(\frac{2\varepsilon}{\kappa\pi} \right)^{1/3} \qquad \text{Equation 2.7,}$$

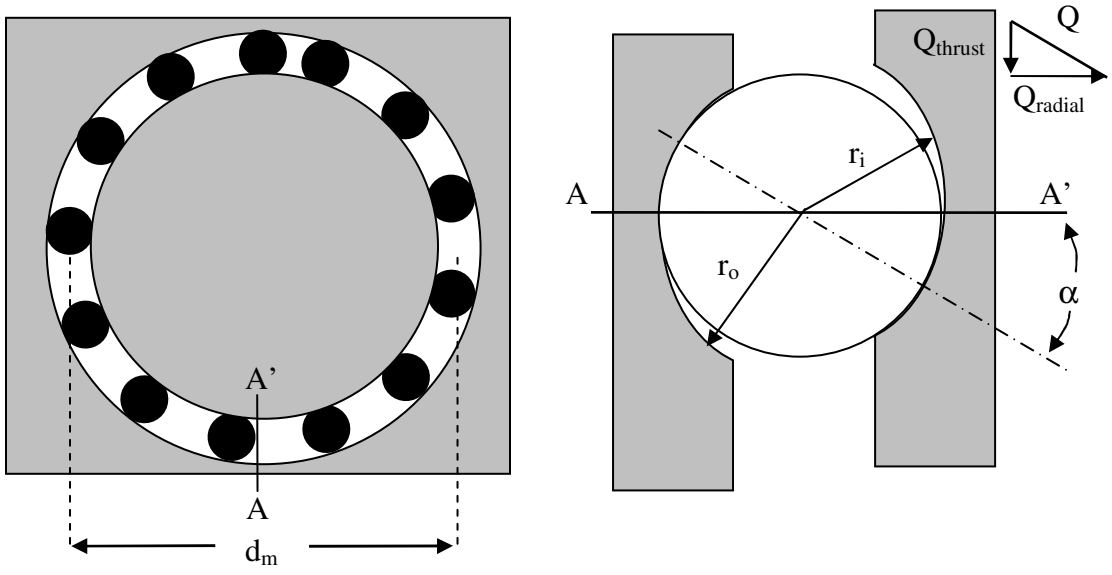

(a) (b)

Figure 2.10. Geometrical reference for ball bearings. (a) depicts the top down view and (b) depicts the cross section A-A'.

where the subscript *I* denotes the ball and the subscript *II* denotes the raceway, ν is Poisson's ratio (0.285 for stainless steel and 0.22 for silicon), *E* is the Modulus of elasticity (200 GPa for stainless steel and 165 GPa for silicon), κ is *a*/*b*, and ε is the complete elliptic integral of the second kind. The curvature sum, $\Sigma\rho_i$, between the inner raceway and the microball is defined by:

$$\Sigma\rho_i = \frac{2}{r_{ball}} + \frac{1}{r_{race}} + \frac{1}{d_m/2 - w_{race}} \qquad \text{Equation 2.8.}$$

The curvature sum, $\Sigma\rho_o$, between the outer raceway and the microball is defined by:

$$\Sigma\rho_o = \frac{2}{r_{ball}} + \frac{1}{r_{race}} - \frac{1}{d_m/2 + w_{race}/2} \qquad \text{Equation 2.9}$$

where r_{ball} is the radius of the microball, $r_{race,i}$ and $r_{race,o}$ are the radius of curvature of the inner and outer raceway in the thrust direction, d_m is the bearing pitch, and w_{race} is the width of the race. In addition to the contact area, the deformation of the race due to a load exerted by the microball can be calculated using formulations from Hertzian contact mechanics as follows:

$$\delta = \delta^* \left[\frac{3Q}{2\Sigma\rho} \left(\frac{\left(1-\nu_I^2\right)}{E_I} + \frac{\left(1-\nu_{II}^2\right)}{E_{II}} \right) \right]^{2/3} \frac{\Sigma\rho}{2} \qquad \text{Equation 2.10}$$

$$\partial^* = \frac{2\Im}{\pi} \left(\frac{\pi}{2\kappa^2\Gamma} \right)^{1/3} \qquad \text{Equation 2.11}$$

where $\Im$ is the complete elliptic integral of the first kind.

The calculation of the contact area is made difficult, since Equation 2.6, Equation 2-7, and Equation 2-11 depend on the ratio of *a/b* (κ) and the computation of the complete elliptic integral of the first and second kind. Harris [53] computes a^*, b^*, δ^*, as a function $F(\rho)$, representing the curvature difference, by evaluating the elliptical integrals. The difference function is calculated as follows:

$$F(\rho) = \frac{(\kappa^2+1)\varepsilon - 2\Im}{(\kappa^2-1)\varepsilon} = \frac{\left(1/r_{xball} - 1/r_{yball}\right) + \left(1/r_{xrace} - 1/r_{yrace}\right)}{\Sigma\rho} \qquad \text{Equation 2.12,}$$

where r_{xball}, r_{yball}, r_{xrace}, and r_{yrace} are respectively the radius of the microball and race longitudinal and transverse directions with respect to the bearing motion. *Harris* calculated a^*, b^*, and δ^* for possible values of $F(\rho)$ and provided a look-up table [53]. It becomes very difficult to choose the appropriate values, because there is not a good curve-fit to allow accurate calculation for a wide range of $F(\rho)$. *Houpert* developed another solution allowing an empirical formula to be used for different ranges of *k*, the ratio of the radii R_x and R_y as well as a dimensionless load parameter W_{PC} which are found by [54]:

$$\frac{1}{R_y} = \frac{1}{R_{yball}} + \frac{1}{R_{yrace}} \qquad \text{Equation 2.13}$$

$$\frac{1}{R_x} = \frac{1}{R_{xball}} + \frac{1}{R_{xrace}}$$ Equation 2.14

$$k = \frac{R_y}{R_x}$$ Equation 2.15

$$W_{PC} = \frac{Q}{E \cdot R_x^2}$$ Equation 2.16.

Equation 2.13 – 2.16 along with the coefficients *Cte1* and *Cte2* found in Table 2.2 can be used to determine the contact area ($A_C = \pi ab$), the deformation, δ, and the maximum compressive stress on the raceway, σ_{max} using the following empirical relationships [54]:

$$\frac{a}{R_x} = Cte1 \cdot k^{cte2} \cdot W_{PC}^{1/3}$$ Equation 2.17

$$\frac{b}{R_x} = Cte1 \cdot k^{cte2} \cdot W_{PC}^{1/3}$$ Equation 2.18

$$\frac{\delta}{R_x} = Cte1 \cdot k^{cte2} \cdot W_{PC}^{2/3}$$ Equation 2.19

$$\frac{\sigma_{\max}}{E} = Cte1 \cdot k^{cte2} \cdot W_{PC}^{1/3}$$ Equation 2.20.

Equations 2.17 – 2.20 will be used to characterize the design of the two bearings. The key differences will be in the radius of curvature and how it may change due to wear. Due to the inaccuracies in Hertzian mechanics the bearing analysis can only use the behavioral trends to give insight into operational differences between the two designs.

	$k<1$		$1<k<8.74$		$8.74<k<122.44$		$122.44<k<13576$	
	Cte1	*Cte2*	*Cte1*	*Cte2*	*Cte1*	*Cte2*	*Cte1*	*Cte2*
a/Rx	1.1521	0.52564	1.1552	0.4676	1.3088	0.4091	1.5528	0.3737
b/Rx	1.2742	-0.0704	1.1502	-0.1876	1.1687	-0.1974	1.1063	-0.1866
d/Rx	1.4329	-0.086	1.3201	-0.1946	1.4586	-0.2414	1.7138	-0.2743
Pmax/E	0.3252	-0.4553	0.3593	-0.2799	0.3122	-0.2117	0.2779	-0.1871

Table 2.2. Curve-fit values [54].

2.3 Tangential Flow Microturbine using the Point-contact Bearing

The first rotary actuator designed, fabricated and tested for the micro-turbopump was a tangential flow microturbine using a point-contact microball bearing design. The primary goal of this device was to be the first demonstration of an encapsulated microball bearing and to investigate the performance and wear behavior of the raceway design.

The designs of the point-contact bearing and tangential flow microturbine are detailed in this section along with the amount of sag exhibited, which is important in designing precise gaps for the turbopump. A contact analysis based on Section 2.2 is

performed for the point-contact bearing design. A discussion of the fabrication, the testing, and the performance and wear behavior are provided at the end of the section.

2.3.1 Point-contact Bearing Design

The first design of a silicon-square groove raceway employed a point-contact scheme to encase the microball (Figure 2.11). In this design, w_2 can be varied with h to change the contact angle, α, between the microball and the bearing race. The contact angle allows compressive stress minimization on the raceway depending on the load vector (i.e. a thrust load or radial load).

For devices employing the point-contact bearing in this research α was designed to be 45˚ so both thrust and radial loads would be evenly distributed. The dimensions of the point-contact bearing mechanism are listed in Table 2.3. Taking into account the

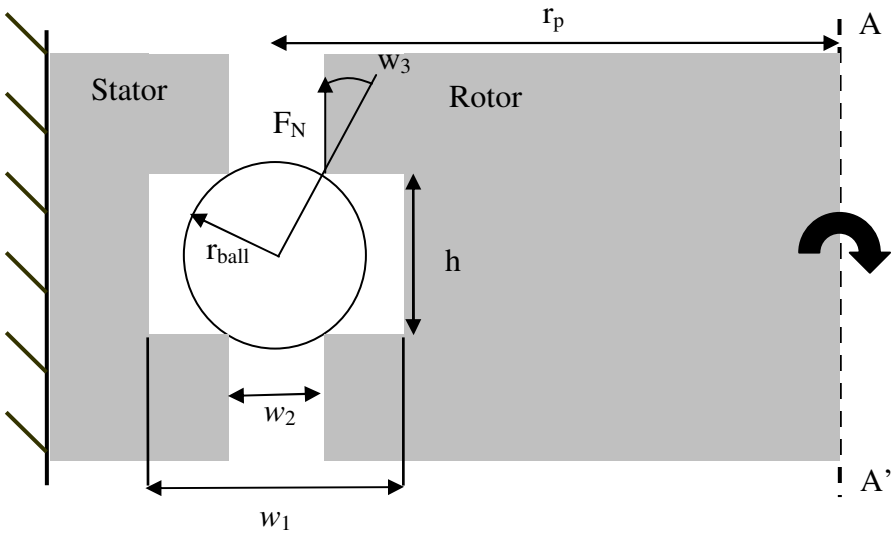

Figure 2.11. Schematic showing the point-contact microball bearing design. The rotational axis of the rotor is shown by the A-A' dashed line.

fabrication tolerances involved, the width of the raceway, w_1, is 290 μm to ensure the balls fit into the race. The width of the nested race, w_2, is $d_{ball}/\sqrt{2} + \delta w_2$, so that the balls contact at the $\alpha = 45°$ corners or 205μm with the tolerances, δw_2, added in. The total height of the race between the contact points, h, is the same as the width, w_2. Both δh and δw_2 include the necessary tolerance due to misalignment and poor etch depth uniformity.

Parameter	Dimension
d_{ball}	285 μm
r_p	4 mm
$h = d_{ball}/\sqrt{2} + \delta h$	205 μm
w_1	300 μm
$w_2 = d_{ball}/\sqrt{2} + \delta w_2$	205 μm

Table 2.3. Dimensions of the point-contact ball bearing mechanism.

2.3.2 Tangential Flow Microturbine Design

The design of the tangential flow microturbine is shown in Figure 2.12. Rotor blades for the turbine are fabricated on one side of the rotor (Figure 2.12a). Measurement geometry is fabricated on the opposite side (Figure 2.12b) to track the rotational speed of the rotor.

The device operates by momentum transfer between the fluid and the turbine blades. The fluid enters from one side of the device and exits by traversing the rotor. This causes a radial load on the rotor because the inlet and exit of the device are

asymmetric. When the devise is packaged, thrust loading occurs from pressure build up due to flow resistances underneath the turbine rotor.

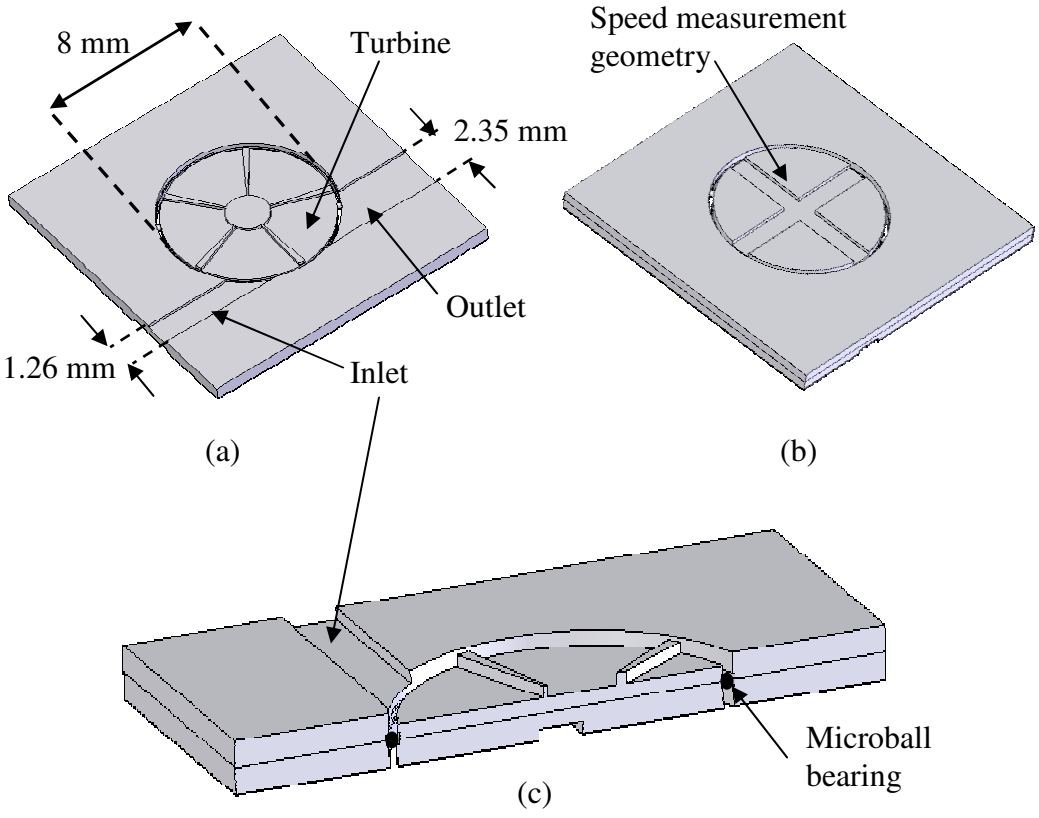

Figure 2.12. Schematic drawing of a tangential air turbine design for microball bearing characterization: (a) tangential air turbine design on one side, (b) measurement geometry on the other side, and (c) cross-sectional view.

The measurement geometry was included on the backside of the rotor for an optical displacement sensor (ODS) to measure the speed during operation. The ODS requires features larger than 150 μm on a side. The first generation of devices used the turbine blades themselves for speed measurements; however, due to a very small duty cycle in the signal (blade widths/circumference) it was difficult to pick out the first

harmonic representing the true speed. The simplest way to convert the ODS signal to rpm data is using a Fast Fourier Transform (FFT) algorithm. Therefore, on later versions, geometry with a larger duty cycle was designed on the backside of the turbine rotor.

A more detailed cross-section of the device is shown in Figure 2.13. The point-contact bearing geometry and dimensions were described in Figure 2.11 and Table 2.3. The dimensions of the turbine blades, $h_{turbine}$, and measurement geometry, $h_{measure}$, were kept equal at 200 μm. The radius of the turbine, r_{rotor}, was designed to be 4 mm.

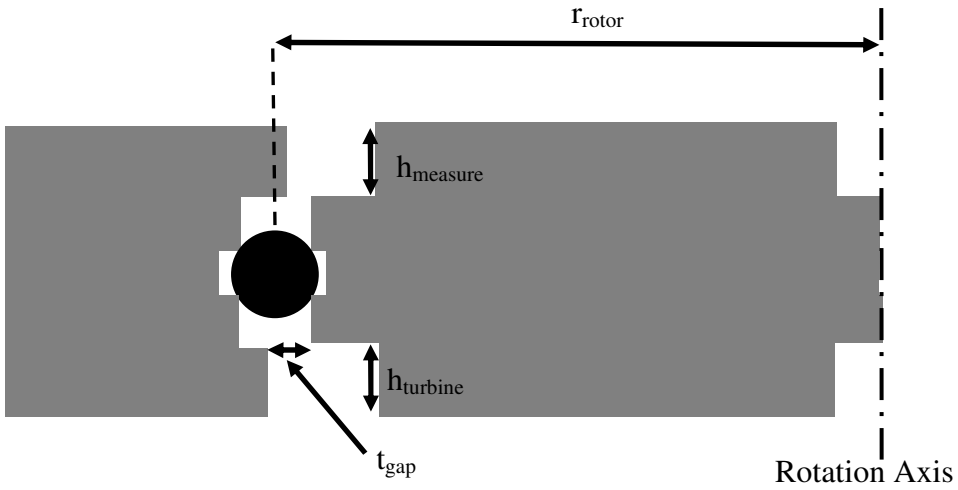

Figure 2.13. Schematic cross-section of the tangential air turbine.

2.3.3 Rotor sag

The feature critical to the application of turbopumps and other rotary applications using the microball bearing support is the gap created by the sag of the rotor. In the turbopump, the sag of the rotor determines the clearance above the pump impeller. Too

large a clearance may lead to poor pump performance. Too small a clearance may lead to the rotor crashing into the surface after wearing of the raceway.

The sag comes from the fabrication tolerances for the width w_2 and height h. Figure 2.14 is a schematic depicting the gap created due to the changes of $\delta\omega_2$ and δh to the designed geometry w_2 and h. By geometry, the gap is calculated to be:

$$gap = (h + \delta h) - d_{ball}\sqrt{1 - \frac{(w_2 + \delta w_2)^2}{d_{ball}^2}} \qquad \text{Equation 2.21.}$$

Due to wear, the race geometry is also expected to change during the operation. Wear will depend on speed, friction, and the compressive stress exerted on the race by

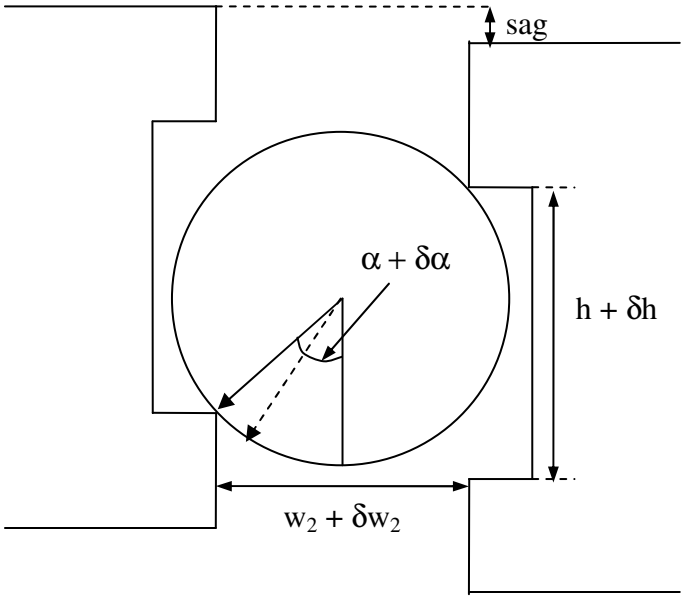

Figure 2.14. Schematic of the point-contact bearing showing the dimensions including fabrication tolerances.

the microball. As mentioned in the previous section, characteristics for determination of wear behavior are the compressive stress and the deformation of the race calculated from the contact area and load.

2.3.4 Bearing Contact Analysis

The compressive stress from Equation 2.2 and Equation 2.3 depends highly on the contact area between the microball and the raceway. In the point-contact design, the initial contact area is very small due to the initial sharp corners. According to Equation 2.2, this means that the maximum compressive stress is extremely high. The point, however, will wear down in the first few rotations because of the extremely high stress and will have a small concave radius of curvature (Figure 2.15). As the race wears, the radius of curvature, r_{race}, will change accordingly and, therefore, so does the contact area.

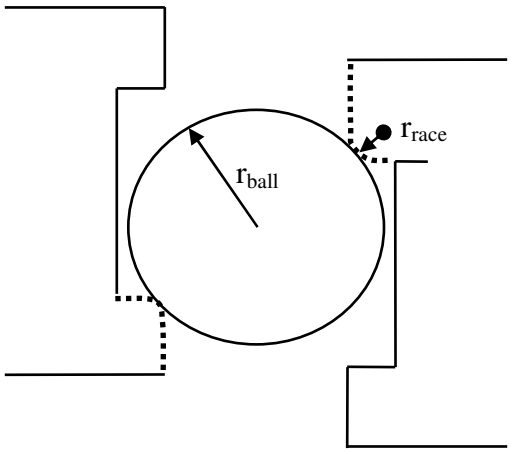

Figure 2.15. Schematic of the point-contact bearing describing the geometry for contact area calculation.

Figure 2.16 and Figure 2.17 show the change in contact area, compressive stress and deflection with a change in r_{race} and a normal load of 500mN using Equations 2.17 – 2.20. Assuming there is no change in asperities (surface roughness), meaning the raceway wears to a condition of minimum stress, the compressive stress will decrease as the race wears. The plots provided give an insight into the trends necessary to understand the bearings and optimize the designs.

The compressive stress on the race according to Hertzian contact mechanics, which underestimates the compressive stress, is in the range of the silicon fracture strength, approximately $7x10^9$Pa (Figure 2.16). It is therefore expected that the race will wear until a minimum stress state is reached. This ultimately will limit the minimum sag capability of the bearing and eliminate it from applications requiring small, precise gaps.

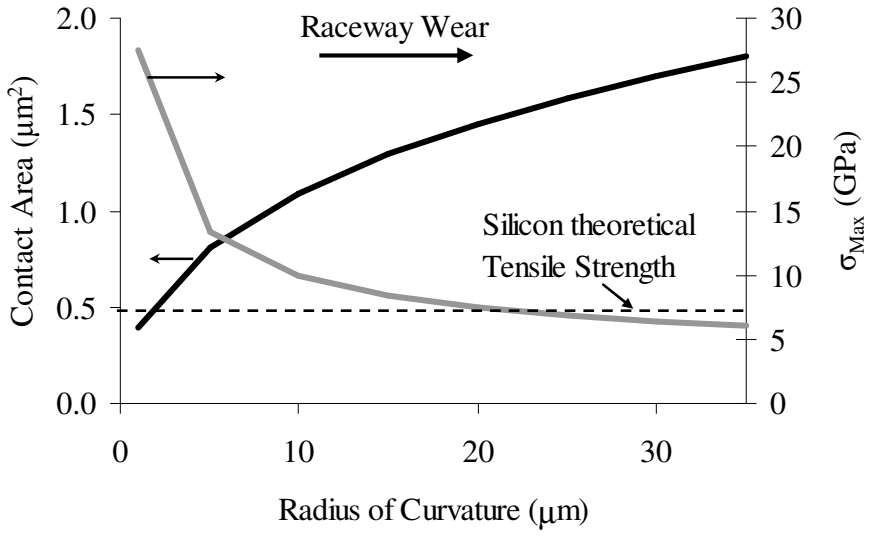

Figure 2.16. Initial contact area and corresponding maximum compressive stress on the raceway plotted for increasing raceway curvature due to wear and ball load of 500mN.

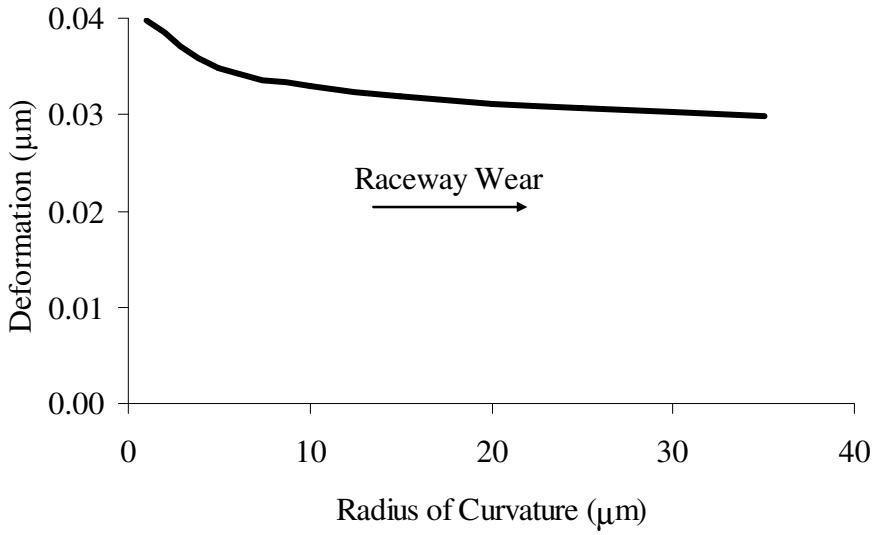

Figure 2.17. The raceway deformation plotted for increasing raceway curvature due to wear with a ball load of 500mN.

2.3.5 Fabrication

The key steps of the fabrication sequence for the tangential air turbine supported by the point-contact microball bearing are illustrated in Figure 2.18. The starting wafer is a 4" double-sided polished (DSP) silicon wafer with a thickness of 420 μm (+/- 25 μm wafer-to-wafer and +/- 5 μm across each wafer). The first step is to grow a 1.1 μm thermal silicon dioxide layer for the nested DRIE process (Figure 2.18a). The next step is to define the 290 μm wide race and alignment pits (described in Section 2.1) using patterned photoresist as a masking layer to etch the silicon dioxide by RIE (Figure 2.18b). Depending on the layer being processed, this step is repeated on the backside using front-to-back alignment to pattern the tangential turbine blades or the speed measurement geometry (Figure 2.18c).

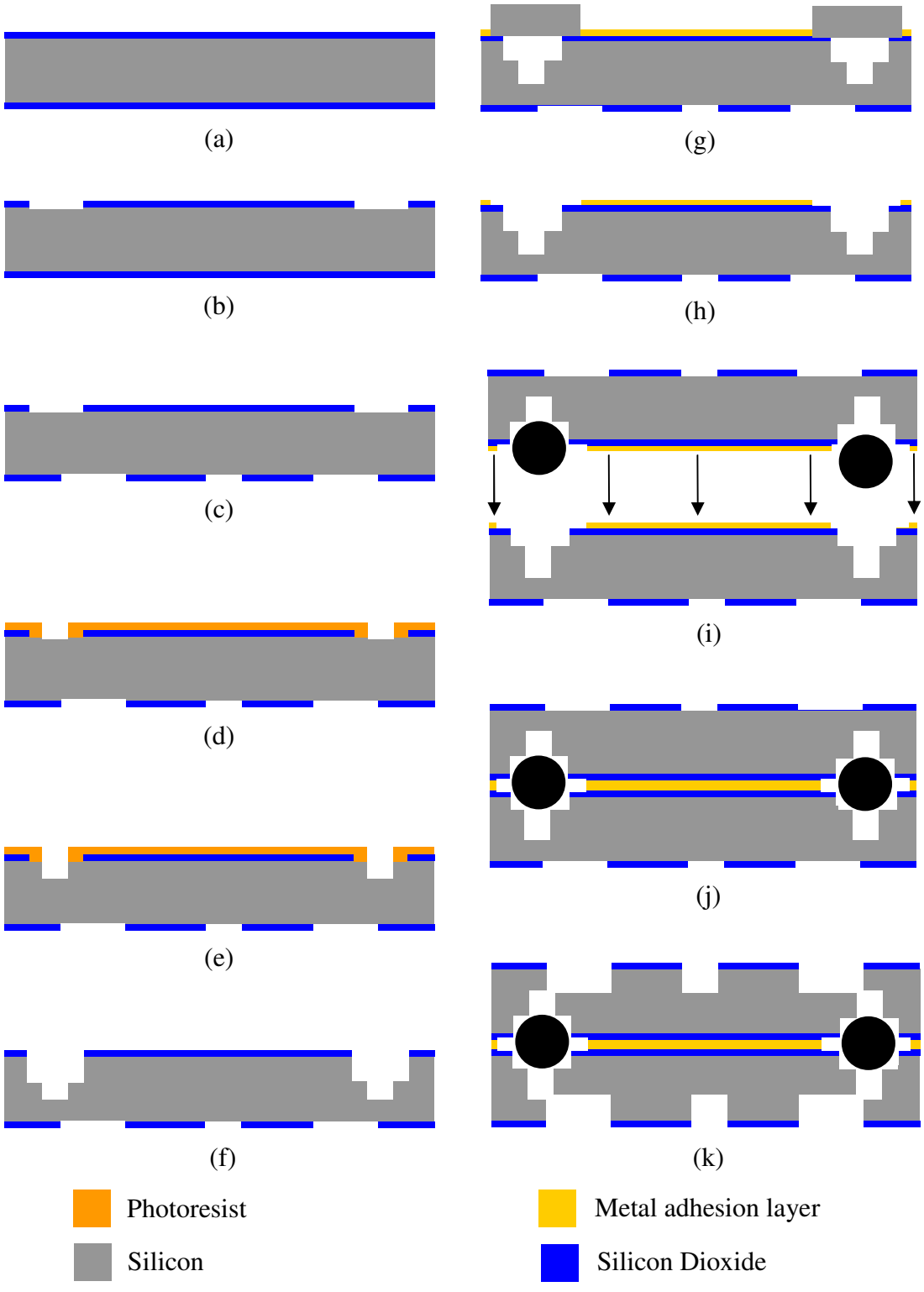

Figure 2.18. Fabrication sequence for the point-contact microball bearing support for the tangential air turbine.

Once the silicon dioxide is patterned on both sides of the wafer, photoresist is patterned on the topside to form the 205 μm wide annular trench that the microballs will make contact to (Figure 2.18d). This feature is etched by DRIE to a depth necessary for the rotor to release during the step that defines the turbine blades or speed measurement geometry (Figure 2.18e). After the narrow trench is etched, the photoresist is stripped in a positive photoresist stripper and cleaned using Piranha to ensure the silicon race area is clear of masking debris. The 290 μm wide annular trench and the alignment pits are etched by DRIE to a depth of 102.5 μm or *½h* (Figure 2.18f). A silicon shadow mask (made by DRIE through etching) is then aligned to the bond side using a microscope and alignment marks and attached to the wafer using photoresist and Kapton tape (Figure 2.18g). Electron-beam deposition is used next to deposit the metal adhesion layer, which consists of 50nm Cr/50nm Au/1 μm$Au_{80}Sn_{20}$/50nm Au (Figure 2.18h). Afterwards, the wafer is soaked in acetone to release the shadow mask and rinsed in methanol and isopropanol baths. Each wafer containing the turbine and the speed measurement geometry is diced with a dicing saw. Figure 2.19 shows a completed die at this stage of the fabrication sequence.

Die level bond alignment was performed using the etched alignment pits with an alignment tolerance of 5 μm (Figure 2.18i). As described previously, the dies are bonded using a Karl Suss SB6 bonder in a 5%-H_2/95%-N_2 atmosphere (Figure 2.18j). After bonding, each die is attached to a carrier wafer using Cool grease from AI Technologies and etched until released on both sides of the die (Figure 2.18k). To ensure the release of the rotor, an over-etch of 5 μm – 10 μm was typically performed for each die.

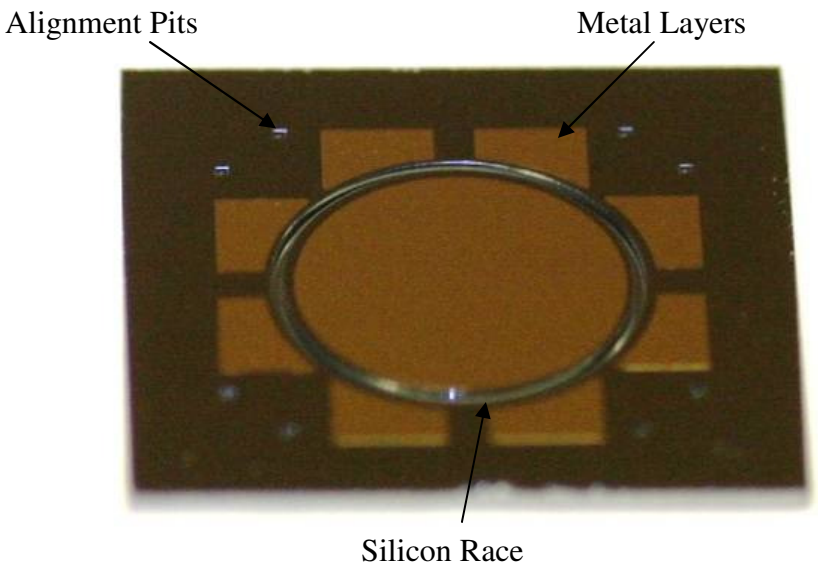

Figure 2.19. Optical photograph of a finished rotor layer before bonding.

Figure 2.20 shows a photograph of a completed air turbine device. Inspection of other devices showed some flaws in the fabrication. One potential severe defect occurs in the race due to an over-etch effecting the raceway during the DRIE release step. Figure 2.21 is an SEM image taken of a rotor (tested rotor) in which divots created by the over-etch are pointed out. These divots are spaced the same distance as the diameter of the microballs and seem to occur in the positions between each ball. Due to wafer thickness variations some die could have up to 10 μm difference in the divots. In later devices care is taken to minimize the over-etch required.

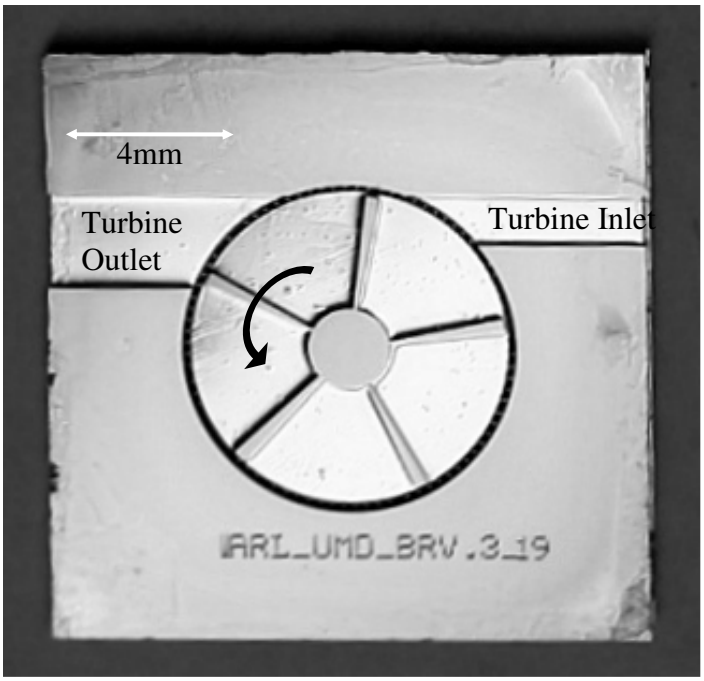

Figure 2.20. Optical photograph showing a release tangential air turbine with the inlet and outlet.

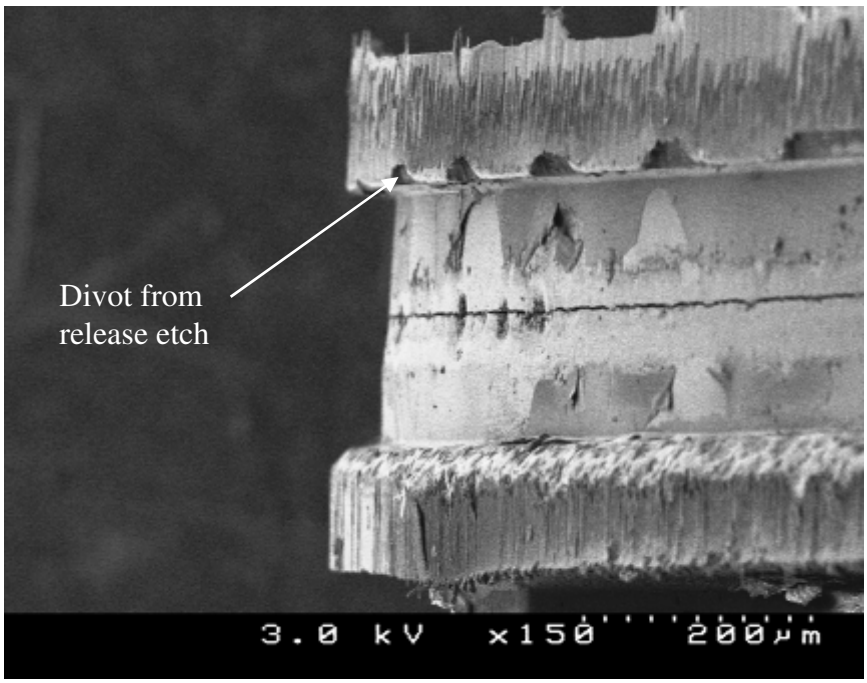

Figure 2.21. SEM image of a released rotor showing the divots caused by an over etch during the release.

Some initial devices had metal particles wedged between the balls inside of the raceway. This invariably caused jamming of the rotor preventing any use of the device. Squeeze-out of the metal adhesion layer, which occurs because of the high temperature and force during the bond, was determined as the cause of the metal particles. Bond parameters can be optimized to reduce the squeeze out effect, but complete elimination of squeeze out is difficult due to a detrimental effect on the bond quality. Trenches were, therefore, designed on each side of the raceway to act as traps for the metal (Figure 2.22). Using the trenches led to raceways completely clear of squeeze-out metal particles.

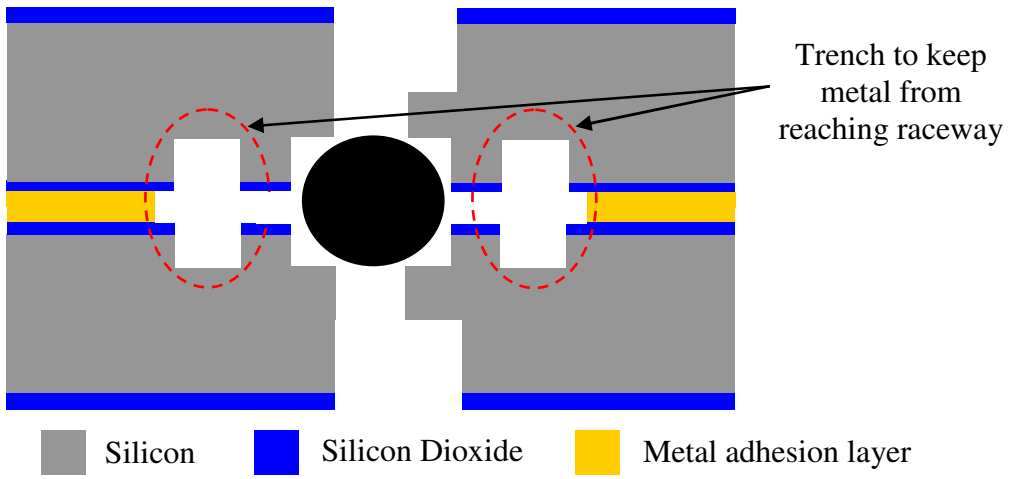

Figure 2.22. Schematic demonstrating the metal over flow trench.

2.3.6 Testing

Figure 2.23 illustrates the flow diagram for testing the tangential air turbine. The turbine spins due to the momentum of the N_2 gas coming from a house line which is controlled using a pressure controller (Alicat Scientific, *PC Series* Electronic Pressure

Controller). A Philtec D6 optical displacement sensor (ODS) is placed within 1 mm above the speed measurement geometry. The ODS has a bundle of fibers that send out a light signal and a bundle of fibers that feed reflected light back to an optical receiver. A voltage is read proportional to the distance the light travels; therefore, the speed geometry produces a train of square pulses with a duty cycle according to the radial height profile. The signal is fed into a 0-200kHz amplifier and then into a DAQ card (National Instruments 6024E DAQ card.).

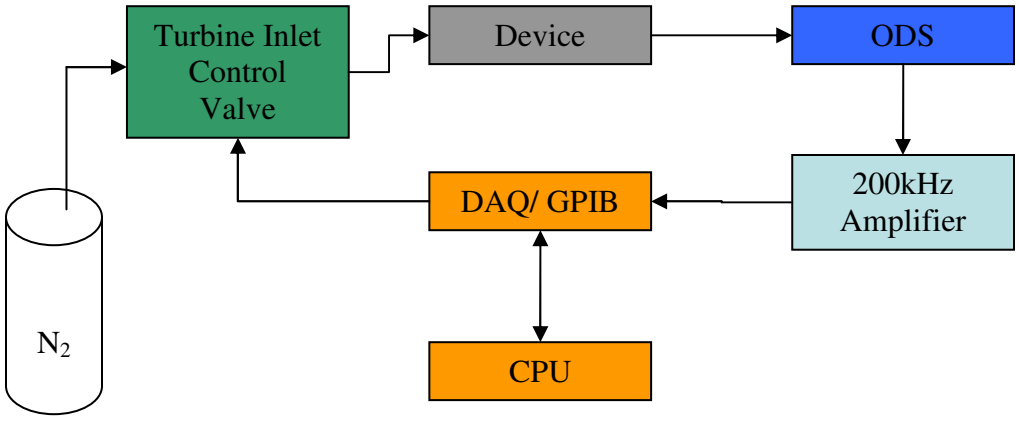

Figure 2.23. Flow used for testing the tangential air turbine.

A LabView program (Figure 2.24) was developed to convert the voltage signal into the units of rpm using either an FFT algorithm or a peak detect algorithm depending on the quality and shape of the signal. An example of data captured by the ODS sensor of an operating rotor is provided in Figure 2.25. In some cases, the ODS is tilted and sharp peaks are seen in the signal because the light is only reflected by the sidewalls of the etched features. In this case, a peak detect algorithm is required to extract the rpm.

In other cases, a square wave is produced when the ODS is placed perpendicular to the geometry. If the duty cycle is between 20% and 80%, an FFT algorithm is used to convert the signal to rpm. If the duty cycle is below 20% or above 80%, it became difficult to distinguish the first harmonic required to obtain the correct frequency of the signal and therefore the proper rpm data. In this case, the peak detect algorithm is again selected.

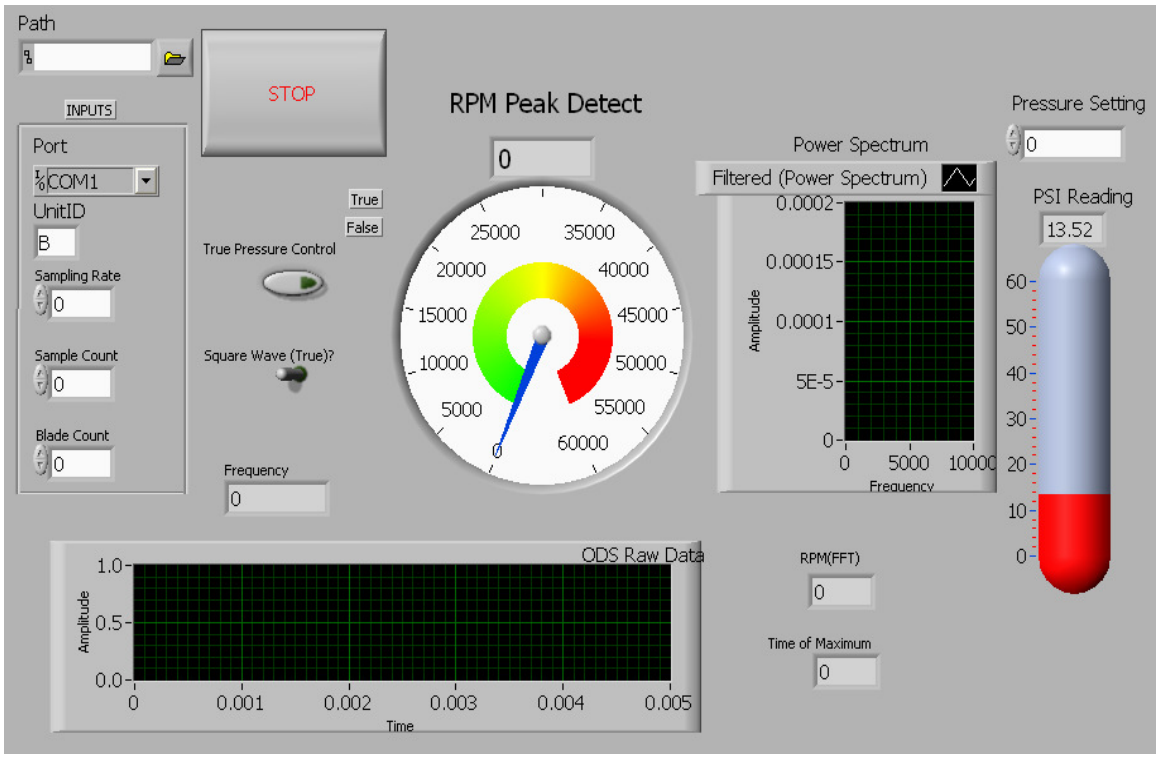

Figure 2.24. Screenshot of the LabView program front panel used to control the N_2 line pressure, collect ODS data, and compute the revolutions per minute.

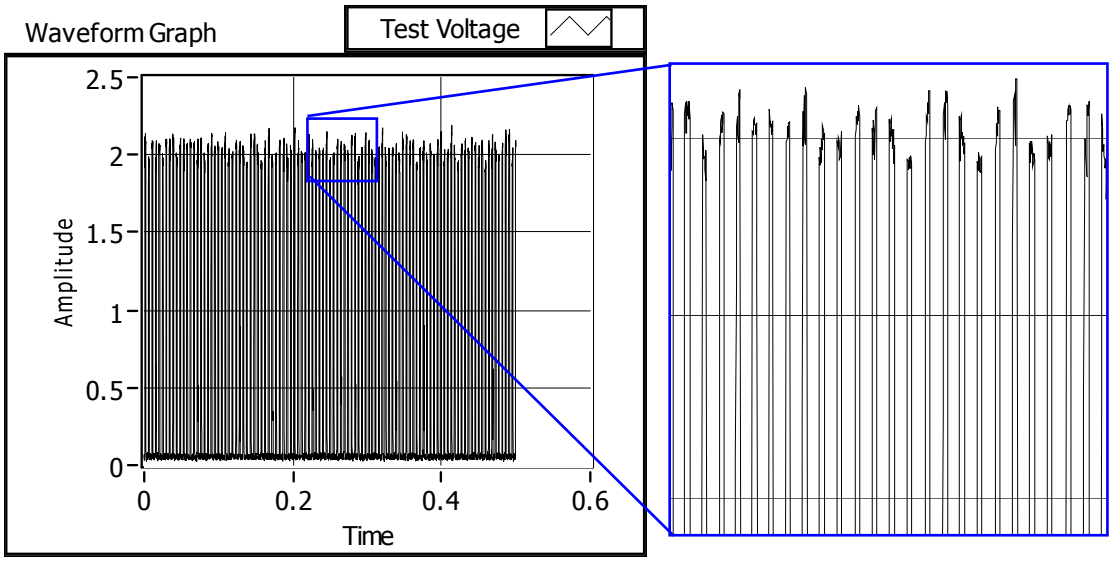

Figure 2.25. Example of captured data from the optical displacement sensor showing rotation.

A fixture formed using a Stratasys FDM Titan rapid prototyping tool enables testing without the need to integrate fluid connections onto the silicon device (Figure 2.26). The turbine side faces down in a pocket having a 125 μm (minimum layer thickness for tool) clearance below the turbine rotor permitting rotation without interference. Inlet and outlet nitrogen ports butt up against the inlet and outlet channels etched into the device during the final DRIE step. An O-ring is placed between the top of the device and a lid is clamped down using screws. Slots are fabricated into the lid allowing the ODS sensor to be placed at the appropriate height.

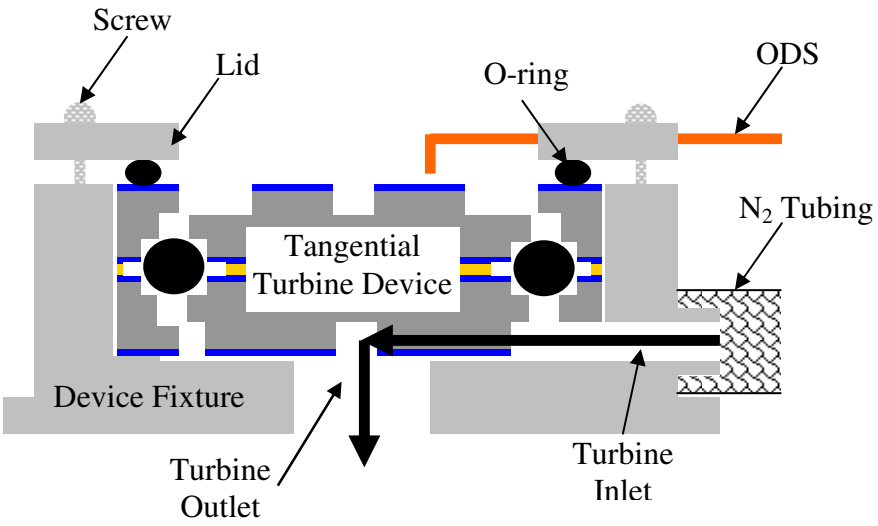

(a)

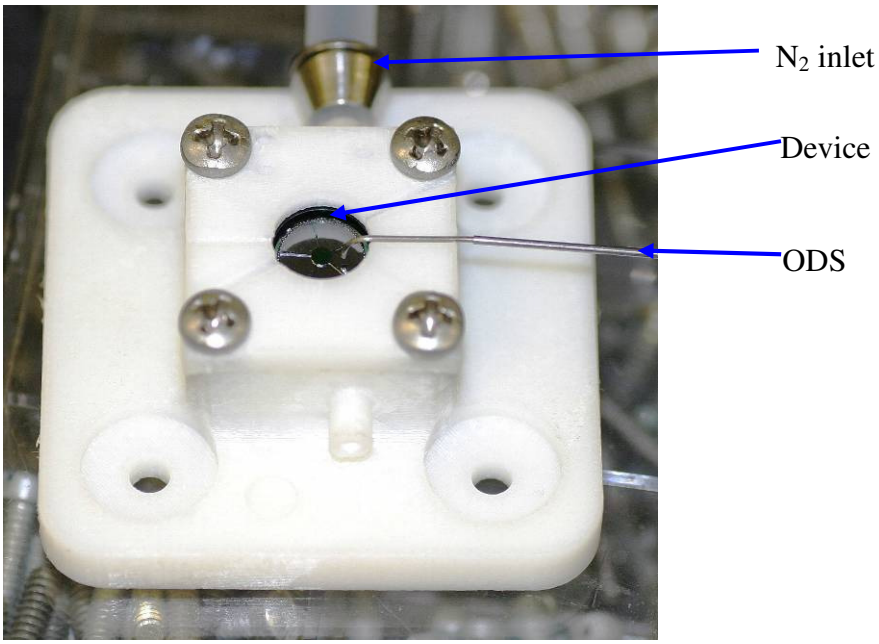

(b)

Figure 2.26. (a) Schematic and (b) optical picture of the tangential air turbine test fixture.

2.3.7 Results and discussion

To demonstrate the tangential air turbine two separate experiments were performed: 1) the nitrogen line pressure was ramped from 10 psi to 60 psi and 2) operation with a constant 10 psi line pressure. In the first set of experiments speeds in excess of 37,000 rpm were demonstrated for multiple devices with a maximum line pressure of 60 psi. One set of data where the rpm was recorded in 5 psi increments as the nitrogen line pressure was varied is shown in Figure 2.27.

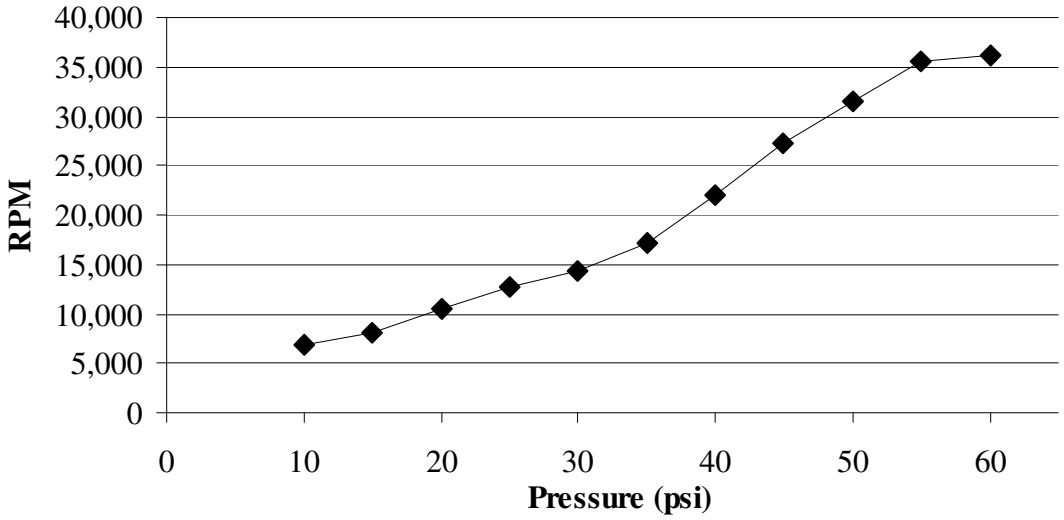

Figure 2.27. Plot showing rotational rate versus N_2 line pressure.

It seems as though the increase of the rate of revolution with pressure was starting to slow down somewhere around 55 and 60 psi (Figure 2.27). This could be due to a balance of the frictional torque due to the load caused by the pressurized Nitrogen and the amount of torque available on the rotor. Increase in pressure causes normal load and ball

velocity to increase as well. This in turn causes the frictional torque to increase. Unfortunately, 60 psi was the maximum line pressure available. It is expected that the rate of revolution would start to decrease with a further increase of line pressure due to the domination of the frictional torque.

Long-term operation was conducted using a constant line pressure of 10 psi for over 24 hours (Figure 2.28). In Region A, the rotational rate steadily increases before settling around 20,000 rpm in Region B. After 24 hours of operation the nitrogen line pressure was ramped down. The device was re-started multiple times before being de-bonded and inspected.

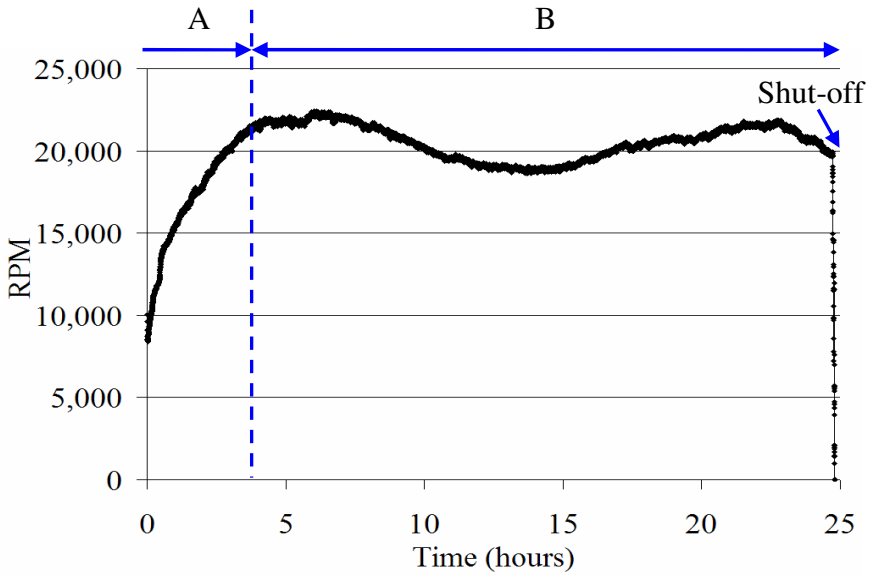

Figure 2.28. Graph of a turbine run at a constant 10 psi N_2 line pressure for over 24 hours.

Wear within the microball bearing was investigated by de-bonding the devices and inspecting the race and balls using SEM. The AuSn bonding method used allowed the devices to be de-bonded on a hotplate set to 400˚C with a razor inserted into the bond interface. The outside of the die is 'popped' apart with the razor, leaving the rotor completely intact and bonded together.

Figure 2.29 shows the rotor after the 24-hour long operation. Wear is only observed on the bottom side of the race, the side on which the air turbine is located. The outer race diagonal to the worn race in Figure 2.29 also exhibits the same wear profile (Figure 2.30). The other two races do not see any wear. The reason for this is the driving pressure causes the rotor to push upwards and the fabrication tolerances prevent the microball from contacting both sides of the raceway (Figure 2.31).

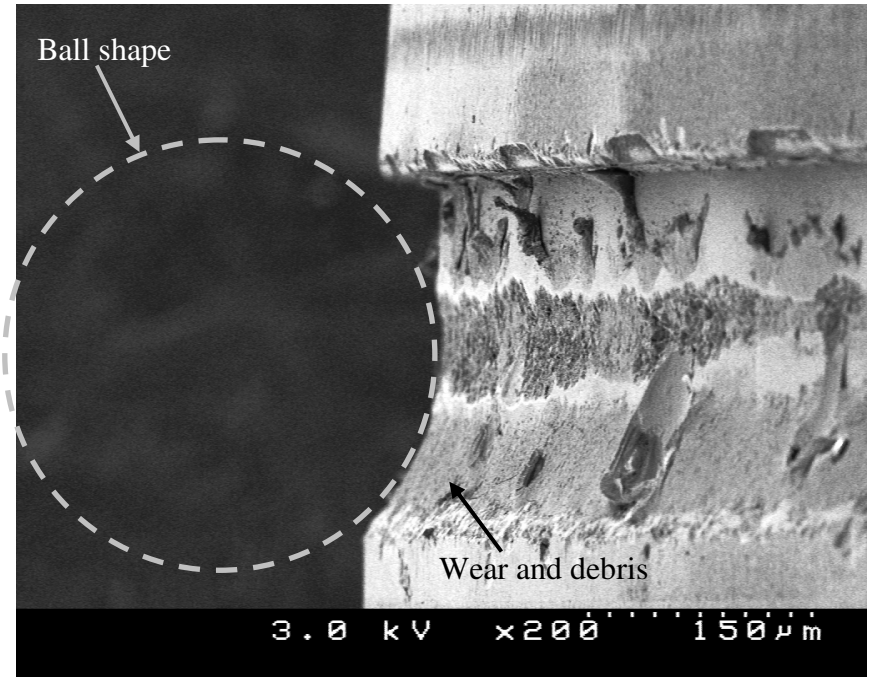

Figure 2.29. Edge view of the silicon race on the rotor after more than 25 hours of operation at an average speed of 20,000rpm.

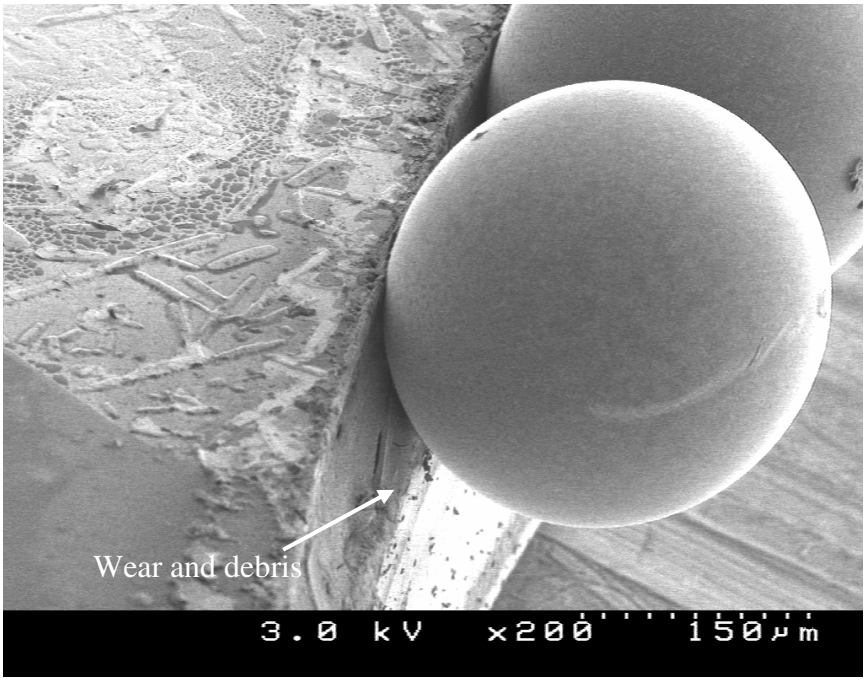

Figure 2.30. SEM showing the outer race after more than 25 hours of operation at an average speed of 20,000 rpm. The microballs exhibited minimal damage and were lightly adhered to the race surface.

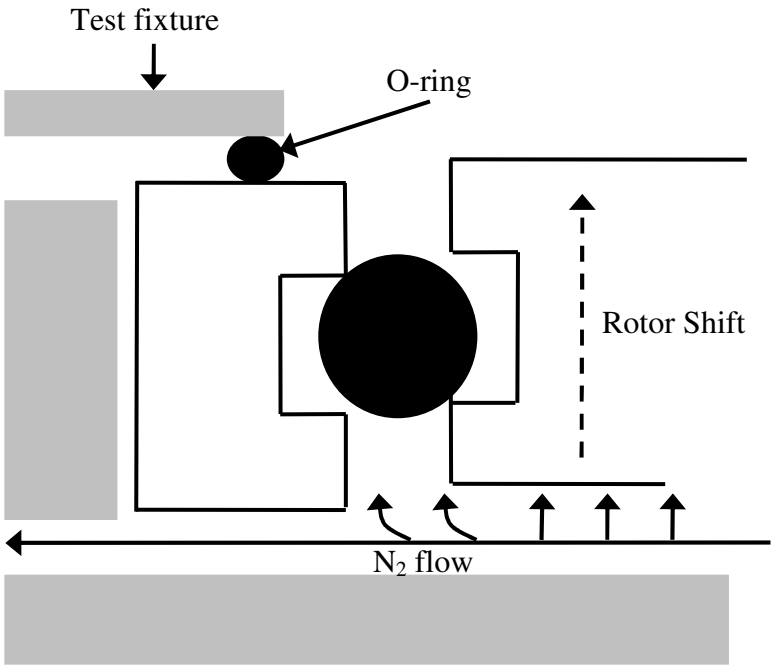

Figure 2.31. Schematic drawing showing how the rotor is shifted up due to the N_2 pressure.

The microball from the >24 hour operation was also extracted (Figure 2.30). The microballs were lightly adhered to the bearing surface due to the large contact area and adhesion forces. Light tapping easily removed them from the race. Little wear can seen on the microballs, even after the long operation time. This suggests that the silicon raceway is the dominant contribution to debris and wearing.

After the long operation the raceway appears to wear into the shape of the microball. From Figure 2.29, the re-shaping of the raceway appears to be caused by a combination of the wear at the corner and the debris buildup. The new radius of curvature of the raceway can be estimated from wear track in Figure 2.29 to be just larger than the radius of the microballs. The contact area can be calculated by the estimated radius of curvature and normal force on the rotor from the pressure build up beneath the rotor. An estimated 4.3 N of force acting on the rotor was estimated using the 10 psi driving pressure of the nitrogen and the area underneath the rotor encased by the fixture. Figure 2.32 plots the contact area and the maximum compressive stress for a range of raceway curvatures.

A closer look at Equation 2.13 and Equation 2.20 show that, when R_y equals the microball radius, a minimum compressive stress state is reached. This state is shown in Figure 2.32 at the point where the raceway curvature equals the radius of the microball. The calculation is ideal and does not include adhesion forces or surface roughness, but alludes to a state in which minimal wear may occur. These trends are consistent with the behavior seen in region B (Figure 2.28) where there would be no wearing of the race, and therefore, no change in the operation of the bearing.

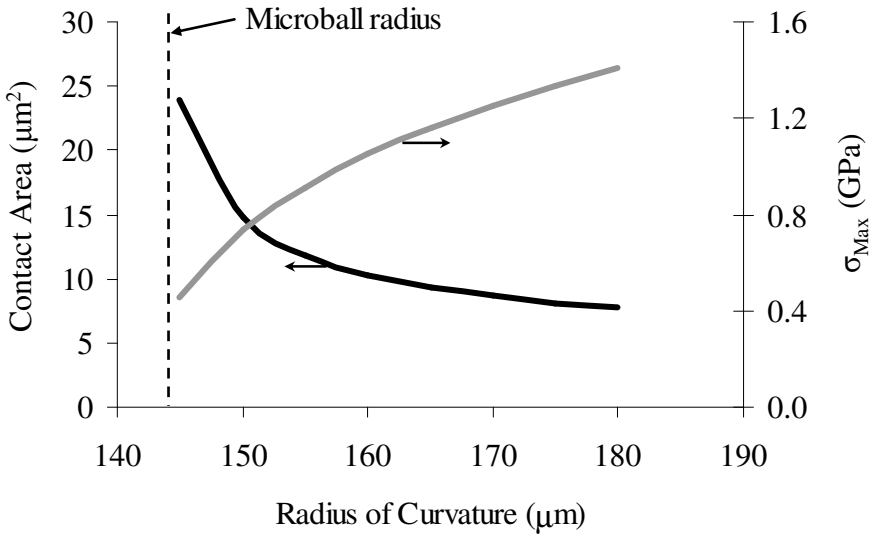

Figure 2.32. Contact area and maximum compressive stress plotted for a range of estimated raceway curvatures and an estimated ball load of 4.3N.

After the experiments were performed it was realized that the testing setup did not allow for a comprehensive characterization of the frictional torque versus load on the microball bearings. A different testing scheme is utilized in the following section to allow for a more comprehensive testing platform.

The wear exhibited in these experiments causes a large change in the sag of the rotor. This in turn means the control of any gap above the rotor, which is important for turbomachinery applications, is difficult. The δh from the calculation of the gap in Equation 2.21 is increased by the wear from the fabrication tolerances. The wear, from Figure 2.30, is estimated to be in the range of 10 μm, much greater than the built-in tolerances of 4 μm. The minimum gap achievable just from the sag of the rotor is then increased from 7 μm to 17 μm using the values from Table 2.3.

In terms of applications using the point-contact bearing design some limitations can now be addressed. As just described, the first limitation is the minimum gap associated with this design. The second limitation is the need for a "burn-in" to wear the bearing until the more stable region, region B (Figure 2.28), is reached. This bearing design is really only suitable for applications that do not require a small gap and can handle small changes in the gap over time.

2.4 Radial In-flow Microturbine using the Planar-Contact Bearing

The tangential flow microturbine was non-symmetric and required large driving pressures to operate. The non-symmetric design creates large pressure variations circumferentially around the rotor. These variations make it difficult for sealing between liquid and gas sections for micro-pumps as well as determination of bearing contact mechanics due to a circumferential variation of normal load on the rotor.

The point-contact bearing exhibited large wear and change in rotor sag. These characteristics make it difficult to design a micropump or other rotary devices where the rotor sag will play a role in determination of clearances and gaps as will be seen in Chapter 3 when the design of the micro-pumps are described.

In this section, a new raceway design is described that reduces the wear of the raceway and allows the rotor sag to be designed to within the micron level. Additionally, a radial in-flow microturbine design is described that is axisymmetric and can operate at driving pressures lower than those required for the tangential flow microturbine.

Spin-down testing was made possible by packaging the radial in-flow microturbine with a thrust balance plenum allowing control over the normal load on the

rotor. Spin-down testing allowed for the development of an empirical relationship between the normal load on the rotor and the friction torque caused by the microball bearings. The ability to measure the frictional torque from the microball bearing will enable future motoring schemes (i.e. MEMS micro-motors) to be optimized for the proper torque requirement.

2.4.1 Planar-Contact Bearing Design

A variation to the point-contact scheme was devised in hopes of minimizing the wear to the raceway and obtaining small, well-controlled gaps. To reduce wear, the compressive stress on the race must be minimized. This can be done by making the contact angle, α, perpendicular to the load. To facilitate this, the bearing race design was developed for application when the normal load is predominantly in the thrust direction (Figure 2.33). This is the case when using a radial in-flow air turbine as described more in the next section.

From Figure 2.33, h and w_1 must be large enough to ensure proper encapsulation of the microball, w_2 must be made large enough to provide sufficient clearance for rotation, and w_3 must be made large enough to extend past the entire contact area between the microball and silicon race. Unlike the point-contact design, this design does not have flexibility in choosing a contact angle. Additionally, this design is limited to operation in only one load direction; i.e. the direction from A' to A along the rotational axis (Figure 2.33). If the bearing were to operate in the opposite orientation, the ball would revert back to riding on a corner with a higher wear rate. Additionally, the sag in the opposite direction is much larger than the intended direction due to the off-center journal design.

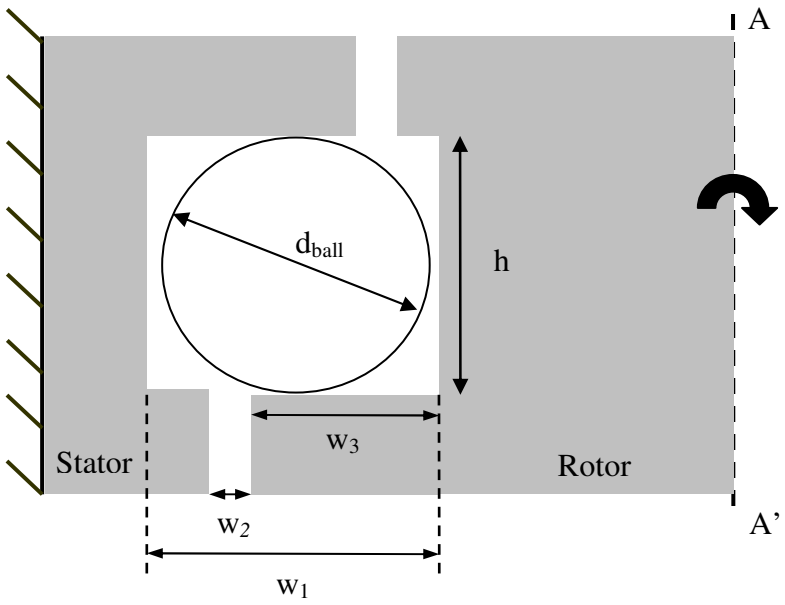

Figure 2.33. Schematic of the planar-contact design employing an off-center journal.

The dimensions for applications that employed this design are shown in Table 2.4. The choice of w_3 was to ensure the race extended well past the expected contacting area given predicted fabrication tolerances. On the other hand, the remaining length, w_1-(w_2 + w_3), must be sufficient enough to still capture the rotor when the load is flipped in the opposite direction during fabrication and assembly.

Bearing Race Parameter	Designed Dimension
d_{ball}	285 μm
$h + \delta h$	290 μm
$w_1 + \delta w_1$	290 μm
$w_2 + \delta w_2$	30 μm
w_3	190 μm

Table 2.4. Parameters for the planar-contact bearing.

2.4.2 Radial In-flow Microturbine Design

The performance and wear of planar-contact bearings are investigated in this section using a radial in-flow air turbine designed for an approximate speed of 100,000 rpm [19]. To allow for uniform flow, the microturbine design was implemented in place of the tangential air turbine thereby making it possible to perform measurements for loading and turbine performance (Figure 2.34). The packaging scheme (Figure 2.35), was designed to accommodate a pressure tap and fluidic ports on the backside of the microturbine rotor, acting as a controlled thrust balance plenum [19]. In this manner, the load on the rotor can be decoupled from the driving pressure of the air turbine to allow for spin down measurements with a controlled load. The rate at which the rotor slows down is determined by the amount of frictional torque caused by the microball bearing design and materials.

The planar-contact bearings are orientated such that the rotor is lifted by the thrust balance plenum on the backside (Figure 2.34b). The topside of the device consists of 24 turbine inlet orifices and measurement spokes in the center of the rotor for the ODS. The underside of the device is sealed by O-rings and a pressure cavity formed by the testing rig. By pressurizing the backside of the device the rotor is lifted into proper ball bearing contact and spun with pressurized nitrogen passing through the radial-inflow microturbine.

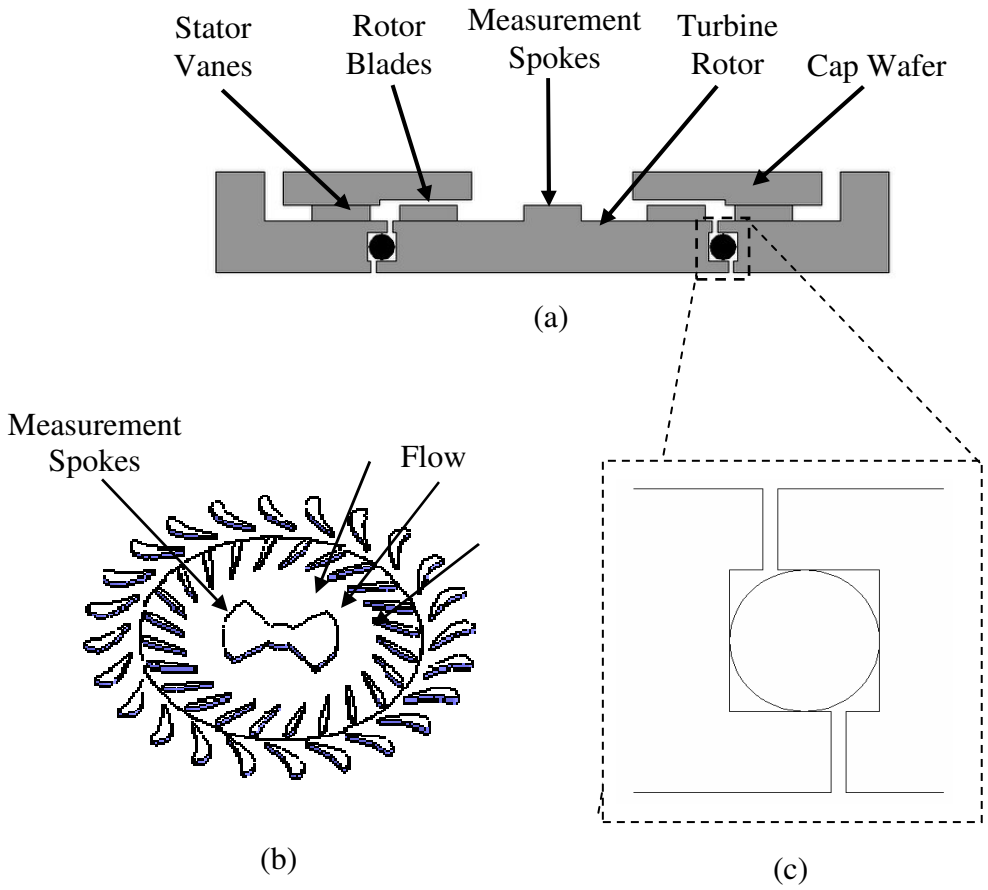

Figure 2.34. Illustrations showing: (a) cross-sectional view of the radial in-flow turbine supported by the encapsulated microball bearing; (b) radial in-flow air turbine design; and (c) planar-contact bearing orientation.

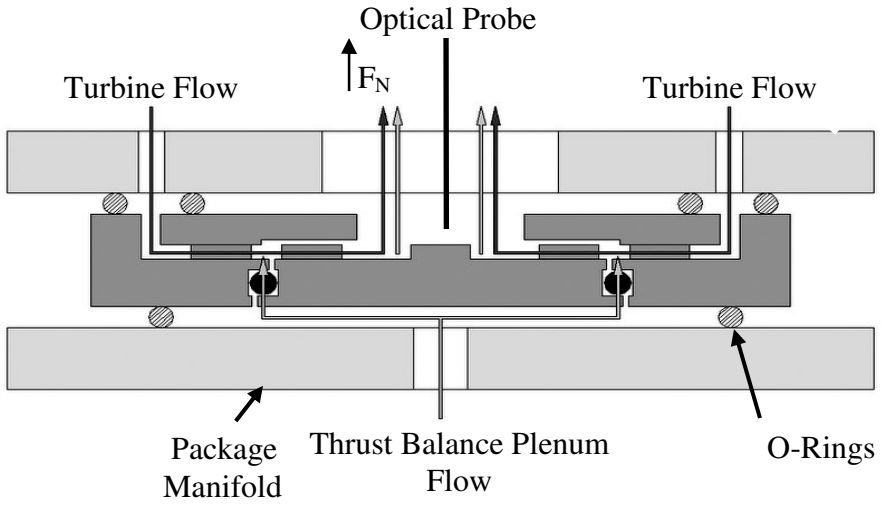

Figure 2.35. Illustration of the packaging scheme for the microturbine tribology device.

The thrust balance plenum allows a prescribed thrust load during spin-down testing. The development of this device enables: (1) investigation of raceway wear for the planar-contact bearing design; (2) investigation of frictional behavior as a function of normal loads and wear using spin-down testing; (3) characterization of the radial in-flow turbine as an axisymmetric motoring scheme for the turbopump application; and (4) a platform to study various material systems for the microball and raceway. The first three capabilities of the device are explored in this section. The last is left for future work using this device when optimized solutions are required for high-speed operation, low friction behavior when integrating a micromotor, and high reliability for a fielded system.

2.4.3 Rotor sag

As in the other bearing design, fabrication tolerance plays an important role in determining the sag of the rotor, which further determines the gap in the turbopump application. In the designed direction, the gap is determined only by the race etch depth, which can be controlled to be less than 2 μm. The ability to control the gap and the expected low wear of the raceway enable a higher degree of gap control for the micro-turbopump than is capable with the point-contact bearing design. However, the sag when the bearing operates in the opposite orientation is more complicated.

Figure 2.36 has been included to clarify geometry and orientation and to investigate the rotor sag due to the built in fabrication tolerances. For orientation, a $+F$ is a normal load in the direction of the designed bearing and a $-F$ is a normal load in the opposite direction.

The sag of the rotor is found by first calculating the shift in the y-direction on one side of the bearing, which is δy_F from Figure 2.36 as follows:

$$\begin{aligned} \delta y_{-F} &= r_{ball} + \Delta h_1 - \left[r_{ball}^2 - \left(r_{ball} + \Delta w_1 - w_2 \right)^2 \right]^{1/2} && \text{for} - F \\ \delta y_{+F} &= \Delta h_1 && \text{for} + F \end{aligned}$$

Equation 2.22.

The gap is then created by the shift due to both the inner race and the outer race, or

$$gap = 2\delta y$$

Equation 2.23.

Using Equation 2.22, Δh_1 can be tailored to achieve the correct gap for applications in which the orientation is in the designed direction (+*F*). Conversely, if the application requires the bearing direction be reversed (-*F*), then Δh_1, Δw_1, and w_2 can be tailored to achieve the desired gap. Furthermore, in the +*F* direction wear is expected to be low and the gap is expected to change linearly with wear. In the –*F* direction, on the other hand, the wear is expected to be high and the gap is expected to change like in the point-contact bearing design.

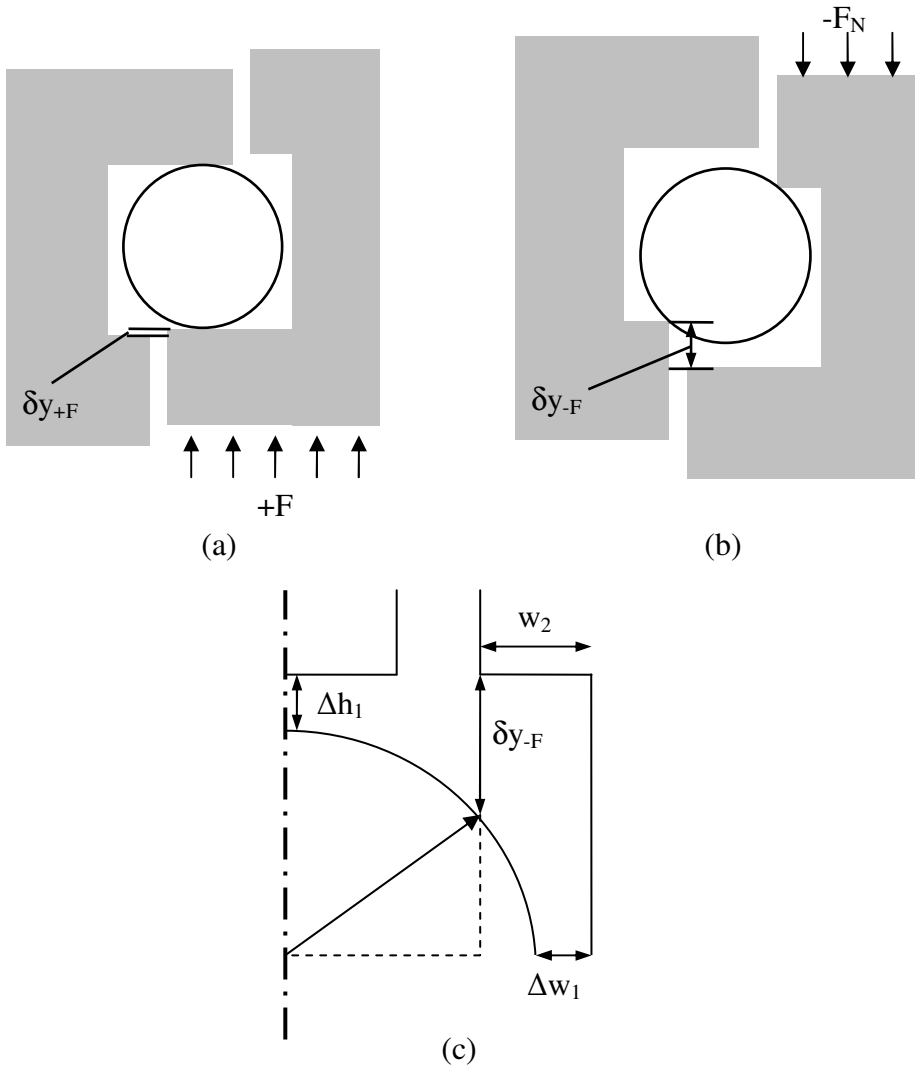

Figure 2.36. Schematic of the planar-contact bearing for a normal load in the (a) designed direction, (b) non-designed direction, and (c) a schematic showing the geometry required to calculate the sag of the rotor.

2.4.4 Bearing Contact Analysis

The same bearing analysis can be performed for the planar-contact bearing design as for the worn point-contact raceway. In this case, however, the number of microballs is increased to approximately 108 balls to fill the 5 mm radius raceway completely. The raceway curvature in the, R_y-direction, depends on the fabricated fillet radius formed by

the DRIE etch (Figure 2.37). The etch fillet radius can be measured by taking an SEM image of the raceway cross-section and estimating the radius of curvature.

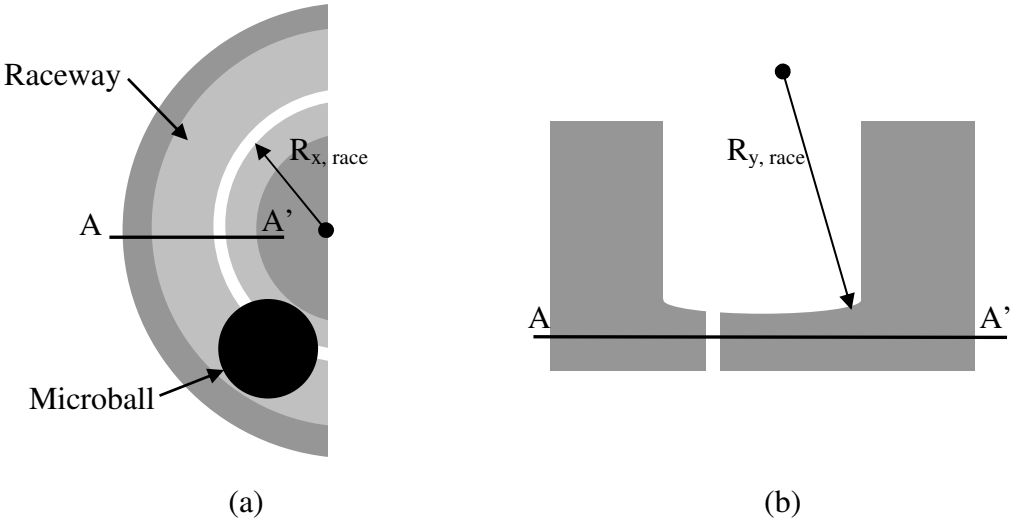

Figure 2.37. Schematics showing the planar bearing design radius of curvature in (a) the top down view of the raceway and (b) profile view.

Figure 2.38 shows the calculated contact area and corresponding maximum compressive stress plotted for a ball loading of 500mN and a range of raceway curvatures. The figure indicates that for fillet radii above the microball radius, the compressive stress will be below the theoretical tensile strength of silicon. This means much lower wear can be expected than what was experienced in the point-contact design. Furthermore, the etch fillet radius for the 290 μm wide raceway is expected to be well above 400 μm, in which any wear will result in unnoticeable compressive stress change and therefore unnoticeable change in the bearing operation.

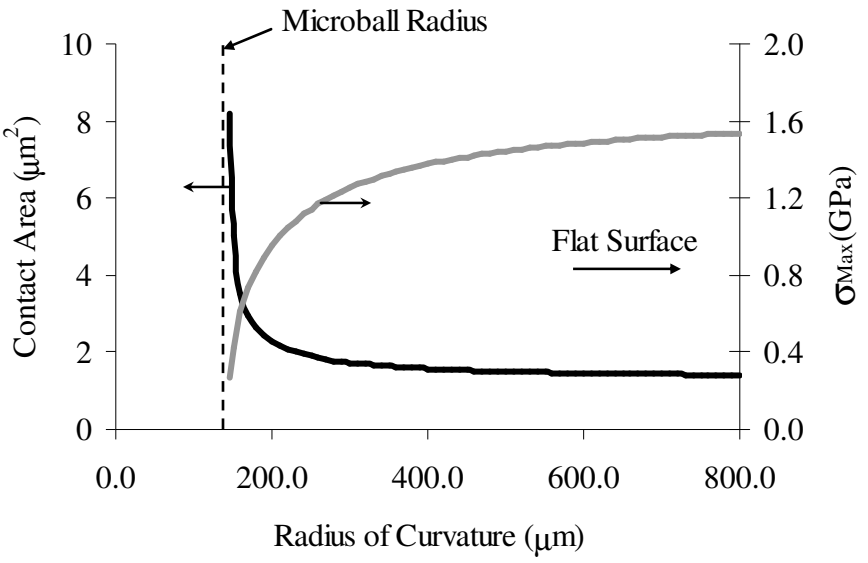

Figure 2.38. Plot showing the contact area and maximum compressive stress (σ_{Max}) trends for a 500mN load and increasing raceway curvature of a planar-contact bearing.

Lower wear suggests that planar-contact bearings can maintain a much smaller gap than point-contact bearings. The sag is dependent on the amount of wear in the y-direction and the etch depth precision using DRIE, which is typically less than 2 μm (Equation 2.23). The gap above the rotor that can be supported in applications such as the turbopump (Section 3.3) is dictated by the sag in the rotor and the bonding layers between the rotor wafer and the capping wafer. Using the AuSn eutectic bonding described previously, gaps on the order of 4 μm could be possible.

2.4.5 Fabrication

The fabrication of the microturbine tribology device is performed in two separate sections before assembly (Figure 2.39). First, the two-layer rotor is fabricated, sharing similar fabrication steps as the tangential air turbine device but using different optical mask designs and lithography alignment procedure. The alignment marks for the photolithography steps are etched into the silicon wafer prior to the thermal oxidation so that alignment will not be effected by any prior fabrication steps. As before, the planar-contact bearing structure and alignment pits are fabricated using photoresist and a nested silicon dioxide pattern (Figure 2.39a and b). The bottom of the raceway, etched in step (b), has an estimated radius of curvature, Ry, greater than 2 mm that is associated with the DRIE process used. The raceway curvature is well within the region in which the compressive stress remains stable for changes in curvature (Figure 2.38).

The microballs are placed in the annular race and alignment pits and the layers are aligned (Figure 2.39c) and bonded (Figure 2.39d) on the wafer level using the AuSn adhesion process. After the layers are bonded together the wafers are diced and the radial air-turbine geometry is patterned and etched on one side and the through wafer journals are patterned and etched on the other side releasing the rotor (Figure 2.39e).

A silicon capping layer is created with a shallow recess to provide clearance for the spinning rotor (Figure 2.39f) and a through-etch is used to define inlet and outlet ports (Figure 2.39g). Finally, the released rotor and capping layer are bonded using a temporary photoresist layer (Figure 2.39h and i). As a result, the capping layer can be de-bonded between tests to examine the turbine and bearing structures without having an effect on the rotor bond. Figure 2.40 shows images of a completed microturbine device.

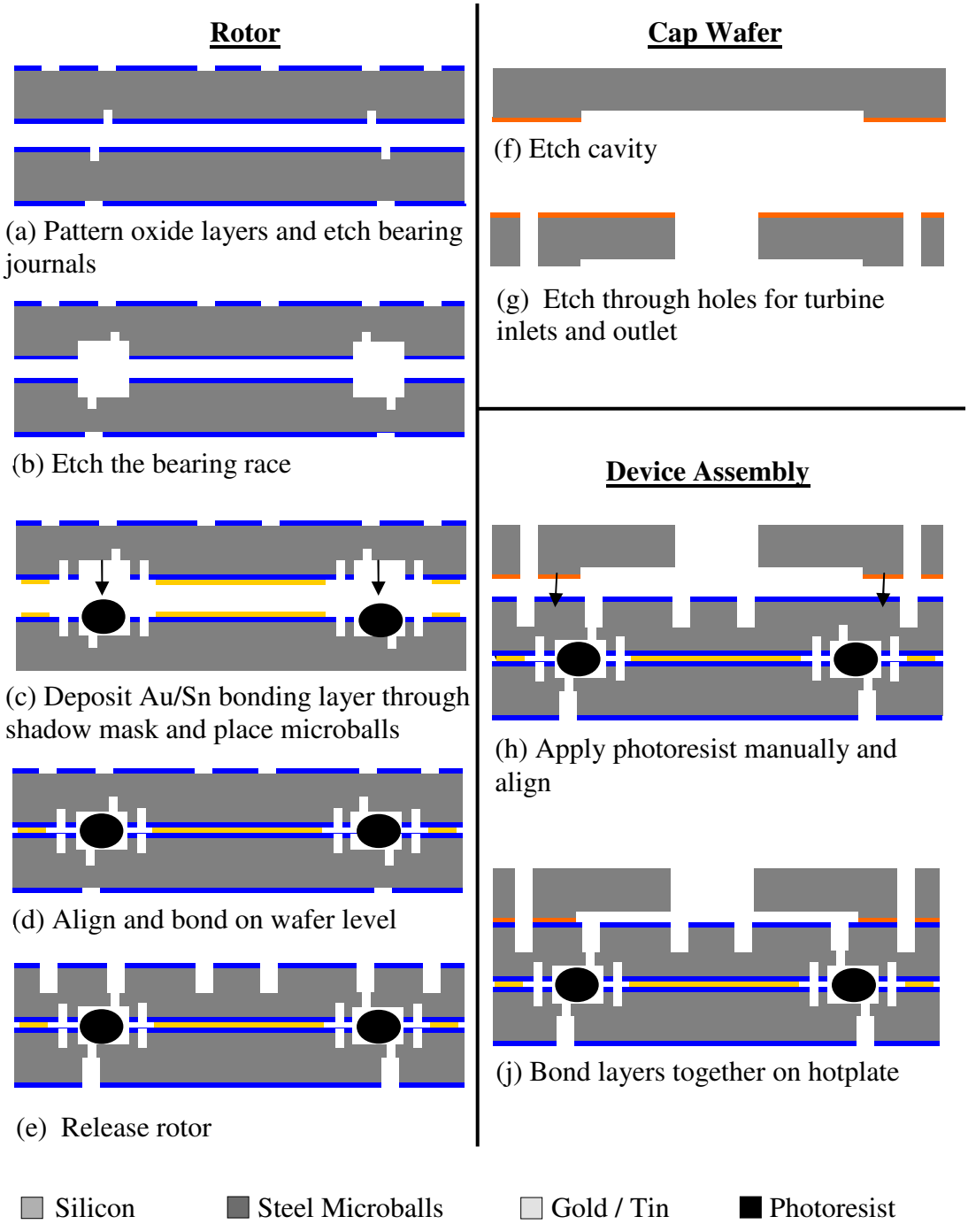

Figure 2.39. Fabrication sequence for the microturbine tribology device.

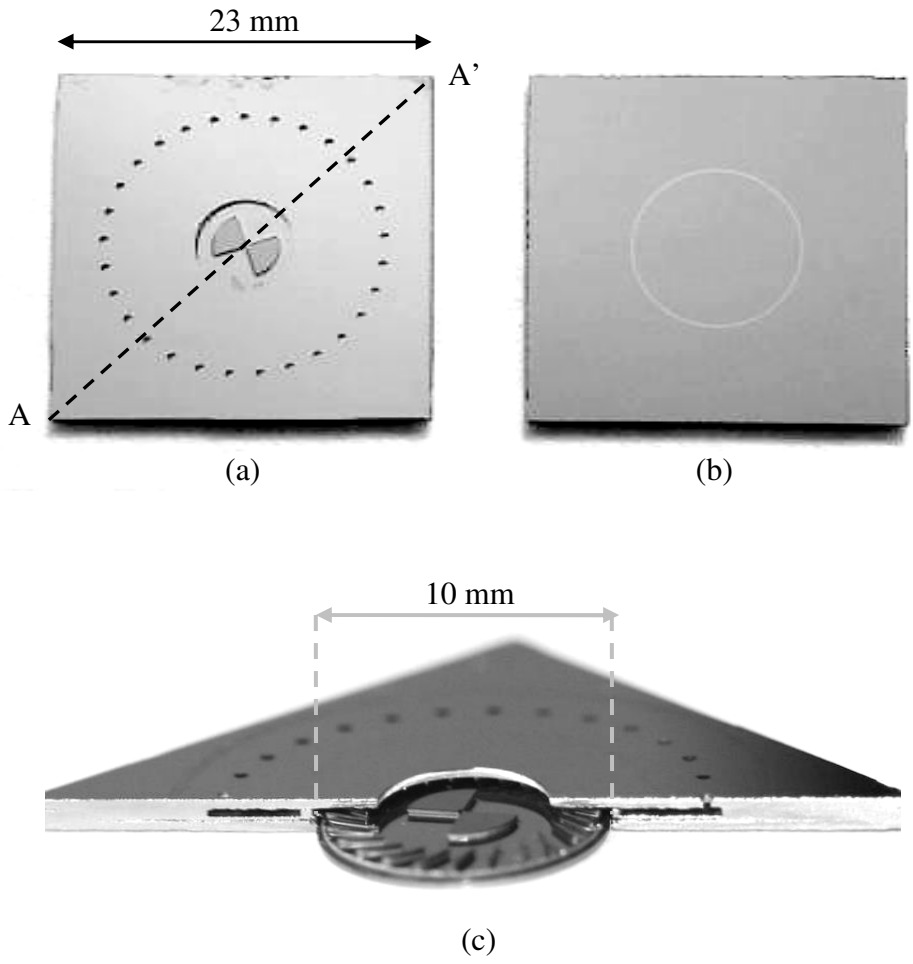

Figure 2.40. Photos of a completed microturbine device showing (a) the turbine side and (b) the thrust bearing side of the device with the cross-section A-A' in (c).

2.4.6 Characterization

This section describes the experimental platform for both the radial in-flow microturbine drive mechanism and the planar-contact bearing mechanism characterization. It is critical to understand the performance and behavior of these mechanisms before incorporation into a turbopump design. This requires measurements of the rotor speed, the turbine driving flow rate and pressure, and the thrust bearing

pressure. To perform a study on the frictional torque and its relationship to speed and normal force it is critical to monitor both the angular position and normal load (via the thrust bearing pressure) versus time during a spin down period.

The gas control and measurement setup and the speed measurement setup with a computer interface are shown in Figure 2.41. A picture of the packaged device is shown in Figure 2.42. The device can operate with or without pressure provided by the thrust balance plenum. In both cases, turbine inlet pressure causes the pressure in the plenum to elevate and increase the force acting to push the rotor against the designed planar-contact bearing (normal force).

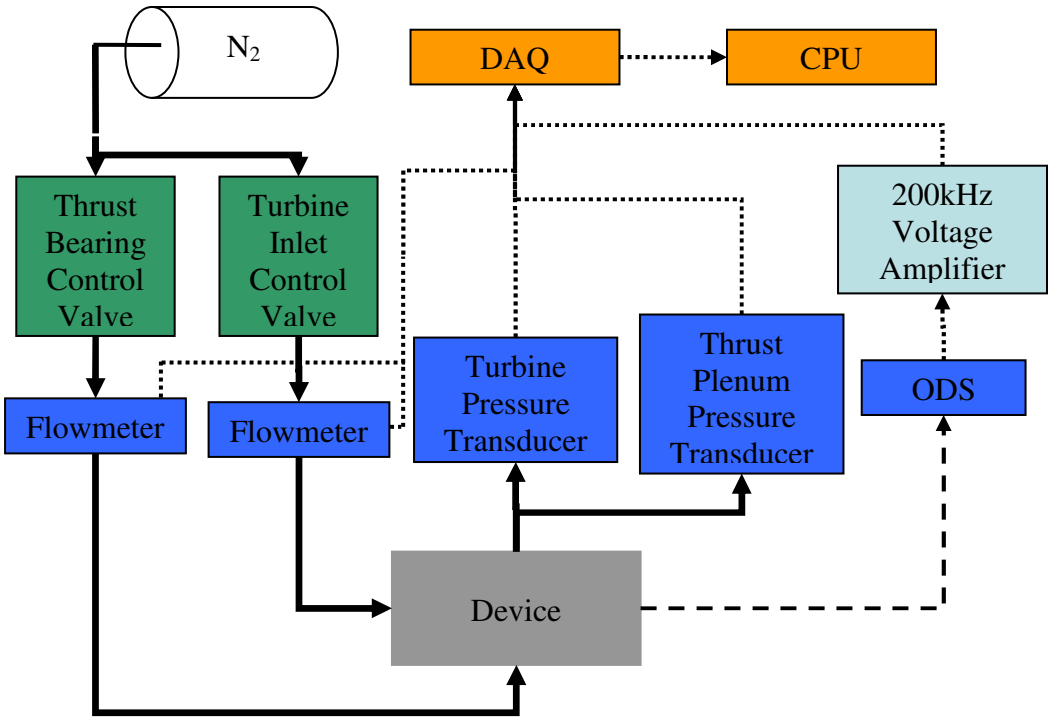

Figure 2.41. Schematic of the experimental apparatus used for testing the microturbine tribology device.

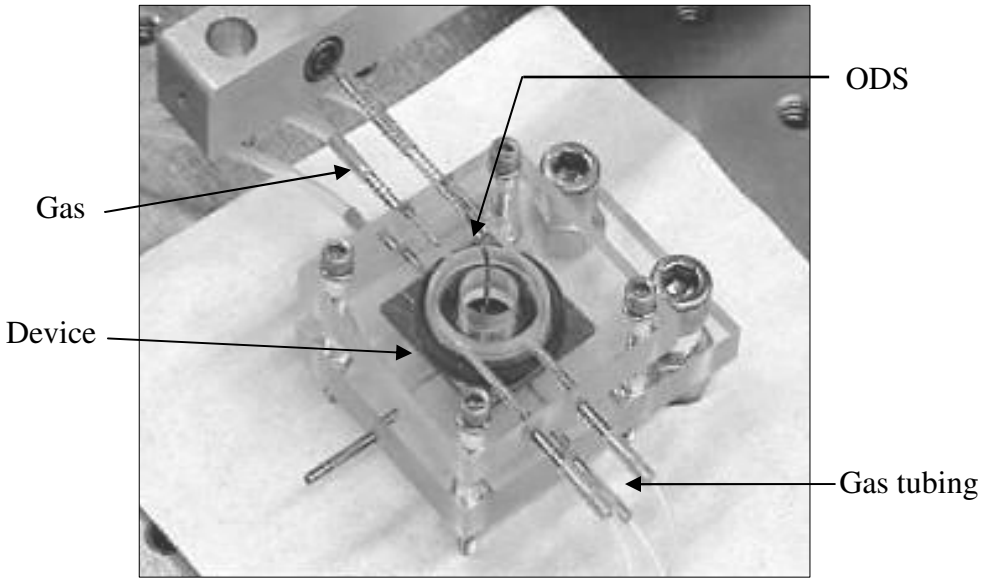

Figure 2.42. Optical photograph of a packaged microturbine showing various pneumatic connections and the optical displacement sensor.

Performance curves of the microturbine are shown in Figure 2.43. As seen from the speed versus pressure plot there is a specific pressure (greater than 0.1 psi) required to overcome the static friction force of the microball bearing for this particular device when starting from rest. Additionally, decreasing the driving pressure below 0.1 psi while the rotor is spinning causes an undesired behavior in that the speed drops significantly. Within the speeds of interest for the turbopump application (as will be seen in chapter 3, the range of interest is 5,000 to 10,000 rpm), the microturbine is stable for close to 1,000,000 revolutions.

The characterization curves (Figure 2.43), however, were not produced by continuous operation of the microturbine. The turbine performance degradation after a certain period of time is believed to be a result of debris build-up during operation. Successive tests, in which the microturbine was cleaned in an ultrasonic bath between

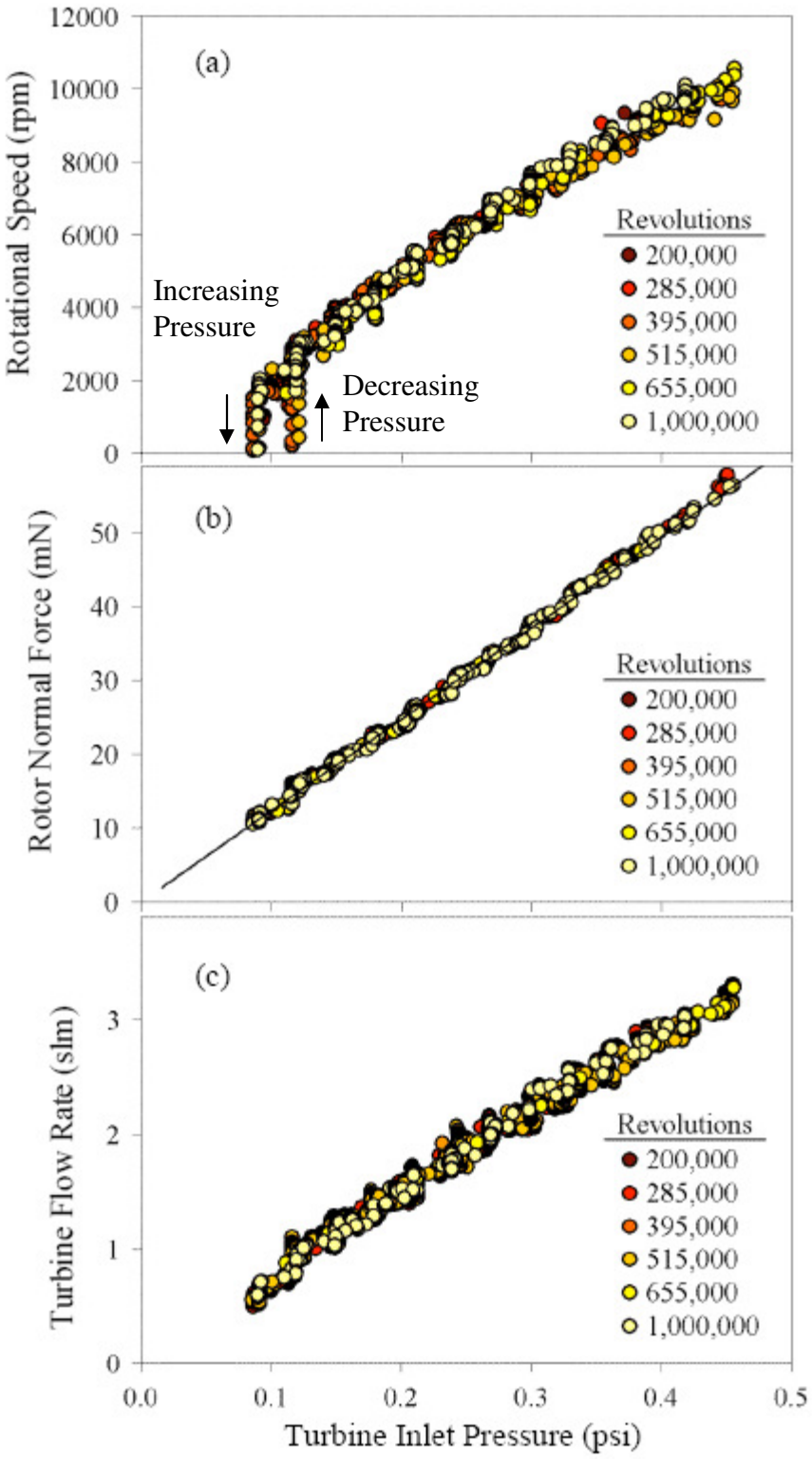

Figure 2.43. Turbine performance curves showing the rotational speed, rotor normal force (without applied thrust pressure) and turbine flowrate plotted for turbine operation pressures.

runs, showed the microturbine returning to the maximum performance after cleaning, until once again, build up of debris occurred (Figure 2.44). Each test exhibits longer and longer continuous running operation of the microturbine with an increasing number of revolutions. This suggests reduction of the bearing raceway wear.

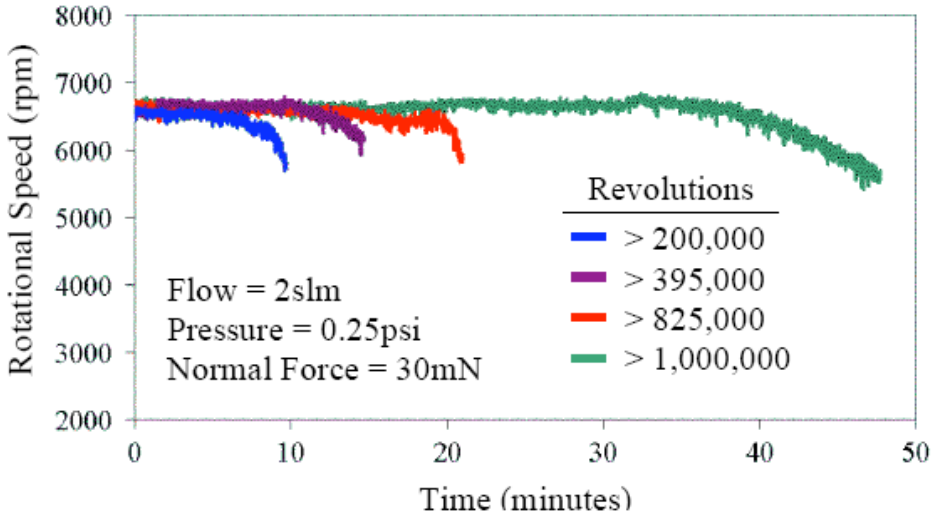

Figure 2.44. Speed plotted against time for the microturbine after successive cleaning procedures showing the microturbine having longer stable operation with increased revolutions.

The raceway wear of the devices can be inspected in a similar manner to the tangential air turbine. The capping wafer of a microturbine device, operated for more than 1,000,000 revolutions at an average speed of 8,000 rpm, was detached in acetone and the rotor de-bonded on a hotplate. An SEM image of the rotor shows the raceway before and after testing (Figure 2.45). A 1µm x 25 µm wear track is visible, suggesting minimal wear occurs at the base of the raceway. The edge of the raceway, close to the

journal etch, exhibits some roughness due to micro masking at the corner during the nested etch (Figure 2.39b).

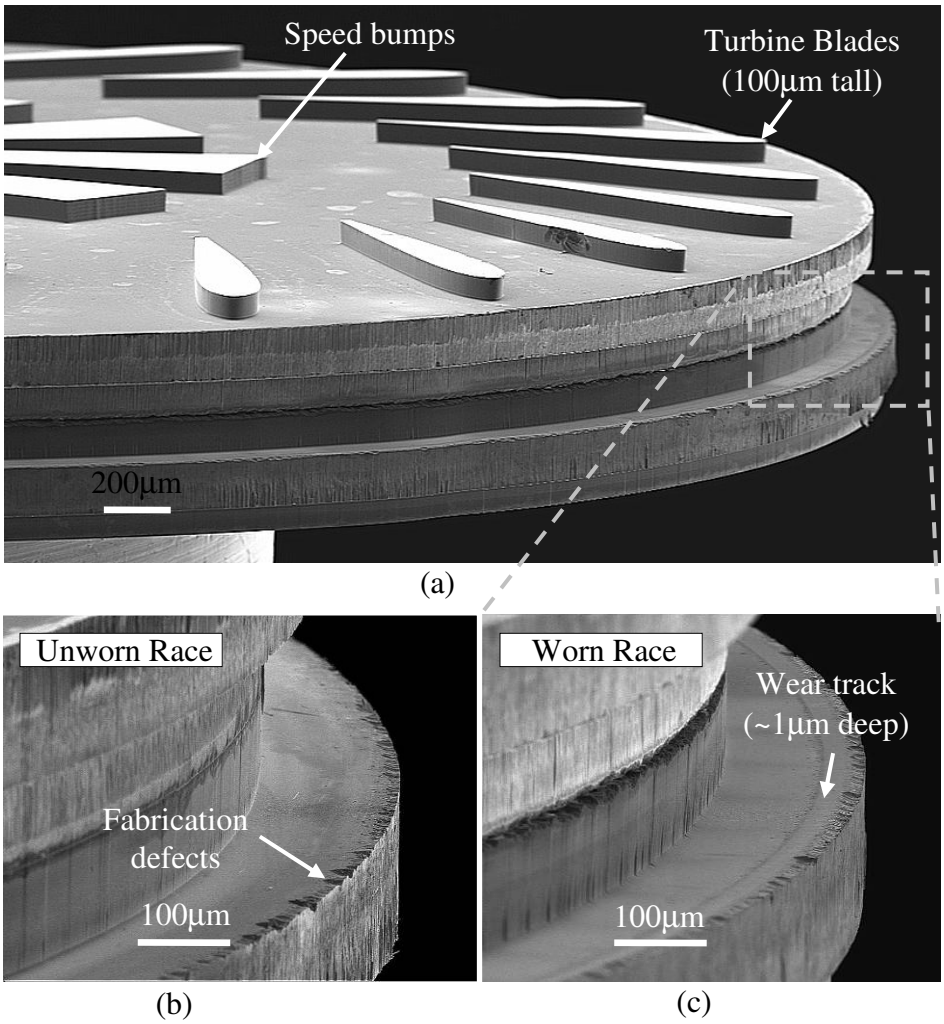

Figure 2.45. SEM images of (a) the microturbine rotor and (b) an image of the unworn race and (c) an image of the worn race.

The wear track observed for the planar-contact bearing is greatly reduced from the observed wear track in the point-contact bearing design (Figure 2.29). This is due partly to the decrease in the required pressures to spin the turbine and therefore lower

normal load on each ball. It is also due to the planar-contact design with a 90˚ contacting angle and large race curvature.

Not all devices that employed the planar-contact bearing operated at the same performance as the device described above that were used to characterize the microturbine operation. In some cases the operation of the microturbine would decrease after the first minute of operation and never return, even with the ultrasonic cleaning step. The sudden decrease in the turbine operation, from 10,000 rpm at a turbine flow rate of 8 slm to less than 5,000 rpm at the same flow, suggests an increase in the bearing friction.

After inspection of the device, the possibility of the rotor rubbing the outer housing became evident (Figure 2.46). Figure 2.47 shows an image of the rubbed surface of the rotor close to the area of the journal misalignment that is demonstrated in Figure 2.46b. The misalignment between the journal and raceway photolithography step is typically estimated to be 2 μm. The bond alignment tolerance between the two rotor layers is 5 μm set by the alignment pit width. The front-to-back misalignment is measured to be 5.5 μm on the thrust balance plenum side between the two journal patterns (Figure 2.48). Together, these alignment errors can cause the 30 μm wide journal to be reduced to 17.5 μm. In addition to these fabrication tolerances, significant raceway wearing, close to 10 μm deep and 50 μm wide, was observed at the bonding interface (Figure 2.49). When the 10μm wear on both the rotor bond interface and the outer raceway bond interface combine with the fabrication tolerances it is possible for the surfaces of the rotor and the housing to rub in the area of the journal.

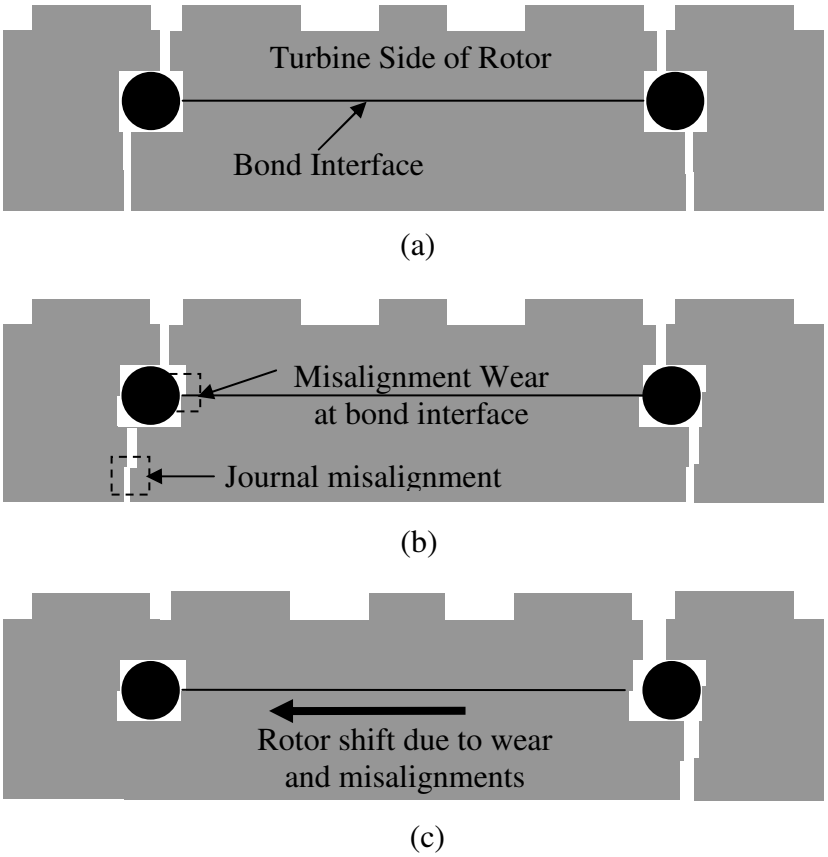

Figure 2.46. Cartoon drawing describing the rotor shift and eventual rubbing on the stator. (a) shows ideal case, (b) shows areas of misalignment and wear, (c) shows contact points when rotor rubs due to whirl.

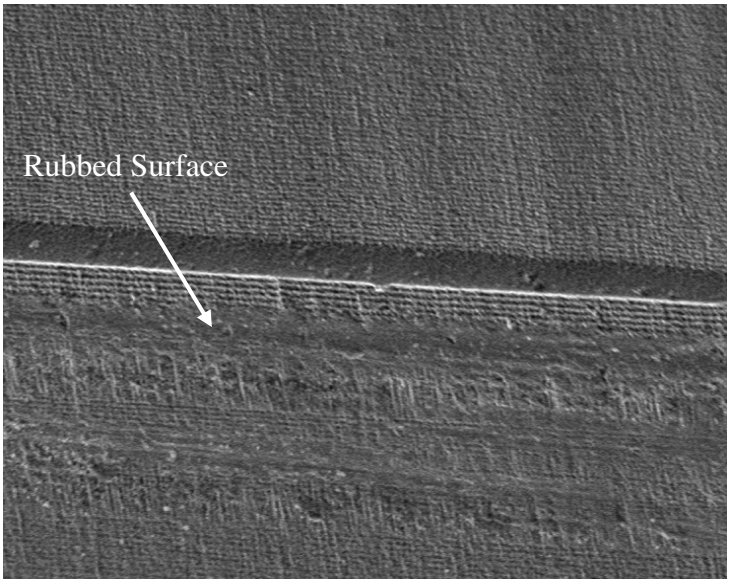

Figure 2.47. SEM image showing evidence of the rotor rubbing.

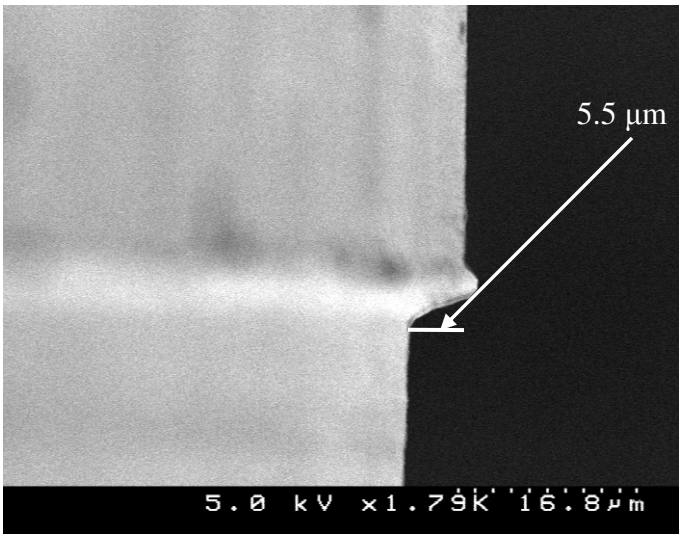

Figure 2.48. SEM showing the misalignment between the topside journal definition and backside journal definition.

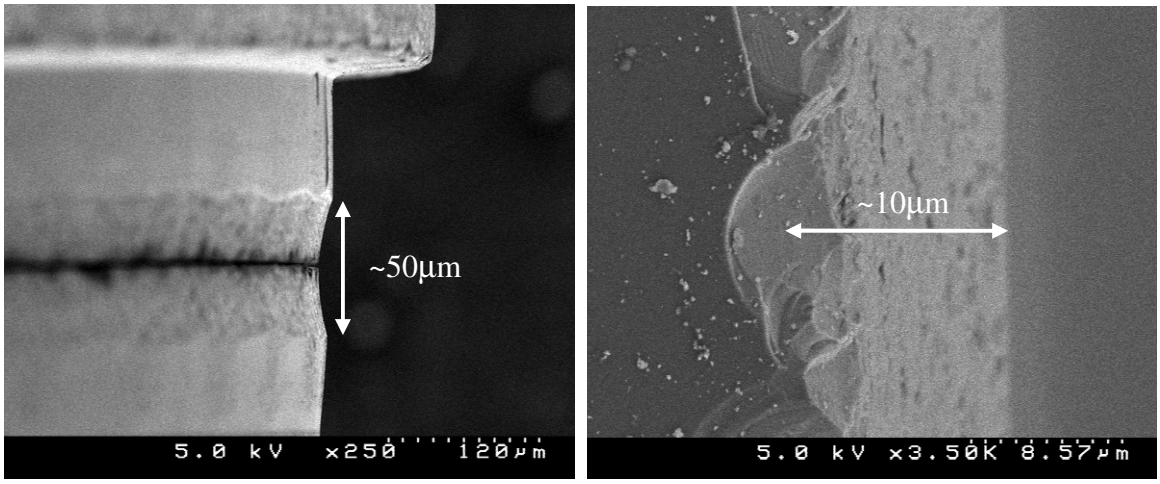

(a) (b)

Figure 2.49. SEM image showing the wear exhibited at the bond interface between the two raceways; the radial bearing surface. (a) shows the profile view of the rotor raceway and (b) shows the top-down view of the bond interface wear.

To minimize the wear created at the bond interface and to eliminate rubbing between the rotor and the housing, the bonding interface can be moved away from the expected wear track, which was measured to be 25 μm wide (Figure 2.45c). When the microballs ride on the flat surface, away from the bond interface, the wear can be expected to be less than 2μm (Figure 2.45c). In addition to a reduction in wear, the debris caused by the fracturing of the silicon at the bond interface will also be reduced. This is a benefit because the debris is believed decrease performance over time and necessitates the periodic ultrasonic cleaning. This factor will be taken into consideration in the design of the micro-turbopump raceway and the fabrication steps required to move the bond interface will be described in the following Chapter.

2.4.7 Spin-down Friction Testing

Spin-down testing was performed for a range of normal loads on the rotor to find an empirical relationship between the frictional torque created by the bearing system and the speed. This allows the design for microturbines and micromotors to be optimized for compactness and efficiency while providing the required torque for the range of operational loads expected.

Spin-down testing was enabled by the packaging scheme (Figure 2.35), which allowed a thrust balance plenum on the backside of the rotor to control the normal load. Increasing the pressure within the plenum causes a further increase to the pressure and the normal force acting on the rotor. When the turbine inlet pressure is turned off the pressure underneath the rotor will equilibrate to the plenum pressure supplied.

Testing begins by setting the thrust balance plenum pressure to obtain the desired normal load on the rotor. The turbine pressure is then increased until the desired speed is reached, approximately 10,000 rpm for the device reported in this section. Once this desired speed is reached, the raw ODS data, time, and thrust bearing pressure data collection is started (largest amount of data possible from the DAQ card) and the turbine driving pressure is abruptly shut off.

Figure 2.50 shows the operation and the data collected during the spin-down procedure. Region 1 depicts the operation where the thrust force (calculated by the measured thrust bearing pressure) includes both the set pressure in the balance plenum and the turbine driving pressure. Region 2 shows the operation after the turbine driving pressure is turned off and the speed decreased due to the bearing friction. The spin-down data is analyzed only when the backside equilibrates to the pressure of the balance plenum set by the thrust flow (region 3 of Figure 2.50). This ensures that the deceleration measured is due only to the prescribed normal load.

The angular position, θ, versus time is shown in Figure 2.51 for normal loads of 6, 14, 25, and 50 mN. An exponential was fit with the following form:

$$\theta = A(1 - \exp(-Bt)) \qquad \text{Equation 2.24,}$$

which is used to accommodate for a linear relationship between the frictional torque, τ, in the bearing (proportional to the angular acceleration, $\ddot{\theta}$) and the bearing speed, ω, (angular velocity, $\dot{\theta}$):

$$\frac{\tau}{\omega} = \alpha \cdot F_N^{\beta}$$ Equation2.25,

where α and β are empirical constants. Figure 2.52 shows τ/ω as a function of F_N for spin-down tests performed periodically through the device operation and cleaning cycles. As the amount of debris caused by wear decreased with the number of cycles, the

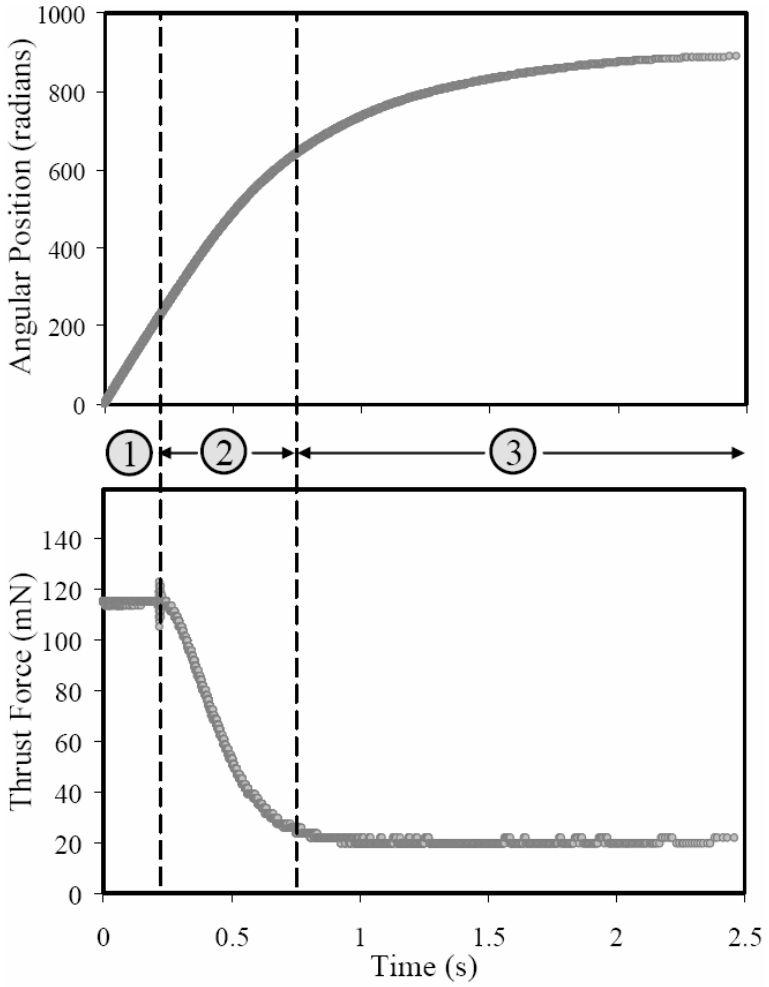

Figure 2.50. Spin-down data showing the angular position and the thrust force over time. Region 1 exhibits the constant operation of the turbine. At the beginning of region two, the turbine driving flow was turned off (can see the spike from flipping the valve) and region 3 is when the thrust load equilibrates to the load prescribed by the thrust bearing.

empirical constants were found to settle to 9 x 10^{-5} for α, and 0.444 for β, over the 6 periodic testing cycles. This information can ultimately be used in designing other motoring mechanisms that use the planar-contact bearing design.

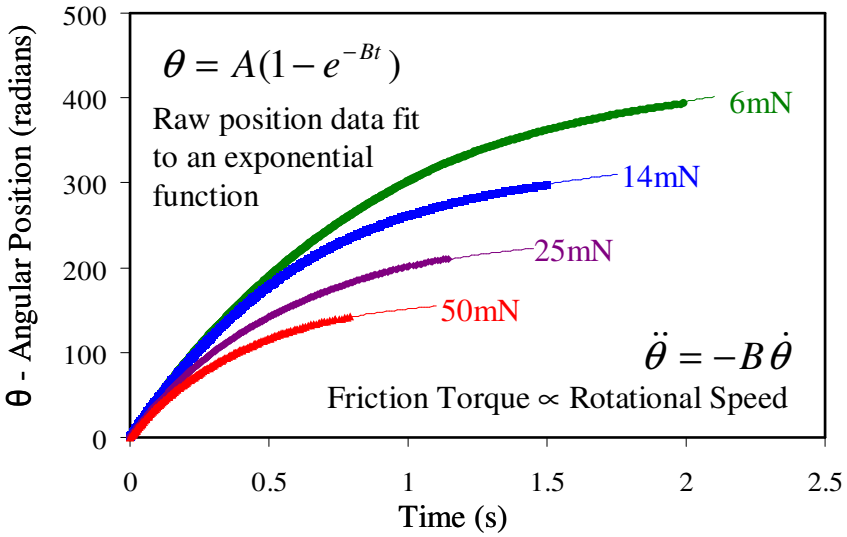

Figure 2.51. Spin-down data for thrust loads of 6, 14, 25, and 50 mN.

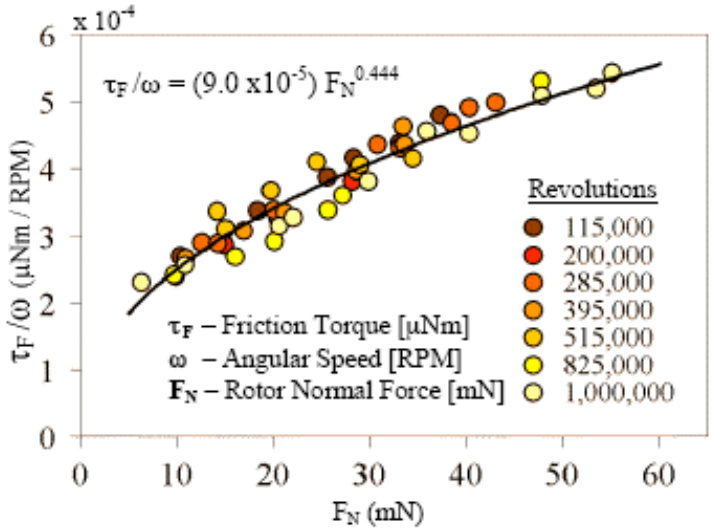

Figure 2.52. Plot of τ/ω versus the normal load on the rotor.

2.5 Summary

The encapsulated microball bearing was introduced in this chapter along with critical fabrication methods. Included in the fabrication methods was a novel alignment technique using tailored alignment pits and the microballs themselves. The methods developed for the microball bearings can serve as a platform for many applications and are not limited solely to the micro turbopump and microturbine devices detailed in this dissertation.

Two microball bearing configurations were designed, fabricated, and characterized: 1) the point-contact bearing and 2) the planar-contact bearing. The point-contact bearing was devised with the intent to control the contact angle between the microball and the raceway for applications in which both thrust and radial loads are present. The characterization of this bearing design using the tangential air-turbine resulted in high raceway wearing and was found to be useful only in applications not requiring small rotor sag.

The planar-contact bearing was then designed to reduce the wear on the raceway allowing for small rotor sag and to allow the microball to ride on a relatively flat surface rather than a sharp corner. This allowed an order of magnitude reduction in the compressive stress (from approximately 25 GPa to 2 GPa) between the microball and the raceway and, therefore, reduced the wear track depth from approximately 10 μm to 1 μm. The planar-contact bearing can be used in applications requiring small gaps with 4 μm feasible using thin bonding layers.

A radial in-flow microturbine was developed as an axisymmetric rotary actuator. This design allowed uniform pressure distribution circumferentially around the raceway

by enabling better calculation of the normal load exerted on the microball bearing. The operation of the microturbine was characterized along with the wear exhibited within the raceway. The combination of the microturbine and a thrust balance plenum created by the packaging scheme facilitated spin-down testing, which led to an empirical relationship between bearing frictional torque and speed for a range of normal loads.

Studies are underway to further investigate the friction and wear behavior for the planar-contact bearings using both a linear, low speed tribology setup and the microturbine tribology device. These studies will focus on the addition of hard coatings on the silicon raceway such as such SiC and Ultrananocrystalline diamond. Preliminary results show promise for these materials to provide microball bearings with lower friction and wear for high-speed/high-load applications.

In addition to hard coatings on the silicon raceway, alternative microball materials such as ceramics may provide for better operation than the stainless steel/silicon system. Both raceway and microball materials can be investigated using the microturbine tribology.

3 Microfabricated Turbopump Designs

The primary objective of this dissertation is to demonstrate a compact liquid pump capable of supplying fuel to portable power generators. To meet this objective, rotary pumping mechanisms were investigated for three key reasons: 1) the pumping action is purely mechanical; 2) the designs can be realized using batch silicon microfabrication; and 3) the mechanisms are scalable to meet a broad range of flow rate and pressure requirements. The rotary operation of centrifugal and viscous-type pumps allows an air turbine drive mechanism. These pumps are then considered turbopumps. The air turbine can provide a large amount of torque and is simpler to integrate with the microball bearing mechanism when compared to other drive mechanisms, like micromotors, not yet fully developed.

The design concept of the microball bearing supported turbopump is again depicted in Figure 3.1. Two of the key components of the turbopump, the microball bearing and the air turbine, were developed in Chapter 2. The last key component is the pumping structure, which is presented in this chapter.

Two rotary pump configurations were investigated for the final turbopump demonstration: centrifugal and viscous. Both variations of pumping have advantages and disadvantages. The working principles of viscous pumps allow for design with smaller dimensions since, due to a larger surface area to volume ratio, viscous forces begin to dominate at the micro-scale. Additionally, analytical solutions are available to enable

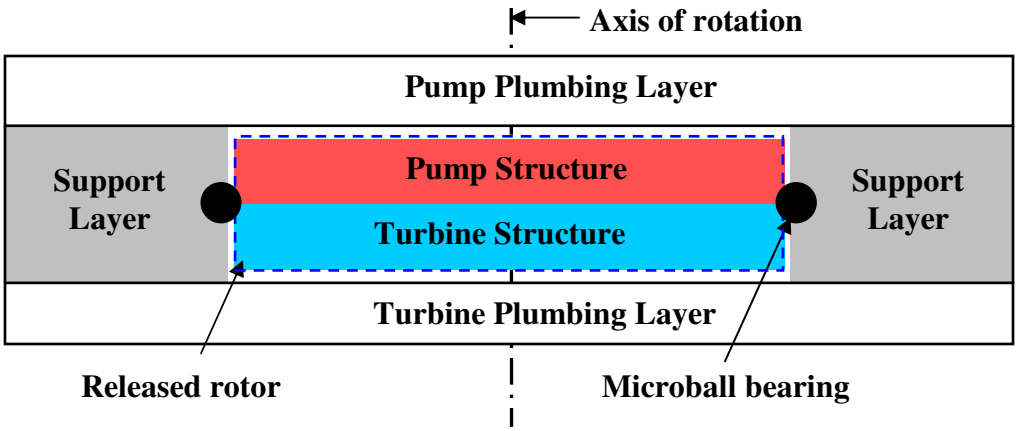

Figure 3.1. Schematic illustrating the micro turbopump concept.

their design [55]. On the other hand, the viscous pump performance relies on precise dimensional control of a gap to take advantage of this scaling.

Since a microball bearing is utilized as the rotational support mechanism it is important to consider the effect of raceway wear and the ability to maintain a critical gap. Centrifugal-type turbopumps do not require the same gap control precision as viscous pumps, which may make them a better match to microball bearing support. The centrifugal-type pump, however, does not allow for as compact a design as the viscous pump. Turbomachinery pump mechanisms such as the centrifugal pump also require the use of CFD and empirical models for their efficient designs to study the low Reynolds flow (e.g. flow separation).

This chapter first presents the design and implementation of a centrifugal turbopump on the platform of the point-contact bearing and tangential air turbine. Second, the characterization of this device will be presented along with a discussion for improvements. In addition, the design and implementation of a spiral-groove turbopump on the planar-contact bearing and radial in-flow turbine platform will be discussed. The

experimental set up, results, and discussion of the spiral-groove turbopump will be presented in Chapter 4.

3.1 Micro Turbopump Requirements

The goal of the turbopump is to pump heavy fuel; specifically JP-8 diesel fuel for heat engines or fuel cells (or fuel reformers). This application sets the criteria for the fuel flow rate and pressure while the driving mechanism (air turbine or integrated motor) sets the torque available. Future implementations of the pump will replace the turbine with an integrated MEMS micromotor, which are limited by the torque created. The pump structures will, therefore, be designed to minimize the torque required. For most micromotors, the amount of active area is directly linked to the available torque from the motor and can be increased for larger torque requirements.

Portable power generation applications producing 10-100 W of electrical power with an efficiency of 10% require the fuel flow rates to be in the range of 10-100 mL/hour (assuming JP-8 diesel fuel with a density of 0.86 kg/L and an energy density of 12.03 kW·hr/kg). In compact combustion systems, fuel is passed through an injector or fuel atomizer before being mixed with air and combusted. Hence, the pressure required will be set by the fuel injector. Effective fuel atomization for fuel cells and heat engines, at the scales of interest, are not yet fully developed. Yale University, however, has developed an electrospray technology as part of a program focusing on the fuel/air control for Power MEMS [10]. The pump was designed with specifications that can meet the requirements of the fuel atomizer at Yale University [9, 10]. The pressure

requirement from the fuel atomizer is a minimum of 0.75 psi using the multiplexed electrospray design [10].

3.2 Centrifugal Turbopump

The first approach to develop a micro-turbopump was to mimic macro-scopic centrifugal designs that are most common at that scale. The design, fabrication, and testing of a centrifugal turbopump that incorporates the point-contact bearing and tangential air turbine are described in this section (Figure 3.2). The key parameters of the centrifugal turbopump are displayed in Table 3.1.

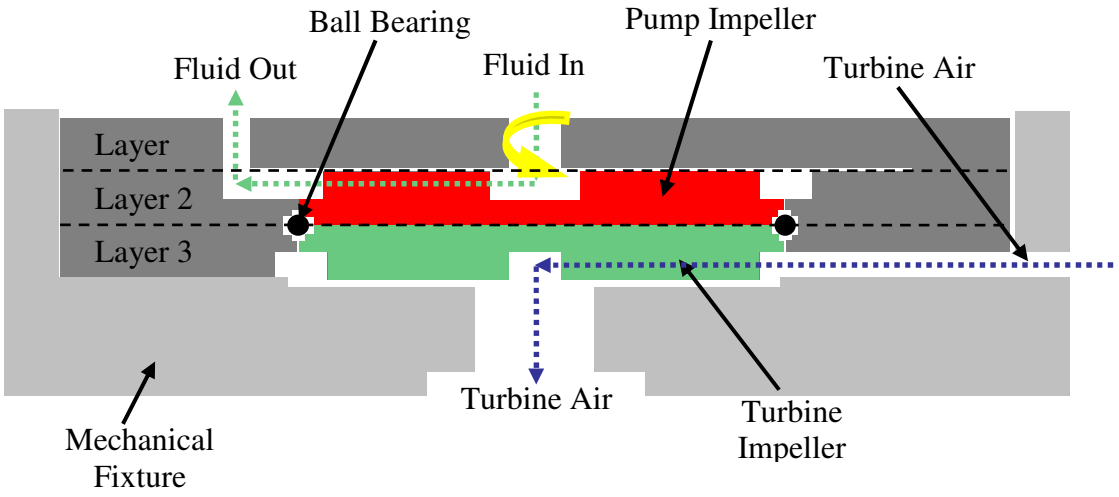

Figure 3.2. Schematic of the centrifugal turbopump.

The complete microfabricated turbopump consists of 3 layers, two of which make up the rotor. The point-contact bearing and the tangential air turbine are applied to support and drive the centrifugal impeller respectively. An impeller is added to the rotor

face opposite to the turbine and a plumbing wafer is attached above the impeller for fluidic ports. The turbine side of the device is placed in a mechanical fixture containing the turbine inlet and outlet ports.

Centrifugal Impeller	
Outer radius, r_2	4 mm
Inner radius, r_1	2 mm
Blade height	200 μm
Blade angle	60˚
No. of blades	4
Volute exit width	50 μm
Tangential Air Turbine	
Outer radius	4 mm
Blade height	100 μm
No. of blades	8
Point-contact Bearing	
Race width, w_1	290 μm
Journal width, w_2	150 μm

Table 3.1. Centrifugal turbopump parameters

The centrifugal pump is a radial-type pump. In this fashion, the rotor pulls fluid axially inward from the center and pushes it radially outward (Figure 3.2). The pumping mechanism is the transfer of momentum from the rotating impeller blades to the fluid. In this work, the rotation is accomplished by the torque created from the tangential air turbine, or other motor for applications without an air turbine.

The fluid enters the centrifugal impeller from the plumbing layer above, is pushed radially outward by the impeller blades, and finally collected into the volute and exit of the device (Figure 3.3). The centrifugal impeller and the volute are designed according to

the flow rate and pressure requirements of the fuel atomizer. When optimizing for these parameters, compactness, required torque and rotational speed are compromised. These designs are presented in the following sections.

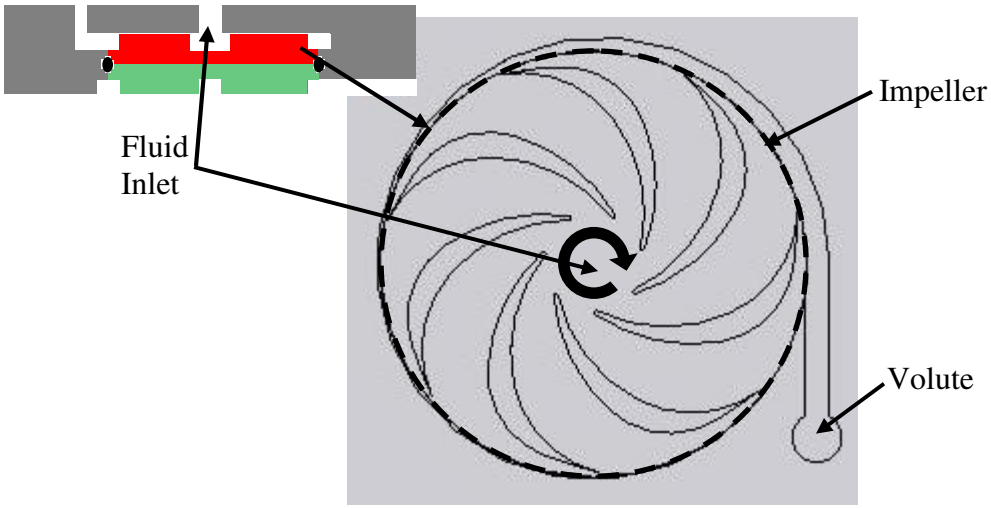

Figure 3.3. Schematic drawing of the pump rotor level showing the rotating component inside the dotted line.

3.2.1 Impeller design

The impeller blade shape and features dictate both the flow rate and the pressure capability of the pump. The flow vectors shown in Figure 3.4 were used in conjunction with Euler's turbomachine equations to investigate flow rate, pressure rise, and torque for a rotor in the millimeter scale that meets the requirements of the fuel atomizer.

The first order volumetric flow rate (Q) through the impeller, derived from the Euler Turbine Equation based on compressible, inviscid flow, can be found by [56]:

$$Q = 2\pi r_1^2 b_1 N \cot \beta_1 \qquad \text{Equation 3.1,}$$

where subscript 1 denotes the leading edge of the impeller blade (pump entrance), r is the radius, b is the height of the flow passage or rotor blades, N is the speed of rotation in rad/sec, and β is the flow angle between the mean velocity vector (U) and the relative velocity vector (W) (Figure 3.4). The pressure rise across the pump impeller (from the leading edge to the trailing edge) is given by [56]:

$$\Delta P = P_2 - P_1 < \frac{\rho N^2 (r_2^2 - r_1^2)}{2} \qquad \text{Equation 3.2,}$$

where ρ is the density of the fluid and the subscript 2 denotes the trailing edge of the impeller blade (pump exit). The torque required for a given flow rate and pressure rise is then [56]:

$$T_{shaft} = \rho Q N r_2^2 \approx \frac{Q \Delta P}{N} \qquad \text{Equation 3.3.}$$

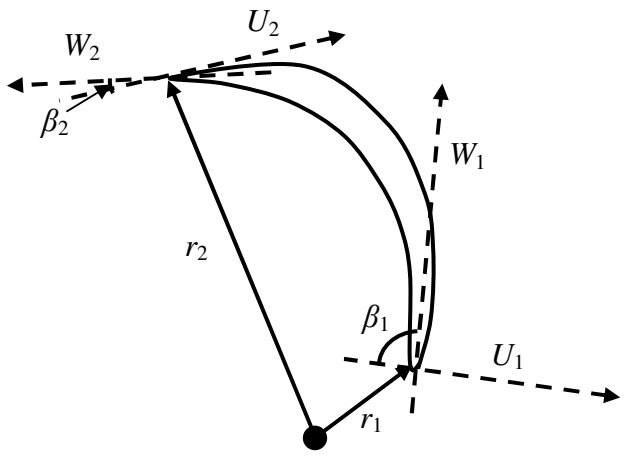

Figure 3.4. Velocity vectors for the pump impeller where subscript 1 denotes inlet flow, subscript 2 denotes outlet flow, U is the mean velocity vector (rotational vector), and W is the relative velocity vector.

Together, these equations form the first order design equations for the centrifugal pump. Figure 3.5 shows plots of the flow rate, pressure, and torque versus the rotational speed for an inner radius, r_1, of 100μm, a blade height, b_1, of 100μm, a flow angle of 67° and a fluid density equal to 0.80 g/cm^3 for JP-8 diesel fuel. These parameters were developed for flow rates of tens of mL/hour.

From the plot of pressure versus rotational speed (Figure 3.5b) it is shown that the pressure can be tailored, without affecting the volumetric flow rate, by varying the outer radius. A flow rate of 10 mL/hour requires a rotation rate of approximately 10,000 rpm (Figure 3.5a). This fulfills the requirements for the Yale University fuel injector, which also requires the pressure rise to be above 0.75 psi. An outer radius of 4mm will be sufficient to meet this requirement (Figure 3.5b). A larger radius can be chosen to achieve high pressure rises; however, the torque required to spin the impeller increases and is limited by the motor capability (Figure 3.5c). For this research, the torque will be

supplied by compressed air, but for a stand alone pump using an integrated MEMS motor, the torque needs to be in the range of 1-10 μN for the envisioned micromotor design of [50].

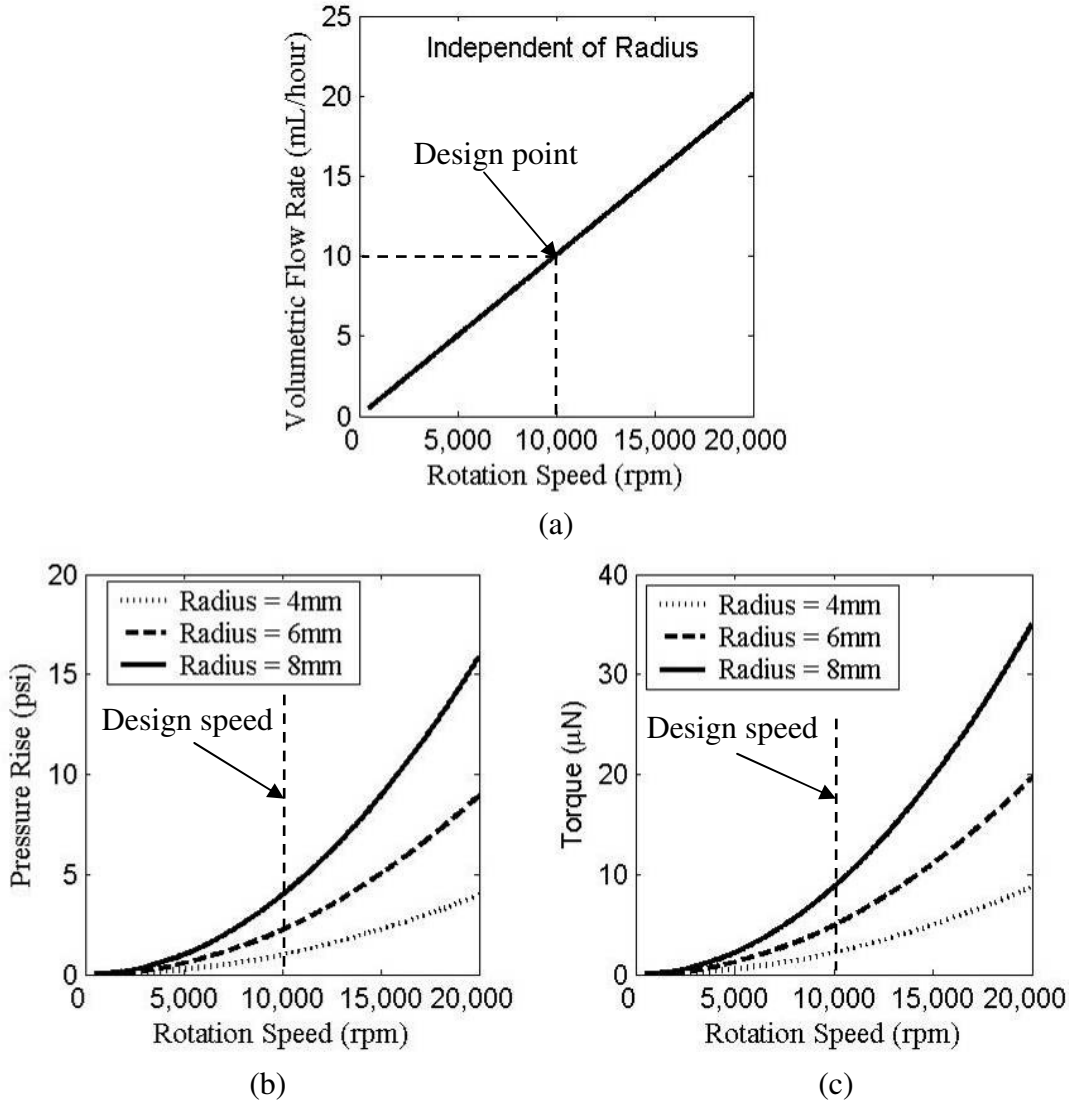

Figure 3.5. Graphs showing the relationship between impeller rotational speed and: (a) volumetric flow rate, (b) the pressure rise across the impeller, and (c) the required torque for the desired flow rate and pressure rise. In these graphs, the inner radius is set to 100μm, the height of the leading edge flow passage is 100μm, the flow angle is 67°, and JP-8 diesel fuel is assumed.

3.2.2 Volute design

Some discussion of different volute design methods are presented by *Chan et al.* [57]. The goal in the design of the volute is to reduce the pressure variation circumferentially to minimize any imbalance in the radial and axial forces on the rotor due to the pumping action. Figure 3.6 shows a top down view of the impeller and volute. From this, the outer radius of the volute is found using the constant mean velocity method by [57]:

$$r_4 = \frac{Q \cdot \theta}{360 \cdot b_3 \cdot C_m} + r_3 \qquad \text{Equation 3.4,}$$

where θ is the angular position from the tongue, b_3 is the volute passage height equal to the impeller passage height b_1, r_3 is the distance to the tongue from the rotor center including the gap between the trailing edge and the tongue of the volute. The mean velocity, C_m, is found by:

$$C_m = k_3 \sqrt{2 \frac{\Delta p}{\rho}} \qquad \text{Equation 3.5}$$

where k_3 is an empirical factor found in a plot versus specific speed in the work by *Chan et al.* [57]. The equation for specific speed is [56]:

$$\overline{N} = N \sqrt{Q} \left(\frac{\Delta P}{\rho} \right)^{-3/4} \qquad \text{Equation 3.6.}$$

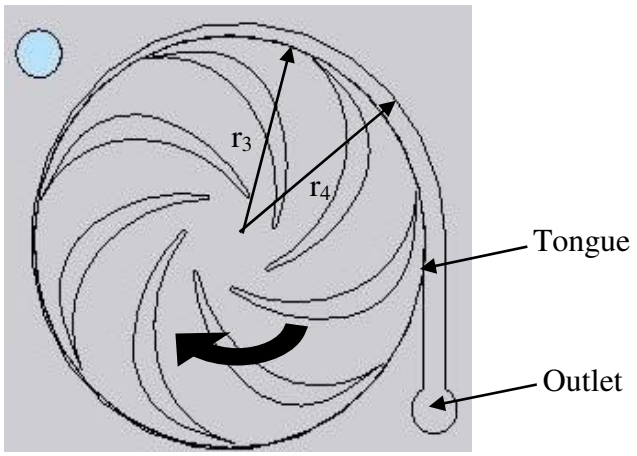

Figure 3.6. Schematic for the design of the centrifugal pump volute.

For the impeller design of 10 mL/hour, a 0.75 psi pressure rise, and a speed of 10,000 rpm (N = 1047 rad/sec), the specific speed is then 0.014 making a mean velocity of 60 m/s. This makes the width of the ideal volute exit (equal to $r_4 - r_3$) on the order of 0.5μm with a height of 100μm fixed to the impeller blade height by fabrication. This dimension is not feasible using conventional microfabrication techniques due to an aspect ratio of two hundred. The passage height could be reduced by four times, making the dimensions tolerable for fabrication (2μm at 25μm height), but the flow rate would change. To keep the same flow rate you either have to double the size of the impeller inner radius and, therefore, the impeller outer radius that increases the required torque or you have to increase the rotational speed by four. As seen in Chapter 2, speeds in the range of 10,000 rpm are desired and therefore increasing the design speed is not optimal. Furthermore, the diameter of the rotor should be minimized to keep a low operational torque.

The design in this work neglect effects of the pressure variation to maintain a compact device and speeds in the range of 10,000 rpm. Values of 50 μm for the gap between the trailing edge and the volute tongue and 50 μm for the volute exit were chosen. The forces on the rotor are expected to have a minimal effect since there is not a problem with the stiffness of microball bearings. Designs where the notion of stiffness exists and can be a challenge (e.g. air bearings) would have to account for those forces.

3.2.3 Fabrication

The fabrication of the centrifugal turbopump is not too different from the tangential air-turbine fabrication. The pump impeller and volute are patterned in place of the speed measurement geometry on the side opposite the turbine blades. No change to the fabrication process flow occurs for the two rotor layers. The only real changes are alignment pits on the pump side to align and bond a plumbing layer on the top using the same metal adhesion layer that bonds the rotor layers together.

The fabrication process flow for the centrifugal turbopump with point-contact bearings is shown in Figure 3.7. The process leading up to Figure 3.7a is identical to that shown in Figure 2.19 in which the raceways were patterned and etched and the rotor layers bonded together using the AuSn eutectic bonding method. The centrifugal impeller and volute were patterned into the silicon dioxide on the topside of the stack (Figure 3.7a) and the turbine blades, inlet, and outlet were patterned into the silicon dioxide on the bottom side of the rotor stack. The pump impeller side is etched using DRIE until the raceway is reached, which is equal to b_1, or 100 μm (Figure 3.7b). Figure 3.8 shows a fabricated impeller after the initial release step (Figure 3.7b). A

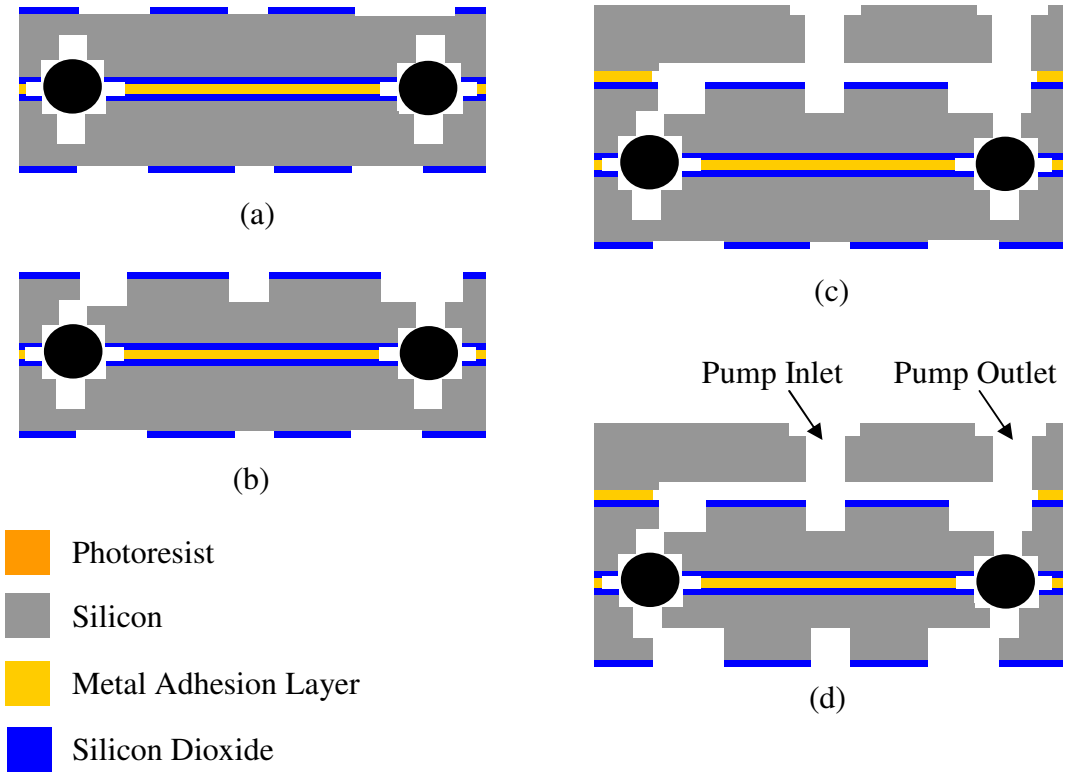

Figure 3.7. Fabrication sequence for the centrifugal turbopump.

plumbing layer, fabricated using multiple photolithography and DRIE steps is then aligned (using microballs and alignment pits) and bonded on top of the impeller layer using the same metal adhesion layer process as before (Figure 3.7c). Next, the turbine side is etched using DRIE with the patterned silicon dioxide used as the masking layer. This etch completely releases the rotor and the device is finished.

The plumbing layer has three key features: 1) through etches for the pump inlet and outlet (diameters of 1.5 mm); 2) impeller cavity etched 80 μm deep placed above the impeller to ensure no rubbing between the two surfaces; and 3) shoulders etched at the inlet and outlet ports such that tubing can be aligned over the through holes and attached with epoxy. The impeller cavity creates a gap above the centrifugal impeller that acts as

a leakage path to reduce the performance and efficiency of the pump. The gap can be minimized in later versions once the wear and the required tolerance are better understood.

Non-uniform release of the rotor is critical. The centrifugal impeller/volute experienced a non-symmetric breakthrough to the previously etched race journal during the release step (Figure 3.9). Since the volute exit is a large area not close to the sidewall it releases before the areas close to the sidewall that are affected by the etch fillet radius. This causes divots in the bearing raceway in the areas closer to the volute exit where the rotor releases early on. To minimize the release uniformity, an axisymmetric design of the rotor layers is needed.

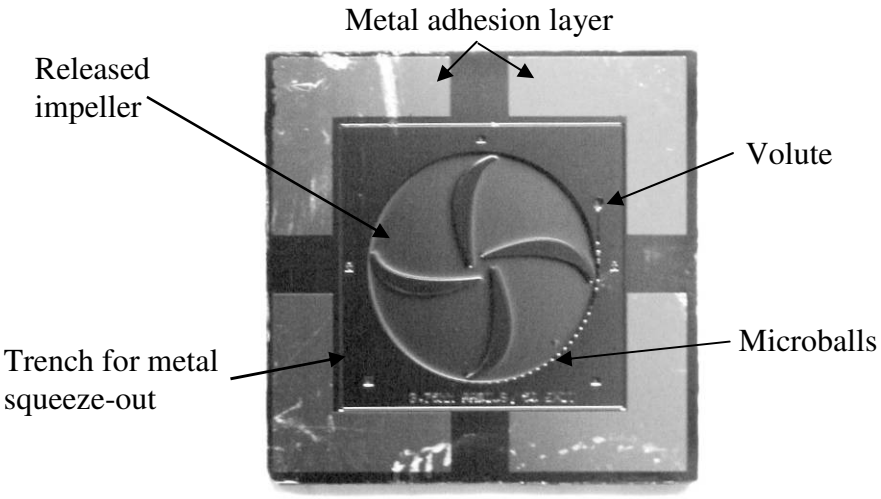

Figure 3.8 Optical image showing a completed centrifugal impeller and volute.

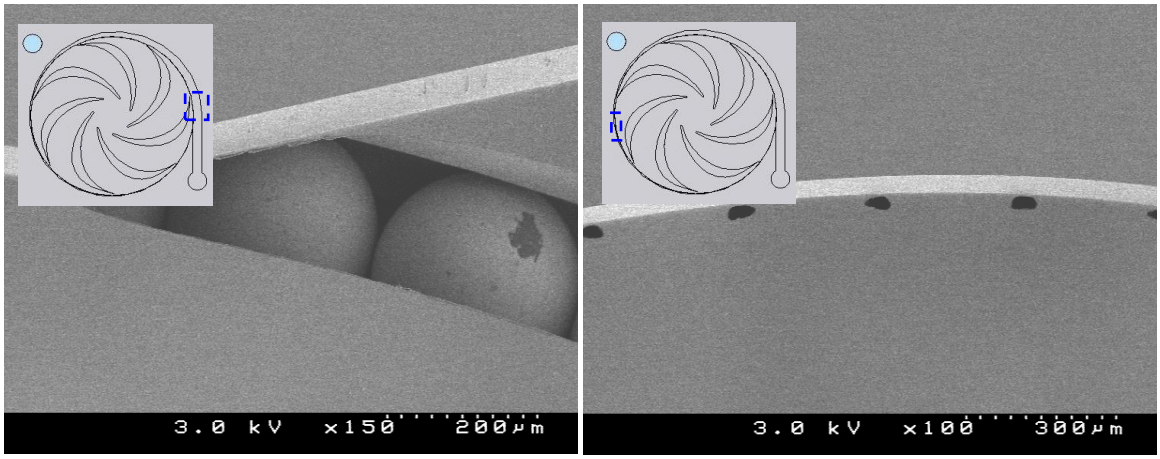

(a) (b)

Figure 3.9. SEM images of a partially released rotor demonstrating the non-uniform etching during the release process. The race (a) extending across the volute exit is released before (b) other areas due to the effect of the DRIE fillet radius.

3.2.4 Testing

An experimental apparatus was constructed for the centrifugal turbopump consisting of two pressure transducers to monitor liquid pressure, an optical displacement sensor (ODS) to monitor rotor speed, a pressure controller for the turbine driving flow, an aluminum fixture to interface tubing with the device, and a computer for control and data logging via LabView. The aluminum fixture (Figure 3.10) was designed and fabricated so that the device fits into a cavity. One major difference from the experiments performed in Chapter 2 is the requirement for the ODS to be placed underneath the air turbine rotor since the impeller side must be sealed for liquid. The ODS aligns underneath the turbine rotor via a slot fabricated within the aluminum fixture. The ODS is mounted on an x-y-z stage so that it can be positioned properly to detect the turbine

blades. Tubing is attached to the fixture via an NPT connection on one end and to the house nitrogen line on the other end.

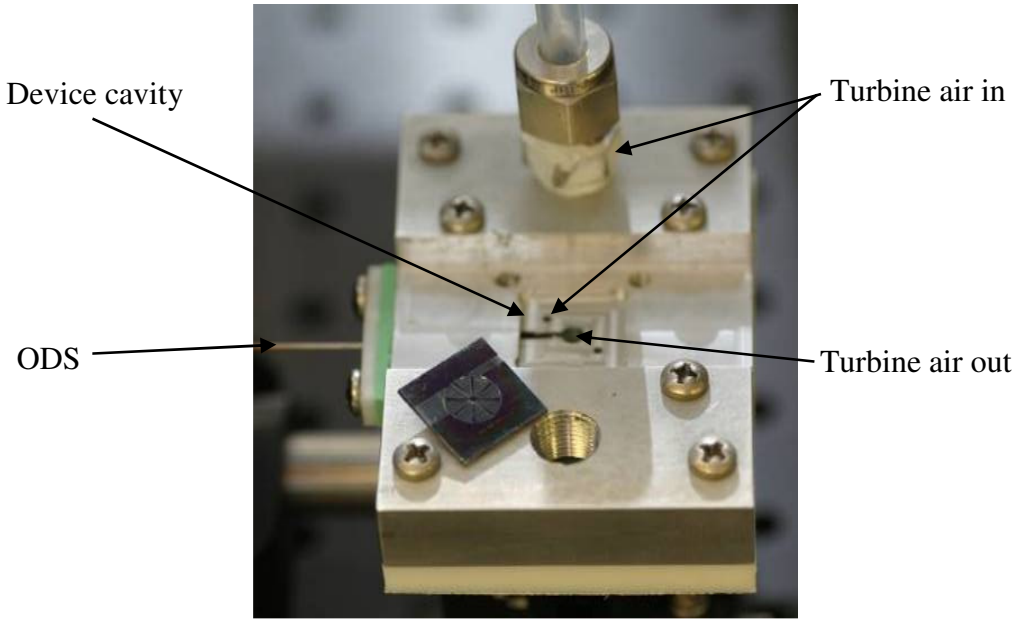

Figure 3.10. Optical image of the aluminum testing fixture with the Nitrogen line hooked up and the ODS in place within the fixture.

The centrifugal turbopump was first tested without any liquid to characterize the turbine operation with the pump capping layer. A total of five devices were used to test the turbine operation for the centrifugal pump (Figure 3.11). All devices had similar behavior in the driving pressure versus speed. The tangential air turbine rotor with the pumping structures and plumbing layer did not operate as expected; for instance the speed did not react noticeably to increasing pressures, and the rotor exhibited large speed fluctuations.

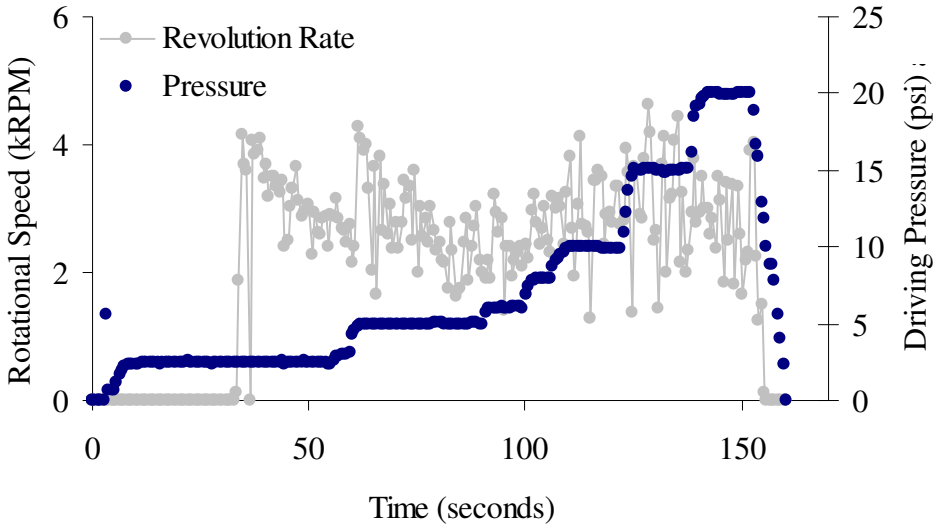

Figure 3.11. Plot demonstrating centrifugal and turbine operation.

Two factors were determined to cause the poor performance of the air turbine: 1) speed bumps arising from the non-uniform etching to release the rotor and 2) coupling of the turbine driving pressure and the normal load exerted on the rotor by pressure buildup. The first factor is related to divots on the raceway caused by the non-uniform release of the rotor, as discussed in the fabrication of the centrifugal turbopump. This effect is directly related to the non-axisymmetric design of the volute and the tangential air turbine and can only be overcome by re-designing the device to be axisymmetric. The second factor is an effect not accounted for in the design of the centrifugal turbopump and limits the torque available for pumping at higher rotational speeds. A re-design of the plumbing layer allowing the pressure on the pump side of the device to be alleviated at higher turbine driving pressures is necessary.

Static devices were used to test the ability to seal between the air driving the turbine and the liquid on the pump side. Inspection of the centrifugal impeller and volute

shows that the critical gap between liquid and gas will be near the volute exit (Figure 3.12). In the case of the 50 µm volute exit width, the largest gap is approximately 80 µm from the journal etch that released the rotor. The critical pressure difference between the fluid and the gas for sealing to occur can be approximated by setting the differential pressure force, ΔP, between the two fluids equal to the surface tension force between the nitrogen and water (Figure 3.13) in the following equation:

$$\Delta P = P_A - P_B = \frac{2\sigma \cos\theta}{h} \qquad \text{Equation 3.7}$$

where P_A and P_B are the two fluids of interest shown in Figure 3.13, σ is the surface tension between water and Nitrogen (0.072 N/m [58]), h is the critical gap and θ is the contact angle assumed to be 45˚ for silicon. The allowed pressure difference for sealing

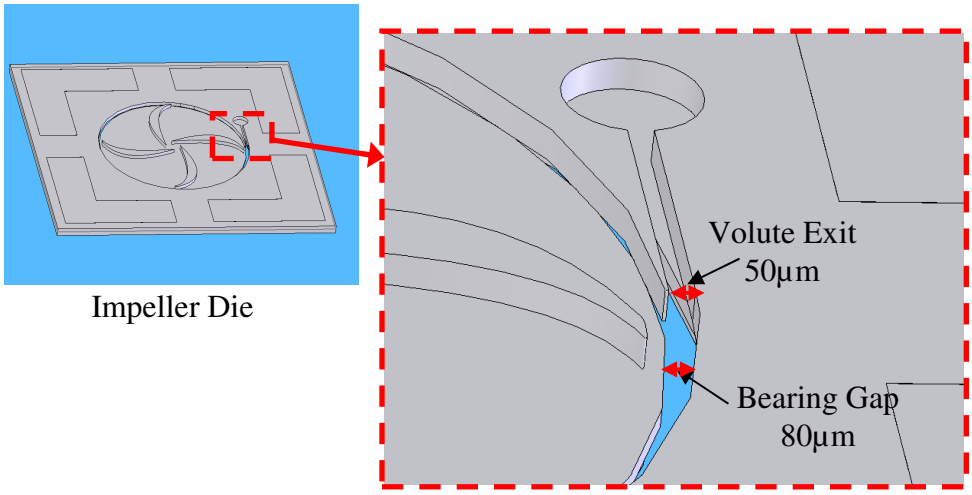

Figure 3.12. Illustration of the centrifugal volute and the critical sealing gap.

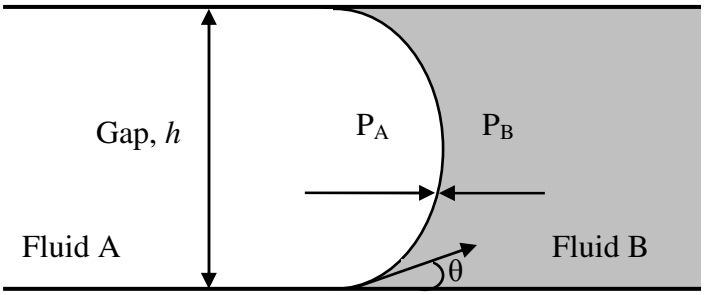

Figure 3.13. Illustration of the force balance between two fluids.

to occur between the liquid and gas is estimated to be less than 0.3 psi from the plot of Equation 3.7 in Figure 3.14 for a minimum spacing of 50 µm. This requires accurate control of both the driving pressure of the turbine and the operating pressure of the pump. Since both the tangential air turbine and centrifugal volute are non-axisymmetric designs there can be a large pressure variation circumferentially around the rotor making it difficult to seal between the liquid and driving gas

.

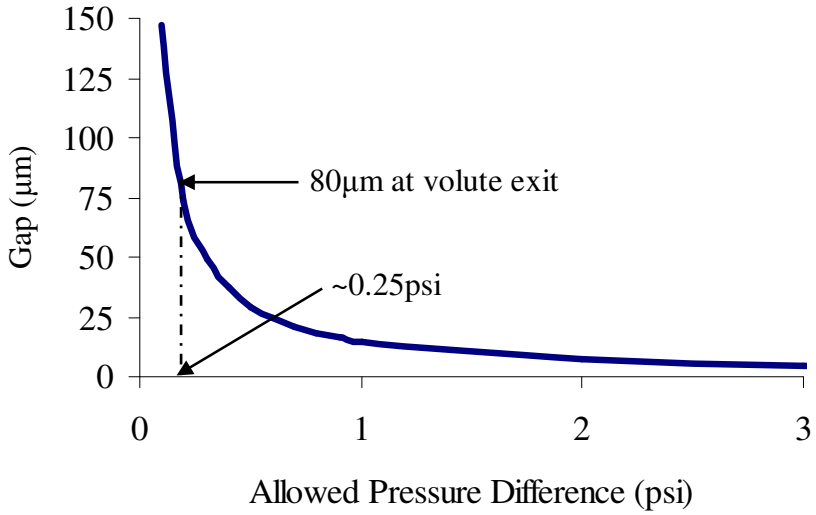

Figure 3.14. Plot showing the relationship between the critical gap and the allowed pressure difference between two fluids for sealing.

Experiments were performed using a pressurized vessel to control the liquid pressure and a pressure manifold to control the nitrogen pressure entering the turbine side of the device. The rotor in the devices used to test the sealing capability was not able to spin due either to large over etching during the rotor release or particle contamination jamming the rotor. Attempts were made to get liquid to flow from the pump inlet to the pump outlet while nitrogen was flowing into the turbine entrance. In all attempts the pressure difference between the nitrogen and the water could not be maintained and water was observed leaking from the turbine or from the bond interface in the bearing raceway. Large pressure variations circumferentially around the impeller volute and the tangential air turbine rotor are likely to prevent the required pressure difference between nitrogen and water from being maintained. In order to achieve proper sealing, a more axisymmetric design is required.

3.2.5 Summary

A centrifugal turbopump was designed and fabricated utilizing the point-contact bearing and the tangential air turbine. Although the tangential air turbine was demonstrated successfully, design flaws became apparent with the addition of the pump capping layer and the centrifugal impeller and volute structure. Two key flaws arising from the non-axisymmetric design were discovered during fabrication and testing. First, the release etch step of the rotor was non-uniform, which caused divots on the raceway and prevented reliable operation of the rotor during turbine operational testing. Second, the circumferential pressure variation from the poor symmetry caused an unrealistic control required for sealing given the geometries and design. It is critical, therefore, to

develop a micro-turbopump with an axisymmetric design to allow for uniform rotor etch-release and uniform pressures within the device.

3.3 Spiral-Groove Viscous Turbopump

From the previous section, a non-axisymmetric design of the pump impeller and air turbine led to problems in both sealing and fabrication. An axisymmetric design is now presented and analyzed in this section with testing and results presented in Chapter 4. Instead of a tangential air turbine, the radial in-flow air turbine from Chapter 2 will be integrated with an axisymmetric pump design and a planar-contact bearing due to the observed higher performance. A viscous pump was chosen due to its potentially more compact design when compared to a centrifugal pump and the beneficial use of viscous forces at the scales of interest. The viscous pump requires precise gap control between the rotor and pump structures, therefore the planar-contact bearing design is chosen since it demonstrated lower wear than the point-contact design.

A viscous pump has three distinct advantages over centrifugal pumps: 1) viscous forces are the primary pumping mechanism; 2) analytical equations have been developed and demonstrated to predict the behavior very well [25, 59]; and 3) viscous pumps can be designed with smaller diameters than centrifugal pumps while meeting the same flow specifications, allowing for smaller required torque.

3.3.1 Design Overview

The spiral-groove turbopump is designed using the microturbine tribology platform. Pump plumbing layers composed of two wafers and a spiral-groove pattern are added to the topside of the previous microturbine tribology device to make up the turbopump (Figure 3.15).

The turbopump consists of a radial in-flow air turbine, a microball bearing, a static spiral-groove disc, and a sealing surface. The first three layers, with the exception of through holes for inlets and outlets, are taken from the tribology device (Figure 3.15). The fourth layer contains the static spiral-groove structure, the pump inlet and outlet channels, and channels for thrust balance control. The fifth layer is a Pyrex capping layer to seal the pump inlet and outlet channels allowing them to be routed to the edge of the die and eventually out of the backside of the device.

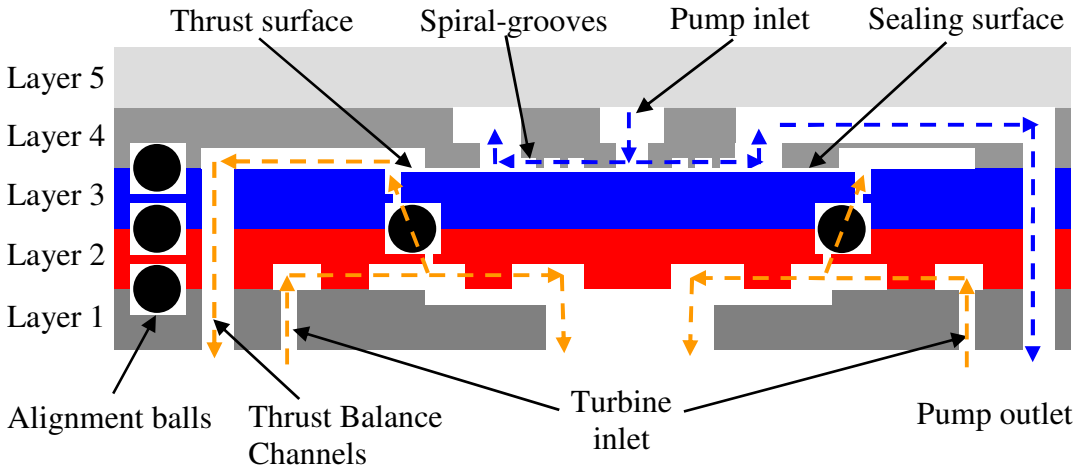

Figure 3.15. Schematic cross-section of the spiral-groove turbopump.

Pressurized gas enters the air turbine through static vanes, flows radially inward, and exits through the center of the rotor. The rotor is supported by the microball bearings and the normal load is coarsely controlled by thrust balance channels placed above the bearings and edge of the rotor on the pump side. During operation, the rotor is forced downward by the pressure buildup and creates the desired gap between the rotating disc and the spiral-grooves (Figure 3.15). The pump will draw liquid in from the backside of the device and pump radially outward via a rotating flat disc suspended below the spiral-groove plate.

During the operation of the device, the normal force on the rotor will vary with the speed because it is coupled with the driving pressure of the air turbine. The pump side of the rotor is sealed off by the liquid and high flow resistance paths so that the pressure will build up on the pump side. This build up of pressure causes the normal load on the rotor to be positive from the pump side to the turbine side; i.e. the rotor will always be shifted towards the turbine exit. The normal load exerted on the rotor is coupled to the turbine driving and increases with the speed of rotation.

Thrust balance channels on the pump side are included into the design in an attempt to reduce the coupling between the turbine flow and rotor normal load. In addition to the ability to decrease the normal force acting on the rotor, the bleed channels will allow for a small control on the sealing pressure between the nitrogen and liquid from the pump. As the pump outlet pressure varies, the nitrogen pressure will have to change to maintain an allowed pressure drop between the two for sufficient sealing (Figure 3.14). The thrust balance channels were incorporated into the device to help manage the pressure buildup and therefore the normal force on the rotor (Figure 3.15).

Both the radial in-flow turbine and planar-contact bearings were discussed in Chapter 2. Some modifications to the prior planar-contact design were made to further reduce the friction and wear. These modifications, as well as the design of the spiral-groove pump structure will be described in this section. The spiral-groove turbopump can be operated both radially outward and radially inward. In the latter case, the fluid is being pumped against centrifugal forces and the pressure is low at the seal between the liquid and nitrogen pressure. When operated in a radially outward fashion, the pressure is high at the outer radius of the pump where the seal occurs with the nitrogen and will better match the higher pressure from nitrogen driving the turbine. The spiral-groove structures can be placed on either the rotating structure or the non-rotating disc. All configurations were fabricated; however, only the radially outward configuration with the spiral-grooves patterned on the non-rotating disc was demonstrated. Other configurations and other pumping structures such as those presented in [60] can be implemented on this platform by changing the rotating or non-rotating disc pattern.

3.3.2 Spiral-groove design

The design of the spiral-grooves for the turbopump is based on the work produced by *Muijderman and Hsing* [55, 61] for spiral-groove thrust bearings and pumps. The key geometrical parameters for the spiral-groove viscous pump (Figure 3.16) are discussed in this section using the symbols and definitions in Table 3.2. Of interest is the pressure versus the flow rate relationship for various operating speeds (the pump curves). The model used by *Muijderman* and *Hsing* is based on the Reynolds equation assuming

fully developed viscous flow, incompressible fluid, uniform pressure and density across the thickness of the fluid, and constant viscosity.

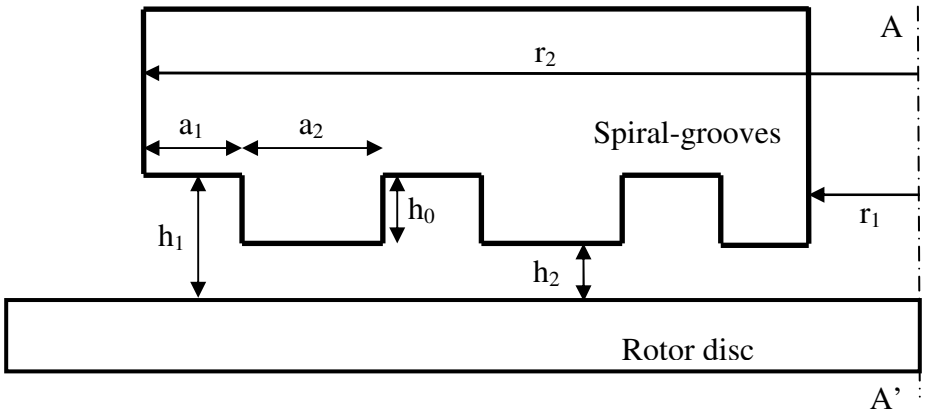

Figure 3.16. Diagram illustrating the groove geometry and gap within the spiral-groove viscous pump. The rotational axis is denoted by the A-A' dashed line.

Symbol	Definition	Symbol	Definition
η	Dynamic viscosity	δ	$h_2/h_0 = 0.4$ = Fluid Ratio
ω	Rotational speed (rad/second)	H	$h_2/h_1 = \delta/(1+\delta)$ = Gap Ratio
γ	$a_1/a_2 = 1$ = groove width/blade width	H_1	$\frac{H^2\left(1+\cot^2(\alpha)\right)\left(\gamma+H^3\right)}{\left(1+\gamma H^3\right)\left(\gamma+H^3\right)+H^3\left(\cot^2(\alpha)\right)\left(1+\gamma^2\right)}$
α	Spiral angle	H_2	$\frac{3\gamma H\cot(\alpha)(1-H)\left(1-H^3\right)}{\left(1+\gamma H^3\right)\left(\gamma+H^3\right)+H^3\cot^2(\alpha)(1+\gamma)^2}$
ρ_0	Density	$g_1(\alpha, H, \gamma)$	$\frac{\gamma H^2\cot\alpha(1-H)\left(1-H^3\right)}{\left(1+\gamma H^3\right)\left(\gamma+H^3\right)+H^3\cot\alpha(1+\gamma)^2}$
α	Spiral angle = 16.6°	$g_2(\alpha, H, \gamma)$	$(\gamma+H)+\frac{3\gamma H^2(1-H)^2\left(1+\gamma H^3\right)}{\left(1+\gamma H^3\right)\left(\gamma+H^3\right)+H^3\cot\alpha(1+\gamma)^2}$

Table 3.2. Symbols used for the design of the viscous groove turbopump.

To develop the pump curves for the spiral-groove viscous pump the following relationship, neglecting the end effect is used [55]:

$$\Delta p_{21} = \frac{3\eta\omega}{h_2^2}\left(r_2^2 - r_1^2\right)g_1(\alpha, H, \gamma) - \frac{6\eta\dot{m}(1+\gamma)}{\pi\rho_0 h_1 h_2^2} H_1(\alpha, H, \gamma)\ln(\frac{r_2}{r_1}) \qquad \text{Equation 3.8,}$$

where $\dot{m}$ is the mass flow rate and the subscripts 1 and 2 represent locations at the inner radius and outer radius of the spiral-grooves respectively. The first term is the pressure build up due to viscous forces while the second term is the pressure drop due to the mass flow through the impeller. The pressure increase across the pump can be maximized by optimizing the value of the dimensionless parameter $g_1(\alpha,H,\gamma)$. *Muijderman* provides the optimum ratios for the spiral angle, α, the gap ratio, H, and the groove to blade width ration, γ, (Table 3.2).

A boost to the pressure rise across the pump can be accomplished by increasing the outer radius, r_2 and rotational speed, ω, or decreasing the gap, h_2, and the total passage height, h_1. These changes are limited by the corresponding torque required to drive the pump, which is found by [55]:

$$Torque = \frac{\pi\eta\omega r_2^4}{2h_2}\left(1-\lambda^4\right)\frac{g_2(\alpha, H, \gamma)}{(1+\gamma)} - H_2(\alpha, H, \gamma)\left(r_2^2 - r_1^2\right)\frac{\eta\dot{m}}{\rho h_1 h_2} \qquad \text{Equation 3.9}$$

where the first term is the torque from viscous drag and the second term is the torque from a reduction in viscous drag due to the mass flow through the pump. From

Equations 3.7, h_2 should be made as small as possible to create a large pressure rise, and r_2 minimized to keep the torque within a reasonable range.

The gap is determined by the amount of sag in the rotor and the thickness of the bonding layer between the rotor and the plumbing layer. A gap of 10μm was chosen as a result of reasonable fabrication tolerances and bonding layer thickness. More discussion on the fabrication tolerances and bonding layer thickness is provided in section 3.3.4. Using a design point of 0.75 psi and 10 mL/hour, the parameters in Table 3.3 were developed for a rotational speed below 10,000 rpm and minimizing the outer radius. The corresponding pump curves are shown in Figure 3.17. The torque required to operate the turbopump (without bearing friction) is 4.6 μN·m, well within in the range of the reported torque available from the envisioned micromotor [50].

Target Gap (h_2)	10 μm
r_2	2.25 μm
r_1	625 μm
α	16.6°

Table 3.3. Table showing designed values for the spiral-groove turbopump.

It is critical to assess the effect of the gap on the performance of the pump. Due to fabrication tolerances and bearing wear, the actual gap in the device will differ from the designed gap. Figure 3.18 shows the relationship between $g_1(\alpha,H,\gamma)$ and δ, which is the gap, h_2, divided by the groove depth for the current turbopump design. For small changes in the gap there is not a significant change in $g_1(\alpha,H,\gamma)$. In the current turbopump configuration the gap will increase as the device wears. From the

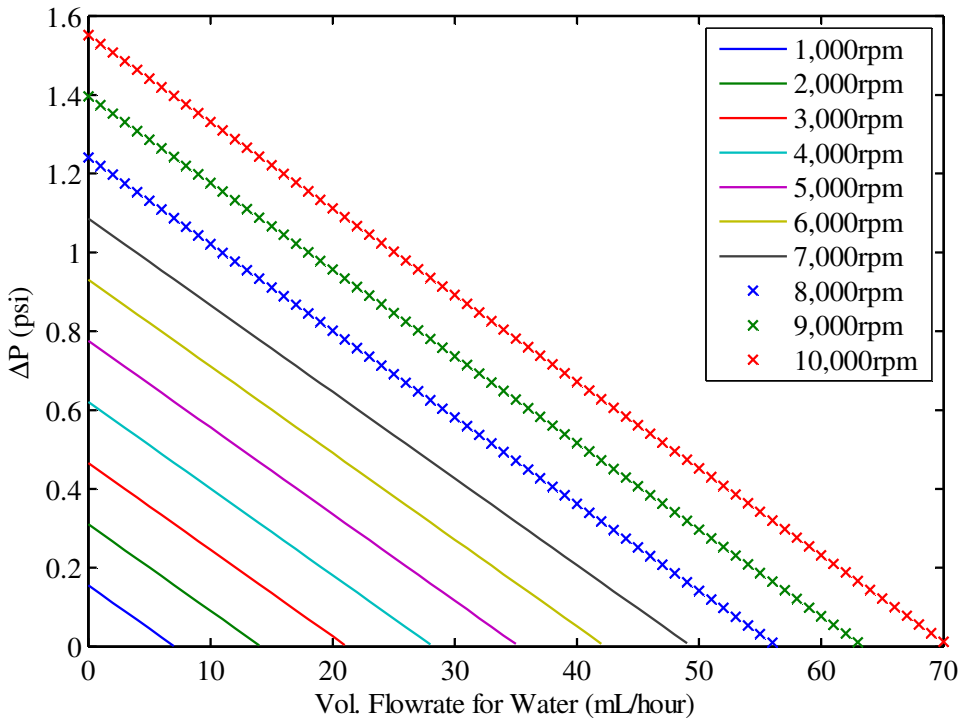

Figure 3.17. Pump curve for a gap of 10um.

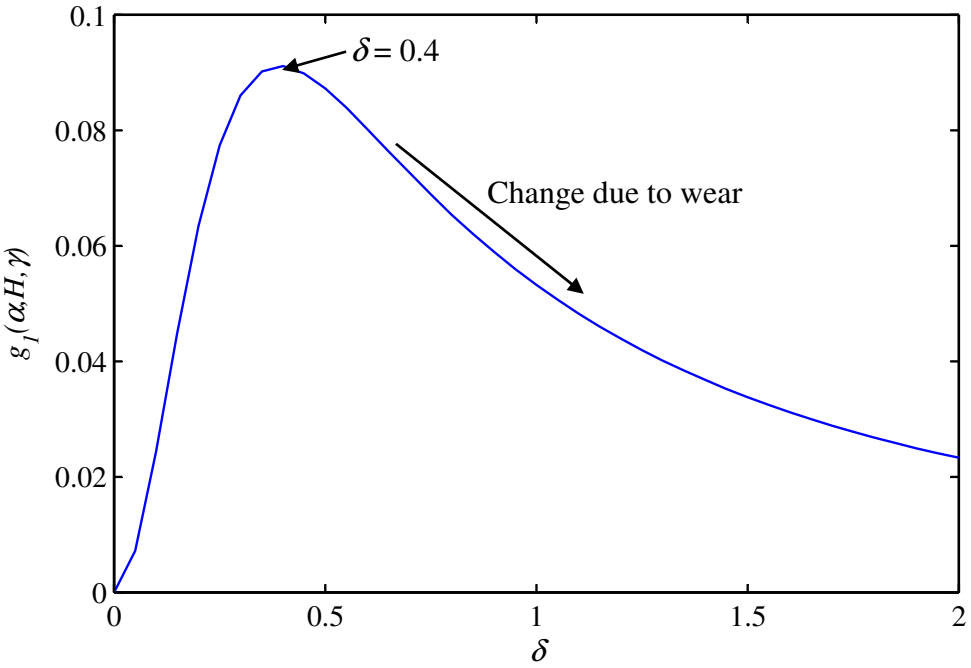

Figure 3.18. Plot showing the relationship between the Flow Ratio, δ, and g_1 for a spiral angle α=16.6˚ and groove to blade width ratio γ=1.

microturbine tribology device, the expected wear is approximately 1 µm after 1 million revolutions. For the speed of 6,000 rpm the change in the pump operation curves versus gaps ranging from 10 to 22 µm is shown in Figure 3.19. If the bearing wears by 2 µm, the maximum pressure with no flow changes from 1.1 psi to 0.75psi, a 32% change.

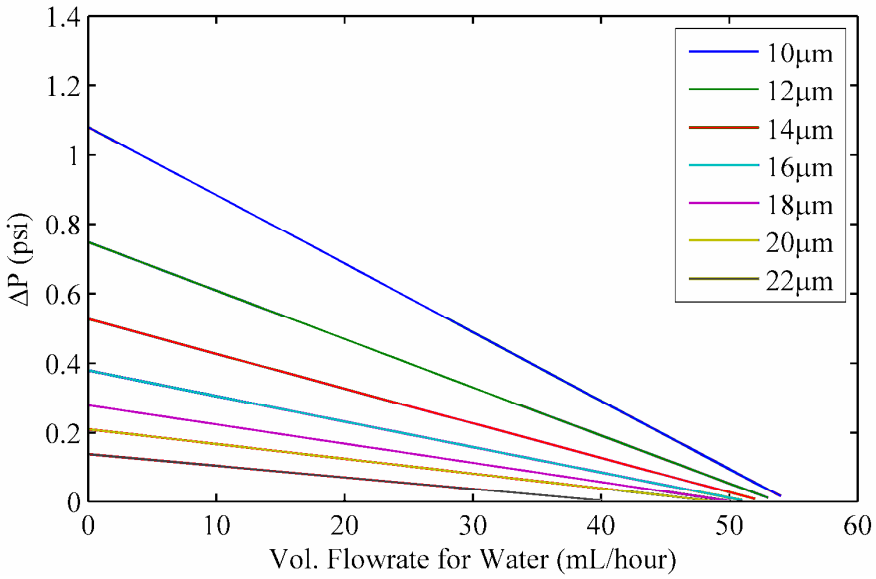

Figure 3.19. Pump curves for gaps ranging from 10 µm to 22 µm.

3.3.3 Power Balance

This section describes the power curves developed for the turbine-microball bearing combination and the viscous drag created by the spiral-groove pump. The power curves provide, to the first order, an understanding of the stable operating points of the turbopump.

It is important to understand the balance of power between the available energy coming from the turbine and the major power losses within the turbopump device. The available power is that generated in the turbine minus that dissipated through bearing friction. The required power is that necessary to overcome viscous drag in the pump. The intersection of these power curves, when the power loss from viscous drag balances with the power available from the turbine-microball bearing mechanisms, determines the device operating speed. The power is calculated from the torque and speed:

$$Power = \tau \times \omega \qquad \text{Equation 3.10.}$$

At steady-state, the following statement will hold:

$$\tau_{viscous} \times \omega = \left(\tau_{turbine} - \tau_{bearing}\right) \times \omega \qquad \text{Equation 3.11.}$$

From the Euler turbomachine equation the torque produced by the turbine is [56]:

$$\tau_{turbine} = Q\rho_{air}\left[r_{trb,1}C_{\theta 1} - r_{trb,2}C_{\theta 2}\right]$$
$$\tau_{turbine} = Q\rho_{air}\left[\frac{Q}{2\pi h}\left(\tan(\theta_1 + \delta\theta_1) - \tan(\theta_2 + \delta\theta_2)\right) - r_{trb,2}^2\omega\right] \qquad \text{Equation 3.12,}$$

where, Q is the volumetric flow rate through the turbine, ρ_{air} is the density of air (1 kg/m^3), $r_{trb,1}$ and $r_{trb,2}$ are the radial distance to the turbine rotor inlet and outlet (5 mm and 3.33 mm respectively), $C_{\theta 1}$ and $C_{\theta 2}$ are the absolute rotor inlet and outlet angular flow velocities respectively, θ_1 and θ_2 are the absolute vane outlet and blade outlet angles

respectively (60.35˚ and -37.55˚), $\delta\theta_1$ and $\delta\theta_2$ are the deviation of the flow from the vane outlet and blade outlet angles respectively, h is the blade height determined by the etch to release the turbine rotor, and ω is the speed of rotation in radian/sec.

Lee has shown a strong dependence between the deviation of the flow, $\delta\theta_1$ and $\delta\theta_2$, and Reynolds number (Re) in micro-turbomachinery, for 100<Re<1,000, where Re is defined using the chord length and inlet conditions [25]. These deviations have a complex relationship with turbine flow parameters and change with operating conditions. Computational fluid dynamics (CFD) is necessary to accurately model flow deviations from ideal. Using CFD, *Lee* has shown that for a rotor blade cascade with a solidity and chamber comparable to the microturbine in this work, the exit flow angle varies nonlinearly up to +/- 10% of the designed blade angle, over the range of Re considered [25].

The power loss due to the frictional torque of the planar-contact microball bearing can be estimated from the spin-down testing performed in Chapter 2. Using the information for normal load versus speed in Figure 2.43 along with the empirical formula developed for the friction torque/speed ratio as a function of normal force in Equation 2.25, the frictional torque from the microball bearing can be estimated as:

$$\tau_{bearing} = 9\times10^{-5} F_N^{0.444} \omega \times \frac{2\pi}{60} \times 10^{-6} \qquad \text{Equation 3.13,}$$

where F_N is estimated from a linear fit between the rotational speed and normal force in the plot shown in Figure 2.43. In this case, F_N has unit of mN and the rotational speed has the unit of rpm making N the unit for $\tau_{bearing}$.

The viscous losses due to the spiral-groove pump and the sealing region at the larger radii (Figure 3.20) dominate the losses from viscous forces. The regions at the pump inlet (from the center to radius r_1) and outlet (from r_2 to r_3) can be neglected since the minimum gap in those regions is two orders of magnitude larger than the gap between the rotor and the spiral-groove and sealing regions.

The torque from the viscous forces in the spiral-groove region is found from the torque due to friction (Equation 3.9). The viscous torque due to the left most quantity in Equation 3.9 is close to two orders of magnitude greater than the reduction to the torque caused by the mass flow. The reduction in torque due to the mass flow (right most quantity in Equation 3.9) can, therefore, be neglected due to the very low flow rates

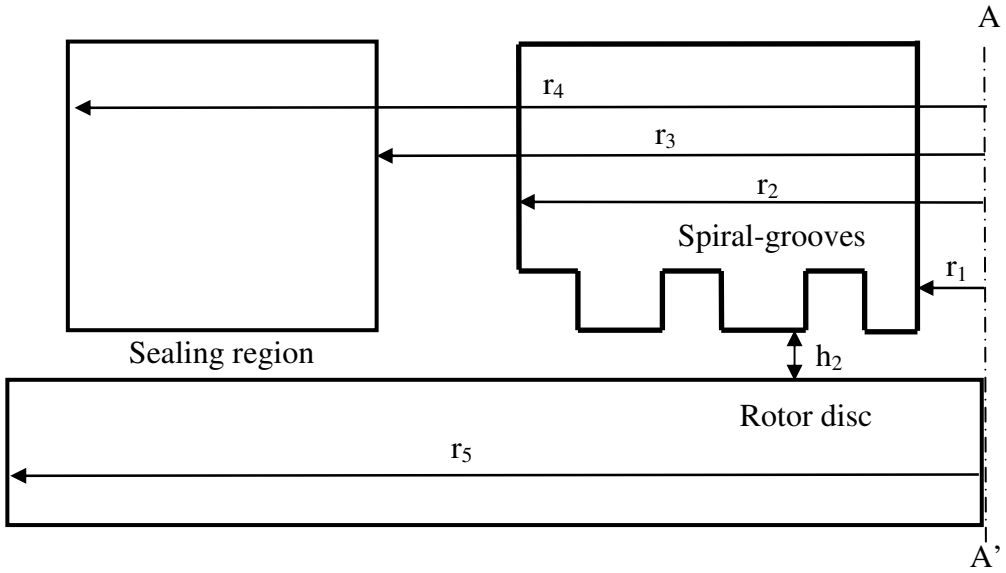

Figure 3.20. Illustration of the spiral-groove region, the gap, h_2, within the viscous pump, and the sealing region. The rotational axis is denoted by the A-A' dashed line.

envisioned for the turbopump. The power loss due to the viscous drag in the region of the spiral-grooves, assuming no air bubbles, can then be calculated from:

$$\tau_{spiral-grooves} = \frac{\pi \eta_{water} \omega r_2^4}{2h_2}\left(1-\lambda^4\right) g_2(\alpha, H, \gamma) \qquad \text{Equation 3.14.}$$

If the seal between the air and the liquid is assumed to occur at the edge of the sealing region (i.e. at r_3) then the viscous drag in that region is due solely to air:

$$\tau_{seal} = F_{viscous} \times r = \eta_{air} \frac{\pi \omega}{h_2} \int_{r_3}^{r_4} r^3 dr$$

$$\tau_{seal} = \eta_{air} \frac{\pi \omega}{4h_2}\left(r_4^4 - r_3^4\right) \qquad \text{Equation 3.15,}$$

where η_{air} is the dynamic viscosity of air (1.82 x 10^{-5} Pa·s), r_4 is the maximum radial extent of the sealing area and r_3 is at the beginning of the sealing region (Figure 3.16). If the air/liquid interface moves radially outward into the sealing region the viscous drag will increase drastically, since the dynamic viscosity of water (η_{water} = 8.9 x 10^{-4} Pa·sec) is approximately 50 times greater than air. It is, therefore, critical to ensure liquid does not enter the sealing surface by maintaining a large sealing pressure controlled by the thrust balance pressure.

The power available from the turbine and the power loss due to viscous drag assuming no liquid in the sealing region, are plotted in Figure 3.21. The available power from the turbine/microball bearing combination is plotted for ideal flow angle velocities

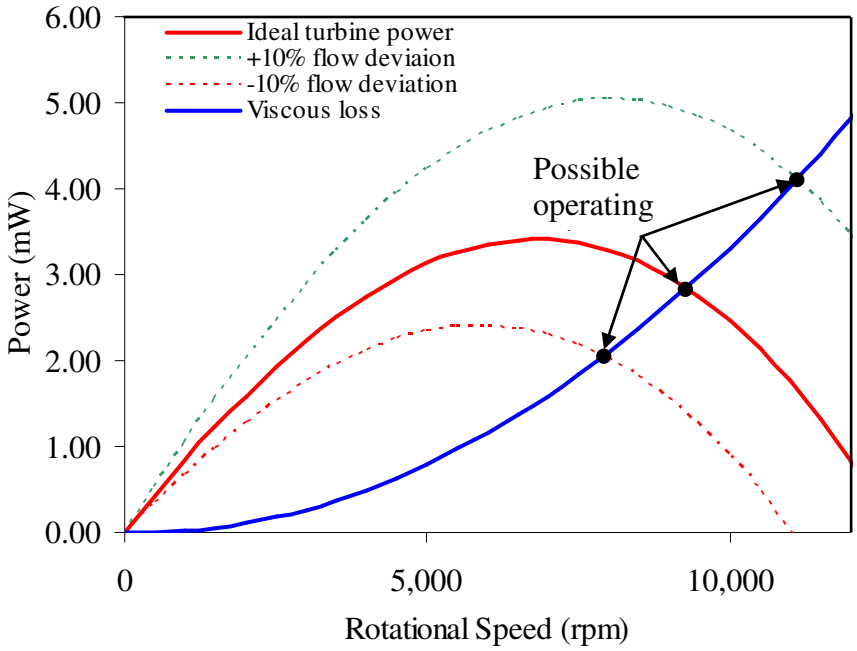

Figure 3.21. Power curves showing the ideal and deviated turbine power considering bearing friction and the power dissipated due to viscous forces on the pump side for a minimally wetted surface area.

and ±10% deviation from ideal flow angle velocities. The turbine-microball bearing power curves are produced for a constant turbine flow rate equal to 3.5 slm and a turbine blade height of 200 µm. The calculation of the normal load (to estimate $\tau_{bearing}$) assumed there was no starting normal load exerted on the raceway, i.e. the pump inlet and outlet were at ambient pressure. During the operation of the turbopump, the normal is not only coupled to the driving pressure of the turbine, but also to the pump inlet and outlet. The pressures there will cause the power curve for the turbine to change. The viscous power loss curves are plotted for a gap of 10 µm and spiral-groove depth of 25 µm.

The operating speed of the turbopump will be the point where the power delivered from the turbine/bearing mechanism crosses the power loss to viscous drag. The optimum design point will be when the viscous loss curve crosses the power turbine

power curve at its peak power. The key geometry of the turbine that can be used for optimization for a desired design point are the rotor flow angles, θ_1 and θ_2, the diameter of the turbine, the blade shape, and the blade heights.

There is a large potential operating range depending on the turbine efficiency and the amount of bearing friction as can be seen from the plot of the power curves (Figure 3.21). If the efficiency of the turbine is lower or the friction torque from the bearings increases (possibly due to an increase in normal force on the rotor) then the turbine power curve shifts downward and the operating speed, for the same flow rate, will decrease. Similarly, air bubbles passing through the pump will cause the viscous loss to decrease, but if the sealing surface becomes wetted then the viscous loss will increase, both causing fluctuations in the operating speed. The power curves demonstrate that stable operation of the turbopump is possible and that the turbine provides sufficient power to allow pumping within the desired ranges of rotational speed even with fluctuations in the operating point.

3.3.4 Design Summary

The spiral-groove turbopump incorporates the microturbine tribology device and a static spiral-groove suspended over the back side of the turbine rotor. A radial in-flow turbine was chosen due to the axisymmetric design allowing for uniform release of the rotor and uniform pressure to circumferentially seal around the rotor on the pump side. Gap control within the spiral-groove turbopump was shown to be critical to the pump performance. The planar-contact bearing was chosen over the point-contact design

because of significantly reduced wear. The critical parameters of the spiral-groove turbopump are summarized below (Table 3.4).

Spiral-groove	
Designed gap	10 μm
Groove depth for designed gap	27.5 μm
Outer radius (r_2)	2.5 mm
Inner radius (r_1)	625 μm
Spiral Angle	16.6˚
Radial Air Turbine	
Rotor outer radius	5 mm
Blade height	200 μm
Operating flow rates*	<20 L/min
Driving pressure*	~1 psi
Planar-contact Bearing	
Etch Depth	145 μm
Race width	290 μm
Bond line offset	50 μm
Journal offset	70 μm
Journal width	30 μm

*Estimated from experiments conducted in Chapter 2.

Table 3.4. Spiral-groove turbopump critical parameter summary.

3.3.5 Layout and fabrication

The turbopump is composed of a five patterned wafer stack. The fabrication process comprises fifteen optical masks and over eighty processing steps. The fabrication is not simple due to the precision DRIE steps required to obtain a desired 10 μm gap between the spirals and the rotating disc via bearing sag and bonding layer thickness. The fabrication of the bottom three layers (Figure 3.15) follows closely to the fabrication of the microturbine tribology device while the fabrication of the other two

layers are new to the process flow. The next sections describe the functions of each layer and the fabrication process flow designed to realize it.

3.3.5.1 Pump plumbing layer (Layers 4 & 5)

The pump plumbing layer (Layers 4 & 5, Figure 3.15) is made up of two wafers, one containing all of the critical pump geometry and the other acting to seal the fluidic channels. The bottom of the pump plumbing layer includes the thrust balance channels, the spiral-grooves, and the inlet and outlet through holes for the pump inlet and outlet ports (Figure 3.22).

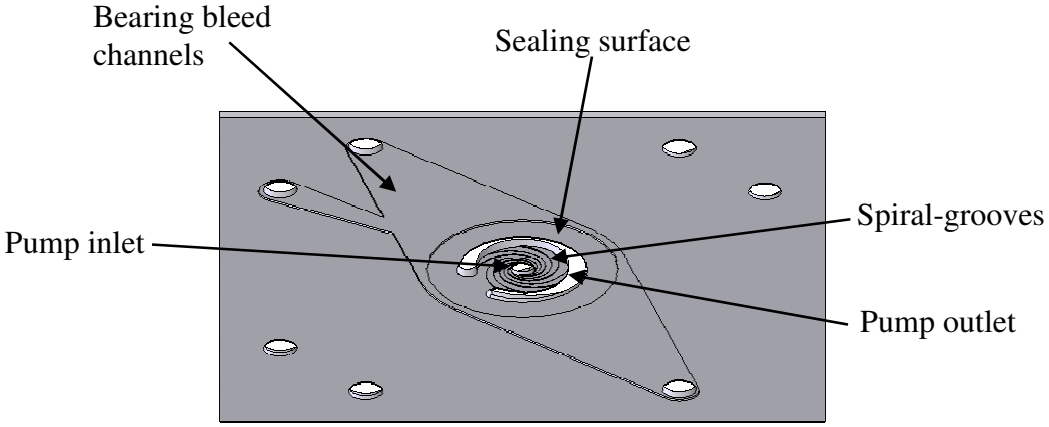

Figure 3.22. Schematic showing the bottom of the pump plumbing layer.

The spiral grooves are designed using a logarithmic spiral equation [55]:

$$r = r_1 \exp(\theta \cdot \tan \alpha) \qquad \text{Equation 3.16}$$

where r_1 is the inner radius of the spiral (Figure 3.23). The thrust balance channels are positioned at the outer radius of the rotor above the journal through etch from the rotor release. They are designed to have an etch depth equal to 145 µm minus the spiral-groove depth; where 145 µm is required by the alignment pit.

The sealing surface extends from the pump outlet to the thrust surface (Figure 3.15). The length of the sealing surface approximately 1 mm and the seal clearance is set by the pump gap. From the previous discussion about sealing between the nitrogen and the pumped liquid, a 10µm seal clearance can sustain over a 1 psi difference between the two fluids. The thrust balance channels can be used to aide in maintaining the seal with a changing pump outlet pressure.

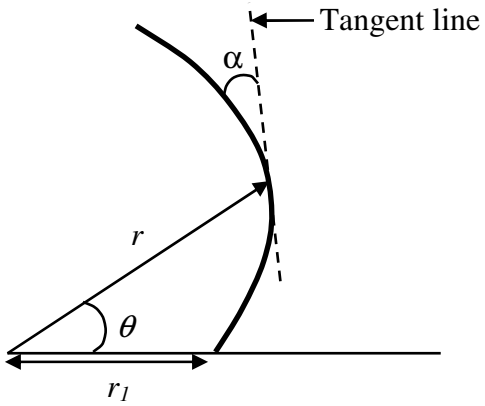

Figure 3.23. Schematic of the logarithmic spiral.

The thrust surface at the edge of the rotor was designed to enable some control over the normal load on the rotor. The thrust surface extends from a 4.8 mm radius to the edge of the rotor at a radius of 5 mm. As the rotor speed is increased with the driving flow, and therefore pressure, the thrust balance channels on the pump side can be throttled open to alleviate some of the pressure on the thrust surface and reduce the normal load on the rotor. On the contrary, during startup, the thrust balance channels can be used to supply pressure to the thrust surface, which forces the rotor onto the proper bearing raceway surfaces before the rotor is spun. This will also allow introduction of liquid (i.e. liquid priming) into the pump area and maintain a pressure seal without requiring the rotor to spin.

The top of the pump plumbing layer contains the through holes and the liquid channels for the pump inlet, outlet, and pressure taps (Figure 3.24). The inlet pressure tap and outlet pressure tap are placed in close proximity to the pump inlet and outlet, respectively, to minimize any loss due to the channel flow resistance.

The process flow for layers 4 and 5 is shown in Figure 3.25. The nested oxide process is again used enabling multiple DRIE steps to etch through the wafer completely. The oxide layer is first patterned by RIE on both sides of a 420 μm thick DSP silicon wafer with 1.1 μm of silicon dioxide (Figure 3.25a). The topside pattern includes through holes and the larger channel patterns. The backside is patterned with the spiral-grooves, the thrust balance channels, the sealing surface, and the through holes. DRIE is used to pre-etch the through holes after the top is patterned using photoresist (Figure 3.25b). Next, the bottom is patterned with thrust balance channels and alignment pits (~117.5 μm) using DRIE while a photoresist layer masks the spirals (Figure 3.25c). The

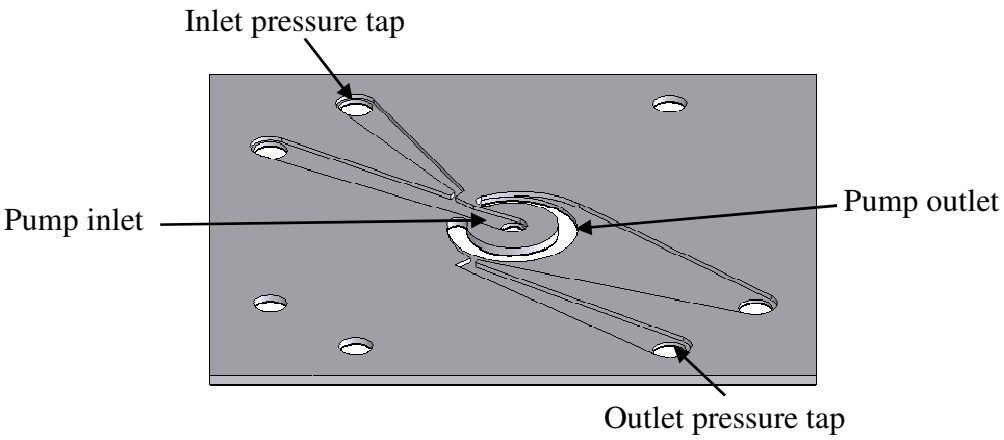

Figure 3.24. Schematic showing the top of the pump plumbing layer.

fluid channels on top are then etched using DRIE and masked by the oxide layer to a depth of 200 µm (Figure 3.25d). On the backside the spirals, h_0, are etched to the desired depth, 27.5 µm (Figure 3.25e) for a gap, h_2, of 10 µm.

To cap the wafer, borosilicate glass (Pyrex) is anodically bonded to the patterned silicon wafer. First, the oxide is completely stripped using concentrated HF, ensuring a uniform surface with low surface roughness (Figure 3.25f). Both the patterned silicon and Pyrex wafers are then cleaned of organic materials in a Piranha solution for 10 minutes and rinsed in a spin/rinse dryer. The two wafers are aligned by the wafer flat and bonded in a Karl Suss SB6 wafer bonder at 375˚C, 650N and 1000 V (Figure 3.25g). Figure 3.26 and Figure 3.27 show the topside and bottom side of a completed pump plumbing layer. The anodic bond is void free and the topside of the pump plumbing layer is shown in Figure 3.26. The bottom surface of the channels is covered with a thin layer of residue believed to be polymer build up from the DRIE through etch. Better carrier attachment of the die during the through etch can be performed to alleviate the residue found at the bottom of the channels. A ring from the center of the bonding chuck

also evident (bottom right corner of Figure 3.27); however, it is a residue on the topside of the Pyrex and will not affect the pump.

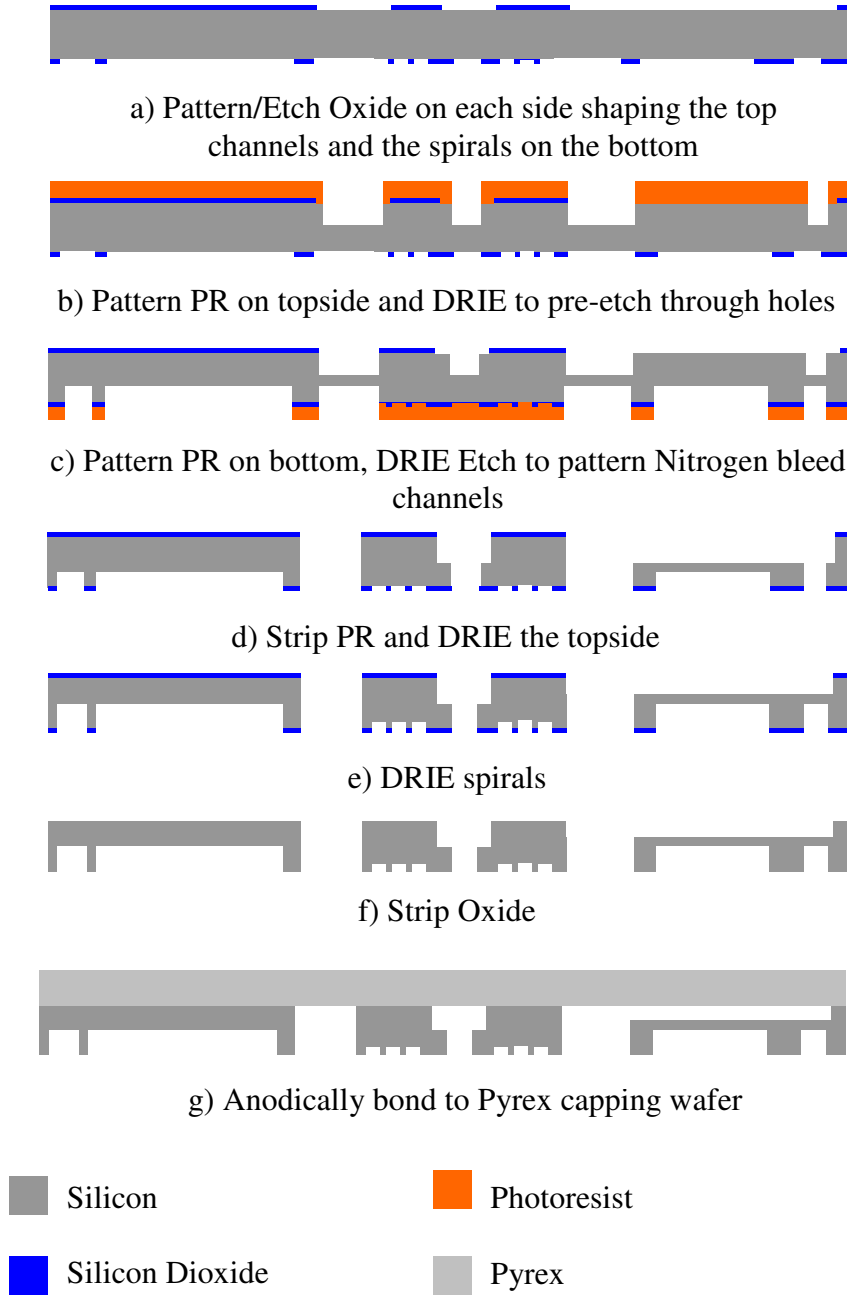

Figure 3.25. Fabrication sequence for the pump plumbing layer including the spirals.

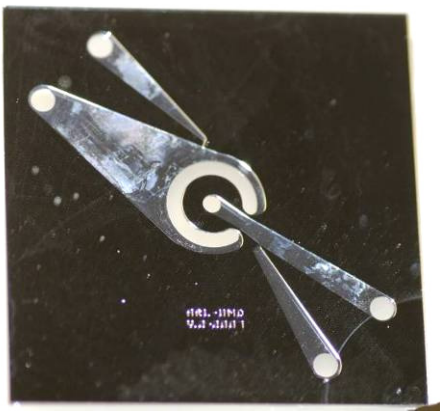

Figure 3.26. Optical image showing the topside of the pump plumbing layer and the residue left behind from the Cool Grease DRIE carrier attachment.

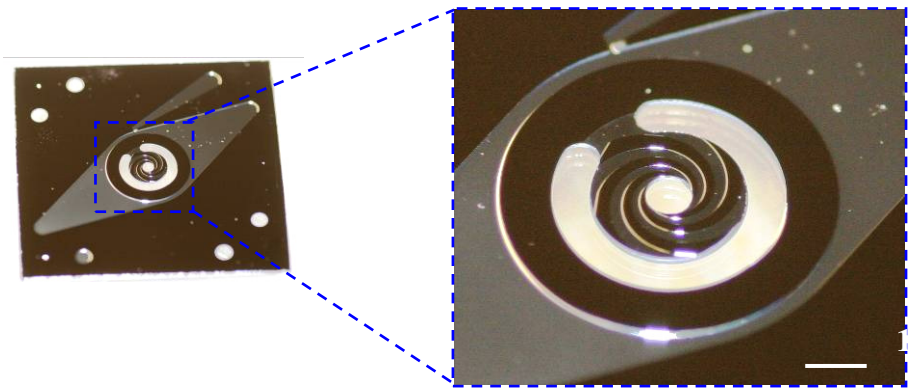

Figure 3.27. Optical image showing (a) the bottom of the pump plumbing layer and (b) a close up view of the spirals.

3.3.5.2 Rotor and Turbine (Layers 3 & 4)

The fabrication of the rotor layers 2 and 3 from Figure 3.15 is similar to the rotor layers of the microturbine tribology device, except for the addition of through holes and modifications to the planar-contact bearing design. The planar-contact bearing

fabrication implemented for the spiral-groove turbopump (planar-contact bearing V.2) had two modifications from the planar-contact bearing demonstrated in the microturbine tribology device (planar-contact bearing V.1). First, the bond interface was moved out of the expected microball wear track to minimize the wear on the radial raceway surface and second, the journal etch was not performed before the raceway etch to eliminate the etch artifact near the microball wear track.

The bond interface was moved away from the wear track expected by the microballs. The wear track width was observed to be 25 µm on the thrust surface using Figure 2.45. Therefore, the bond interface was moved 50µm from the center of the raceway by etching the raceway 95µm on the turbine side and 195 µm on the pump side (Figure 3.28). The journal design is kept 30 µm wide and 70 µm from the closest edge to ensure it is not in the path of the microball. This also prevents a large sag in the improper direction.

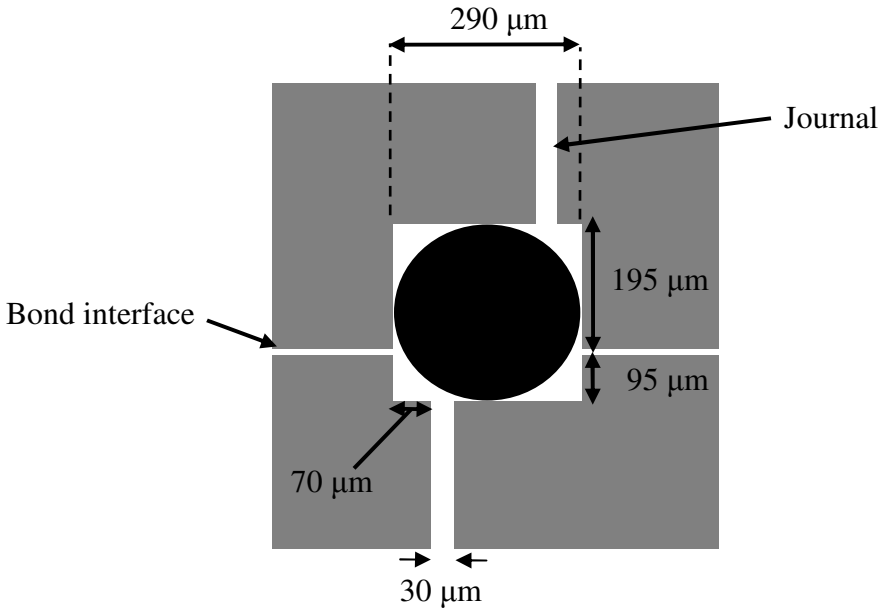

Figure 3.28. Schematic drawing of the planar-contact bearing V.2 implemented in the spiral-groove turbopump.

The second modification was implemented to eliminate the etch artifact close to the journal edge (Figure 3.29a), which arises from the nested oxide etch process where the race edge is pushed down during the second etch. To eliminate the roughness at the edge of the journal and create a smooth surface over the entire race track, an alternate fabrication sequence was developed with the use of a photoresist spray coater. Both the previous nested mask and the new raceway fabrication sequences are shown in Figure 3.30 and the raceway result comparison is shown in Figure 3.29.

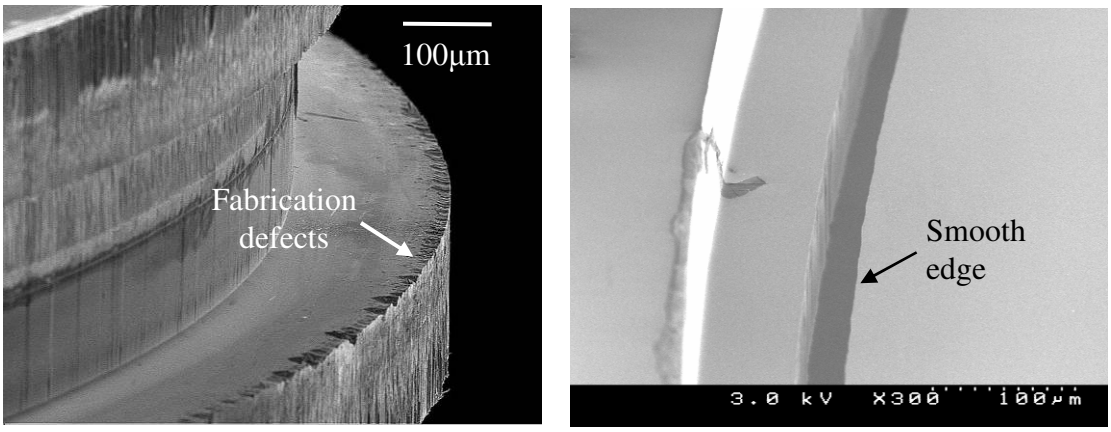

(a) (b)

Figure 3.29. SEM images showing the planar bearing race fabricated with (a) the nested masking technique and (b) the spray coating technique.

The modified process starts by etching the 290 µm wide annular raceway using DRIE masked by the silicon dioxide that was patterned by RIE (Figure 3.30b step 1 and step 2). The etch depth is chosen to be 95 µm on the turbine side and 195 µm on the pump side. The resulting rotor sag is approximately 5.5 µm. For accurate bond alignment between the two layers, these etches are performed in two steps so that the microball alignment pits are 145 µm on both the turbine and pump sides. On the turbine

side, the alignment pit is pre-etched to 55 μm using a photoresist mask and then the 95 μm deep raceway etch is performed using the silicon dioxide mask. On the pump side, the raceway is pre-etched to 50μm using a photoresist mask. The rest of the raceway depth is etched to the final 195 μm using the silicon dioxide masking layer with the alignment pits opened.

After the raceways are defined on the turbine side and pump side of the rotor, a thick photoresist spray process is used to coat the wafer and pattern the journal at the bottom of the raceways (Figure 3.30b step 3). The thickness of the photoresist was measured to be much thinner at the bottom of the trench than on the wafer surface (Figure 3.31). Furthermore, the two raceway depths had two different photoresist thicknesses. Although the same photoresist spray coating recipe was applied to both, the 95 μm deep raceway had a photoresist layer approximately 8 μm thick, while the 195 μm deep raceway had a photoresist layer approximately 3.6 μm thick. Each race should have specific exposure and development times associated with the different layer thickness at the bottom of the raceway. An exposure time of 10 seconds and a development time of 90 seconds were sufficient to clear away the 8 μm thick photoresist, no matter how overexposed and developed the 3.6 μm thick photoresist (30 μm wide line became 35 μm wide). Since the photoresist thickness on the surface was 10 μm, the patterns on the wafer surface were exposed for an additional 5 seconds using a second optical mask to ensure complete development.

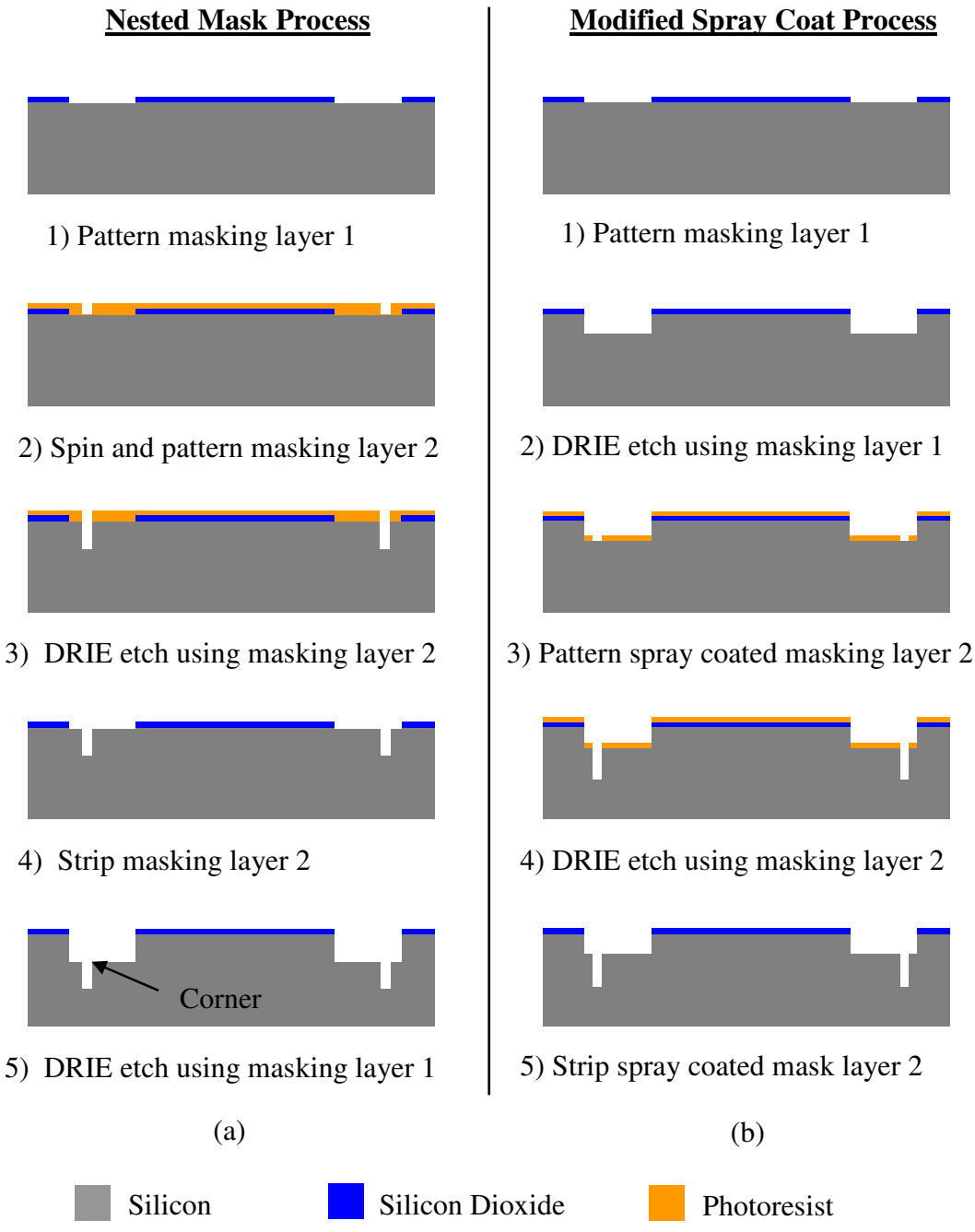

Figure 3.30. (a) Original planar bearing fabrication process using nested photoresist and silicon dioxide masks and (b) new planar bearing fabrication process eliminating the nested masking technique for a smooth bearing surface.

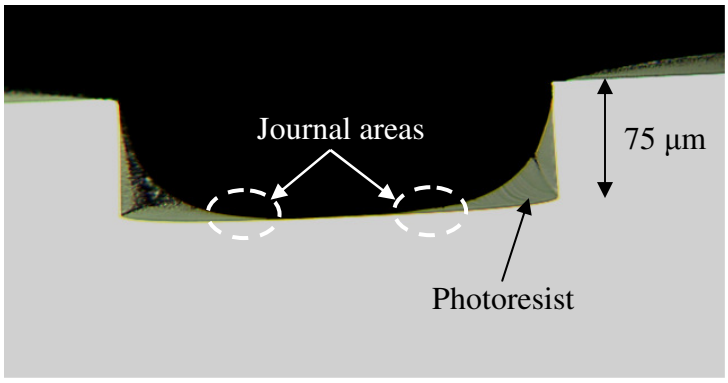

Figure 3.31. Optical photograph of a silicon trench cross-section demonstrating the buildup of photoresist at the corners of a trench. Note the different photoresist thickness between the wafer surface and the trench bottom.

A variable thickness at the base of the etched trench is also a concern when designing the position of the journal (Figure 3.31). The sidewall of the etched trench acts to capture the dispersed photoresist droplets in addition to the normally incident photoresist droplets. The added photoresist builds up at the corners of the trench causing a large thickness variation at the bottom. The design of patterned features at the bottom of the trench must take the variable thickness into account.

Once the journal pattern is obtained in the photoresist at the bottom of the raceway, DRIE is used to etch the turbine side to a depth of 125 μm (Figure 3.30b step 4) so that the release etch on the opposite side will be 200 μm (turbine blade height). The pump side journal was etched to a depth of 80 μm so that the release on the opposite side will be 145 μm required by the microball alignment pits to align to the pump plumbing layer.

After the raceways and journals are patterned into the rotor layers, the fabrication sequence proceeds in the same manner as described in Chapter 2. The metal adhesion

layers (Cr-Au-AuSn-Au) are deposited through silicon fabricated shadow masks using electron-beam evaporation. Next the rotor wafers are diced into individual die, microballs are placed into the raceway and alignment pits, and then the die are aligned and bonded together. Once bonded, the turbine side is etched using DRIE and the patterned silicon dioxide until the journal is reached (approximately 200 μm). The die is then flipped over and etched using DRIE and again patterned silicon dioxide on the pump surface until the rotor is completely released (approximately 145 μm). The turbine side of a completely released die is shown in Figure 3.32. The release process begins by etching until approximately 10 μm of silicon remain. Short, one minute etches with inspections in between are then performed until the release is completed. The short etch and inspection cycles enable well controlled release and minimize the effect of over etching.

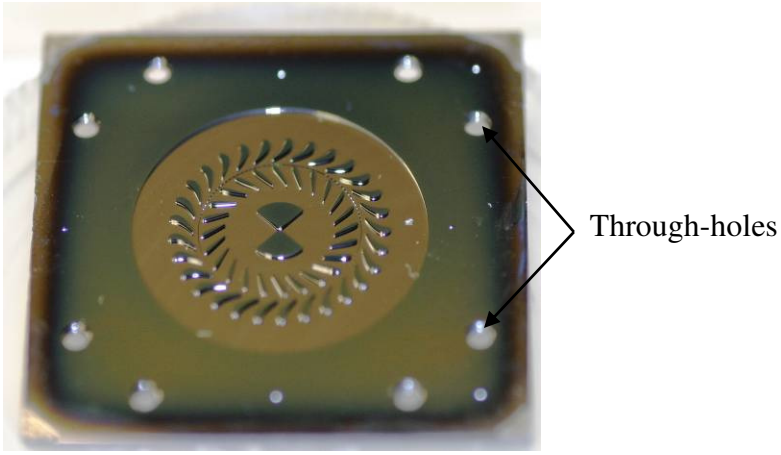

(a)

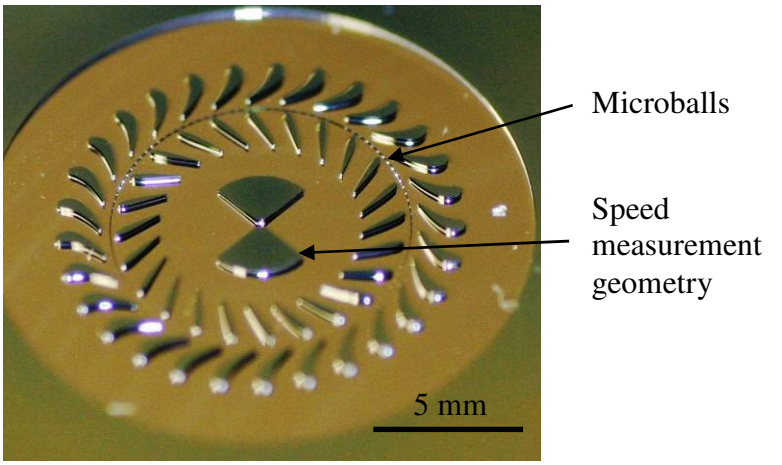

(b)

Figure 3.32. Optical image showing (a) the turbine side of the rotor layer #2 and (b) a close up of a released turbine rotor.

3.3.5.3 Turbine plumbing layer (Layer 1)

The turbine plumbing layer serves to house the turbine and provide the inlet and outlet of the turbine and is the interface layer between tubulations and the test fixture. The top of this layer has a cavity etched into it so that the turbine cannot rub on the plumbing layer cavity (Figure 3.33). The depth of the cavity is determined by the sag of the rotor and the desired amount of clearance above the rotating blades. A minimum clearance above the turbine blades is desired, however, the efficiency of the turbine is not critical to the demonstration of the turbopump because a large pressure nitrogen source. The cavity depth is chosen to be less than 10% of the turbine blade height plus the amount of sag measured in the rotor. In the case of devices fabricated for this work, the sag was measured to be between 3 µm and 6 µm and the blade heights were greater than 200 µm. The cavity depth was made to be 25 µm.

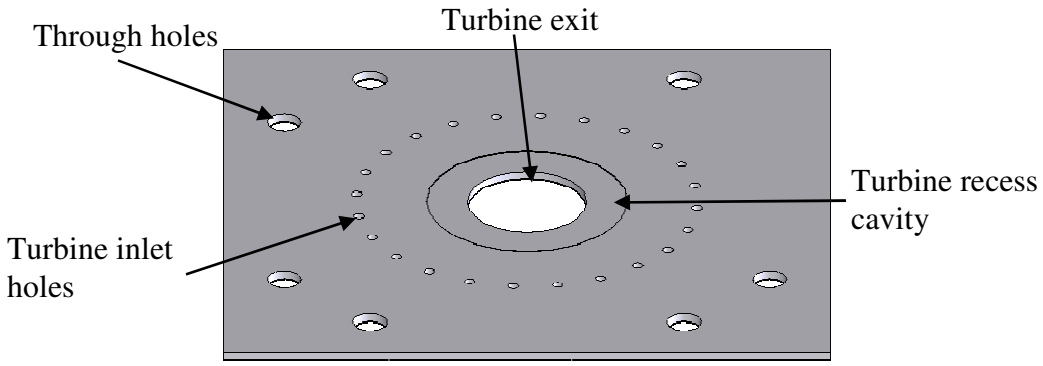

Figure 3.33. Schematic showing the top of the rotor layer.

Both the top and bottom turbine plumbing layers (Figure 3.33 and Figure 3.34 respectively) include 1.7 mm diameter through holes for the pump inlet, pump inlet pressure tap, pump outlet, pump outlet pressure tap, thrust balance channels, and thrust pressure tap. Other through holes in this layer include 24 turbine inlets (diameter of 500 μm) allowing the turbine flow to enter at the opening of each diffuser vane and 1 large turbine outlet at the center with a diameter of 6 mm.

The fabrication process for the turbine plumbing layer is shown in Figure 3.35. The starting wafer is a 4-inch, 440 μm thick DSP wafer with a 1.1 μm thermally grown silicon dioxide on both sides. The first steps (Figure 3.35a) are to pattern the silicon dioxide on the top for the through holes and cavity and the through holes on the bottom. The silicon dioxide is patterned by RIE and a photoresist masking layer. Once the silicon dioxide is patterned, the next step is to pattern the alignment pits into a photoresist layer (Figure 3.35b). The alignment pits will be pre-etched into the silicon so the total etch depth will become 145 μm once the cavity is etched, which is the proper depth for the microballs. Contact profilometry is used to verify the etch depth before the

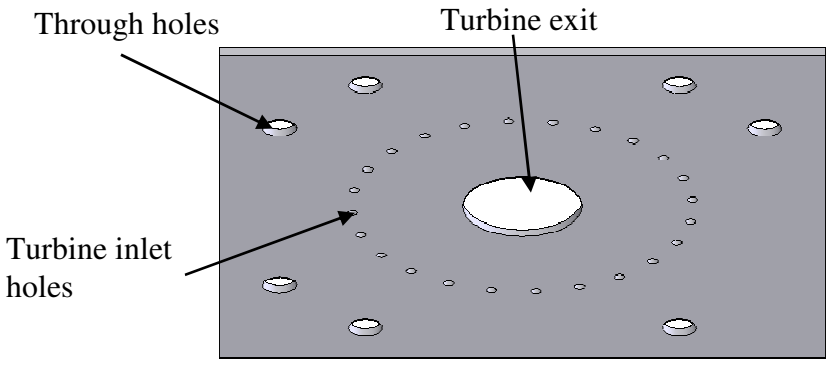

Figure 3.34. Schematic showing the top of the rotor layer.

photoresist is stripped of using PRS-3000 heated to 85˚C. DRIE is then used again on the top side to define the proper cavity depth of 25 µm (Figure 3.35c) using the patterned silicon dioxide as the masking layer. The last etch step in the turbine plumbing layer fabrication is to etch from the backside, using the patterned silicon dioxide as the masking layer for DRIE (Figure 3.35d), until the through etch holes are completed. At this point the wafer is diced and ready for the assembly process. Figure 3.36 shows the topside in (a) and the bottom side in (b) of a completed turbine plumbing layer die.

a) Pattern and etch silicon dioxide on both sides for turbine cavity, alignment pits, and through holes

b) Pattern PR and etch using DRIE on top to pre-etch alignment pits

c) DRIE topside to define turbine clearance and pre-etch through holes

d) DRIE etching to complete the through holes

Figure 3.35. Fabrication flow of the turbine plumbing layer (Layer #1).

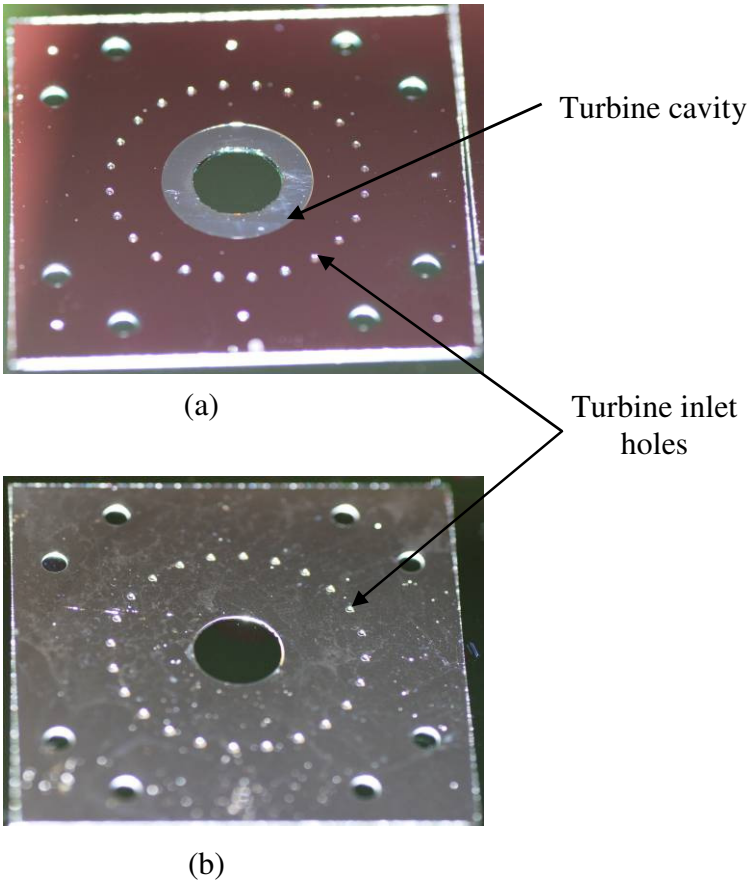

Figure 3.36. Optical images showing (a) the top of the turbine plumbing layer with the silicon dioxide layer still present and (b) the bottom of the turbine plumbing layer.

3.3.5.4 Turbopump assembly

The turbopump is assembled in 2 bonding steps (Figure 3.37). The turbine plumbing layer and rotor layers are completed separately. The assembly process begins by attaching tubulations with epoxy to the turbine plumbing layer (Figure 3.38). Next,

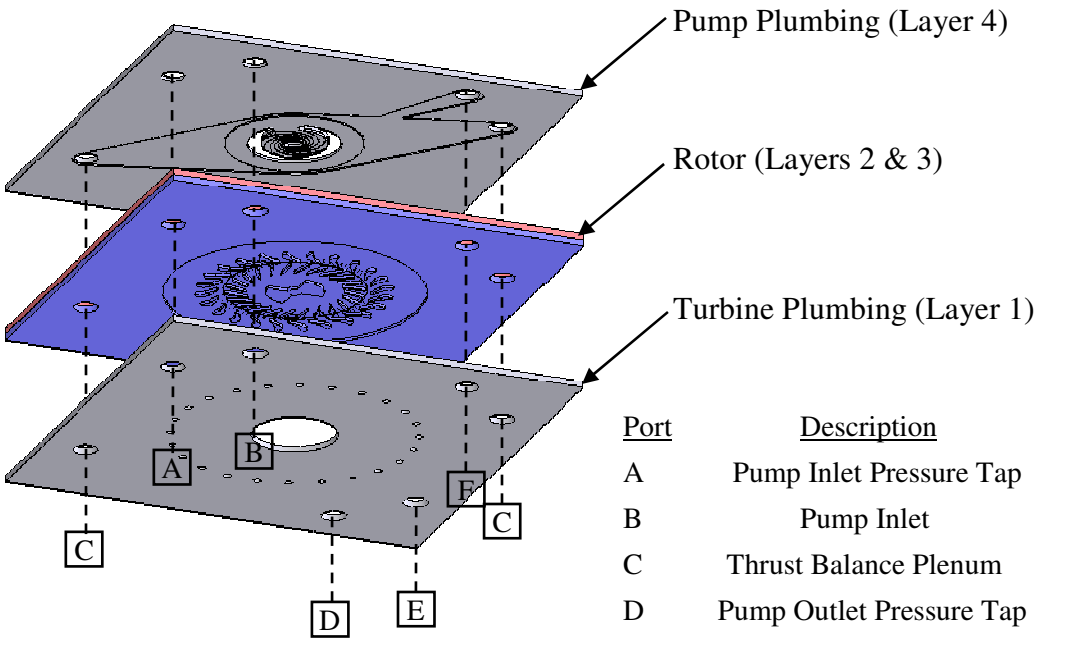

Port	Description
A	Pump Inlet Pressure Tap
B	Pump Inlet
C	Thrust Balance Plenum
D	Pump Outlet Pressure Tap
E	Pump Outlet
F	Thrust Balance pressure Tap

Figure 3.37. Schematic of the assembly and ports for the turbopump device.

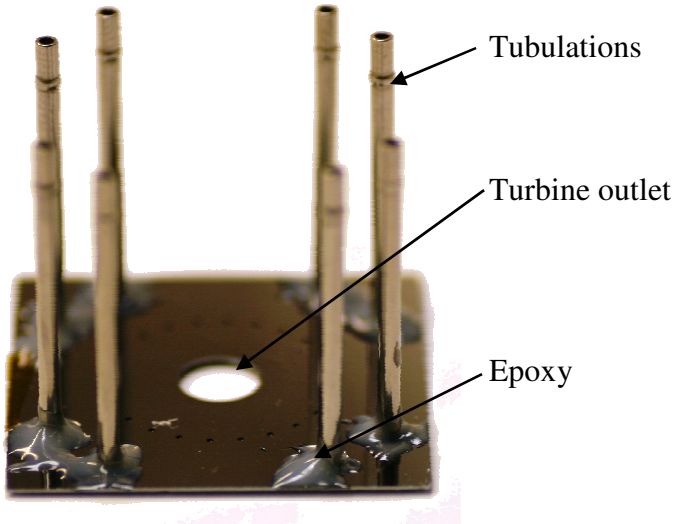

Figure 3.38. Optical image showing tubulations attached to the bottom of the turbine plumbing layer.

the pump plumbing layer is bonded to the rotor layer using photoresist as the temporary bonding layer. The alignment of the two layers is performed using the three sets of alignment pits with microballs placed in them.

The photoresist bonding thickness is critical in determining the pump gap. Controlled photoresist thickness ranging from 4 to 20μm is possible using a Suss Microtec Altaspray system. The photoresist was sprayed onto the die using a shadow mask fabricated in silicon. The photoresist bonding was performed on a hotplate at 110˚C for 3 minutes with a weight placed on top. The sprayed-on photoresist thickness was measured on a separate sample using the same curing temperature and time, but without compression. In these measurements, the thickness variation was +/- 0.5μm. The thickness of the bonded photoresist was not directly measured, but is believed to shrink due to squeeze-out from the compression and temperatures applied. The assumed gap in this work was, therefore, an estimation of the maximum gap value.

The last step in the assembly of the turbopump device is to bond the turbine plumbing layer to the bottom of the stack using a manual application of photoresist (thickness is not critical). A completed spiral-groove turbopump is shown in Figure 3.39.

In an application setting, silicon fusion bonding (or any bonding method) can be used for smaller pump gaps. For the work presented in this dissertation, a photoresist bonding layer was essential to enable disassembly of the turbopump stack without disrupting the rotor bonding layer. In this case, both plumbing layers could be removed in Acetone while the rotor layer remains bonded together. This allows for cleaning of the device via Acetone flushing and ultrasonic as well as substitution of the plumbing layers using only a single rotor device.

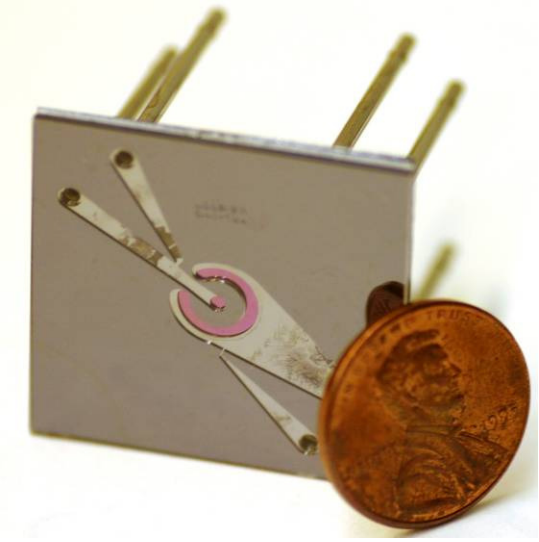

Figure 3.39. Optical photograph of a completed spiral-groove turbopump.

3.4 Turbopump Summary

The centrifugal-type turbopump design and implementation with a tangential air-turbine and point-contact bearings was presented at the beginning of the chapter. Demonstration of pumping was hindered by to the poor symmetry of the device. The asymmetry caused sealing to be unrealistic and created divots on the raceway created from the non-uniform etching, which limited rotary operation. These results led to the improved axisymmetric design using a radial in-flow air turbine and the elimination of the asymmetric volute design. The centrifugal-type pump was exchanged for a spiral-groove pump allowing for a smaller rotor diameter. This reduced the torque required to operate, an important detail for future micromotor integration. The planar-contact bearing design V.2 was chosen over the point-contact design due to the significantly less wear that allows for better gap control in the pump. Lastly, the fabrication process of the

spiral-groove viscous turbopump was presented. By changing only the optimal masks, many configurations of the spiral-groove turbopump can be realized using the fabrication process presented. Thus, not only can spiral-groove viscous turbopumps be fabricated with the process techniques developed, but other viscous type and centrifugal (axisymmetric) designs can be as well.

4 Micro Turbopump Characterization

This chapter presents the first demonstration of a microball bearing supported turbopump. The experimental procedure, apparatus, and key characteristics of the final assembled devices are described first. Characterization of the turbine rotor before and after assembly of the pump plumbing layer is examined, proving that the fabrication and assembly processes do not prevent rotor operation. Next, two different liquid start-up methods are detailed, and finally, the turbopump characterization for two different pump gaps is presented.

The design and fabrication of two micro turbopump designs supported on microball bearings were introduced in the previous chapter. A summary of testing the centrifugal turbopump concluded that an axisymmetric spiral-groove viscous turbopump design would be more effective for the applications of interest. Therefore, the viscous turbopump was designed using a modified planar-contact bearing mechanism along with the radial in-flow air turbine. The planar-contact bearing V.1 was designed to lower raceway wear due to point-contacts, while the modified planar-contact bearing V.2 was designed to further reduce the amount of wear and debris created by the bond interface. When compared to the tangential air turbine, the radial in-flow air turbine is axisymmetric and produces larger torque at lower driving pressures, which allows for low normal load operation. The integration of these components led to a turbopump designed for flow rates up to 100 mL/hour with operating pressures greater than 1 psi.

4.1 Experimental Apparatus and Test Setup

This section describes the experimental apparatus and test setup used to characterize the microturbine and spiral-groove turbopump. The device test jig serves to interface between the turbopump and measurement suite. Following the description of the device test jig is a description of the experimental setup and the measurement suite used to characterize the devices. The experimental apparatus is comprised of the test jig, measurement suite, computer interface and data acquisition, and the gas and liquid flow controls. The turbopump cross-section diagram is shown in Figure 4.1 with the port designations corresponding to those described by Figure 4.2.

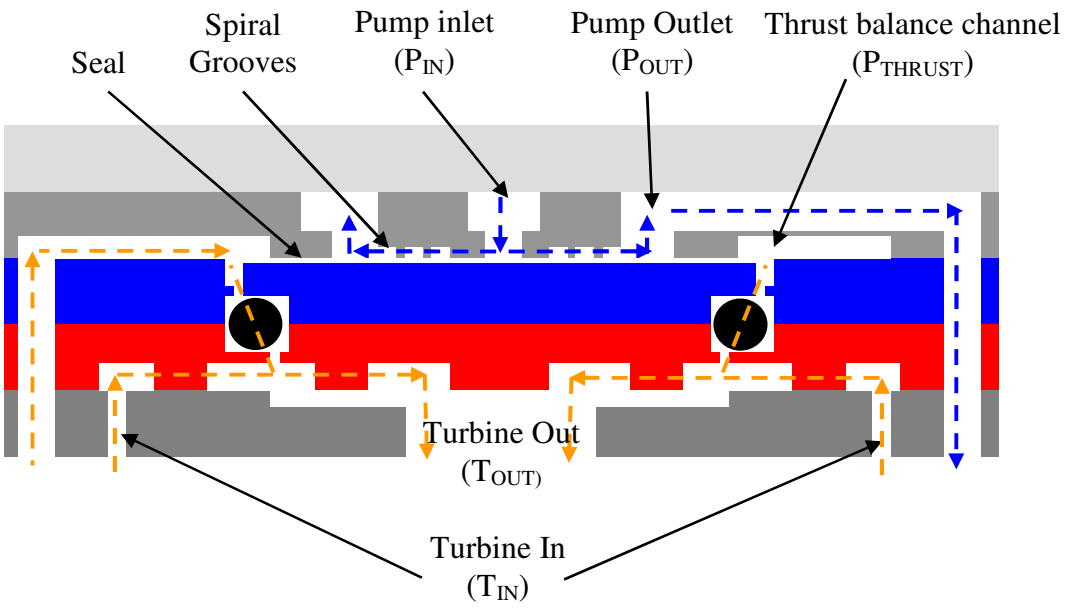

Figure 4.1. Liquid and gas designations for the spiral groove turbopump.

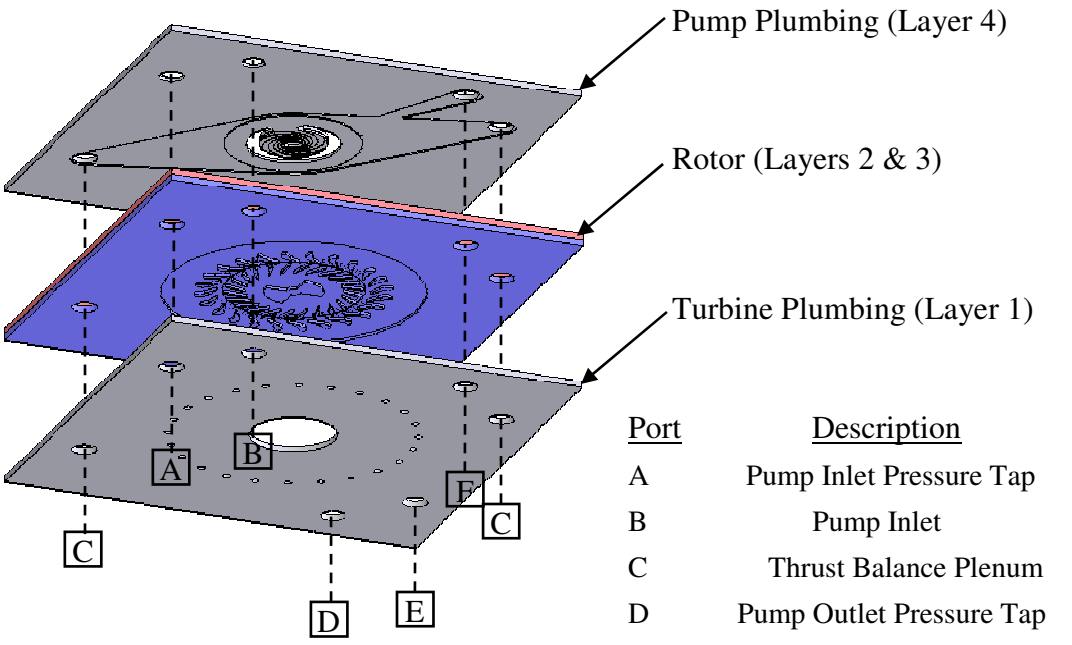

Port	Description
A	Pump Inlet Pressure Tap
B	Pump Inlet
C	Thrust Balance Plenum
D	Pump Outlet Pressure Tap
E	Pump Outlet
F	Thrust Balance pressure Tap

Figure 4.2. Schematic of the assembly and ports for the turbopump device.

4.1.1 Device Testing Jig

An aluminum jig was developed to interface the silicon turbopump device with the measurement suite and liquid/gas ports (Figure 4.3 and Figure 4.4). The turbopump device, measuring 27 mm on a side, is fit into the cavity with the holes provided for the protruding tubulations, turbine inlet, and turbine outlet. The turbine outlet also provides access to the measurement geometry on the turbine rotor for the ODS. O-rings are placed into the jig to separate the turbine inlet air flow and the turbine outlet air flow. The device is compressed onto the o-rings using an aluminum lid that is screwed to the base of the jig.

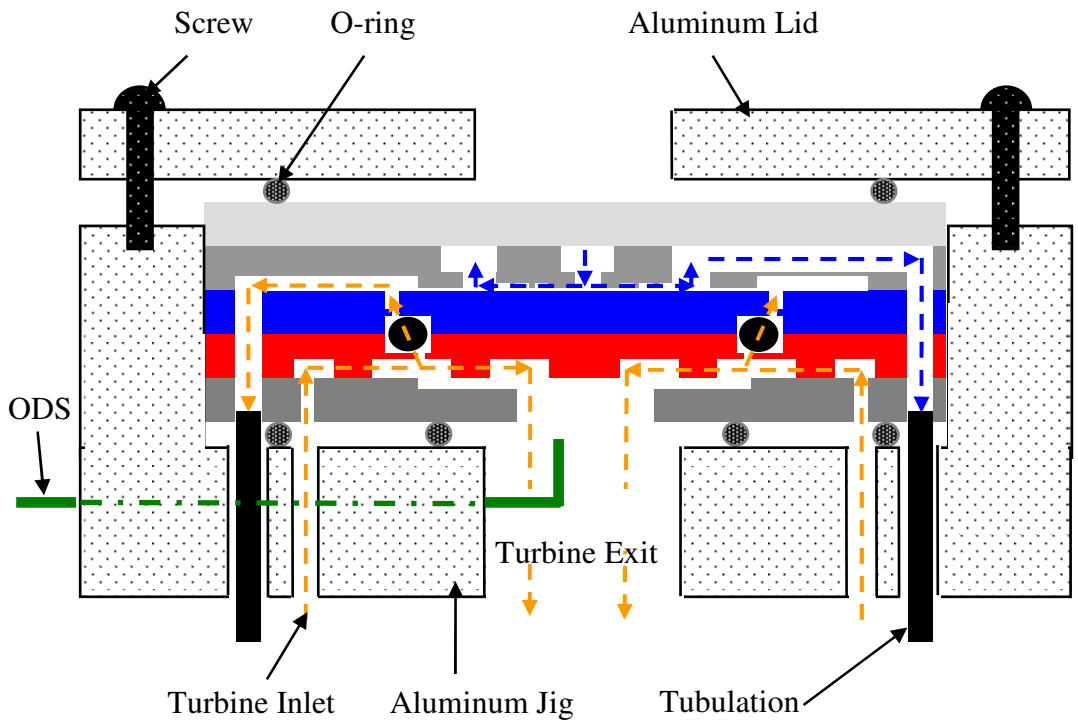

Figure 4.3. Illustration of the mechanical jig with the turbopump inside.

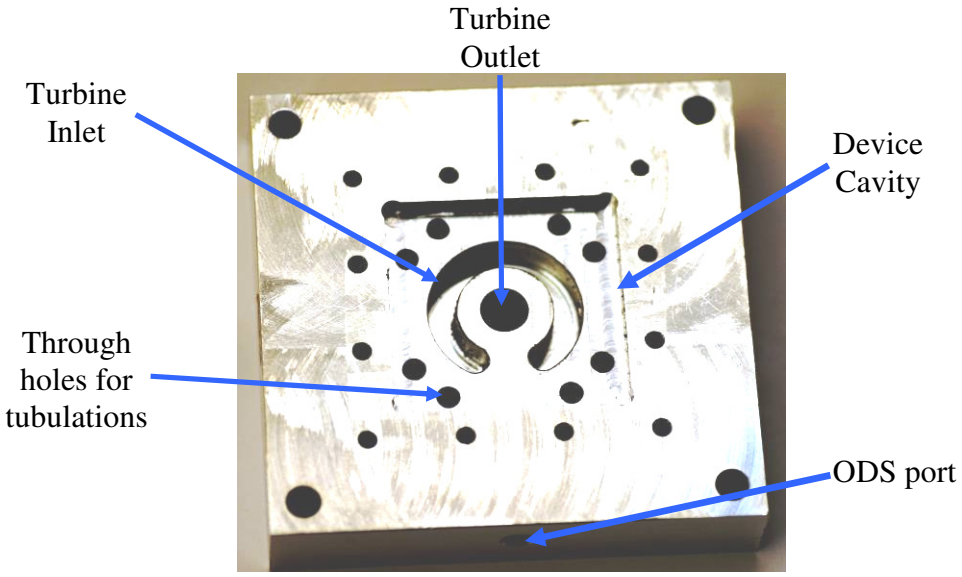

Figure 4.4. Photograph of the turbopump jig.

Once the device is secured in the jig, tubes are attached to the tubulations protruding on the backside (Figure 4.5). Also, to supply pressurized nitrogen to the device, one-quarter inch outer diameter tubing is attached to the jig through holes tapped for an NPT fitting. The ODS access hole is seen in the photograph. The ODS is attached to an x-y-z manipulator for accurate positioning over the measurement geometry.

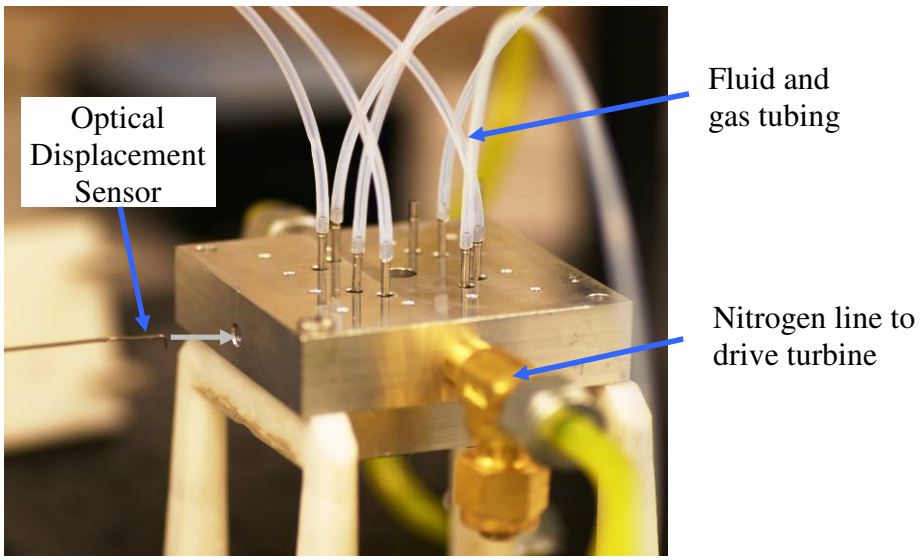

Figure 4.5. Photograph showing a completely packaged turbopump device.

In some cases, turbine characterization was performed without the pump plumbing layer to ensure proper rotor operation before assembling the device as a turbopump. However, when the plumbing layer is not attached, the pressure does not build up on the turbine rotor backside and force the rotor into proper contact with the raceway. To enable the proper axial position of the rotor to be in contact with the

raceway, a gasket is placed on top of the o-ring creating a thrust plenum similar to that described in chapter 2 (Figure 4.6). In this case, the turbine inlet pressure will also serve to pressurize the thrust balance plenum and force the rotor into contact with the raceway.

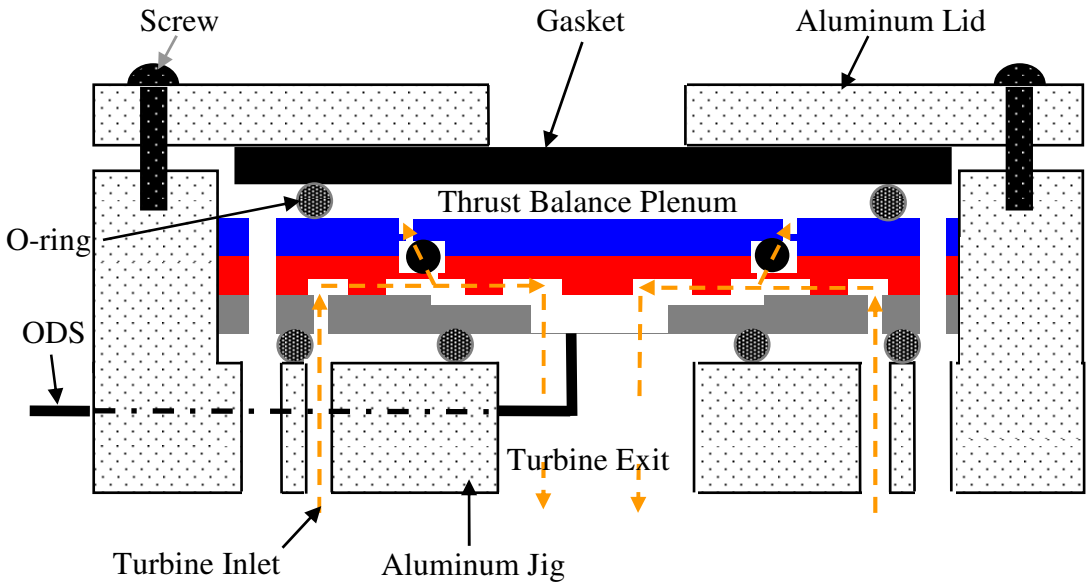

Figure 4.6. Illustration of the packaged turbopump without the pump plumbing layer to characterize the turbine operation.

4.1.2 Measurement Suite

Illustrated below (Figure 4.7) is the experimental apparatus used to characterize the microturbine and turbopump. The pressure, liquid, and gas handling ports correspond to those described in Figure 4.1 and Figure 4.2. Five key areas are outlined: a) turbine inlet, b) pump inlet, c) thrust balance, d) pump pressure differential, and e) pump outlet.

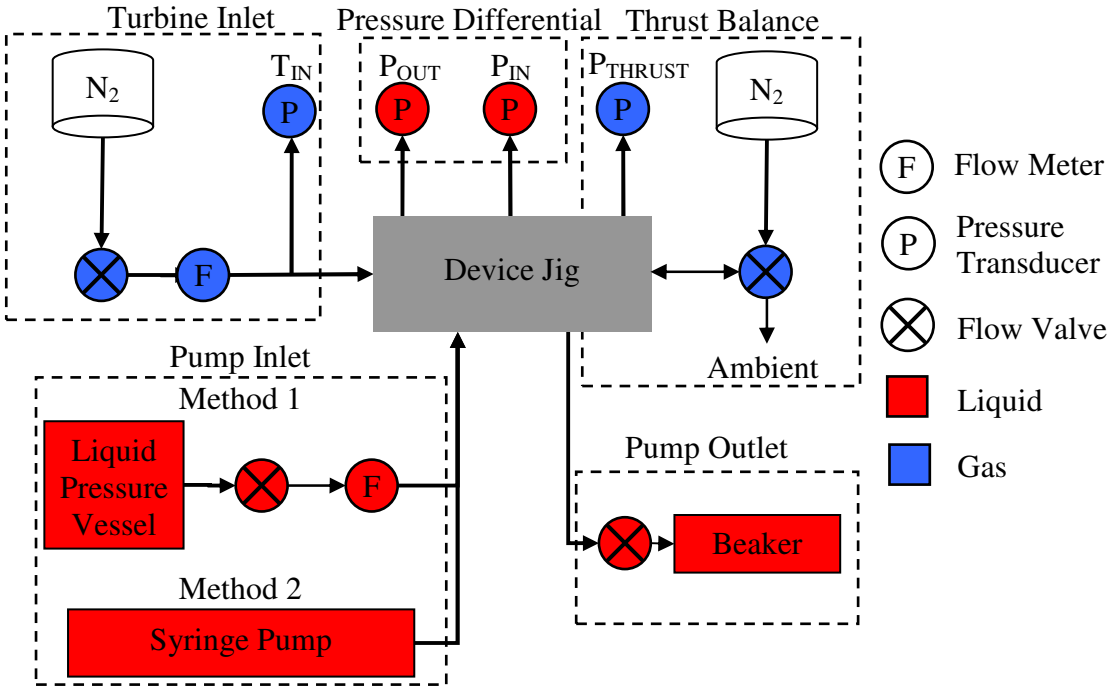

Figure 4.7. Liquid and gas experimental setup diagram for the spiral-groove turbopump.

The turbine inlet is composed of an 80 psi, house nitrogen source, a manual control valve, an Omega FMA series flow meter (0 – 50 slm), and an Omega pressure transducer (0 – 60 psi). The flow rate of the turbine is controlled via the manual valve and logged with the turbine inlet pressure. The turbine exit is exhausted to ambient.

The thrust balance pressure is controlled via a manual control valve in line with the device and house nitrogen source. An Omega pressure transducer (0 – 15 psi) monitors the thrust balance pressure at the periphery of the rotor. The thrust balance pressure can be used to maintain the required pressure for sealing. This is necessary to ensure the microball bearings remain dry during operation of the turbopump device.

The flow rate through the pump can be controlled using two methods: (1) a pressure vessel with an inline rotameter and flow valve or (2) a programmable syringe pump. Method 1 uses a control valve and a direct read rotameter in line with the device and a liquid pressure vessel. The pressure of the vessel is maintained via a regulator and the house nitrogen source. This allows the pump inlet pressure to be fixed and adds an additional control of the normal force exerted on the rotor ensuring proper contact. Method 2 uses a programmable syringe pump (Kent Scientific GENIE Plus), which allows the flow rate to be controlled from below 1 μL/hour to greater than 45 mL/min.

The pump outlet is fed to a beaker and throttled using both a pressure head built-up by varying the elevation of the beaker and a flow valve. The pressure differential rise across the pump region is measured using two pressure transducers (0 – 1 psi with a 0.003 psi accuracy) each placed at the pump inlet and outlet pressure taps.

Not shown in Figure 4.7 is the ODS to detect the speed of rotation. A D6 ODS from Philtec, Inc. is connected in line with a 200 kHz voltage amplifier and then fed to a DAQ card. The voltage signals from the pressure transducers and the flow meter are fed to the same DAQ card.

A 6024 DAQ interfaces the signals coming from the pressure transducers and flow meter to the computer and a LabView program. Figure 4.8 provides a snapshot of the LabView program interface developed to monitor and log data necessary for characterizing the turbopump. The ODS voltage produced by the measurement geometry is converted to a rotational speed using the FFT algorithm developed in previous experiments. The voltage signals from the pressure transducers are converted to psi pressure units and the flow rate voltage signal is converted to slm units and logged, with

the speed measurement and time, in a tab delimited file. The pressure transducers are calibrated to zero using the logged data at ambient conditions so that all pressure measurements are relative to atmospheric pressure.

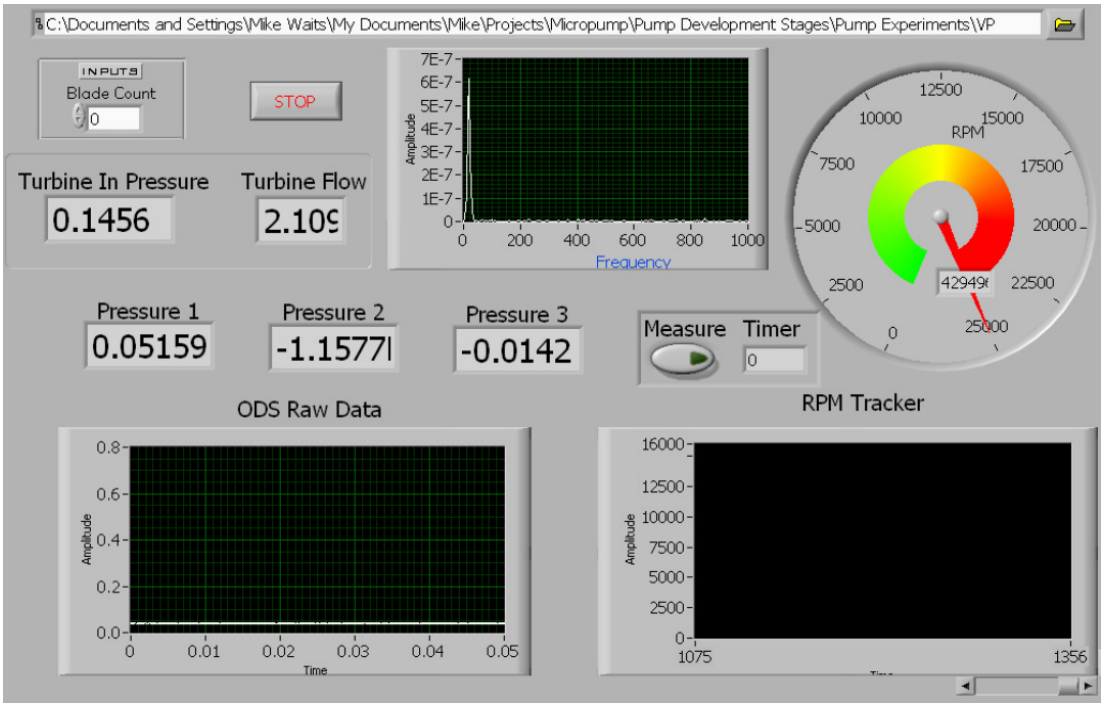

Figure 4.8. Screen shot of the LabView program written for the testing the spiral-groove turbopump.

4.2 Assembled Device

Multiple rotors were fabricated and assembled into turbopumps using both the planar-contact bearing V.1 and planar-contact bearing V.2 (having the bond interface moved out of the wear region). Not all devices operated properly when the turbine was characterized. In this case of some assembled planar-contact bearing V.1 devices, the fabrication tolerance, combined with wear, caused the rotor to rub on the turbine

plumbing layer after a few seconds of operation. This was fixed by moving the bond interface away from the wear track, reducing wear and relieving some of the alignment tolerance through geometrical changes.

Three rotors were fabricated and assembled using the planar-contact bearing V.2 and two of the three rotors were assembled into turbopump devices with a turbine blade height of 200 μm and gaps of 7.4 μm ± 1 μm (Device 1) and 15 μm ± 1 μm (Device 2). The third rotor (Device 3) was not assembled into a turbopump device and only used to characterize the turbine and bearing mechanism. The salient characteristics of all three devices are provided in Table 4.1. The assumed pump gap is an estimation of the maximum gap as was described in Chapter 3. The actual gap is believed to be less, because of shrinkage during the bonding procedure.

	Rotor Sag (μm)	Maximum Photoresist Thickness (μm)	Pump Gap (μm)	Turbine Blade Height (μm)
Device 1	3.4 +/- 0.5	4 +/- 0.5	7.4 +/- 1	200
Device 2	5 +/- 0.5	10 +/- 0.5	15 +/- 1	200
Device 3	5 +/- 0.5	NA	NA	200

Table 4.1. Characteristics of devices tested.

4.3 Turbine Characterization

The turbine rotor is first characterized before liquid testing is performed. This ensures that the fabricated rotors and the assembly process do not affect the performance of the turbine. Two rotor characterizations are performed: 1) before the pump plumbing

layer is attached and 2) after the pump plumbing layer is attached via the photoresist adhesion layer. Characterizing the turbine rotor before the pump assembly means that any failure is due to the rotor layer fabrication. Failure after attaching the pump plumbing layer is attributed to the assembly process.

Characterization is performed by logging the turbine rotational speed of the rotor and pressure versus the turbine flow rate. The rotor is spun to 10,000 rpm and back to rest. If the turbine rotor is observed to operate without large fluctuations it can be assembled as a turbopump. For some devices, fluctuations were observed in the rotational speed versus flow rate. In these cases, the device was cleaned by soaking in an ultrasonic acetone bath. This helped to remove any particle build up inside the raceway. The rotor would then return back to its expected performance.

When the turbine was characterized without the plumbing layer, the device was packaged with the gasket (Figure 4.6). When testing with the plumbing layer attached, the device was packaged without the gasket (Figure 4.3). In this case the ports on the pump side, which are the pump inlet and outlet channels and their pressure taps, and the thrust balance channel and pressure tap, were plugged. Plugging them ensures that pressure can build-up on the pump side and force the rotor into contact with the bearing raceway.

Figure 4.9 shows the turbine characterization curves for Device 1 packaged without the pump plumbing layer. This device reached 10,000 rpm at a turbine flow rate of 1.8 slm and approximately 0.1 psi, slightly less than the turbines characterized in Chapter 2 and used for spin-down testing. In that case, the rotor reached 10,000 rpm at a turbine flow rate of 3 slm and approximately 0.45 psi.

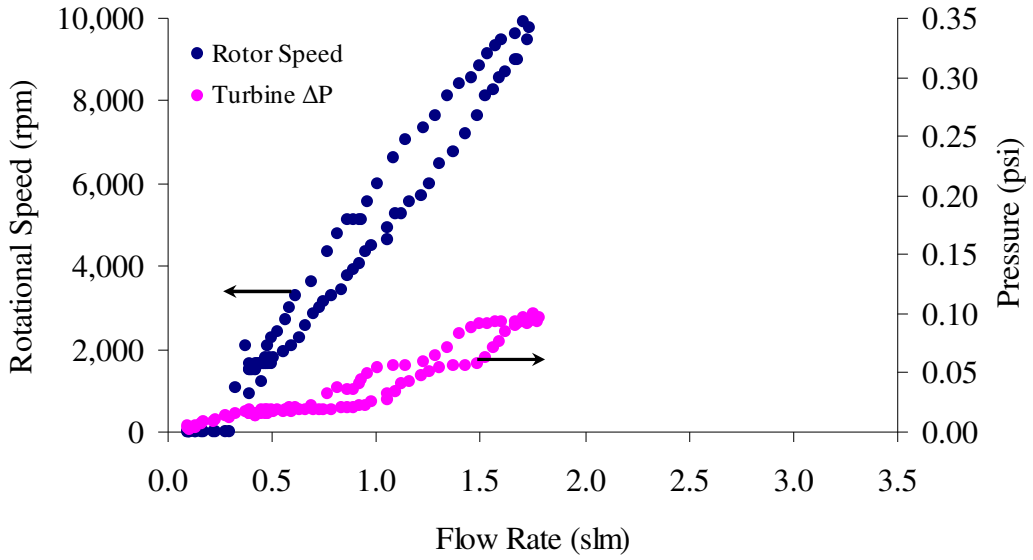

Figure 4.9. Turbine performance curve without liquid using planar-contact bearing V.2 and packaged without the pump plumbing layer.

The discrepancy may be attributed to the difference in blade height, which was 200 µm for the rotor tested here (Turbine V.2) and 100 µm for the device tested in Chapter 2 (Turbine V.1). The smaller blade height of Turbine V.1 increases the fluidic resistance and limits the flow rate through the rotor for a given turbine pressure differential. Turbine V.1 requires a larger pressure differential to create the same flow rate as Turbine V.2 that has larger blade heights. The increased turbine pressure also results in an increased normal load on the rotor due to the coupling between turbine pressure and normal load. The rotational speed of Turbine V.1 is, therefore, slower than Turbine V.2 even though the flow rate is the same and the difference can be attributed to the normal force on the rotor of Turbine V.1 being larger. Increasing the turbine blade height will further increase the speed versus flow rate ratio.

Characterization of Device 1 with the pump plumbing layer assembled and packaged is shown in Figure 4.10. The thickness of the photoresist layer attaching the rotor to the pump plumbing layer was 4 µm ± 0.5 µm. This makes the gap between the rotor disc surface and the pump plumbing layer 7.4 µm ± 1 µm when the rotor is in contact with the planar-contact raceway. The flow rate required to achieve 10,000 rpm increased from the previous 1.8 slm to 3 slm. The difference can be attributed to the viscous drag from the 7.4 µm gap in the areas of the sealing region and spiral-groove region.

The lack of fluctuations in the flow rate versus speed curve (Figure 4.10) is verification that no large particles were trapped in the small pump gap during the pump plumbing layer assembly process. In some cases, satellite photoresist droplets from the spray coating process would deposit on the sealing surface or groove surface.

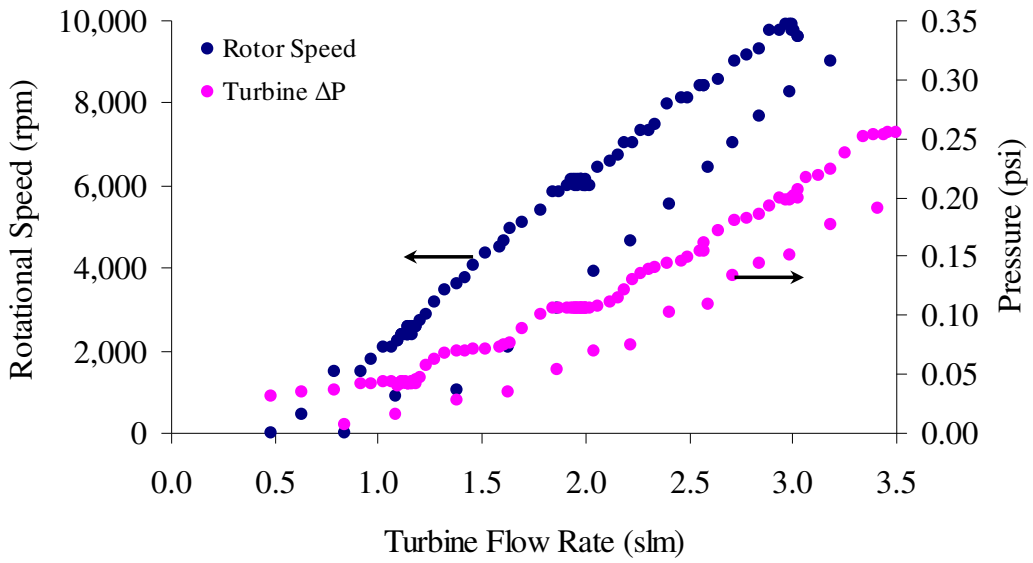

Figure 4.10. Turbine performance curve without liquid using planar-contact bearing V.2 and packaged with pump plumbing layer.

These droplets could cause the rotor to stick to the plumbing layer, which in turn could cause the rotor to exhibit large fluctuations and randomness in the characteristic curve or simply not spin. Devices that exhibited this behavior were soaked in an Acetone ultrasonic bath, re-assembled, and characterized again.

A high-speed test was performed on a device packaged without the pump plumbing layer to investigate the maximum speed of the turbine/bearing system. The flow rate through the turbine is limited by the turbine fluidic resistance and the pressure drop from the turbine inlet upstream of the diffuser vanes and the turbine outlet at ambient. The maximum flow rate with the current experimental apparatus was recorded at 13 slm with an estimated turbine pressure drop of 2 psi (assumed ½ of the pressure drops through the static diffuser vanes and the other ½ drops through turbine blades). At this flow rate the radial in-flow air turbine and planar-contact bearing V.2 were able to achieve rotational speeds greater than 85,000 rpm (Figure 4.11). It is logical to assume that higher rotational speeds are capable if the flow rate of the apparatus can be increased and the normal load exerted on the rotor decreased.

The speed is expected to increase further with flow rate, but will eventually be limited when the normal force on the rotor becomes too large. Two solutions to increase the flow through the turbine are to increase the turbine blade height and decrease the fluidic resistance in the inlet line. The coupling between the driving turbine flow and the rotor normal force, however, will eventually limit the speed of the rotor. As the normal force increases so does the power loss to the bearings. It is crucial to decrease the coupling between the turbine rotor speed and the rotor normal force to enable applications that require higher tip speeds.

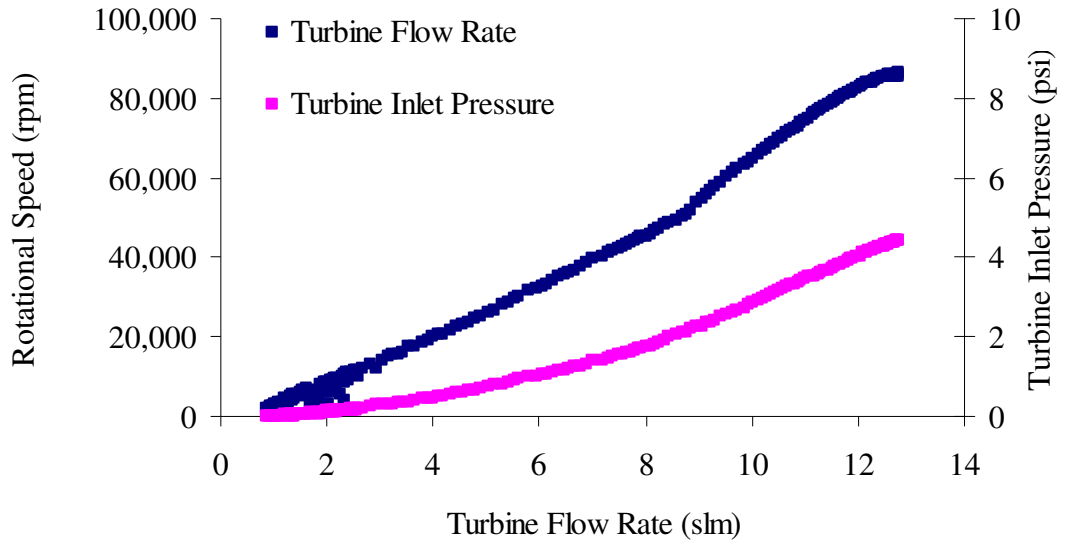

Figure 4.11. Demonstration of high-speed operation with the planar-contact V.2 bearing and the radial in-flow air turbine.

4.4 Pump Characterization

The pump is characterized by the differential pressure rise ($\Delta P = P_{OUT} - P_{IN}$) across the pump area (Figure 4.1), the liquid flow rate, and the rotational speed of the rotor. The flow rate is dictated by the pressure drop between the pressure vessel or syringe pump and the pump outlet and the fluidic resistances of the inlet line, pump, and outlet line. Control of the flow rate is via a manual flow valve placed in line with the pump inlet and the pressure vessel or directly by the syringe pump (Figure 4.7). The rotational rate is controlled by the flow through the turbine and dictated by the power balance of the system.

When the pump is off or not rotating above a critical speed, the flow is purely pressure driven and the ΔP across the pump is negative, i.e. energy from the fluid is lost

and the pump acts as a variable fluidic resistor. When the pump is rotating above a critical speed, the ΔP across the pump is positive, i.e. the pump adds energy to the fluid.

Operation of the turbopump was begun using two different start-up procedures. The rotor can be started with or without liquid in the pump area. In the first case, the rotor is spun using a pre-determined turbine flow rate and pressure such that rotation is maintained when liquid is introduced. After the introduction of the liquid, the rotational speed will decrease to a new operating point that balances viscous drag. This procedure eliminates the large stiction created when the liquid is introduced before the rotor is started. On the other hand, large fluctuations will occur, potentially causing a drastic change in the power balance. This could lead to the turbine stalling or the microball bearings jamming.

In the second case, the thrust balance plenum is pressurized and the liquid forced through the pump before the turbine flow is initiated to spin the rotor (Figure 4.12). The thrust balance plenum pressure is kept larger than the pump outlet pressure and within 1 psi ($0 \text{ psi} < P_{THRUST} - P_{OUT} < 1 \text{ psi}$) for a device gap of 15 μm or 2 psi for a device gap of 7.4 μm to ensure proper sealing between the liquid and the nitrogen. Once the liquid flow rate and pressure settle through the pump region, the turbine flow rate is increased to permit the rotor to spin.

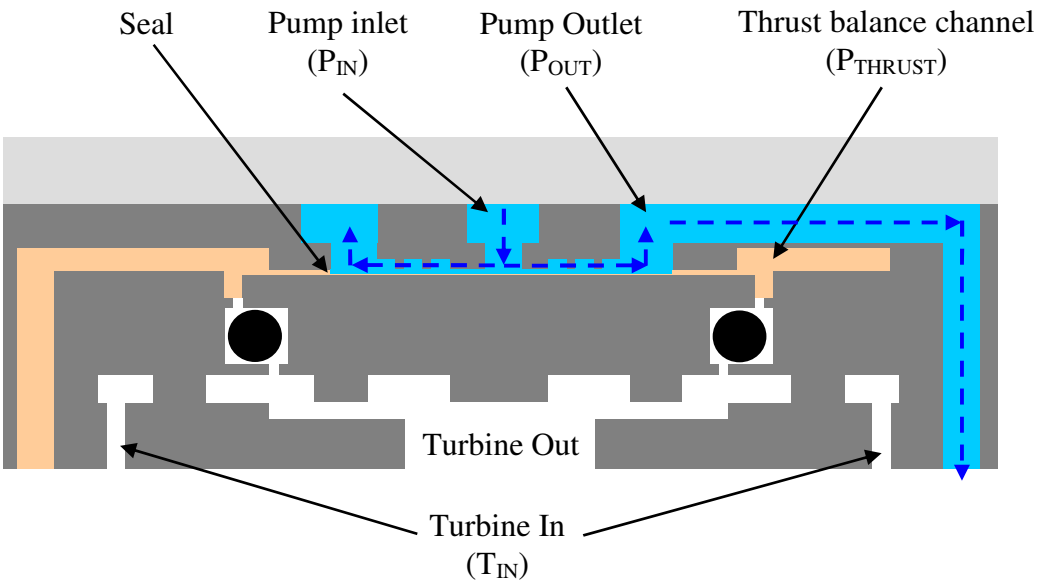

Figure 4.12. Illustration demonstrating the pump priming procedure. The thrust balance channel pressure (tan) is elevated above the liquid (blue) pressure at the pump outlet to seal.

4.4.1 Start-up Behavior

The start-up behavior was characterized using Device 1 having an estimated maximum 7.4 µm pump gap. The turbopump was first started with the rotor spinning before introducing the liquid. The flow rate of the turbine was set to 4.5 slm. At this turbine flow rate, the rotor speed stabilized around 21,000 rpm and, subsequently, the liquid pressure was increased to allow water to flow into the pump inlet. This is shown in Figure 4.13 before time t_1.

When liquid entered the pump at t_1 the rotor seized. When the turbine flow was increased to 5.7 slm, thereby increasing the power available from the turbine, the rotor spun for a few seconds (observed between times t_2 and t_3 in Figure 4.13). During the few seconds of operation the pump inlet pressure began to decrease, while the pressure at the

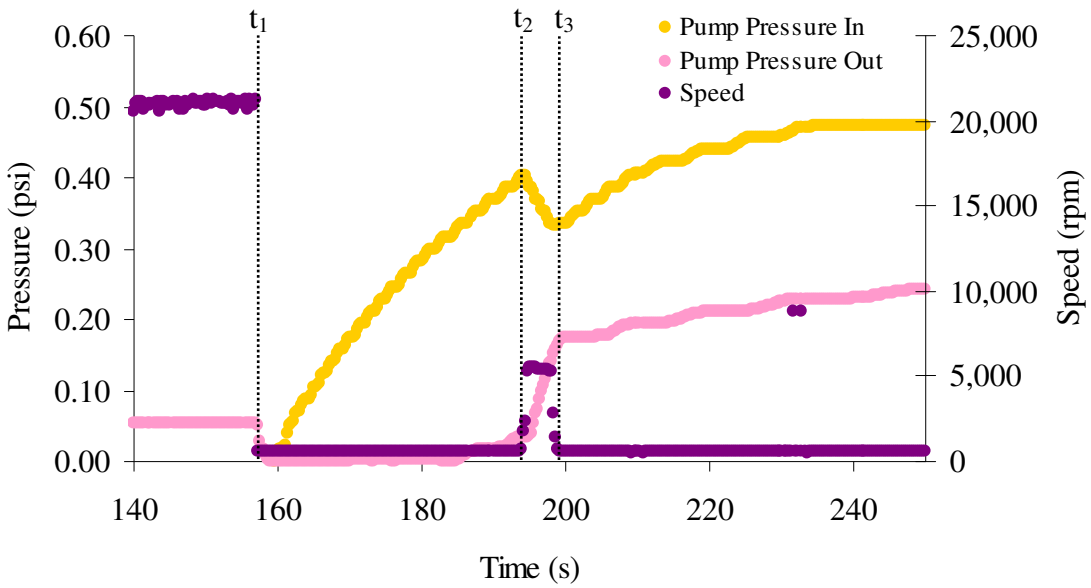

Figure 4.13. Turbopump results when liquid is introduced while rotor is spinning.

pump outlet increased. This demonstrates the spiral-groove pump is beginning to increase the differential pressure. It is logical that the differential pressure rise would have continued to increase above zero (i.e. $P_{OUT} > P_{IN}$) if the rotor spun for a longer period of time.

One potential explanation of the rotor seizing is shock to the bearing system causing too sudden of a change in the power balance when the liquid first comes into contact with the rotor and proceeds to fill the pump area. A second possibility is that the net normal force on the rotor switches direction due to adhesion forces associated with the water coming into contact with the rotor. These forces are primarily meniscus forces and viscous forces [62]. The rotor will no longer ride on the planar-contact raceway If the normal force direction shifts. Instead, the rotor would ride on the spiral-grooves and sealing surface. This would drastically increase the viscous drag or sliding friction and stop the rotor from spinning.

In the next experiment, the same assembled turbopump was tested with two key changes. First, in hopes that the rotor axial position would be resting on the planar-contact bearing raceway, the liquid was introduced before spinning to prime the pump area and let the liquid pressure within the pump settle. This eliminates the sudden change in the power balance and potential shock to the bearing. Second, the turbine flow rate was set to 8 slm (rather than 4.5 slm from the previous experiment) increasing the torque in order to overcome stiction.

To prime the pump area, the thrust balance pressure was increased to 0.4 psi and the liquid introduced with a flow rate approximately equal to 45 mL/hour. This is shown in Figure 4.14 between the times t_1 and t_2. During this period, the liquid pressure at the pump inlet and outlet increases until a pressure differential is met that is dictated by the fluidic resistances through the pump. At this time, the differential pressure is negative since the flowrate is produced by the total fluidic resistance and the pressure drop from the pressure vessel to ambient.

Once the pump inlet pressure and outlet pressure settled, close to 0.5 psi at the pump inlet, the turbine flow was increased to 8 slm, whereupon the rotor began to spin at approximately 4,000 rpm (shown between the times t_2 and t_3 in Figure 4.14). During this time, the pump inlet pressure decreased and the pump outlet pressure increased. However, the differential pressure rise across the pump area was still negative, meaning the flow was still pressure driven rather than pump driven. After time t_3, the differential pressure rise settles to approximately -0.3 psi.

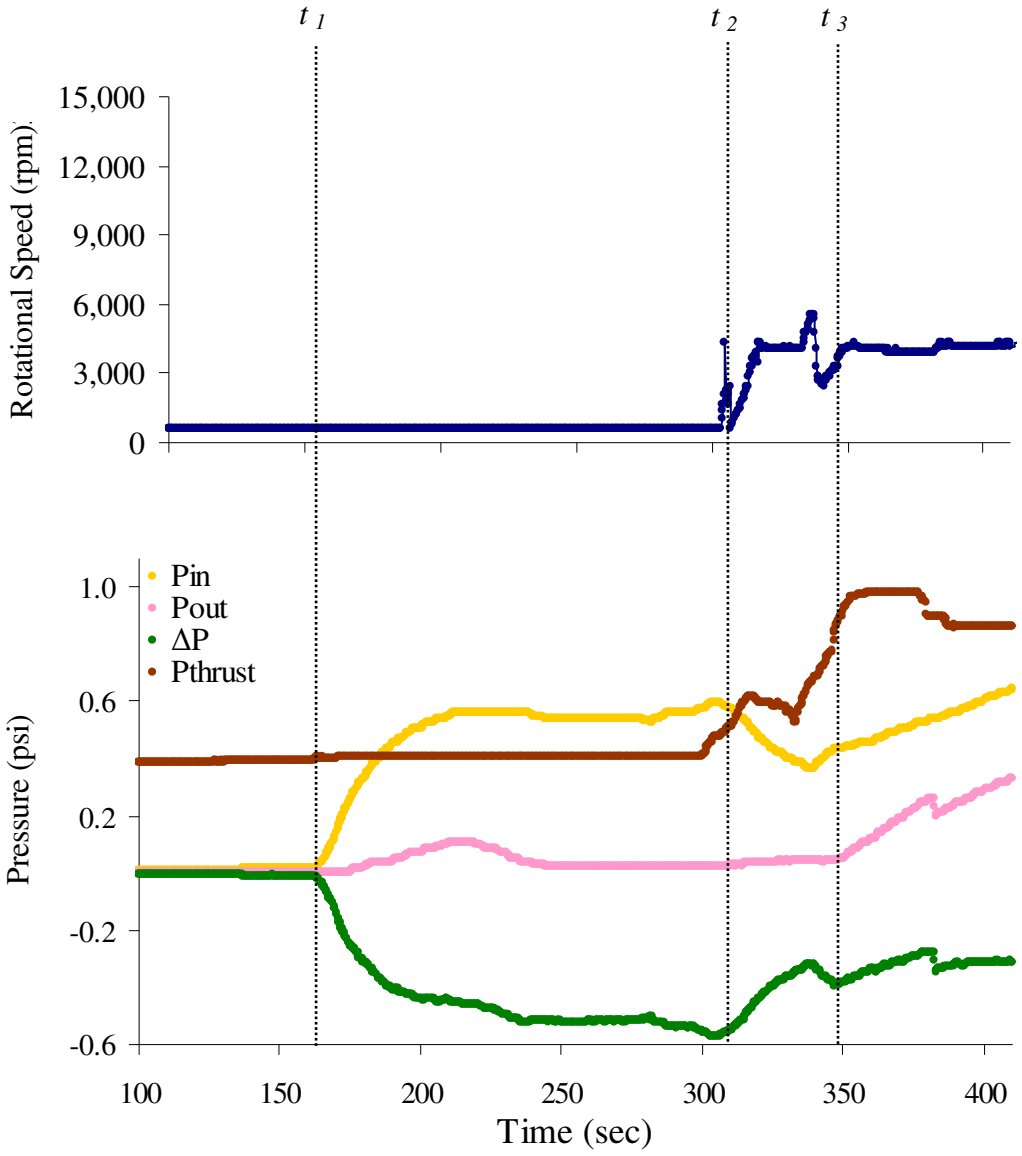

Figure 4.14. Start up behavior for the turbopump with a turbine flow rate set to 8 slm and liquid flow rate in the range of 45 mL/hour and 60 mL/hour.

4.4.2 Device 1 Characterization

Figure 4.15 is a continuation from Figure 4.14 and constitutes the first demonstration of pumping using Device 1. The rotational speed shows a sudden increase from 4,500 rpm to 12,000 rpm at time t_4. Between the times t_4 and t_5 the differential

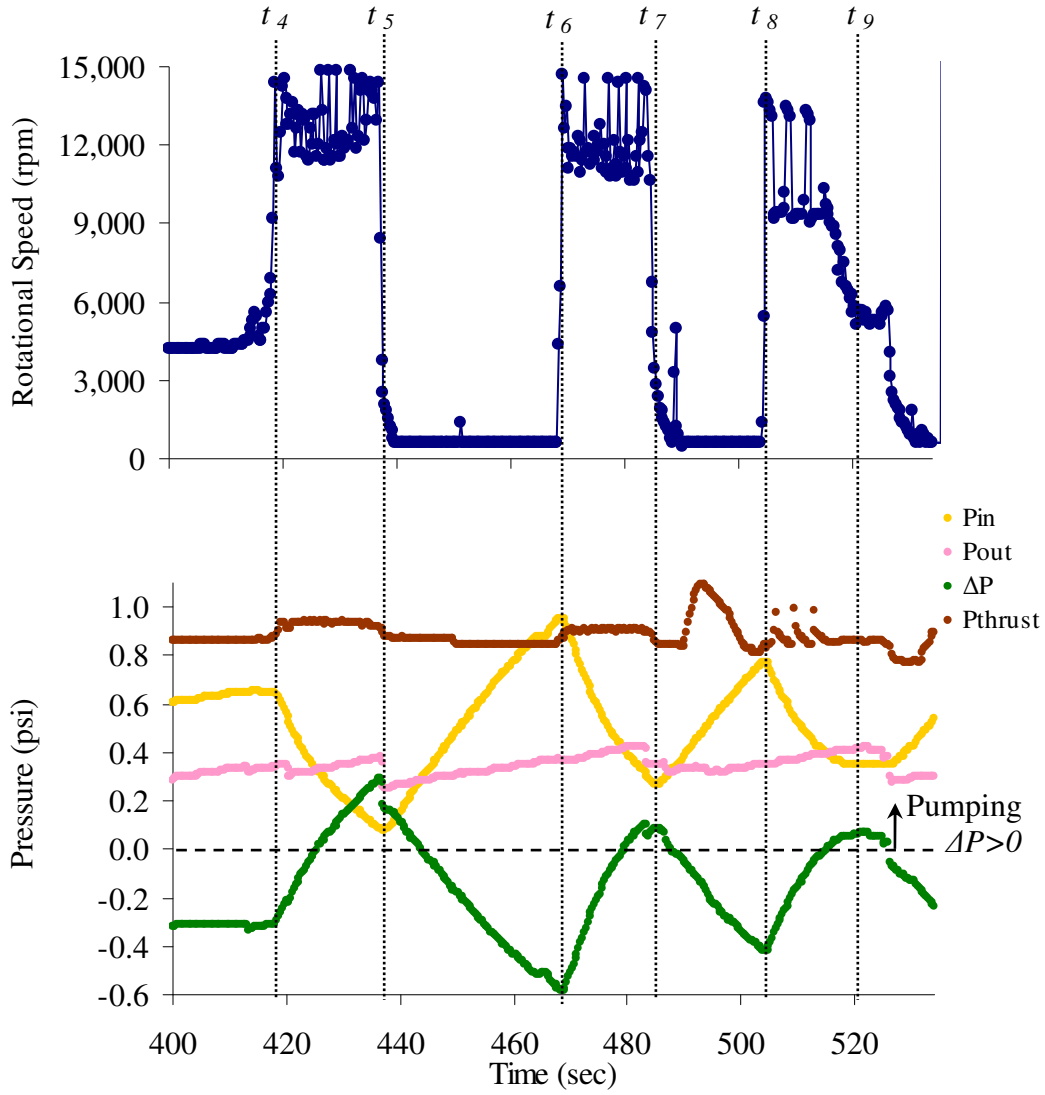

Figure 4.15. Turbopump demonstration with a turbine flow rate of 8slm and liquid flow rate ranging from 45 mL/hour to 60 mL/hour.

pressure rise across the pump climbed to +0.3 psi, meaning the pump is increasing the energy of the water as it passes through the turbopump. After approximately 20 seconds the turbopump seizes. The turbopump then operates on and off with the differential pressure climbing to +0.1 psi between times t_6 and t_7, and to +0.05 psi between the times t_8 and t_9.

The on and off behavior is attributed to power swings from the changing pressure forces on the pump side of the rotor and adhesion forces between the rotor and the pump structures. The pressure forces are directly correlated to the normal force on the rotor, and therefore, the power balance of the system. As the device begins to pump, the pressure at the pump inlet is observed to decrease, while all other pressures remain relatively constant (Figure 4.15). This decreases the overall pressure force exerted on the rotor. Figure 4.16 shows the calculated normal force exerted on the rotor due to the pressure distribution in the liquid and nitrogen during the operation of the turbopump while subtracting the pressure force exerted by the turbine on the opposite side. The pressure drop between the pressure ports is assumed to be linear and the normal force is approximated by half the pressure times the area integral.

The adhesion force (meniscus force) is an attractive force between the pump plumbing layer and the rotor due to the small gap and the liquid. It is considered to be the dominant adhesion force and can be estimated using the following equation [62]:

$$F_m = \frac{A_m \sigma_{water} \left(\cos\theta_1 + \cos\theta_2\right)}{h_2} \qquad \text{Equation 4.1,}$$

where A_m is the meniscus area, σ_{water} is the surface tension for water (73 dynes/cm), and θ_1 and θ_2 are the contact angles between the pump plumbing layer and the rotor disc respectively. The meniscus force, F_m, is estimated to be 125 mN (dotted line in Figure 4.16). This assumes a contacting angle of 45˚ for silicon, half the spiral-groove region having a gap, h_2, of 7.4 μm, and the other half of the spiral-groove region having a gap 27.5 μm plus 7.4μm.

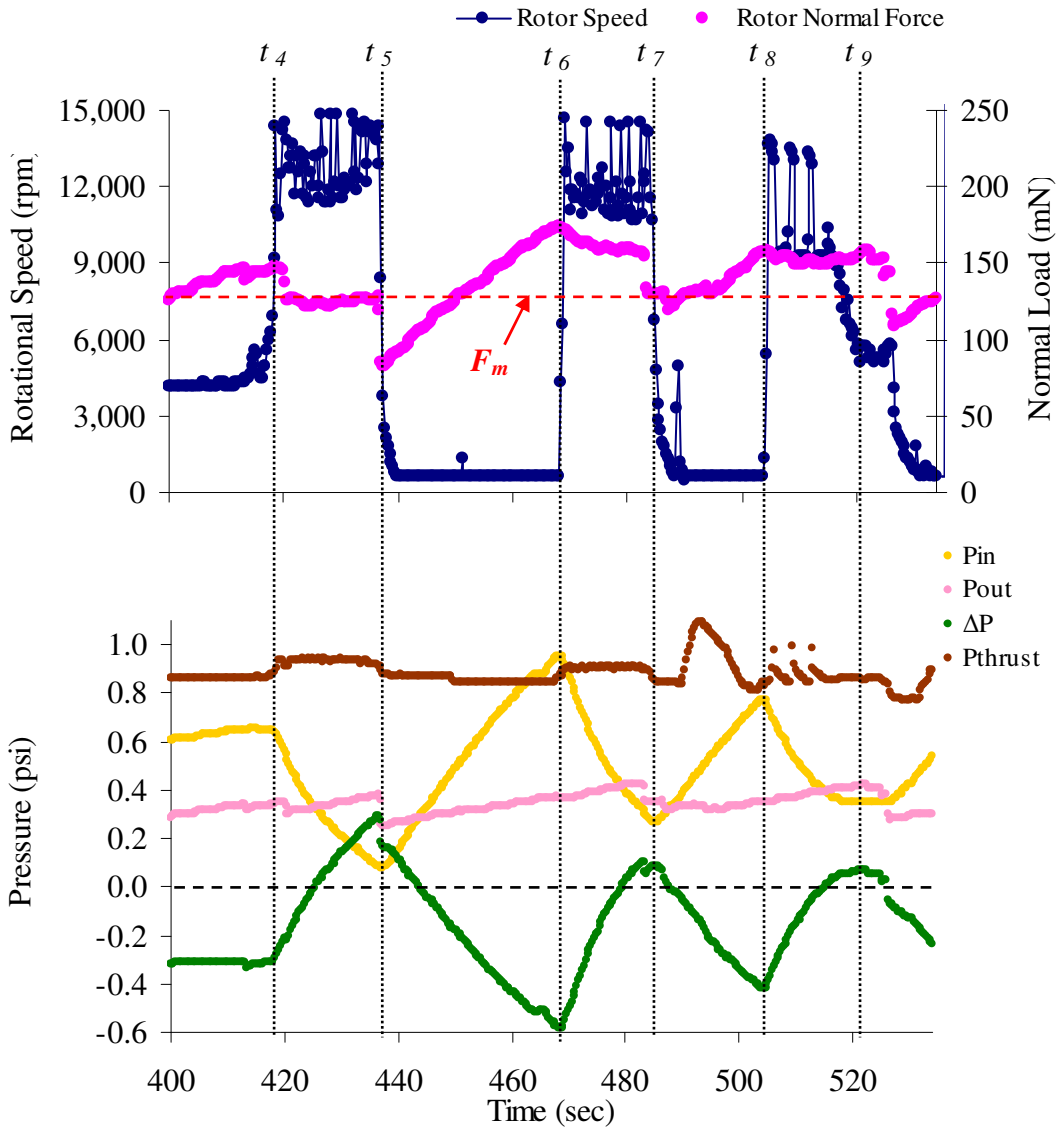

Figure 4.16. Re-print of the plot shown in Figure 4.15, but with the normal force calculation added in.

While spinning, the pump inlet pressure decreases at a more rapid rate than the pump outlet pressure causing the normal force to also decrease slightly, as seen between the times t_4 and t_5, t_6 and t_7, and t_8 and t_9. A perturbation such as a bubble passing

through the pump region decreases the pressure on the pump side and, therefore, decreases the normal force keeping the rotor on the raceway surface. Once the normal force dips below the meniscus force, the rotor will be pulled towards the pump plumbing layer and the gap will decrease. The problem is exacerbated by the increasing viscous drag as the gap shrinks, increasing the viscous loss with gap and changing the power balance of the system (Figure 4.17). The normal force in Figure 4.16 is observed to drop just before the rotor stalls at the times t_5, t_7, and t_9.

After the rotor stops spinning, the pressure at the inlet rises, allowing the normal force to increase again. After a sufficiently large normal force is reached, the meniscus force (much smaller gap than 7.4 μm since the rotor is snapped into the pump plumbing layer) and stiction can be overcome and the rotor can snap back down and contact the

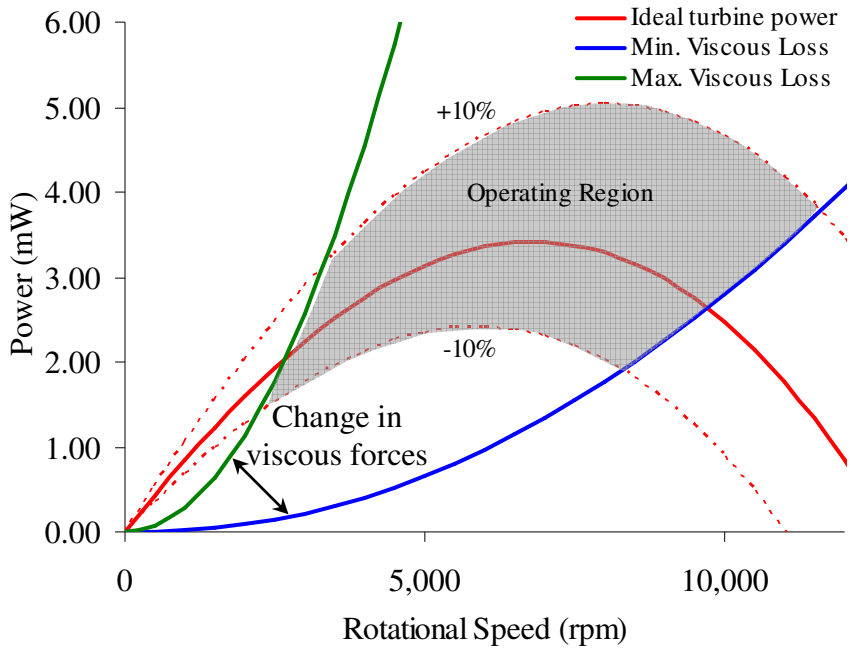

Figure 4.17. Power curves for the turbine power with ±10% flow deviation with bearing friction taken into account and the power loss due to viscous forces on the pump side for a maximum and minimum wetted surface area.

raceway. At this time the rotor is able to spin and the device able to pump again. This cycle is then repeated.

Control of the normal force and maintaining it above that required by adhesion forces may be critical to the continuous operation of turbopumps with a small pump gap. Elevating the normal force in the direction of the raceway will allow the rotor to remain in contact with the raceway and will allow operation to be continuous. The control of the normal force, however, is complex due to the coupling with the turbine and the pump operation.

4.4.3 Device 2 Characterization

Continuous pump operation was achieved using Device 2. The 2x increase in the pump gap of Device 2 allows the adhesion forces to be reduced by half the value observed for Device 1. In addition to reduced adhesion forces, the pressure force on the rotor was raised by closing the valve at the pump outlet along with raising the valve to a different height. This allows the pressure at the inlet to also be increased, while maintaining similar pressure rise throughout the pump. Together, these changes allowed continuous operation of the turbopump for all flow rates and pressure ranges.

A syringe pump was used in this experiment to control the flow rate through the pump device accurately. At each flow rate, the pressure rise through the pump is allowed to settle (Figure 4.18) and the data is taken for three different rotor speeds (Figure 4.19). If 20% shrinkage of the photoresist is assumed during bonding between the rotor and the pump plumbing layer then the resulting gap is 12 μm (from the estimated 15 μm original gap). The analytic pump curves are calculated using Equation 3.8 for the 12 μm gap

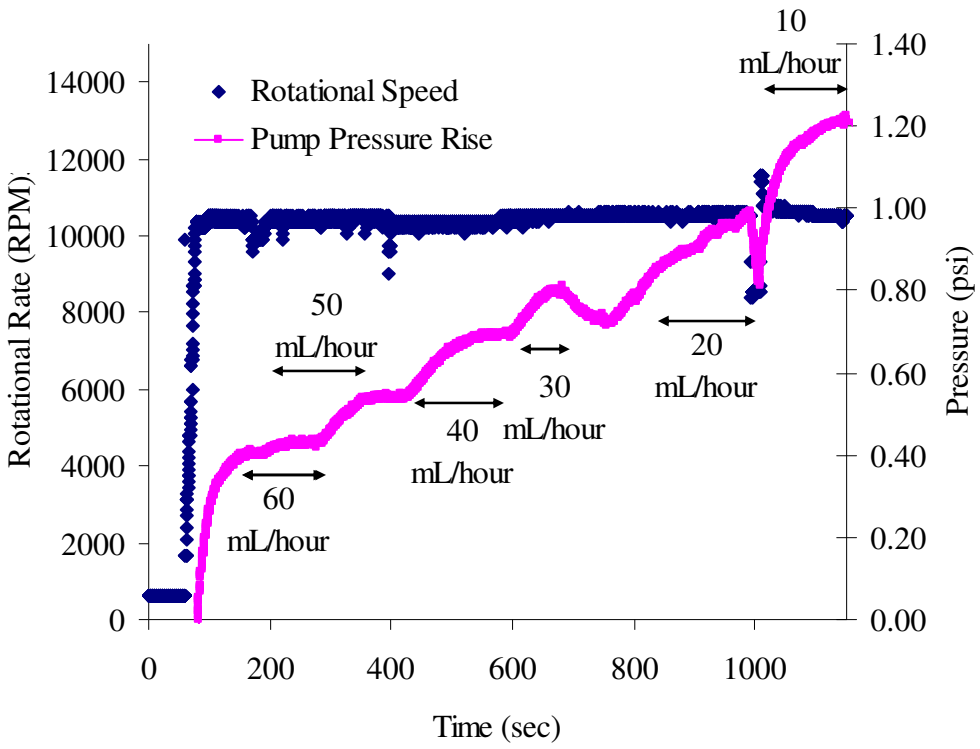

Figure 4.18. Demonstration of continuous pumping at 10,000 rpm and flow rate range from 10 to 60 mL/hour.

and are plotted with the experimental data in Figure 4.19 and show good agreement with the experimental data.

Another discrepancy in the collected data is in the measurement of the pressure rise through the pump. The pump outlet was kept elevated during the experiments and had an average value of 0.55 psi. When the pressure rise through the pump goes above this value, the pressure at the pump inlet is negative. The linear range for the pressure transducers used in these experiments is from 0-1 psi. Therefore, the data points collected for pressure rises above 0.55 psi have an increasing error bar.

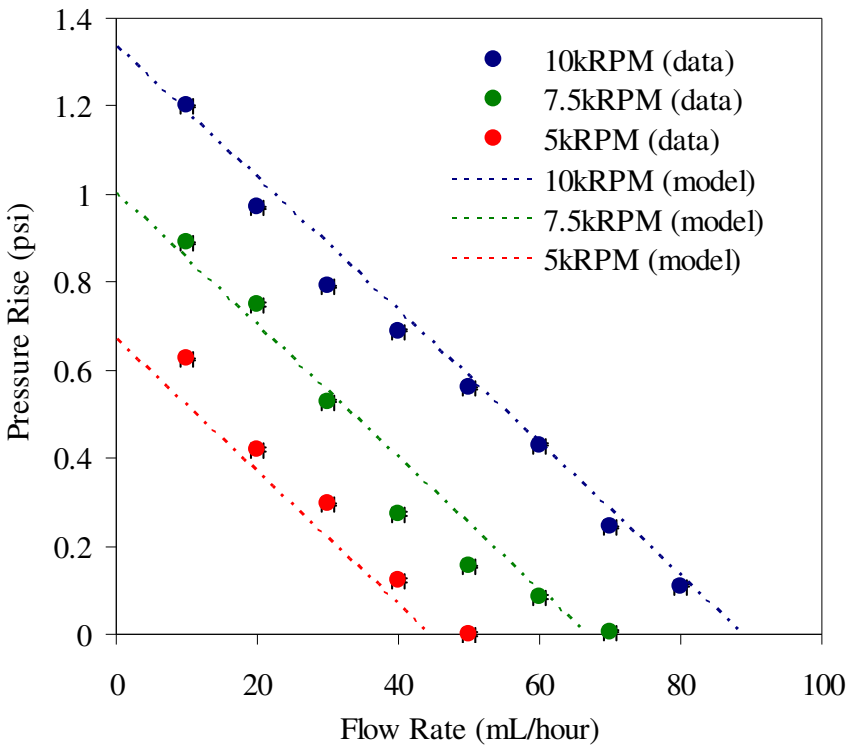

Figure 4.19. Turbopump characterization and comparison to analytical with an estimated gap of 12 μm.

4.5 Summary

An experimental platform was developed to characterize the microturbine, the microball bearings, and turbopump performance. A turbopump was actualized with a radial in-flow air turbine, a modified planar-contact race design, and spiral-groove pump structures. The microturbine was characterized after initial rotor fabrication as well as after being assembled into a turbopump. This demonstrates that the assembly method to achieve a small pump gap does not prevent turbine operation. The turbine performance was observed to improve with the modified planar-contact bearing design and increased blade height when compared with a previous microturbine that was used to study bearing

friction. Furthermore, high speed operation of the turbine and microball bearing was demonstrated with rotational speeds greater than 85,000 rpm.

Two turbopumps having differing pump gaps were investigated. For small gaps, the adhesion force becomes dominant and requires control of the pressure forces on the pump side to achieve continuous operation. Alterations to the design of the turbopump to enable more control on the pressure forces can be realized to investigate the operation with small pump gaps.

Continuous turbopump operation was achieved reducing the adhesion force via an increased pump gap in addition to elevating the pressure forces across the rotor. Experimental pump curves were developed for rotational speeds between 5,000 and 10,000 rpm, which show good agreement with analytical curves assuming 20% photoresist shrinkage during bonding. Pressures between 0 and 1.2 psi were obtained for flow rates ranging from 10 to 80 mL/hour, within the range for portable power applications.

The design of the turbopump and the experimental platform developed allow many configurations of viscous pump geometries to be utilized on the pump plumbing layer without a new rotor. This enables complete characterization of turbopumps and assessment and development of optimized geometries. The first pumping action using a turbopump supported by microball bearings was demonstrated, highlighting the potential of this technology if applied to liquid pumping.

5 Conclusions and Future Work

5.1 Summary

A microfabricated turbopump was designed, fabricated, and demonstrated for applications in liquid fuel-based power generation. The turbopump is comprised of a spiral-groove viscous pump mechanism driven by a radial in-flow air turbine and supported using a novel microball bearing mechanism. Experimental results were obtained for a device with a 15 μm gap, and a 4.5 mm diameter pumping region. A pressure differential rise up to 1.2 psi was demonstrated across the pump region with a rotor speed of 10,000 rpm and liquid flow rate ranging between 10 and 80 mL/hour. The turbine operation, without liquid in the pump region, was thoroughly characterized. Rotational speeds reached greater than 85,000 rpm with minimal raceway wear; the highest speeds ever demonstrated using a MEMS contact bearing mechanism. The flow rates and pressure ranges achieved demonstrate the possibility of the MEMS turbopump to deliver fuel in portable power applications. Table 5.1 summarizes the major technologies developed during this study.

A rotary pump based on the developed turbopump configuration was selected for three key reasons: 1) the pumping action is purely mechanical; 2) batch silicon microfabrication techniques can be used in the designs; and 3) the pump mechanism can be scaled to meet a broad range of flow rate and pressure requirements. Furthermore, a viscous-type rotary pump was selected because the working principle allows it to be designed with high compactness since viscous forces begin to dominate at the micro-scale.

Technology Developed	Critical Knowledge	Fabrication	Reference
1. Point-Contact Bearing	• 1st encapsulated microball bearing demonstrated • 18,000 rpm demonstrated	• 2 wafer levels • 4 optical masks • 25 Process Steps • 1 bonding layer	[16, 17]
2. Tangential Air Turbine w/Point-Contact Bearing	• 1st integrated motor • > 37,000 rpm demonstrated • >24hr operation demonstrated • Exhibited high wear	• 2 wafer levels • 5 optical masks • 1 bonding layer • 25 Process Steps	[18]
3. Centrifugal pump implemented using technology 1 & 2	• 1st turbopump fabricated • Determined axisymmetric design requirement	• 3 wafer levels • 9 optical masks • 2 bonding layer • 45 Process Steps	
4. Planar-Contact Bearing using Radial In-Flow Turbine	• Low-wear demonstrated • Spin-down testing • > 85,000 rpm demonstrated	• 3 wafer levels • 10 optical masks • 2 bonding layer • 45 Process Steps	[19, 46]
5. Viscous pump implemented using technology 4	• 1st turbopump demo w/microball bearing • 10-80 mL/hour and 0-1.2 psi	• 5 wafer levels • 15 optical masks • 3 bonding layer • 80 Process Steps	[47]

Table 5.1. Timeline of technology development

The final turbopump comprised of five wafer levels fabricated using over 80 processing steps and 15 optical masks. The assembly of the five-level die stack consisted of three different bonding methods all utilizing a novel microball alignment technique. Successful fabrication required precision depth control using DRIE with careful etch depth measurements to define the critical gap required for the viscous pumping mechanism. Assembly of the rotors using a AuSn eutectic bond enabled investigation of

the raceway after rotor characterization. This was critical in the initial phase of the microball raceway development. Two different raceway designs were investigated before the final modified planar-contact raceway was chosen for the turbopump.

The novel microball bearing technology developed to support the rotors was a key to the success of the turbopump and microturbine tribology platforms. A fabrication process that includes silicon micromachining and bonding techniques was conceived to develop an encapsulated microball bearing and subsequently a rotor that is supported for both axial and radial loads.

The point-contact bearing design was the first ever demonstration of a rotor completely supported by a microfabricated ball bearing technology. High speed (>37,000 rpm) and long term (> 1day at 20,000 rpm) testing using the tangential air turbine proved the viability of the microball bearing mechanism for use in MEMS rotary applications. However, the point-contact bearing exhibited a large amount of wear, on the order of tens of microns, so an alternative design was developed.

The planar-contact bearing raceway was designed to reduce raceway wear. In this design, the microball was made to contact a flat raceway on the thrust bearing surface rather than a sharp corner. This reduced the compressive stress when compared to the point-contact design using Hertzian contact mechanics. The planar-contact design exhibited minimal wearing on the thrust surface, but still a large amount of wearing on the radial load surface occurring at the bond interface. Therefore, a modified planar-contact design, in which the bond line was moved away from the wear track, was developed for the final turbopump. Using this modified design, the microball contacts

only a flat surface, on both the radial and thrust carrying surfaces. This led to negligible raceway wear and debris generation.

A novel alignment technique was devised to align layers at the die level for bonding. This technique was pivotal in the assembly of all devices during the development of the turbopump. Microballs were used not only in the bearing mechanism but also for the dual purpose of aligning two layers together. This technique enables alignment accuracies better than 5 μm, which are not possible using conventional bond alignment tools. In addition, this technique can be extended to other applications by adding alignment trench patterns to the fabrication process.

An air turbine was incorporated as the drive mechanism for the pump and was used to develop platforms to study the microball bearings. The air turbine is a high power drive mechanism using the house nitrogen source. This made for simple integration to evaluate different bearing geometries and demonstrate the viscous pump. Alternatively, the nitrogen source could be replaced by the energetic exhaust of a heat engine to which the pump is delivering fuel. This exchange of energy sources may enable recuperation of the wasted exhaust stream energy.

Two air turbine designs were investigated. Due to the axisymmetric design and the high-speed capability with low driving pressures, the final turbopump incorporated the radial in-flow air turbine. This turbine was first integrated into a tribology testing platform with a planar-contact bearing design. This platform was used to study the wear and friction of the planar-contact bearing design. Spin-down testing enabled development of empirical models that relate the normal load and speed to the amount of friction lost to the bearing mechanism. Wear at the micron level, which was an order of

magnitude better than the point-contact bearing design, was observed. High-speed, up to 85,000 rpm, was demonstrated using the modified planar-contact bearing in which the bond interface was moved out of the microball wear track.

The next generation micropump is envisioned to operate using a rotary micromotor. This will replace the microturbine for applications without an exhaust stream or other source of pressurized gas. In this dissertation a working foundation for the microball bearing technology has been established using the air turbine drive mechanism. This information can be directly used to design a rotary micromotor with the required rotational speed range and torque.

The design and development of robust methods for encapsulated microball bearings, microturbines, and pumping structures have culminated in the successful demonstration of a micro-turbopump. Not only do the components developed allow for liquid pumping, but alternative applications are envisioned. The microball bearing platform developed and characterized enables other MEMS applications to be effectively designed and incorporated into numerous rotary applications. Lastly, the bearing mechanism and pumping technology can be thoroughly investigated and optimized using the platforms described.

5.2 Summary of Accomplishments

The first silicon turbopump with a microball bearing support mechanism was demonstrated for fuel delivery applications. Before demonstration of the pump, robust rotary microball bearing and drive mechanisms had to be developed and demonstrated. What follows here is a listing of the key contributions of this dissertation:

Design, fabrication and demonstration of a spiral-groove turbopump supported by a microball bearing.

- Developed the design and fabrication process for a spiral-groove turbopump that integrated the viscous-type pump onto a turbomachinery platform using a microball bearing support mechanism.
- Created a platform that uses interchangeable pumping and rotor layers enabling a host of pump, turbine, and bearing designs without necessitating the time-intensive and costly fabrication of all components.
- Developed a comprehensive experimental apparatus to characterize a microfabricated turbopump as well as the turbine and bearing support mechanisms.
- Produced designs and procedures to operate viscous-type and centrifugal-type turbopumps that address both sealing and normal force control when using the passive bearing mechanism.
- Demonstrated a differential pressure rise up to +1.2 psi across the pumping region for a flow rate ranging between 10 and 80 mL/hour.

Encapsulated microball bearing platform. The most influential contribution made is the development of the encapsulated microball bearing for the support of rotary actuation mechanisms. An encapsulation process during the fabrication enables real world applications of the microball bearing technology, which are currently being utilized within the MEMS Sensors and Actuators Laboratory (MSAL) at the University of

Maryland. Three microball bearing configurations were investigated along with two different turbine drive mechanisms.

- Developed a base fabrication sequence for microball bearing encapsulation and rotor release that has been successfully implemented for over 20 wafer builds and is now the standard in the study of the microball bearing mechanism in MSAL.
- Designed a fabrication process to include an impermanent bonding scheme for the rotor assembly and to enable investigation of wear and reliability without destruction of the raceway.
- Produced designs, fabrication methods, and performed a comprehensive study of two microball bearing raceways. This enabled the design of planar-contact bearing V.2 reducing the wear created (less than 2μm) and the debris generated.
- Developed platforms to characterize the performance of microball bearings and microturbines and to study the wear and friction associated with their operation. Provided insight into the wear behavior and explanations based on Hertzian contact mechanics.
- Demonstrated the first encapsulated microball bearing capability by performing a long-term test (greater than 1 day operation) and high-speed operation (greater than 37,000 rpm) using the point-contact bearing design.
- Demonstrated high-speed (greater than 85,000 rpm) operation of the planar-contact bearing and radial in-flow turbine.

- Performed spin-down measurements and extracted empirical relationships between bearing friction and rotor speed and load.

Novel device alignment technique. A novel alignment technique using the microballs and alignment pits was developed to facilitate die level bonding. This method can be utilized in many applications and is not limited to the fabrication of the microball bearing design or the silicon turbopump. Alignments less than 5 μm can now be routinely achieved even at the die level without the need for specialized equipment.

5.3 Future Work

The following sections will mention future work and technological improvements for future investigations based on the concepts developed and findings detailed in this dissertation.

5.3.1 Microball Bearings

The microball bearing designs developed within this work were focused on enabling a turbopump rather than developing them for a broader range of applications like, micromotors, microgenerators, high pressure and flow pumping, and other rotary-based applications. Future work needs to focus on the more fundamental phenomenon related to the materials used in the microball bearing. A more complete understanding of the wear mechanisms, lifetime, and material compatibility will ultimately extend the use of the current microball bearing in which reliability and speed are critical.

Contact mechanic models that include adhesion forces, surface roughness, lubricating films, atomic interaction, and so forth need to be developed using the wealth of knowledge that has been generated for macroscopic ball bearings. Models like these will lead to a better understanding of the observed wear phenomenon and friction. These will be critical to the engineering field during the implementation of the devices in real-world applications where lifetime and performance are critical.

The wear evolution should be studied to understand wear-in (i.e. run-in or burn-in). At the initial phase of start-up the wear will drop off as the raceway is worn into a shape that minimizes the compressive stress and surface area. Experiments in which bearings are operated for varied revolutions and speeds should be performed and the raceways should be inspected. The wear is also believed to be a function of the speed and load. These parameters and their effects on wear-in should be investigated. The results of such a wear-in study will enable proper design changes in either the raceway geometry or the operation to minimize the wear (and debris generated) and maximize the lifetime of the bearing system.

Lubrication can reduce the amount of wear and increase the rotational speed of the microball bearing. Lubrication using JP-8 diesel fuel, the envisioned pumping fluid, was briefly demonstrated in the point-contact bearing design [16]. Drops of fuel were placed into the bearing raceway and the rotor was rotated manually to ensure even coating of the raceway and microballs. A drastic increase in the rotational speed when there is a liquid lubricant in the microball bearing was observed (Figure 5.1). One observation made during the experiment was the rapid evaporation of the JP-8. The bearing seized after rotating for one minute and required replenishing of the lubrication.

Incorporating liquid flow channels (e.g. leakage from the pump inlet) to supply lubricant at a rate matching the evaporation rate may be a significant challenge.

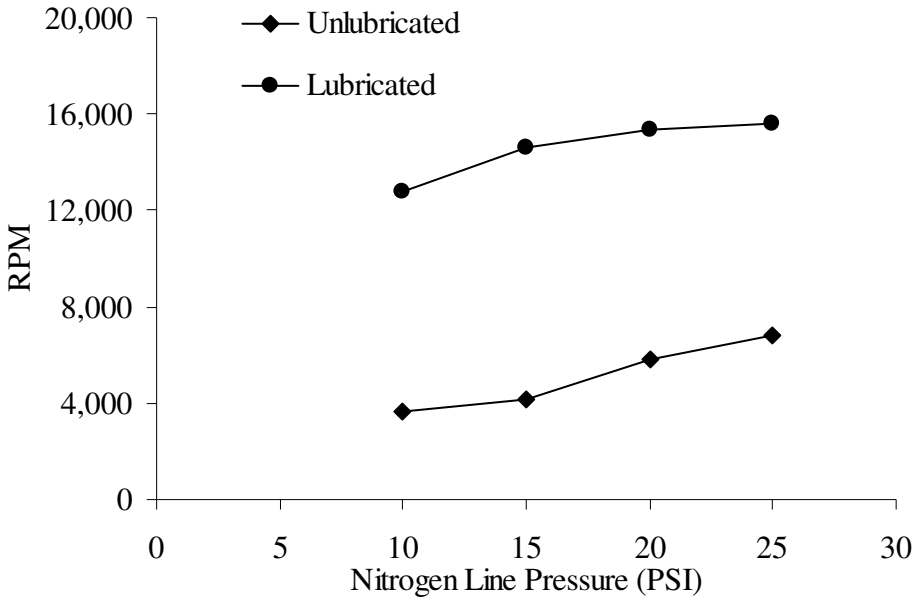

Figure 5.1. Rotational speed plotted for increasing line pressure before and after JP-8 droplets were introduced into the microball bearing race.

Optimized materials and their integration into the fabrication of the encapsulated microball bearing will be a critical step to achieving low wear and high-speed bearing mechanisms for applications such as power generation and turbopumps. *Ghalichechian* [63] implemented a simple sputtered silicon carbide coating on the rotary micromotor raceway demonstrating the first use of solid film lubricant in microball bearings. Investigation of the wear and friction of this coating as well Ultrananocrystalline diamond has begun by *McCarthy* [64] and *Hanrahan* [49] using a linear tribology setup. However, due to the measurement system implemented, their setup is limited to low

speeds. Integration of such hard coatings can easily be done in the fabrication of the encapsulated microball bearing and radial in-flow air turbine platform developed. This will enable high speed and load resolution critical in the assessment and characterization of the material systems.

In addition to raceway material investigations, different microball materials, such as SiN ceramic microballs, should be investigated in conjunction with the solid films on the raceway surface. Macroscopic ball bearings match properties, like hardness of the materials, between the raceway and the ball to maximize bearing lifetime.

Lastly, to increase the rotational rates, macroscopic ball bearings incorporate ball cages, or retainer rings. During operation of the bearings in a full compliment manner, the balls slide against one another causing a large shearing stress and friction. The material of the retainer ring, such as Phenolic-based, provides better sliding friction characteristics than stainless steel to stainless steel. Methods of integrating the retainer ring may include purchasing (or manufacturing) the retainer ring and microball sets to "drop-in" during fabrication or fabricating the retainer ring and raceway together. Although both methods provide a significant challenge, the pay off could be great. A balance between high-speed operation and the load and wear behavior will have to be made as well as an optimized material choice between the microball and the retainer ring material.

5.3.2 Standalone Bearing Module

The microfabrication and characterization provided in this work for an encapsulated microball bearing mechanism that supports a fully rotational platform can

be extended into many applications. The design offers the opportunity to include active and passive elements within the fabrication scheme on both the top and bottom of the platform (Figure 5.2). The platform can be fabricated to the point just after bonding the two silicon raceway layers together. After this the two-wafer stack can be handled just like a thick silicon wafer and processing can be performed to embed or surface micromachine MEMS devices or directly fabricate CMOS devices on the surface. Once the elements are completed, the final step would be to release the rotor.

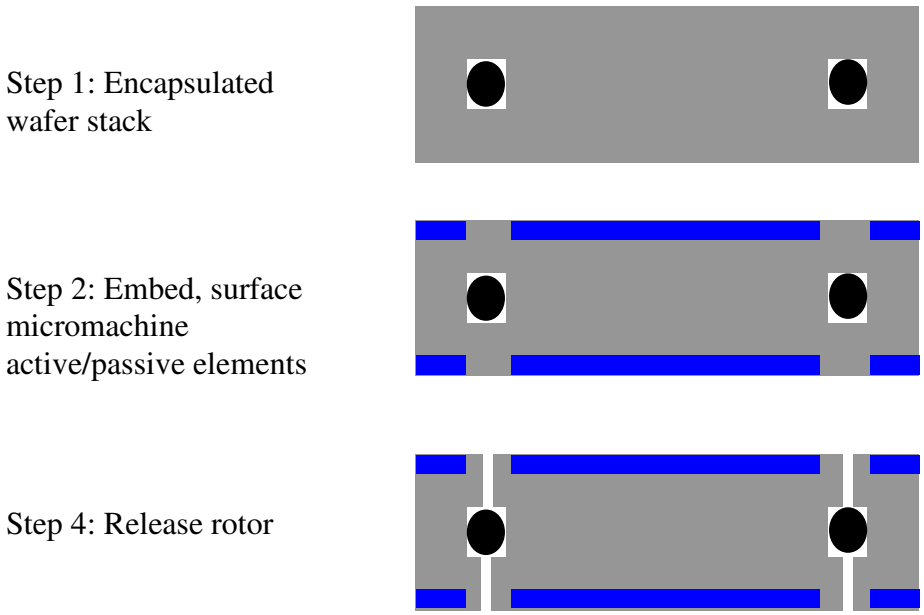

Figure 5.2. Generic fabrication flow for alternative application.

5.3.3 Turbopump Considerations

Experimental observation of the rotor axial position is required to investigate the effect of the adhesion forces between the rotor and the pump plumbing layer. It is not possible to observe the shift of the rotor using the test setup described in this dissertation since the shift is below 10 μm and the optical displacement sensor was placed in the far regime (>200 μm). The device fixture could be altered to allow a second optical displacement sensor to be brought into close proximity (<200 μm) to detect the small axial shift. This would allow tracking of the rotor's axial position during the tests to ensure the rotor is riding on the bearing and not on the pump plumbing layer.

Both the gap uncertainty and pressure rise uncertainty (negative pump inlet pressure) led to discrepancies in the collected experimental data. Installation of +/- differential pressure transducers will allow for accurate pressure rise measurements to be performed. Experiments devised to measure the amount of shrinkage of the photoresist layer during the bonding step will yield accurate estimations of the pump gap. Together, these enhancements will enable an accurate comparison between the experimental pump curves and the pump curves obtained from analytical calculation using Equation 3.8.

The spiral-groove turbopump platform and testing apparatus can be used to study the effect of gap, load, and speed on the viscous loss of the pumping structure. Knowledge of the viscous losses is required to design an efficient motoring mechanism regardless of whether the end design will be a microturbine, an external motor connected via a shaft, or an integrated micromotor. CFD calculations should be performed to investigate the effects of the surface hydrophobicity, liquid pressure, and sealing on the viscous loss in the pumping.

5.3.4 Integrated MEMS micromotor and micropump

The encapsulated microball bearing and viscous pump structures are envisioned to be integrated into a micromotor driven system. The rotary variable capacitance micromotor previously developed in our group by *Ghalichechian* [50] will replace the radial in-flow air turbine detailed in this dissertation. The microball bearing and spiral-groove platform demonstrated will be integrated with the rotary micromotor (Figure 5.3).

Replacing the microturbine with an electrostatic motor will enable the operation of the pump to be simplified from a fluidics standpoint. In this case, the normal force exerted on the rotor can be controlled by electrical means and is no longer coupled to fluidic pumping and fluidic seal. The pump can be designed to be pumped radially inward (Figure 5.3). In this case the inlet can be at ambient pressure. The sealing can then be performed at ambient pressures without requiring an additional balance plenum.

The alignment method developed in this thesis can be implemented to allow die level alignment. Temporary bonding methods can be used so that the bearing/rotor and electrical stator components are interchangeable.

Critical to the design of the micromotor will be the torque requirement. This will dictate the active area required by the micromotor and the overall size of the pump. For the turbopump, the torque was not an issue since the flow through the turbine can be increased until the flow through the nozzle guide vanes is choked. In the case of the rotary micromotor being designed to drive the pump, torque is limited due to the compactness of the design and will be heavily dependent on the gap between the rotor

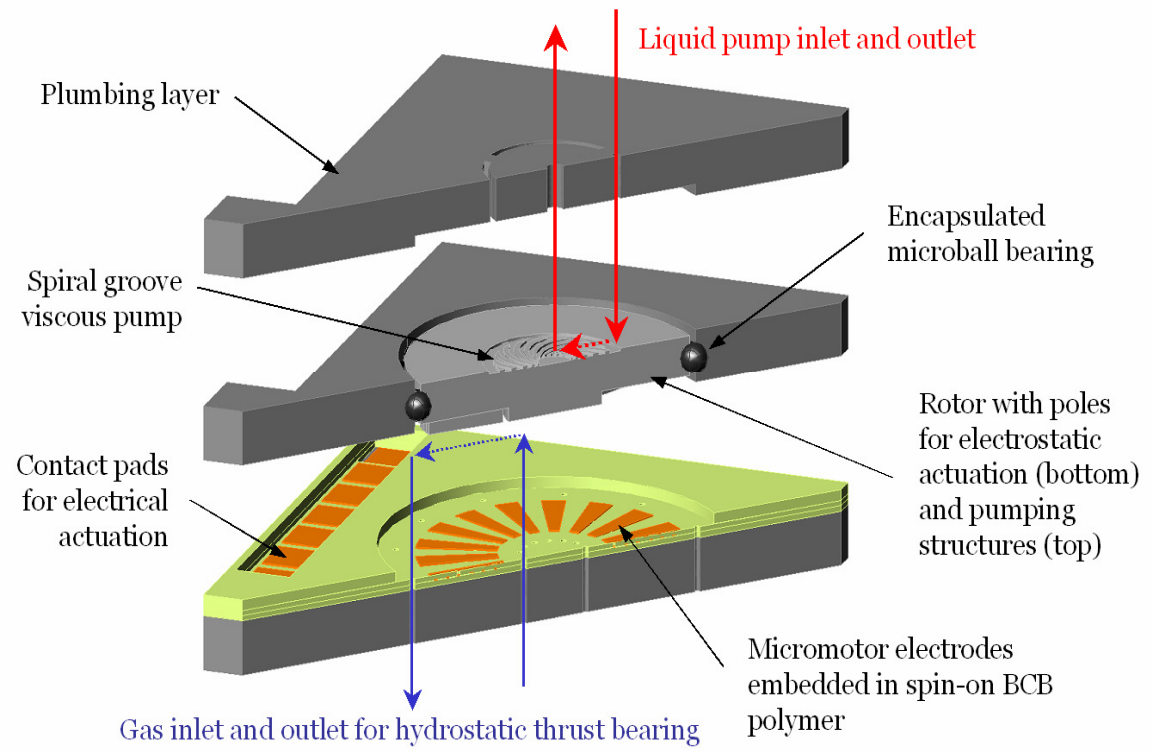

Figure 5.3. Illustration of the electrically driven micropump evolution.

electrodes and stator electrodes, the driving voltage, the number and spacing of electrodes, and the area of the device.

Although torque will be a significant challenge to the micromotor driven pump, the issues of sealing and axial position of the rotor will be greatly simplified. The rotor normal force can be directly controlled via the dc voltage (electrostatic force) and the hydrostatic thrust bearing. This eliminates the coupling between the speed of the rotor (driving pressure of the turbine) and the normal force on the rotor. Additionally, the pump can be designed to pump radially inward. In this case, the periphery can be at ambient to eliminate the need of a controlled sealing pressure.

The work performed in this dissertation focused on the development of the encapsulated microball bearing and the demonstration of the spiral-groove pump

mechanism. These components make up 2/3 of the layers seen in Figure 5.3. Both the development and characterization of these components created a foundation for which the micromotor driven pump device can be realized.

Bibliography

[1] Groshenry, C., "Preliminary study of a micro-gas turbine engine," in *Department of Aerospace Engineering*. Cambridge: Massachusetts Institute of Technology, 1995.

[2] Epstein, A.H., "Millimeter-scale, MEMS Gas Turbine Engines," presented at ASME Turbo Expo 2003 Power for Land, Sea, and Air, Atlanta, Georgia, 2003.

[3] Fréchette, L.G., Lee, C., Arsian, S., and Liu, Y.-C., "Preliminary Design of a MEMS Steam Turbine Power Plant-on-a-chip," presented at 3rd International Workshop on Micro & Nano Technology for Power Generation & Energy Conversion (Power MEMS '03), Makuhari, Japan, 2003.

[4] Walther, D.C. and Pisano, A.P., "MEMS Rotary Engine Power System: Project Overview and Recent Research Results," presented at 4th International Symposium on MEMS and Nanotechnolgy, Charlotte, NC, 2003.

[5] K. Fu, A. Knoblock, F. Martinez, D.C. Walther, A.C. Fernandez-Pello, A.P. Pisano, and D. Liepmann, "Design and Fabrication of a Silicon-based MEMS Rotary Engine," presented at ASME 2001 International Mechanical Engineering Congress and Exposition (IMECE), New York, NY, 2001.

[6] X. Zhang, D. Zheng, T. Wang, C. Chen, J. Cao, J. Yan, W. Wang, J. Liu, H. Liu, J., Tian, X. Li, H. Yang, and B. Xia, "A preliminary study of a miniature planar 6-cell PEMFC stack combined with a small hydrogen storage canister," *Journal of Power Sources*, vol. 166, pp. 441-444, 2007.

[7] S.K. Kamarudin, W.R.W. Daud, S.L. Ho, and U.A. Hasran, "Overview on the challenges and developments of micro-direct methanol fuel cells (DMFC)," *Journal of Power Sources*, vol. 163, pp. 743-54, 2007.

[8] Epstein, A.H., "Power MEMS Compact Power Sources Overview," presented at Collaborative Technology Alliance Conference (CTAC), Crystal City, Virginia, 2005.

[9] W. Deng, J.F. Klemic, X. Li, M.A. Reed, and A. Gomez, "Liquid fuel microcombustor using microfabricated multiplexed electrospray sources," presented at Proceedings of the Combustion Institute, 2007.

[10] W. Deng, J.F. Klemic, X. Li, M.A. Reed, and A. Gomez, "Increase of electrospray throughput using multiplexed microfabricated sources for the scalable generation of monodisperse droplets," *Journal of Aerosol Science*, vol. 37, pp. 696-714, 2006.

[11] D.P. Arnold, G. Herrault, I. Zana, P. Galle, J.-W. Park, S. Das, J.H. Lang, and M.G. Allen, "Design optimization of an 8W, microscale, axial-flux, permanent-magnet generator," *Journal of Micromechanics and Microengineering*, vol. 16, pp. S290-6, 2006.

[12] C. Livermore, A. Forte, T. Lyszczarz, S.D. Umans, and J.H. Lang, "Microscale electric induction machines for power applications," presented at Electrostatics 2003, Edinburgh, Scotland, UK, 2003.

[13] R.S. Besser, and W.C. Shin, "Toward autonomous control of microreactor system for steam reforming of methanol," *Journal of Power Sources*, vol. 164, pp. 328-335, 2007.

[14] Kwon, T. Kim and S., "Design, fabrication and testing of a catalytic microreactor for hydrogen production," *Journal of Micromechanics and Microengineering*, vol. 16, pp. 1760-1768, 2006.

[15] C. Zhang, K. Najafi, L.P. Bernal, and P.D. Washabaugh, "Integrated combust-thermoelectric micro power generator," presented at 11th International Conference on Solid-State Sensors and Actuators (Transducers '01), Berlin, Germany, 2001.

[16] C.M. Waits, B. Geil, R. Ghodssi, "Encapsulated ball bearings for rotary micro machines," *Journal of Micromechanics and Microengineering*, vol. 17, pp. S224-S229, 2007.

[17] C.M. Waits, R. Ghodssi, and B. Geil, "Rotary Ball Bearing Platform for Advanced Power MEMS Components," presented at Sixth International Workshop on Micro and Nanotechnology for Power Generation and Energy Conversion Applications (Power MEMS '06), Berkeley, CA, 2006.

[18] C.M. Waits, N. Jankowski, B. Geil, and R. Ghodssi, "MEMS Rotary Actuator Using an Integrated Ball Bearing and Air Turbine," presented at The 14th International Conference on Solid-State Sensors, and Microsystems (Transducers '07), Lyon, France, 2007.

[19] M. McCarthy, C.M. Waits, and R. Ghodssi, "Development of a Hybrid Gas/Ball Bearing Support Mechanism for Microturbomachinery," presented at Power MEMS 2007, Frieburg, Germany, 2007.

[20] Nam-Trung Nguyen, Xiaoyang Huang, and Toh Kok Chuan, "MEMS-Micropumps: A Review," *Transactions of ASME*, vol. 124, pp. 384-392, 2002.

[21] Santiago, D.J. Laser and J.G., "A Review of Micropumps," *Journal of Micromechanics and Microengineering*, vol. 14, pp. R35-R64, 2004.

[22] Jamonet, L., "Testing of a Microrocket Engine Turbopump," in *Aerospace Engineering*. Cambridge: Massachusetts Institute of Technology, 2002.

[23] Deux, A., "Design of a Silicon Microfabricated Rocket Engine Turbopump," in *Aerospace Engineering*. Cambridge: Massachusetts Institute of Technology, 2001.

[24] Pennathur, S., "Micro-scale Turbopump Blade Cavitation," in *Aeronautics and Astronautics*. Cambridge: Massachusetts Institute of Technology, 2000.

[25] Lee, Changgu, "Development of a Microfabricated Turbopump for a Rankine Vapor Power Cycle," in *Mechanical Engineering*: Columbia University, 2006, pp. 266.

[26] L.G. Fréchette, S.A. Jacobson, K.S. Breuer, F.F. Ehrich, R. Ghodssi, R. Khanna, C.W. Wong, X. Zhang, M.A. Schmidt, and A.H. Epstein, "Demonstration of a Microfabricated High-Speed Turbine Supported on Gas Bearings," presented at Hilton Head Solid-State Sensor & Actuator Workshop, Hilton Head Island, SC, 2000.

[27] Danny Blanchard, Phil Ligrani, and Bruce Gale, "Miniature Single-Disk Viscous Pump (Single-DVP), Performance Characterization," *Journal of Fluids Engineering*, vol. 128, pp. 602-610, 2006.

[28] M. Mehregany, K. J. Gabriel, and W.S.N. Trimmer, "Integrated fabrication of polysilicon mechanisms," *IEEE Transactions on Electron Devices*, vol. 35, pp. 719-723, 1988.

[29] L.G. Fréchette, S.A. Jacobson, K.S. Breuer, F.F. Ehrich, R. Ghodssi, R. Khanna, C.W. Wong, X. Zhang, M.A. Schmidt, and A.H. Epstein, "High-Speed Microfabricated Silicon Turbomachinery and Fluid Film Bearings," *Journal of Microelectromechanical Systems*, vol. 14, pp. 141-152, 2005.

[30] C. Ruffert, R. Gehrking, B. Ponick, and H.H. Gatzen, "Magnetic Levitation Assisted Guide for a Linear Micro-Actuator," *IEEE Transaction on Magnetics*, vol. 42, pp. 3785, 2006.

[31] C. Shearwood, K.Y. Ho, C.B. Williams, and H. Gong, "Development of a levitated micromotor for application as a gyroscope," *Sensors and Actuators A: Physical*, vol. 83, pp. 85, 2000.

[32] C.B. Williams, C. Shearwood, P.H. Mellor, and R.B. Yates, "Modeling and testing of a frictionless levitated micromotor," *Sensors and Actuators A: Physical*, vol. 61, pp. 469, 1997.

[33] J.U. Jeon, S.J. Woo, and T. Higuchi, "Variable-capacitance motors with electrostatic suspension," *Sensors and Actuators A: Physical*, vol. 75, pp. 289, 1999.

[34] X.S. Wu, W.Y. Chen, X.L Zhao, and W.P. Zhang, "Micromotor with electromagnetically levitated rotor using separated coils," *Electronics Letters*, vol. 40, pp. 996-997, 2004.

[35] K. Deng, W.H. Ko, and G.M. Michael, "A preliminary study on friction measurements in MEMS," presented at International Conference on Solid-State Sensors and Actuators, TRANSDUCERS '91, San Francisco, Ca, 1991.

[36] K. Noguchi, H. Fujita, M. Suzuki, and N. Yoshimura, "The measurements of friction on micromechatronics elements," presented at IEEE Micro Electro Mechanical Systems (MEMS'91), Nara, Japan, 1991.

[37] W. Zhang, G. Meng, and H. Li, "Electrostatic micromotor and its reliability," *Microelectronics Reliability*, vol. 45, pp. 1230, 2005.

[38] Hiroshi Satoh, Kazuo Uchida, and Yinchun Cao, "Designing An Ultra-Low Specific Speed Centrifugal Pump," presented at 22nd International Pump Users Symposium, 2005.

[39] A.P. London, A.H. Epstein, and J.L. Kerrebrock, "A High Pressure Bipropellant Microrocket Engine," *AIAA Journal of Propulsion and Power*, vol. 17, pp. 780-787, 2001.

[40] A. Modafe, N. Ghalichechian, A. Frey, J.H. Lang, and R. Ghodssi, "Microball-Bearing-Supported Electrostatic Micromachines with Polymer Dielectric Films for Electrocmechanical Power Conversion," *Journal of Micromechanics and Microengineering*, vol. 16, pp. S182-S190, 2006.

[41] N. Ghalichechian, A. Modafe, J.H. Lang, and R. Ghodssi, "Dynamic Characterization of a Linear Electrostatic Micromotor Supported on Microball Bearings," *Sensors and Actuators A. Physical*, vol. 136, pp. 416-503, 2007.

[42] R. Ghodssi, D.D. Denton, A.A. Seireg, and B. Howland, "Rolling Friction in a linear microactuator," *Journal of Vacuum Science and Technology A*, vol. 11, pp. 803-807, 1993.

[43] T.-W. Lin, A. Modafe, B. Shapiro, and R. Ghodssi, "Characterization of Dynamic Friction in MEMS-based Microball Bearings," *IEEE Transactions on Instrumentation and Measurement*, vol. 53, pp. 839-846, 2004.

[44] T-W. Lin, D. Wendland, B. Shapiro, and R. Ghodssi, "Measurement of Rolling Friction for MEMS Applications," presented at American Vacuum Society 48th International Symposium, San Francisco, CA, 2001.

[45] X. Tan, A. Modafe, and R. Ghodssi, "Measurement and Modeling of Dynamic Rolling Friction in Linear Microball Bearings," *Journal of Dynamic Systems, Measurement, and Control*, vol. 128, pp. 891-898, 2006.

[46] M. McCarthy, C.M. Waits, and R. Ghodssi, "Dynamic Friction and Microturbine Performance Using A Planar-contact Encapsulated Microball Bearing," presented at To be presented at the 2008 Solid-State Sensor, Actuator, and Microsystems Workshop, Hilton Head, South Carolina, 2008.

[47] C.M. Waits, M. McCarthy, and R. Ghodssi, "Microfabricated Turbopump Using Microball Bearings," *To be submitted to IEEE Journal of Microelectromechanical Systems*, 2008.

[48] A. Modafe, N. Ghalichechian, J.H. Lang, and R. Ghodssi, "A Microball-Bearing-Supported Linear Electrostatic Micromotor with Benzocyclobutene Polymer Insulating Layers," presented at The 13th International Conference on Solid-State Sensors, Actuators, and Microsystems (Transducers '05), Seoul, Korea, 2005.

[49] B. Hanrahan, M. McCarthy, C. Zorman, and R. Ghodssi, "Wear in MEMS-Based Microball Bearings," presented at American Vacuum Society 54th International Symposium, Seattle, WA, 2007.

[50] Ghalichechian, Nima, "Design, Fabrication, and Characterization of a Rotary Variable-Capacitance Micromotor Supported on Microball Bearings," in *Department of Electrical and Computer Engineering*. College Park, MD: University of Maryland, 2007.

[51] C.M. Waits, Brian Morgan, M.J. Kastantin, and R. Ghodssi, "Microfabrication of 3D Silicon MEMS Structures using Gray-scale Lithography and Deep Reactive Ion Etching," *Sensors and Actuators A: Physical*, vol. 119, pp. 245-253, 2005.

[52] "Gold Tin - The Unique Eutectic Solder Alloy." Application Note: Indium Corporation.

[53] Harris, Tedric A., *Rolling Bearing Analysis*, 3rd ed. New York: John Wiley & Sons, Inc., 1991.

[54] Houpert, Luc, "An Engineering Approach to Hertzian Contact Elasticity - Part I," *Journal of Tribology*, vol. 123, pp. 582-588, 2001.

[55] Muijderman, E. A., *Spiral Groove Bearings*. Eindhoven, The Netherlands: N.V. Philips' Gloeilampendabrieken, 1966.

[56] Lakshminarayana, *Fluid Dynamics and Heat Transfer of Turbomachinery*. New York: John Wiley & Sons, Inc, 1996.

[57] Weng Kong Chan, Yew Wah Wong, and Wei Hu, "Design Considerations of Volute Geometry of a Centrifugal Blood Pump," *Artificial Organs*, vol. 29, pp. 937-948, 2005.

[58] Harrison, N.R. Pallas and Y., "A automated drop shape apparatus and the surface tension of pure water," *Colloids and Surfaces*, vol. 43, pp. 169-194, 1990.

[59] Osman, H. A. Arafa and T.A., "Viscous pumps: comparative assessment of effectiveness," *Journal of Engineering Tribology*, vol. 217, pp. 167-174, 2003.

[60] Ligrani, Danny Blanchard and Phil, "Comparisons of different viscous pumps based on physical flow behavior," *Sensors and Actuators A*, vol. 126, pp. 83-92, 2006.

[61] Hsing, F.C., "Analytical Solutions for Incompressible Spiral Groove Viscous Pumps," *Journal of Lubrication Technology*, pp. 365-369, 1974.

[62] Bhushan, B., "Adhesion and stiction: Mechanics, measurement techniques, and methods for reduction," *Journal of Vacuum Science and Technology B*, vol. 21, pp. 2262-2296, 2003.

[63] N. Ghalichechian, A. Modafe, M. Beyaz, and R. Ghodssi, "Design, Fabrication, and Characterization of a Rotary Micromotor Supported on Microball Bearings," *Journal of Microelectromechanical Systems (JMEMS)*, vol. In Press, 2007.

[64] M. McCarthy, B. Hanrahan, C. Zorman, and R. Ghodssi, "Rolling Friction in MEMS Ball Bearings: The Effects of Loading and Solid Film Lubrication," presented at STLE/ASME International Joint Tribology Conference, San Diego, California, 2007.

Record of Publication for Related Work

Journal Papers

1. C.M. Waits, M. McCarthy, and R. Ghodssi, “A Microfabricated Turbopump Using Microball Bearings,” *to be submitted to Journal of Microelectromechanical Systems*, August 2008.
2. M. McCarthy, C.M. Waits, B. Hanrahan, and R. Ghodssi, “Dynamic Friction and Wear in a Planar-Contact Encapsulated Microball Bearing using an Integrated Microturbine”, *submitted to Journal of Microelectromechanical Systems*, April 2008.
3. C.M. Waits, B. Geil, and R. Ghodssi, “Encapsulated Ball Bearings for Rotary Micro Machines”, *Journal of Micromechanics and Microengineering (JMM)*, Vol. 17, pp. S224-S229, 2007

Conference Papers with Proceedings

4. M. McCarthy, C.M.Waits, and R. Ghodssi, “Dynamic Friction and Microturbine Performance Using A Planar-contact Encapsulated Microball Bearing,” *Presented at the 2008 Solid-State Sensor, Actuator, and Microsystems Workshop*, June 1-5, Hilton Head, South Carolina, pp. 170-173, 2008
5. M. McCarthy, C. M. Waits and R. Ghodssi, "Development of a Hybrid Gas / Ball Bearing Support Mechanism for Microturbomachinery," *7th International Workshop on Micro and Nanotechnology for Power Generation and Energy Conversion Application (Power MEMS '07)*, Frieburg, Germany, November 28-29, 2007.
6. C.M. Waits, N. Jankowski, B. Geil, and R. Ghodssi, "MEMS Rotary Actuator using an Integrated Ball Bearing and Air Turbine", *The 14th International Conference on Solid-State Sensors, and Microsystems (Transducers '07),* Lyon, France, June 10-14, 2007.
7. N. Ghalichechian, A. Modafe, M. I. Beyaz, C. M. Waits, and R. Ghodssi, "Design and Fabrication of a Rotary, Electrostatic Micromotor Supported on Microball Bearings," *Sixth International Workshop on Micro and Nanotechnology for Power Generation and Energy Conversion Applications (Power MEMS '06),* pp. 227-230, Berkeley, CA, USA, Nov 29-Dec 1, 2006.
8. C. M. Waits, R. Ghodssi, and B. Geil "Rotary Ball Bearing Platform for Advanced Power MEMS Components," *Sixth International Workshop on Micro and Nanotechnology for Power Generation and Energy Conversion Applications (Power MEMS '06),* pp. 149-152, Berkeley, CA, USA, Nov 29-Dec 1, 2006.